**UNIVERSITY OF SOUTHAMPTON**

FACULTY OF ENGINEERING, SCIENCE AND MATHEMATICS

School of Mathematics

# Equilibria and Oscillations of Magnetised Neutron Stars

by

**Samuel Kenneth Lander**

Thesis for the degree of Doctor of Philosophy

April 2010

UNIVERSITY OF SOUTHAMPTON

ABSTRACT

Faculty of Engineering, Science and Mathematics
School of Mathematics

Doctor of Philosophy

**Equilibria and Oscillations of Magnetised Neutron Stars**

by Samuel Kenneth Lander

We investigate equilibrium configurations and oscillation spectra of neutron stars, modelled as rotating magnetised fluid bodies in Newtonian gravity. We also explore the idea that these model neutron stars could have dynamics analogous to rigid-body free precession.

In axisymmetry, the equations of magnetohydrodynamics reduce to a purely toroidal-field case and a mixed-field case (with a purely poloidal-field limit). We solve these equations using a nonlinear code which finds stationary rotating magnetised stars by an iterative procedure. We find that despite the general nature of our approach, the mixed-field configurations we produce are all dominated by their poloidal component. We calculate distortions induced both by magnetic fields and by rotation; our results suggest that the relationship between the magnetic energy and the induced ellipticity should be close to linear for all known neutron stars.

We then investigate the oscillation spectra of neutron stars, using these stationary configurations as a background on which to study perturbations. This is done by evolving the perturbations numerically, making the Cowling approximation and specialising to purely toroidal fields for simplicity. The results of the evolutions show a number of magnetically-restored Alfvén modes. We find that in a rotating star pure inertial and pure Alfvén modes are replaced by hybrid magneto-inertial modes. We also show that magnetic fields appear to reduce the effect of the $r$-mode instability.

Finally, we look at precession-like dynamics in magnetised fluid stars, using both analytic and numerical methods. Whilst these studies are only preliminary, they indicate deficiencies in previous research on this topic. We suggest ways in which the problem of magnetised-fluid precession could be better understood.

# Contents

# List of Tables

# List of Figures

# DECLARATION OF AUTHORSHIP

I, Samuel Kenneth Lander, declare that the thesis entitled "Equilibria and Oscillations of Magnetised Neutron Stars" and the work presented in the thesis are both my own, and have been generated by me as the result of my own original research. I confirm that:

- this work was done wholly or mainly while in candidature for a research degree at this University;
- where I have consulted or quoted from the work of others, this is always clearly attributed. With the exception of such quotations, this thesis is entirely my own work;
- I have acknowledged all main sources of help;
- where the thesis is based on work done by myself jointly with others, I have made clear exactly what was done by others and what I have contributed myself.
- Chapter 6 is based on a nonmagnetic code written by Nikolaos Stergioulas; chapter 7 is based on a nonmagnetic code written by Ian Jones and improved by Andrea Passamonti. I have extended both codes to include magnetic fields.
- Parts of this work have been published as:
  S.K. Lander and D.I. Jones, "Magnetic Fields in Axisymmetric Neutron Stars", Mon. Not. R. Astron. Soc., **395**:2162-2176, 2009
  and
  S.K. Lander, D.I. Jones and A. Passamonti "Oscillations of Rotating Magnetised Neutron Stars with Purely Toroidal Magnetic Fields", accepted for publication in Mon. Not. R. Astron. Soc., 2010

**Signed:**

**Date:**

# Acknowledgements

Firstly, I would like to thank my supervisor Ian Jones for all his help. If parts of this thesis prove comprehensible, it is probably because I have successfully imitated his unpretentious physics-first style of explanation. I am also grateful to my advisor Nils Andersson; through many discussions and a fair bit of constructive abuse, he has helped to keep my project on track. Rather than now ranking the rest of the Relativity group at Southampton in order of helpfulness, let me just say that they have all contributed to a very good working environment and that I am grateful to everyone for their various contributions to my understanding.

Beyond the realm of the purely scientific, I would like to acknowledge the company of the many friends and acquaintances I have made in my time in Southampton. A list of these would always be incomplete, but at least two people ought to have specific mentions here. Steve Millmore deserves recognition for managing to endure the misfortune of three years sharing an office with me, and still being a good friend beyond its asbestos-ridden walls. In addition Bob Rimington has helped to keep me sane through this last, sometimes tense, year of work.

Finally I would like to thank my family, and my mum especially. I owe her a great deal for her support over the years.

# Chapter 1

# Introduction

## 1.1 Neutron star physics

Of all the objects in the Universe, the properties of neutron stars perhaps rank them as the most extreme and complex yet observed. These stars contain more mass than the Sun, contained within a sphere whose radius is only around 10 km. The binding energy and surface gravity of these objects is hence enormous. The spacing of nucleons in ordinary nuclear matter is dictated by the nuclear force, which is strongly repulsive at short distances; however, this repulsion is in part counter-acted by the great pressure in neutron star interiors. The result is that the mean mass density of a neutron star is around three times that of heavy nuclei. The atomic nature of normal matter is replaced, predominantly, by liquid neutron matter. There are neutron stars that rotate fast enough to tear apart any less-compact object (neutron star periods may be as short as a millisecond) and others whose magnetic fields exceed those on Earth by a factor of $10^{15}$.

We cannot create the extreme conditions present in neutron stars on Earth, which means good modelling and observations are essential to understand these objects. These two disciplines exist in a symbiotic relationship: observations help constrain theoretical models of neutron stars, whilst theory helps in the understanding of current observations and can suggest specific features that observers can look out for. In the process of studying neutron stars, we also gain an understanding of how terrestrial physics changes at the extremes of pressure, density, magnetic field strength and so on. Many branches of physics contribute to the understanding of these com-

plex objects: among others, they include General Relativity, plasma physics, nuclear physics, thermodynamics, superfluidity, superconductivity and particle physics.

Our attempts to understand these stars are obstructed by the difficulty in observing them. Despite a wealth of data from radio astronomers and some other sources, our knowledge of neutron star physics is still limited, particularly in the stellar interior. However, by virtue of their compact nature we should soon have another means of observing them, beyond their signature in the electromagnetic (EM) spectrum. Gravitational radiation, a phenomenon which emerges when modelling gravity within General Relativity, can provide information about its source which could never be seen in the EM data. In a few years from now gravitational-wave detectors on Earth should be greatly enhancing our knowledge of neutron stars, *provided* our theoretical models are good enough; this is an example of the symbiosis described in the previous paragraph.

More detailed descriptions of various topics mentioned here are given in the rest of this chapter and other introductory sections throughout this thesis. In addition, more thorough summaries of the subject may be found in Shapiro and Teukolsky [126] or Haensel, Potekhin and Yakovlev [62]. The remainder of this chapter discusses the formation and structure of neutron stars, with a mention of observations. We then derive the quadrupole formula for gravitational radiation from Einstein's field equations and discuss the prospects for observing neutron stars through their emission of this radiation.

### 1.1.1 The formation of compact objects

Neutron stars (together with black holes and white dwarfs) belong to the astronomical genus of *compact objects*, the dense remnants from the death of a normal star. The mass $M$ of the original star approximately determines which compact object is formed at the end of its life: the lightest stars ($M \lesssim 8M_\odot$)[1] form white dwarfs, while larger ones may form neutron stars or black holes, depending on the details of their collapse.

Why should a star collapse in the first place? Ordinary stars are stable through hydrostatic equilibrium — the balance between thermal pressure and gravitational force. The thermal pressure is sustained by the burning (fusion) of elements within

[1] We use the symbol $M_\odot$ for the mass of the Sun

the star, beginning with hydrogen (which requires the lowest ignition temperature for fusion) and then progressing to the burning of heavier elements with successively higher ignition temperatures. At some point the star will run out of fuel to sustain its thermal pressure and its core will undergo gravitational collapse [126].

For stars with $M \lesssim 8M_{\odot}$ the core will have insufficient heat to fuse elements heavier than those around oxygen and will begin collapse at this point. However its mass will be lower than the Chandrasekhar mass [20], and will thus be supported against further collapse by the pressure of degenerate relativistic electrons; this is a white dwarf. For heavier parent stars ($M > 8M_{\odot}$), the burning around the core continues until the temperature is high enough for the fusion of silicon, whilst the core becomes rich in heavy, iron-group elements. In a complex coda to the evolution, the core implodes rapidly with neither thermal nor electron pressure able to prevent it. The formation of a shock front then leads to the violent ejection of all stellar material apart from the core in a *supernova* explosion [53].

The nature of the compact object left after the supernova depends on the amount of material ejected by the explosion. If a sufficent amount of material is ejected the remaining collapsed core cools and reaches an equilibrium as an object formed of degenerate neutron-rich matter; this is a neutron star. Finally, if insufficient material is ejected at the supernova stage, the core exceeds the *Oppenheimer-Volkoff* mass limit [105, 11], which in analogy to the Chandrasekhar mass is the maximum mass that can be sustained against gravitational collapse by degenerate neutron pressure. In this case the core collapses completely to form a black hole.

### 1.1.2 Neutron star structure

Having looked at the origins of compact objects[2], we now concentrate on neutron stars and their structure. From the description of their creation above, one might envisage a neutron star to be like a giant nucleus, but this simple idea highlights two key differences between neutron stars and more familiar nuclear matter. Firstly, whilst the nucleus is bound together by the strong nuclear force, a neutron star is held together by its self-gravity; secondly the proportion of neutrons in a neutron star is much greater than that of an atomic nucleus. The neutron-rich nature of a

[2]Note that not all black holes, however, are formed from ordinary stars in the simple manner described above

NS comes about from absorption of high-energy electrons by protons in the inverse beta decay:

$$p + e^- \longrightarrow n + \nu_e.$$

This process becomes more energetically favourable at higher densities, reducing the proportion of protons and increasing the neutron fraction within nuclei. Since all but the outermost regions of a NS are at high enough density for this process to occur, the majority of the star will be neutron-rich through this process.

A neutron star has five main regions (see figure 1.1): the inner and outer cores, the crust, the ocean and the atmosphere; the last two of these regions, labelled as the outer envelopes on the figure, contain negligible mass but play important roles in the star's physics [87].

### Outer regions

These outer regions or 'envelopes' contain a majority of nuclei rather than free neutrons. In these regions the nuclei are $^{56}$Fe or lighter and the pressure is provided by degenerate relativistic electrons. The outermost region is the atmosphere, a thin ($\sim$ 1 cm) layer of plasma where thermal electromagnetic radiation emitted from the NS is formed. Below this, there is an envelope extending over a distance of $\sim 10 - 100$ m where the density increases to a point at which the ions become a liquid; this region is called the NS ocean.

### Crust

Below the thin fluid outer regions the ocean solidifies and the crust of the neutron star begins. As the density increases the beta capture of electrons becomes more energetically favourable and protons are converted into neutrons; deeper into the crust the nuclei thus become more neutron-rich. Eventually, around $\sim 0.3$ km into the star, the 'neutron drip density' $4 \times 10^{11}$ g cm$^{-3}$ is reached: at this point neutrons start to leak out of their nuclei and form a free neutron fluid. For temperatures less than $\sim 0.1$ MeV this crustal neutron fluid is thought to be a superfluid [8], which may affect the way the neutron star cools, as well as storing angular momentum that may play a role in pulsar glitches [2]. The crust is sometimes regarded as an outer and an inner crust, with the outer crust extending down to the neutron drip density and the inner crust continuing from there. The inner crust consists of a mixture

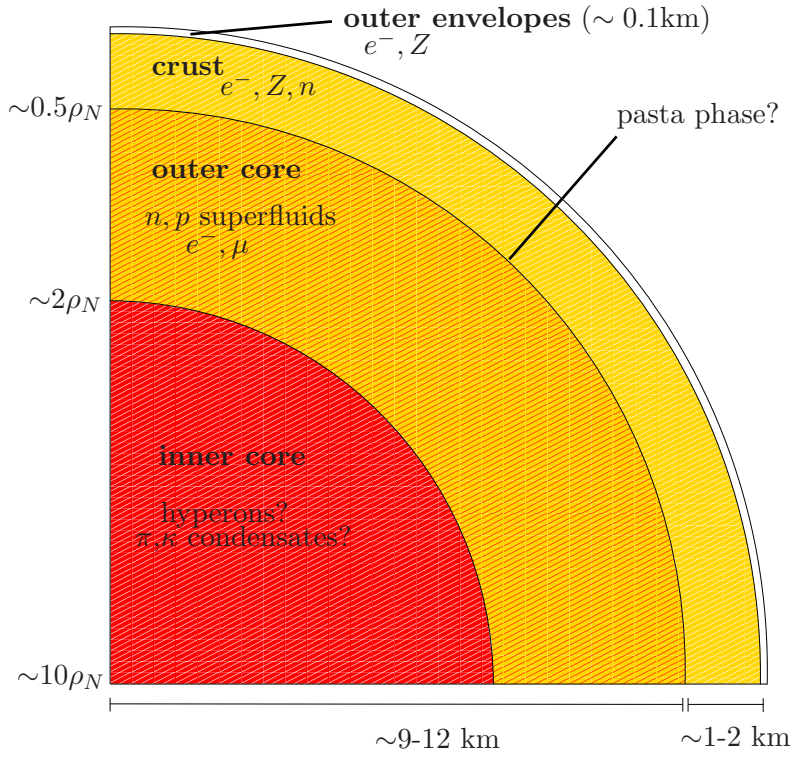


Figure 1.1: Cross-section of the main regions of a neutron star, showing the approximate thicknesses of the largest regions, together with their constituent matter and approximate densities in terms of the nuclear density $\rho_N = 2.8 \times 10^{14}$g cm$^{-3}$. Greek letters represent the corresponding particle — $\mu, \kappa, \pi$ are muons, kaons and pions — whilst $Z$ represents ions.

of nuclei surrounded by a neutron superfluid and is thought to be around $\sim$ 1 km thick.

### Pasta phase

Between the inner crust and the core there may be a transition called nuclear pasta [114] — see figure 1.2. Here the increasing density causes the remaining nuclei to align into first a 3D lattice, then a 2D arrangement of lines of nucleonic matter, then 1D slabs separated by similar slabs of neutron fluid. The nuclei have lost any 'identity' by this point; the nucleonic matter also contains neutron fluid, mixed with

protons, electrons and muons. Deeper still the (neutron superfluid) voids themselves form a lattice surrounded by nucleonic fluid, before a final smooth transition into a uniform mixture of nucleonic matter — the outer core. It should be pointed out, however, that the existence of this pasta layer is highly dependent on the equation of state used to model the NS[62].

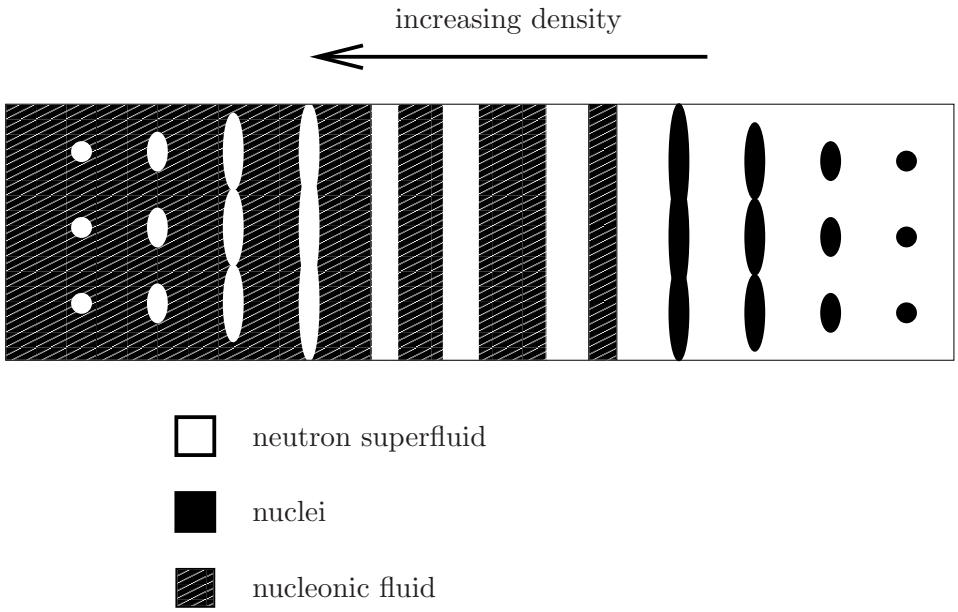


Figure 1.2: Nuclear pasta. At the right-hand side the neutron drip density has already been exceeded, and the remaining lattice of nuclei is surrounded by neutron fluid. As the density is increased (i.e. further into the star) the remaining nuclei are compressed first into 2D lattice of vertical nucleonic lines, then nucleonic slabs. Further in still, we may regard the original neutron fluid as forming a lattice of voids surrounded by nucleonic fluid, before finally becoming a uniform soup of nucleons on the left-hand side.

### Core

The core may contribute up to 99% of the neutron star's mass and is often predicted to be composed of two separate regions, the outer and inner core, both several kilometres thick. The outer core is thought to consist of superfluid neutrons and superconducting protons, as well as electrons and muons. The density in this region

increases beyond the nuclear density $\rho_N = 2.8 \times 10^{14}$ g cm$^{-3}$ to $\sim 2\rho_N$ to a region where the physics is least certain: the inner core. The extreme densities of this region — predicted to be as high as $\sim 10\rho_N$ at the centre — may contain unfamiliar kinds of matter that have not been found experimentally in the laboratory. The inner core may contain an abundance of exotic particles such as hyperons (baryons with one or more of their three quarks being strange) or perhaps a Bose condensate of pions or kaons[8, 9].

Like the pasta region, the nature of the inner core differs considerably between equations of state. It is far from clear, in fact, that the region even exists in real neutron stars — it requires the star to be sufficiently compact for the central density to exceed $\sim 2\rho_N$. Otherwise, the core will be entirely composed of the 'outer core' matter described above [62].

### 1.1.3 Equation of state

To build models of neutron stars one needs an *equation of state* to relate the star's pressure $P$ to its mass density $\rho$ and temperature $T$. This has to encode the properties of all the different NS regions from centre to surface. For all but very young neutron stars, the internal temperatures are thought to be around $10^6 - 10^8$ K — a number which is 'hot' for many physical situations but cold compared with the Fermi energy $T_{\rm Fermi} \sim 10^{12}$ K. It is therefore assumed that $T = 0$, so that the equation of state is *barotropic*; $P$ is a function of $\rho$ alone.

Calculations of neutron star equations of state involve detailed consideration of the microphysics of nuclear interactions. The results are tabulated pressure-density relations rather than simple analytic models; Haensel, Potekhin and Yakovlev [62] provide a good survey of these studies. These 'realistic' equations of state include relativistic effects and so are suitable for constructing stellar models in General Relativity, but by the same token there is no real benefit to using them in Newtonian gravity.

For Newtonian stars, it is common to use a polytropic EOS $P(\rho) = k\rho^\gamma \equiv k\rho^{1+1/N}$, where $k, N$ and $\gamma$ are constants. The $N = 1$ (or equivalently, $\gamma = 2$) polytrope provides a simple neutron star model that nonetheless shares many features with more sophisticated models: for example, the pressure-density dependence $P \propto \rho^2$ provides a rough approximation of realistic EOSs. Another similarity is in

the mass-radius relation. For $N = 1$ polytropes, the radius is given by

$$R = \sqrt{\frac{\pi k}{2G}}$$

— see, e.g., Chandrasekhar [22] — and hence is independent of the mass. This is mirrored by realistic EOSs, where radius is only weakly dependent on mass[86]. In this thesis, neutron stars are modelled in Newtonian gravity, so we typically use the $N = 1$ polytropic EOS.

In much of the literature on neutron stars, and within this thesis, the parameters of mass and radius are given the 'canonical' values of $M = 1.4M_{\odot}$ and 10 km, respectively. The former value is more certain than the latter; the mass of a NS is quite closely constrained on theoretical grounds. Beyond a certain mass a neutron star will collapse to a black hole, whilst if a NS is too light it will be unstable to radial oscillations[53]. A recent estimate by Strobel and Weigel [132] has a (nonrotating) NS mass lying between $M_{min} = 0.9 - 1.3M_{\odot}$ and $M_{max} = 1.7 - 2.7M_{\odot}$; these estimated ranges are typical for EOSs that assume normal nuclear matter (rather than any kind of 'exotic' matter consisting of hyperons or quarks) [62]. For typical EOSs the mass of $1.4M_{\odot}$ corresponds to a radius of $\sim 10$ km; no direct measurements of NS radii exist.

### 1.1.4 Observing neutron stars

The prospects for detecting a tiny, dark object (neutron stars do not undergo the incandescent fusion of ordinary stars) in the sky would seem very poor; for this reason Baade and Zwicky's early predictions about the existence of neutron stars[7] received little attention. However, neutron stars are observed today in many manifestations; these include radio pulsars, anomalous X-ray pulsars, soft gamma repeaters and low-mass X-ray binaries (the latter being a binary system with a neutron star and another less compact star). Depending on the class of neutron star, their visible emission may be predominantly X-rays, gamma-rays, or most commonly in the radio spectrum. In many cases, signals from neutron stars are powered by their strong magnetic fields; details of this are given in section 2.1.

Their characteristically regular radio emission has enabled over 1500 pulsars to be recorded to date[95], which has greatly increased our knowledge of the properties of neutron stars. Pulsar timing data has shown that NSs have a wide range of spin

rates; although rotational periods of around $0.1 - 2$ s are typical, there is also a family of millisecond-period pulsars[94]. Measuring the luminosity of a NS gives information on its magnetic field; at the stellar surface the field strength may reach $\sim 10^{12}$ G for ordinary pulsar-NSs and $\sim 10^{15}$ G for magnetars, an exceptionally highly magnetised class of NS.

Over time a neutron star will lose angular momentum and magnetic field strength. With some theory about how long these processes take, we are thus able to use observed periods and luminosities to estimate the ages of NSs. An isolated NS will eventually drop below the 'death line', where its luminosity is so low and period so long that it can no longer be detected. The oldest pulsars we know are those who form a binary system with a main-sequence star, accreting material from the companion star and gaining angular momentum. This process results in 'recycled' pulsars, who have low surface magnetic fields ($\sim 10^8$ G) but periods that may be of the order of milliseconds.

We conclude this section with an effect that is *not* seen in many pulsar observations, but which one might naïvely expect to be very common: precession. We know that whilst neutron stars are very close to spherical, they are likely to have some modest degree of distortion due to crustal deformations and their magnetic fields. If the distortion is not symmetric about the rotation axis, then a rigid-body analogy suggests that the star should precess; this would be seen as some long-term modulation of the radio pulses [73]. However precessing pulsars seem to be very rare, with one strong candidate[92], but few others; the reasons behind this are unknown. This topic is covered in more detail in chapter 3.

## 1.2 Gravitational waves

One of the key predictions of General Relativity is the existence of gravitational waves which, with their promise of carrying information from distant points of the Universe to Earth with little interference, are of great interest to astrophysicists. Neutron stars are promising sources of detectable gravitational radiation — and should we manage to observe NSs through this radiation, not only would we have another test to confirm GR, but we would also find out a lot more about the physics of neutron stars.

Here we outline the steps to establishing a wave-generation formalism from the

Einstein equations. Firstly we linearise the full Einstein equations (1.2.1) in the metric perturbation $h_{\mu\nu}$ and use gauge freedoms to yield a wave equation (1.2.9). We then solve this wave equation with some general physical assumptions to find the quadrupole formula (1.2.16), which relates gravitational wave amplitude to the second time derivative of the source's mass distribution. We conclude the section with a discussion of neutron stars as gravitational wave sources.

### 1.2.1 The linearised Einstein equations

We begin with the Einstein field equations [42, 102]:

$$G_{\mu\nu} = 8\pi T_{\mu\nu} \tag{1.2.1}$$

where as usual $T_{\mu\nu}$ is the stress-energy tensor and $G_{\mu\nu} = R_{\mu\nu} - \frac{1}{2}Rg_{\mu\nu}$ is the Einstein curvature tensor, formed from contractions of the Riemann curvature tensor $R_{\mu\nu} = R^{\alpha}{}_{\mu\alpha\nu}$ and $R = R^{\mu}{}_{\mu}$. The Riemann curvature tensor itself is defined by

$$R^{\alpha}{}_{\beta\gamma\delta} = \Gamma^{\alpha}{}_{\beta\delta,\gamma} - \Gamma^{\alpha}{}_{\beta\gamma,\delta} + \Gamma^{\alpha}{}_{\mu\gamma}\Gamma^{\mu}{}_{\beta\delta} - \Gamma^{\alpha}{}_{\mu\delta}\Gamma^{\mu}{}_{\beta\gamma} \tag{1.2.2}$$

where

$$\Gamma^{\alpha}{}_{\beta\delta} = g^{\alpha\mu}\Gamma_{\mu\beta\gamma} = \frac{1}{2}g^{\alpha\mu}(g_{\mu\beta,\gamma} + g_{\mu\gamma,\beta} - g_{\beta\gamma,\mu}) \tag{1.2.3}$$

are the *connection coefficients* or *Christoffel symbols*.

We now use some general physical assumptions to simplify these equations into a formalism for calculating gravitational waves. First we use the shortwave approximation: let $\lambda$ be the typical wavelength and $\mathcal{R}$ the typical radius of curvature of the background, then we require that $\frac{\lambda}{2\pi}/\mathcal{R} \ll 1$. With this assumption we can average the metric over several wavelengths to obtain a 'background curvature' $g^{(B)}_{\mu\nu} = \langle g_{\mu\nu} \rangle$ and then write the full metric as a sum of this background and a perturbation piece:

$$g_{\mu\nu} = g^{(B)}_{\mu\nu} + h_{\mu\nu} \tag{1.2.4}$$

where we have chosen an appropriate coordinate frame so that $|h_{\mu\nu}| \ll 1$. When studying weak gravitational field situations we can expand the field equations (1.2.1) in powers of $h_{\mu\nu}$; with only the linear terms we have 'the linearised theory of gravity', which we now work with. In this theory, the (linearised) connection coefficients are

$$\begin{aligned} \Gamma^{\mu}_{\alpha\beta} &= \frac{1}{2}g^{\mu\nu(B)}(h_{\alpha\nu,\beta} + h_{\beta\nu,\alpha} - h_{\alpha\beta,\nu}) \\ &= \frac{1}{2}(h_{\alpha}{}^{\mu}{}_{,\beta} + h_{\beta}{}^{\mu}{}_{,\alpha} - h_{\alpha\beta}{}^{,\mu}). \end{aligned} \tag{1.2.5}$$

Note that when expanding in powers of $h_{\mu\nu}$ we raise and lower indices with $g^{\mu\nu(B)}$ and $g^{(B)}_{\mu\nu}$ rather than the usual $g^{\mu\nu}$ and $g_{\mu\nu}$. With a similar linearisation of the Ricci tensor $R_{\mu\nu} = \Gamma^{\alpha}_{\ \mu\nu,\alpha} - \Gamma^{\alpha}_{\ \mu\alpha,\nu}$ and defining the trace-reversed pseudotensor

$$\bar{h}_{\mu\nu} \equiv h_{\mu\nu} - \frac{1}{2} g^{(B)}_{\mu\nu} h \tag{1.2.6}$$

(where $h \equiv h^{\alpha}_{\ \alpha} = g^{\alpha\beta(B)} h_{\alpha\beta}$), we find that the linearised field equations are

$$-\bar{h}_{\mu\nu,\alpha}^{\ \ \ \ \alpha} - g^{(B)}_{\mu\nu} \bar{h}_{\alpha\beta,}^{\ \ \ \ \alpha\beta} + \bar{h}_{\mu\alpha,}^{\ \ \ \alpha}{}_{\mu} + \bar{h}_{\nu\alpha,}^{\ \ \ \alpha}{}_{\mu} = 16\pi T_{\mu\nu}. \tag{1.2.7}$$

We denote the D'Alembertian term by $\Box\bar{h}_{\mu\nu} \equiv \bar{h}_{\mu\nu,\alpha}^{\ \ \ \ \alpha}$ and without loss of generality we may impose the Lorentz gauge conditions

$$\bar{h}^{\mu\alpha}_{\ \ \ ,\alpha} = 0 \tag{1.2.8}$$

under which the equations (1.2.7) become

$$\Box\bar{h}_{\mu\nu} = -16\pi T_{\mu\nu}. \tag{1.2.9}$$

So far we have shown that linearising the full Einstein equations (1.2.1) in the shortwave approximation leads to the wave equation (1.2.9). We now wish to solve this wave equation to find a formula for gravitational wave generation for slow-motion sources and weak fields.

### 1.2.2 The quadrupole formula

Equation (1.2.9) can be solved using a Green's function to give the retarded integral

$$\bar{h}_{\mu\nu}(t, \mathbf{x}) = 4 \int \frac{T_{\mu\nu}(t - |\mathbf{x} - \mathbf{x}'|, \mathbf{x}')}{|\mathbf{x} - \mathbf{x}'|} \, \mathrm{d}\mathbf{x}'. \tag{1.2.10}$$

We proceed using the equations of energy-momentum conservation $T^{\mu\nu}_{\ \ ;\nu} = 0$; neglecting the source's self-gravity, this set of equations reduces to the flat-space version (the background metric $g^{(B)}_{\mu\nu}$ is now just the Minkowski metric $\eta_{\mu\nu}$):

$$T^{\mu\nu}_{\ \ ,\nu} = 0. \tag{1.2.11}$$

We work in a globally inertial frame so that coordinate time derivatives $x^{j}_{\ ,0}$ are zero and using the conservation equations find that

$$T^{00}_{\ \ ,00} x^j x^k = (T^{lm} x^j x^k)_{,lm} - 2(T^{lj} x^k + T^{lk} x^j)_{,l} + 2T^{jk}. \tag{1.2.12}$$

Integrating (1.2.12) over a volume so that the divergence terms vanish leaves the expression

$$2\int T^{jk}\ \mathrm{d}\mathbf{x} = \int T^{00}{}_{,00}x^j x^k\ \mathrm{d}\mathbf{x}. \tag{1.2.13}$$

We return to the retarded integral (1.2.10) and rewrite it using $|\mathbf{x}-\mathbf{x}'| = r$ and (1.2.12). Then

$$\bar{h}^{jk}(t,\mathbf{x}) = \frac{2}{r}\frac{\mathrm{d}^2}{\mathrm{d}t^2}\int T^{00}(t-r,\mathbf{x}')x'^j x'^k\ \mathrm{d}\mathbf{x}'. \tag{1.2.14}$$

Let us assume that the source is moving slowly, in the sense that its velocity $v \ll c$. Then its energy density is dominated by the mass density contribution, $T^{00} \approx \rho$. Now defining the *mass quadrupole moment* as

$$\mathcal{I}_{jk} \equiv \int \rho x_j x_k\ \mathrm{d}\mathbf{x} \tag{1.2.15}$$

we see from (1.2.14) that

$$h_{jk} = \frac{2}{r}\ddot{\mathcal{I}}_{jk}(t-r) \tag{1.2.16}$$

— this is the quadrupole formula. Finally we recall the definitions of the reduced quadrupole moment $\mathcal{I}_{jk}$ and moment of inertia $I_{jk}$:

$$\mathcal{I}_{jk} = \int \rho\left(x_j x_k - \tfrac{1}{3}r^2\delta_{jk}\right)\ \mathrm{d}\mathbf{x} \tag{1.2.17}$$

$$I_{jk} = \int \rho(r^2\delta_{jk} - x_j x_k)\ \mathrm{d}\mathbf{x}. \tag{1.2.18}$$

In transverse-traceless gauge[3] we note that these three tensors are equal (up to a sign): $\mathcal{I}^{TT}_{jk} = \mathcal{I}^{TT}_{jk} = -I^{TT}_{jk}$. Using (1.2.16) and TT-gauge we arrive at formulae for gravitational wave polarisations in terms of the moment-of-inertia tensor:

$$h_+ \equiv h^{TT}_{11} = -h^{TT}_{22} = -\frac{2}{r}\ddot{I}^{TT}_{11} \tag{1.2.19}$$

$$h_\times \equiv h^{TT}_{12} = h^{TT}_{22} = -\frac{2}{r}\ddot{I}^{TT}_{12}. \tag{1.2.20}$$

### 1.2.3 Gravitational radiation from neutron stars

Having seen how the Einstein field equations predict the existence of gravitational waves (under certain assumptions), it is natural to ask which astrophysical objects and events are likely to lead to detectable gravitational wave signals. From (1.2.16) we see that a signal's strength depends on the proximity of the source and the

[3] See Section 3.2 and [102] for more details

second time derivative of its moment of inertia tensor; i.e. the magnitude of the acceleration of the source's mass distribution. Concentrating on this latter attribute, there are a number of promising sources of gravitational waves (the obvious caveat is that the nearest of these sources are the best candidates): supernovae, coalescing binary systems of neutron stars or black holes, the stochastic gravitational radiation background left from the Big Bang and radiation from isolated neutron stars[123].

In fact, gravitational radiation has already been detected indirectly in a binary neutron star system. In this system, the Hulse-Taylor binary pulsar PSR 1913+16, the orbit of the two neutron stars is seen to decrease in a manner that agrees to within 1% with the predictions of the quadrupole formula, providing strong evidence for the explanation that the binary is losing energy through gravitational radiation[68, 134]; this work won the 1993 Nobel Prize for Physics.

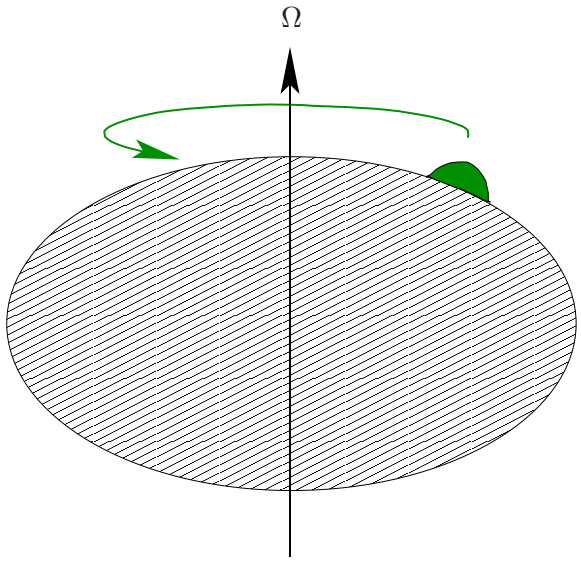


Figure 1.3: A neutron star will be distorted from a sphere into an oblate spheroid by the effects of rotation, but this is still a stationary configuration. However if the NS has an extra distortion (the green lump in this figure) which is not symmetrical about the rotation axis Ω, then as the NS rotates this extra distortion will induce time-variation in the star's mass distribution and so produce gravitational waves.

The focus of this work is, however, a different class of GW sources — the isolated

neutron stars. Since neutron stars are so dense, even relatively small deviations from their predominantly stationary configurations have the potential to induce a significant time-varying mass distribution and hence a relatively strong gravitational wave signal. These deviations could be distortions in the density distribution which are not symmetric about the rotation axis; or from unstable oscillation modes (see, for example, the reviews by Schutz [123] and Andersson [3]).

Note that whilst the most significant distortion to a NS will usually be its centrifugal bulge (discussed in Chapter 4), this is a stationary effect and so does not produce GWs; see figure 1.3. Possible off-rotation axis distortions are crustal irregularities from the star's geological history and the effect of the star's magnetic field. Distortions from the latter are a major focus of this document — see chapters 4 and 6.

Candidates for unstable modes include the $r$-mode associated with stellar rotation, and the $f$-mode associated with pressure fluctuations in the star. If these modes become unstable then their amplitude will grow exponentially (in the absence of any damping mechanism) — and potentially increase to the point where the oscillations induced in the stellar density produce detectable GWs.

Prospects for detection of GW signals from neutron stars are greatly improving with new detector technology. Although the amplitude of signals from isolated NSs is likely to be low, their continuous nature and regular emission are suited to long-term observations using interferometers. Techniques like signal recycling, together with time-integration of a signal over the period of (say) a year will significantly improve our chances of observing isolated NSs through their gravitational radiation signals. It is also essential that we understand what signal to expect beforehand, as searches must be done in a narrow frequency window. Ground-based detectors like LIGO, VIRGO and GEO600 are most sensitive to frequencies of the order of 100 Hz, which makes them suited to the detection of binary inspirals and isolated NS signals. Encouragingly, this technology has already set strain limits as low as $\sim 10^{-25}$ on the gravitational radiation from known pulsars [45].

The next stage is the upgrade of these detectors with more advanced technology; the resulting 'second-generation' detectors should begin science runs around 2015. These advanced detectors will be around an order of magnitude more sensitive than the current ones — a very significant improvement, since current theory suggests that there should be many prospective GW sources in this improved sensitivity window.

Looking further ahead, there are already plans for third-generation detectors (for example, the Einstein Telescope), planned to be another order of magnitude more sensitive still. The hope is that GW observations from third-generation detectors will give us a greatly improved understanding of NSs: their equation of state, crustal deformations, interior magnetic fields and oscillation spectra, among others [4].

## 1.3 Plan of this thesis

This thesis is organised into nine chapters, which in turn are arranged into four larger parts: an introductory part (consisting of chapters 1 and 2); a part on analytic work (chapters 3, 4 and 5); a part on numerical work (chapters 6, 7 and 8); and a final part with discussion and conclusions (chapter 9).

Each chapter of analytic work has a numerical counterpart: chapters 4 and 6 contain studies of equilibria of stars with rotation and magnetic fields; chapters 5 and 7 both focus on oscillation modes of stars, with the numerical chapter including work on magnetic modes; finally, chapters 3 and 8 are concerned with the open problem of precession in magnetised fluid stars.

# Chapter 2

# Magnetic fields in neutron stars

## 2.1 Introduction

The magnetic fields in neutron stars are among the strongest known in the Universe: ordinary neutron stars have surface fields that reach $\sim 10^{12}$ gauss, whilst at the surface of magnetars (an especially highly-magnetised class of neutron star) magnetic fields are thought to reach $\sim 10^{15}$ gauss. For comparison, the magnetic field at the Earth's surface is around 0.5 gauss. It is not outlandish to expect NS interior fields to be an order of magnitude stronger still, i.e. up to around $10^{16}$ gauss; such a value for the field seems to emerge from modelling of magnetar flares [130] and cooling [76]. We should, therefore, anticipate significant magnetic-field effects in the physics of neutron stars.

From the point of view of observation, the most important magnetic-field effect in NSs is that they provide the energy required to make these stars visible from Earth (in many cases). In this chapter we look at two classes of neutron star, distinguished by how they are observed and certain other properties: the 'ordinary pulsars' and the 'magnetars'. The next two subsections are devoted to a summary of each of these classes of neutron star. In the rest of the chapter we summarise the literature on magnetic distortions and oscillations, since these are the major focus of this document, and conclude with a discussion of other aspects of neutron star physics linked to the magnetic field.

### 2.1.1 Pulsars

Soon after the first detection of a pulsar [65], it was suggested by Gold [54] that the extremely regular radio signal could be explained if the source was a rotating magnetised neutron star; the basic idea is the same today. At the poles of a magnetised neutron star, particles are thought to be collimated along the open field lines, causing the emission of radio-frequency curvature radiation [81] — this is shown in figure 2.1. Since the magnetic and rotational axes are typically not aligned, this beam of radiation rotates with the star. The effect is an on-off radio pulsing, like the signal from a lighthouse: as the beam sweeps across the Earth we see radio emission; when the beam is facing away from Earth we cannot see it. Pulsars have to be neutron stars, because the rotation rates observed in many of them would tear the (less compact) white dwarfs apart.

### 2.1.2 Magnetars

Magnetars are a class of neutron star with particularly strong magnetic fields, up to $\sim 10^{15}$ G at the stellar surface. Duncan and Thompson [40] have suggested that these particularly strong fields are generated by a dynamo effect in the first few seconds after the star's formation. These fields cause the star to spin down rapidly, so they are not primarily detected through their radio emission, as most neutron stars are.

The idea of a magnetar was first postulated to explain the Soft Gamma Repeaters (SGRs) [40]. SGRs have long rotation periods and appear to spin down more rapidly than ordinary pulsars. Assuming that this spindown is due to dipole radiation leads to the estimate that their dipole fields are around $10^{14} - 10^{15}$ G. SGRs are characterised by their soft-gamma/hard-X ray emission and their occasional, extremely energetic giant flares.

The magnetar model has also been used to explain the behaviour of the Anomalous X-ray Pulsars (AXPs). The anomaly of these objects is that their observed X-ray luminosity is many times greater than that which could be sourced from the star's spindown; but it is easy to account for if these objects have the huge reservoirs of magnetic energy of a magnetar. Although the two classes of magnetar discussed here differ in a number of respects — most obviously, that the AXPs do not undergo the huge bursts of SGRs — it has been suggested that this can be explained through

varying degrees of twist in their magnetic fields [135].

## 2.2 Magnetic distortions

It has long been predicted that magnetic fields will distort a fluid star; see Chandrasekhar and Fermi [26]. This distortion only becomes appreciable if the magnetic energy $\mathcal{E}_{mag}$ of the star is comparable with its gravitational energy $W$; since neutron stars have tremendous self-gravity it follows that one would only expect very strong magnetic fields to generate any significant distortion. In chapter 6 we will quantify these comments by scaling our code-generated results to real neutron star values. For now, we note that the work of Chandrasekhar and Fermi suggests that magnetars should have the greatest magnetic distortions of all NSs (with the caveat that this early work is for an incompressible fluid and so is of limited relevance to NSs).

A number of studies of magnetically deformed stars exist. These have included work focussed on poloidal, toroidal or mixed fields, and boundary conditions where the field either vanishes at the surface of the star or decays at infinity. Changing any of these can lead to very different results, so the uncertainty we have about the geometry of NS magnetic fields translates into an uncertainty about how distorted they are.

Analytic approaches have been restricted to weak fields and small deformations, as the nonlinear nature of stronger magnetic fields rapidly makes the problem intractable. Early work treated deformations of incompressible fluids (see the work of Roberts, Ferraro, Chandrasekhar and Fermi [118, 43, 26] among others; also section 4.3), a simplifying assumption but not terribly physical for real stars. The first studies of compressible stars assumed very simplistic density distributions and magnetic fields confined within the star[143, 141]; later Goossens [56] treated the problem of a poloidal field matched to an external dipole, extending the work of Ferraro[43]. More recent work by Haskell et al. [64] included a study of deformations in a star with a mixed poloidal-toroidal field confined within the star.

In addition to analytic work, a number of studies have used numerical methods to calculate magnetic distortions. Monaghan[103] and Roxburgh [119] calculated field geometries and surface distortions for various polytropes, allowing for an exterior magnetic field. Their work was perturbative and so restricted to weak fields.

More recently, Ioka [69] has applied a second-order perturbation technique to study the strong fields found in magnetars. Other studies of highly magnetised stars have solved the fully non-linear problem, to allow for more highly deformed configurations than could be accurately determined using a perturbative approach. This was originally done for strong magnetic fields confined within the star[107], by extending an earlier self-consistent field method for rapidly-rotating stars[108]. For purely poloidal fields, Miketinac [101] devised an improved numerical method which enabled the calculation of highly distorted equilibrium configurations; it was found that for very strong fields the maximum density of the star could move away from the centre to make the geometry of the density distribution toroidal. Solutions have also been found using a mixed-field formalism[137]. Finally, relativistic effects have been considered: nonlinear studies for purely poloidal [10] and purely toroidal fields [80] and a perturbative treatment for mixed fields [31]. Another study looked at mixed-field configurations in Newtonian gravity, but including a relativistic correction [78].

## 2.3 Magnetic oscillations

Recently, quasi-periodic oscillations have been observed in the aftermath of giant flares from SGRs [71, 140]. These are thought to be connected with oscillation modes of the star, thus giving us direct information about its oscillation spectrum and potentially a probe of the physics of the interior of neutron stars. Understanding the origin of the QPOs, then, is of great importance for our knowledge of neutron star physics. These observations provide a substantial motivation for better understanding NS modes, in particular their behaviour in a strong magnetic field. Chapter 7 of this document studies the oscillation modes of a simple magnetar model.

Although magnetar QPOs provide fresh motivation for studying oscillations in a magnetised star, the literature on such magnetic modes predates the discovery of these QPOs by several decades. The influence of a star's magnetic field on its oscillation spectrum can be gauged from the ratio of its magnetic energy to the gravitational binding energy, $M/|W|$; this suggests three classes of star where one should take account of the star's magnetic field: in addition to NSs, there are also the rapidly-oscillating type-A peculiar (roAp) stars and magnetic white dwarfs (MWDs).

The earliest studies of magnetic star oscillations were driven by the discovery of $\sim 10^4$ gauss fields — relatively strong for a main-sequence star — in some Ap stars

[28, 88]. Later, some of these stars were found to be oscillating at high frequency — the roAp stars — motivating a number of studies of magnetic effects on high-frequency $p$-modes [138, 41, 117]. In addition to roAp stars, some white dwarfs have strong ($\sim 10^9$ gauss) magnetic fields; however these have shown no evidence of pulsation, perhaps due to magnetic suppression of the $g$-modes that *are* observed in weaker-field white dwarfs[142]. Finally, the internal dynamics of neutron stars will be considerably affected by rotation as well as their strong magnetic fields, leading to interest in magnetic $r$-modes [104].

Many publications to date have reported on analytic studies of magnetic stellar oscillations, necessitating considerable simplications to the problem: typically the model used is an incompressible star with a force-free background magnetic field. Some modern work on the problem has been inspired by the observation of magnetar QPOs, and this has tended to be numerical [128, 127, 19], with the advantages that more sophisticated physics can be modelled (for example, compressible and relativistic stars). Chapter 7 of this thesis extends previous work by solving the system of governing equations self-consistently, allowing for background stars which may be nonspherical by virtue of both their magnetic fields and their rotation.

## 2.4 Other magnetic effects

The effects of magnetic fields on equilibrium configurations and oscillation spectra are of primary interest in this thesis, but a neutron star's physics is affected in many other ways by its magnetic field. An obvious observable effect is the spindown of a neutron star: though this contains a contribution from gravitational radiation, it is primarily due to magnetic dipole radiation. In particular the magnetars, with their very strong fields, have correspondingly rapid spindown rates. Magnetic-field effects are also important in the physics of the atmosphere and the thermal emission [67]; they alter the properties of dense matter and hence the equation of state [62]; and affect the long-term evolution of the star [111]. A variety of these properties are discussed in the review by Harding and Lai [63].

Finally, if a neutron star has a magnetic field, Goldreich and Julian [55] showed that it cannot exist surrounded by a vacuum. Instead it forms a magnetosphere of electric current beyond the surface of the star, with closed magnetic field lines; see figure 2.1. In the outer magnetospheric gap (just beyond the closed field-line

region) high-energy radiation is emitted, in the visible, X-ray and $\gamma$-ray bands. Some neutron stars are visible through this radiation, as well as in the radio band.

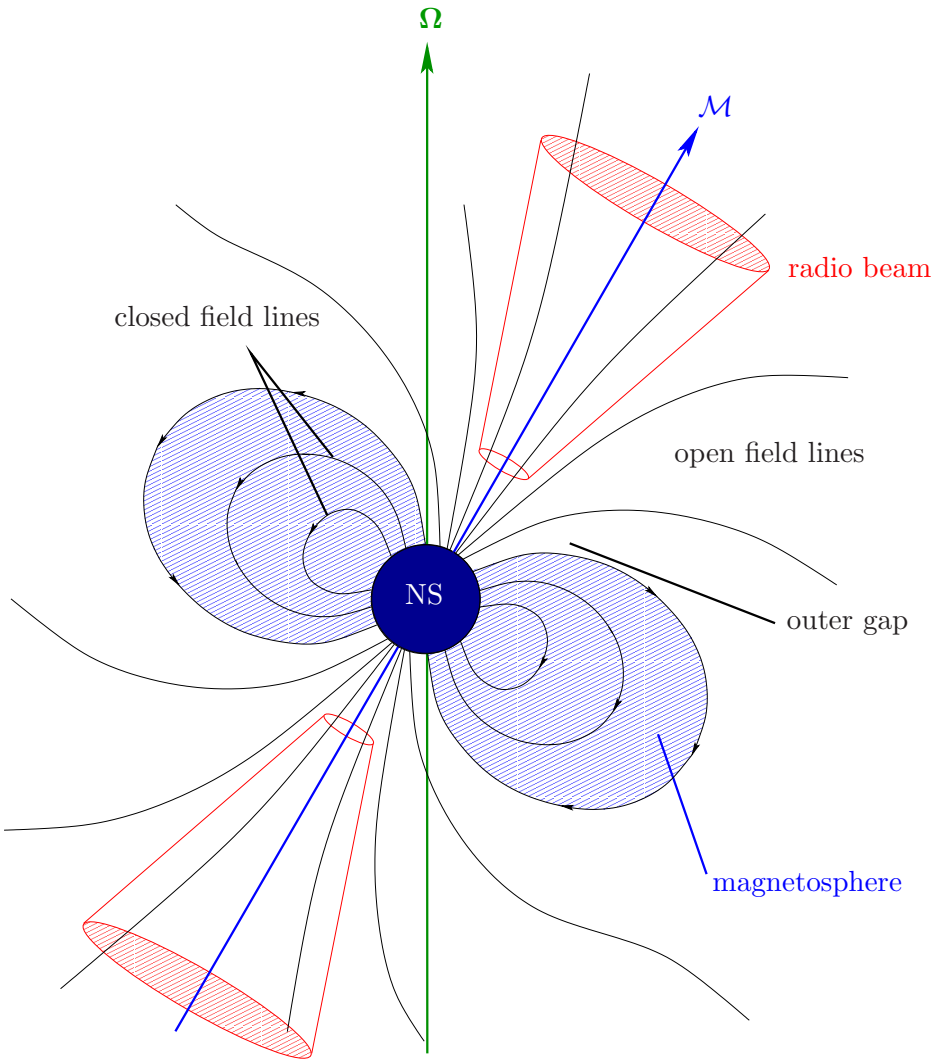


Figure 2.1: Diagram of a pulsar and its exterior magnetic field. Field lines (in black) extend outside the central neutron star (NS); these are open at the poles where the pulsar radio beam originates and closed in the magnetosphere. In the gap just beyond the magnetosphere high-energy radiation is generated. The magnetic field rotates about the $\mathbf{\Omega}$ axis and has a magnetic field symmetric about the magnetic axis $\mathcal{M}$, so the radio beam rotates around $\mathbf{\Omega}$. An observer sees the beam when it faces them but not when it has rotated away, and so observes the NS through a characteristic on-off radio signal.

# Chapter 3

# Precession

## 3.1 Introduction

Free precession is a rigid-body effect in which a body's motion is (in its simplest, biaxial, form) characterised by two superimposed rotations: one rotation of the body about a principal axis of inertia (a *body axis*) and another rotation of this principal axis about the body's angular momentum axis; see figure 3.1. If the angular momentum axis is aligned with a principal axis of inertia, however, the motion will just be ordinary rotation; it follows that a rigid sphere cannot precess.

It has long been thought that stars may precess (see Ruderman [121], for example), in analogy with the case of rigid bodies with misaligned rotation and body axes. For a star to precess it also needs a source of distortion and a rotation axis misaligned from any symmetry axis of the distortion. Returning to figure 3.1, one could imagine stresses distorting the fluid into its biaxial shape, symmetric about the $\mathbf{n}_3$ axis, but being rotated about the $\mathbf{J}$ axis. In the absence of other effects the star would then develop a secondary rotation about the $\mathbf{n}_3$ axis to conserve angular momentum and hence precess; see section 3.4.1.

There are a variety of effects which could distort a neutron star and cause it to precess: the rigidity of the crust allows it to support deformations which may arise through the star's seismic history (like starquakes) or through accretion onto the crust from a companion star; in addition a strong magnetic field could cause a significant asphericity in a neutron star. The most significant distortion of a NS is likely to be the oblateness due to centrifugal forces, but unlike the other effects

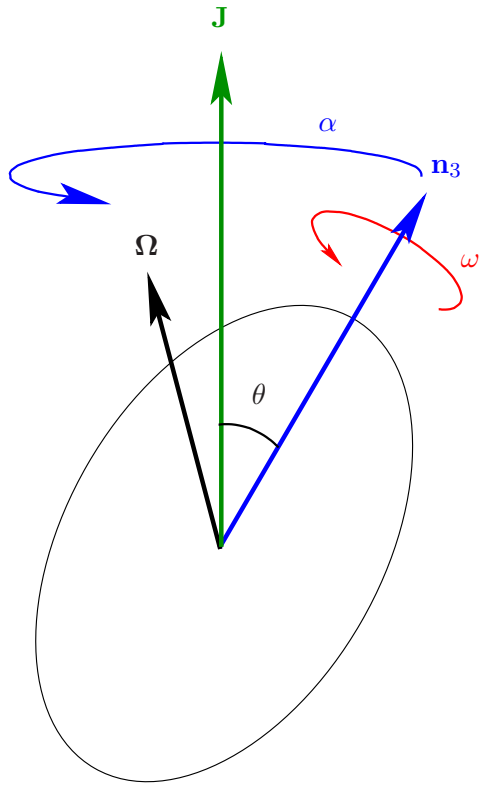


Figure 3.1: The free precession of a biaxial rigid body. The instantaneous rotation axis $\mathbf{\Omega}$ and the body axis $\mathbf{n}_3$ rotate around the invariant angular momentum axis $\mathbf{J}$ at a frequency $\dot{\phi}$. We call $\theta$ the wobble angle and note that if $\theta = 0$ or $\theta = \pi/2$ the motion of the body is simply axial rotation.

listed a centrifugal bulge is a stationary configuration and cannot induce or affect precessional dynamics [73].

Most pulsar observations are of the on-off radio signal that reaches Earth. In a few pulsars a modulation in the radio timing data has been observed, with a periodicity whose timescale is much greater than the ordinary spin period; this has been interpreted as evidence for precession. The most promising candidate for precession in a neutron star is pulsar PSR B1828-11, with a possible precession period of 1009 days and a rather uncertain wobble angle, perhaps $0.02^\circ \lesssim \theta \lesssim 3^\circ$. Other possible precessing pulsars are SN 1987A, PSR B1642-03 and the Vela pulsar PSR B0833-45 [73].

The paucity of candidates for precession (only a few of the 1500+ known pulsars)

presents a major problem to the rigid-body analogue neutron star described above. One would expect off-rotation axis distortions to be reasonably common in NSs, given that some of them have extremely strong magnetic fields, and assuming a NS crust is able to support fairly large irregularities; then the rigid-body analogy suggests that precession should be a generic feature of NSs, rather than a very rare one. One explanation may be that precession *is* reasonably common, but that we are simply unable to observe it in the radio data: if the off-axis distortion is entirely due to (say) magnetic effects, symmetric about some magnetic axis, then the secondary rotation of the star (labelled $\omega$ in figure 3.1) will be precisely about this axis. In the inertial frame the magnetic axis will then appear to be simply rotating rigidly. An extra distortion (like an accreted crust) is needed to produce modulation in the radio timing data, and hence a signature of precession.

Even if precession is more common than radio timing data would suggest, a neutron star is certainly a great deal more complicated than a rigid body; effects like the elastic nature of the crust [36], magnetic coupling [91] and the superfluid interior of the star [125, 1, 52] may all affect precessional dynamics. Additionally, as the star loses energy it may drive the wobble angle to $\theta = 0$ or $\theta = \pi/2$ (see section 3.3 and Cutler [35]), in both cases damping the precession. Despite the many complications involved, however, Wassermann has recently suggested that precession should still be generic to magnetised neutron stars [139].

Precessing neutron stars are interesting as potential sources of detectable gravitational radiation (see section 3.2 and the work of Zimmermann [148, 147]), with distinctive continuous signals which a combination of long interferometer observations and matched filtering may be able to detect. More recently, Zimmermann's calculation has been extended to second order by Van Den Broeck [17]. At this order a new spectral line emerges in the GW signal, containing direct information about the star's wobble angle and asymmetries; such a detection would thus aid our understanding of neutron star structure. It has been claimed that even stars who do not undergo mechanical precession may still emit precession-like signals[49, 72]. However at present it seems that precession, at least that due to crustal deformities, may only result in very small amplitude gravitational waves[74].

In this chapter we calculate the gravitational waves from a freely precessing rigid body, before a calculation which shows the energy lost in precession damping. We then explore the problem of the motion of a magnetised fluid star and the analogy

with rigid-body free precession. This is done with an analytic approach here, and numerically in chapter 8.

## 3.2 Gravitational radiation from a freely precessing spheroid

Here we follow the calculation of Zimmermann and Szedenits [148] to use the quadrupole formula to calculate the expected waveforms from a freely precessing rigid neutron star. We note that for a slowly rotating body this result should be accurate, as the post-Newtonian corrections are negligible[136]. At the end we plot these expected waveforms for some different values of wobble angle.

### 3.2.1 Finding formulae for precessional waveforms

In the corotating or body frame (whose orthogonal triad we define as $(x, y, z)$), the moment of inertia tensor for a rigid biaxial body is given by

$$I_{body} = \begin{pmatrix} I_1 & 0 & 0 \\ 0 & I_1 & 0 \\ 0 & 0 & I_3 \end{pmatrix} \tag{3.2.1}$$

where $I_3$ is the component along $z$, the body's symmetry axis [83].
To find an expression for the moment of inertia tensor $I_{inert}$ in an inertial frame requires finding a series of rotations which move from the inertial axes $(x', y', z')$ back to the body axes $(x, y, z)$: for a general triaxial body, a rotation through each of the three Euler angles is required; for a biaxial body this reduces to rotations through two angles $\theta$ and $\phi$. Here $\theta$ is the angle between the $z$ and $z'$ axes and $\phi$ the angle between the inertial $x'$ axis and the line of nodes (where the inertial and body $x$-$y$ planes intersect). The $z$ and $z'$ axes become parallel after a rotation through angle $\theta$ about the $x'$ axis; a further rotation about the $z'$ axis through angle $\phi$ gives parallel $x$–$y$ and $x'$–$y'$ planes as well. Hence

$$I_{inert} = R_\phi R_\theta I_{body} R_\theta^T R_\phi^T \tag{3.2.2}$$

where $R_\phi = \begin{pmatrix} \cos\phi & -\sin\phi & 0 \\ \sin\phi & \cos\phi & 0 \\ 0 & 0 & 1 \end{pmatrix}$ and $R_\theta = \begin{pmatrix} 1 & 0 & 0 \\ 0 & \cos\theta & -\sin\theta \\ 0 & \sin\theta & \cos\theta \end{pmatrix}$.
The Eulerian equation for $\phi$ reads $\dot{\phi} = \Omega$ where $\Omega$ is the star's angular velocity.

With this explicit time dependence, we can now take the second time derivative of this matrix $I_{inert}$, needed later for calculation of the gravitational radiation of the body with the quadrupole formula:

$$\ddot{I}_{inert} = \begin{pmatrix} 2\cos 2\Omega t \sin\theta & 2\sin 2\Omega t \sin\theta & -\sin\Omega t \cos\theta \\ 2\sin 2\Omega t \sin\theta & -2\cos 2\Omega t \sin\theta & \cos\Omega t \cos\theta \\ -\sin\Omega t \cos\theta & \cos\Omega t \cos\theta & 0 \end{pmatrix} I_1 \epsilon \Omega^2 \sin\theta \tag{3.2.3}$$

where $\epsilon = \frac{I_3 - I_1}{I_1}$.

Consider an observer whose axes $(\hat{x}, \hat{y}, \hat{z})$ are arbitrarily inclined to those of the inertial system $(x', y', z')$, and call the moment of inertia tensor referred to this observer system $I_{obs}$. We wish to find the components of $\ddot{I}_{obs}$ transverse to the $\hat{z}$ axis. Define a unit vector $\mathbf{n}$ parallel to the observer's $\hat{z}$ axis by

$$\mathbf{n} = \begin{pmatrix} \sin\iota \cos\alpha \\ \sin\iota \sin\alpha \\ \cos\iota \end{pmatrix} \tag{3.2.4}$$

where the inclination to the angular momentum vector $\mathbf{J}$ is described by two angles: the 'inclination angle' $\iota$ and the 'azimuthal angle' $\alpha$. Using $\mathbf{n}$ we define the projection tensor $\mathbf{P}$

$$\mathbf{P} = \boldsymbol{\delta} - \mathbf{n} \otimes \mathbf{n} \tag{3.2.5}$$

or in components:

$$P^j_k = \delta^j_k - n^j n_k \tag{3.2.6}$$

This gives

$$\mathbf{P} = \begin{pmatrix} 1 - \sin^2\iota \cos^2\alpha & -\sin^2\iota \cos\alpha \sin\alpha & -\sin\iota \cos\iota \cos\alpha \\ -\sin^2\iota \cos\alpha \sin\alpha & 1 - \sin^2\iota \sin^2\alpha & -\sin\iota \cos\iota \sin\alpha \\ -\sin\iota \cos\iota \cos\alpha & -\sin\iota \cos\iota \sin\alpha & 1 - \cos^2\iota \end{pmatrix} \tag{3.2.7}$$

Given the freedom to rotate the observer axes, we choose the $\hat{x}$–$\hat{y}$ plane so that the azimuthal angle $\alpha = 0$. Then

$$\mathbf{P} = \begin{pmatrix} 1 - \sin^2\iota & 0 & -\sin\iota \cos\iota \\ 0 & 1 & 0 \\ -\sin\iota \cos\iota & 0 & 1 - \cos^2\iota \end{pmatrix} \tag{3.2.8}$$

Note that $\mathbf{P}^2 = \mathbf{P}$ as required for a projection. We now use this tensor $\mathbf{P}$ to obtain the projection of $\ddot{I}_{inert}$ into the plane orthogonal to $\mathbf{n}$ and call the resulting tensor $\ddot{I}_{proj}$:

$$\ddot{I}_{proj} = \mathbf{P}\ddot{I}_{inert}\mathbf{P} - \frac{1}{2}\mathbf{P}\mathrm{Tr}(\mathbf{P}\ddot{I}_{inert}) \tag{3.2.9}$$

This formula ensures $\ddot{I}_{proj}$ is a transverse-traceless matrix, which can be confirmed by checking $\ddot{I}_{proj}\mathbf{n} = \begin{pmatrix} 0 \\ 0 \\ 0 \end{pmatrix}$ (transverse) and $\mathrm{Tr}(\ddot{I}_{proj}) = 0$ (traceless). Now, $\ddot{I}_{proj}$ is a matrix referred to the inertial triad $(x', y', z')$ but with the part transverse to the vector $\mathbf{n}$ projected out. A final rotation $R_\iota$ is required to obtain $\ddot{I}_{obs}$, the second time derivative $\ddot{I}$ of the moment of inertia tensor with respect to the observer's triad (the observer $\hat{z}$-axis is the unit vector $\mathbf{n}$). The condition $\alpha = 0$ means the $y'$ and $\hat{y}$ axes are parallel, so we need a rotation about this axis through angle $\iota$:

$$R_\iota = \begin{pmatrix} \cos\iota & 0 & -\sin\iota \\ 0 & 1 & 0 \\ \sin\iota & 0 & \cos\iota \end{pmatrix} \tag{3.2.10}$$

which gives

$$\ddot{I}_{obs} = R_\iota \ddot{I}_{proj} R_\iota^T = \begin{pmatrix} \mathfrak{A} & \mathfrak{B} & 0 \\ \mathfrak{B} & -\mathfrak{A} & 0 \\ 0 & 0 & 0 \end{pmatrix} I_1 \Omega^2 \epsilon \sin\theta \tag{3.2.11}$$

where

$$\begin{aligned} \mathfrak{A} = &\ \tfrac{1}{2}((3+\cos 2\iota)\cos^2\Omega t \sin\theta + \sin\Omega t(\cos\theta \sin 2\iota - (3+\cos 2\iota)\sin\theta\sin\Omega t)) \\ \mathfrak{B} = &\ \cos\Omega t(4\cos\iota\sin\theta\sin\Omega t - \cos\theta\sin\iota) \end{aligned} \tag{3.2.12}$$

For comparison with previous work [148, 12] we change our definition of origin of (retarded) time with the substitution $\Omega t \to \Omega t + \frac{\pi}{2}$. Now using the quadrupole formula (see Section 2), we find that the gravitational waveforms for a rigid freely precessing spheroid are given by

$$\begin{aligned} h_+ &= -\frac{2}{r}\ddot{I}_{obs_{11}} \\ &= -\frac{2}{r}\mathfrak{A} I_1 \omega^2 \epsilon \sin\theta \\ &= \frac{2 I_1 \omega^2 \epsilon \sin\theta}{r}\left((1+\cos^2\iota)\sin\theta\cos 2\Omega t - \sin\iota\cos\iota\cos\theta\cos\Omega t\right) \end{aligned} \tag{3.2.13}$$

and

$$\begin{aligned} h_\times &= -\frac{2}{r}\ddot{I}_{obs_{12}} \\ &= -\frac{2}{r}\mathfrak{B}I_1\omega^2\epsilon\sin\theta \\ &= \frac{2I_1\omega^2\epsilon\sin\theta}{r}\left(-2\cos\iota\sin\theta\sin 2\Omega t + \sin\iota\cos\theta\sin\Omega t\right). \end{aligned} \tag{3.2.14}$$

### 3.2.2 Waveform plots

We now use typical parameters for a real neutron star to make plots of the gravitational waveforms from a freely precessing solid spheroid — the neutron star model we are concerned with in this section — setting: the moment of inertia $I_1 = 10^{38}$ kg m$^2$, the angular velocity as $2\pi \cdot 100$ rad s$^{-1}$, the ellipticity $\epsilon = 10^{-6}$ (dimensionless) and the distance from the source as $r = 1$ kpc $= 3.09 \times 10^{19}$ m. We also (arbitrarily) set the inclination angle as $\iota = \pi/4$. In addition we need to convert from geometrised units with $c = G = 1$ back to SI units. Accordingly, using the requirement that the wave amplitude $h$ must be dimensionless, we find a factor of $Gc^{-4}$ is needed.

On the final page of this section plots are given of the time variation of the two polarisation amplitudes $h_+$ and $h_\times$ using formulae (3.2.13) and (3.2.14) and physical values as above. For $\theta = 0$ we see from the equations above that the wave amplitude is zero as expected; a body rotating about its symmetry axis has no time-varying moment of inertia, required for gravitational radiation. For $\theta > 0$ the plots show the superposition of two harmonics characteristic of free precession, whilst the final pair of plots for $\theta = \pi/2$ have a simple sinusoidal shape as expected when the body $z$-axis and the angular momentum axis are orthogonal. In reality signals such as the model ones given on the next page would need to be observed for months, making use of matched filtering to bring the effective amplitudes up to, say, the order $10^{-23}$ [123].

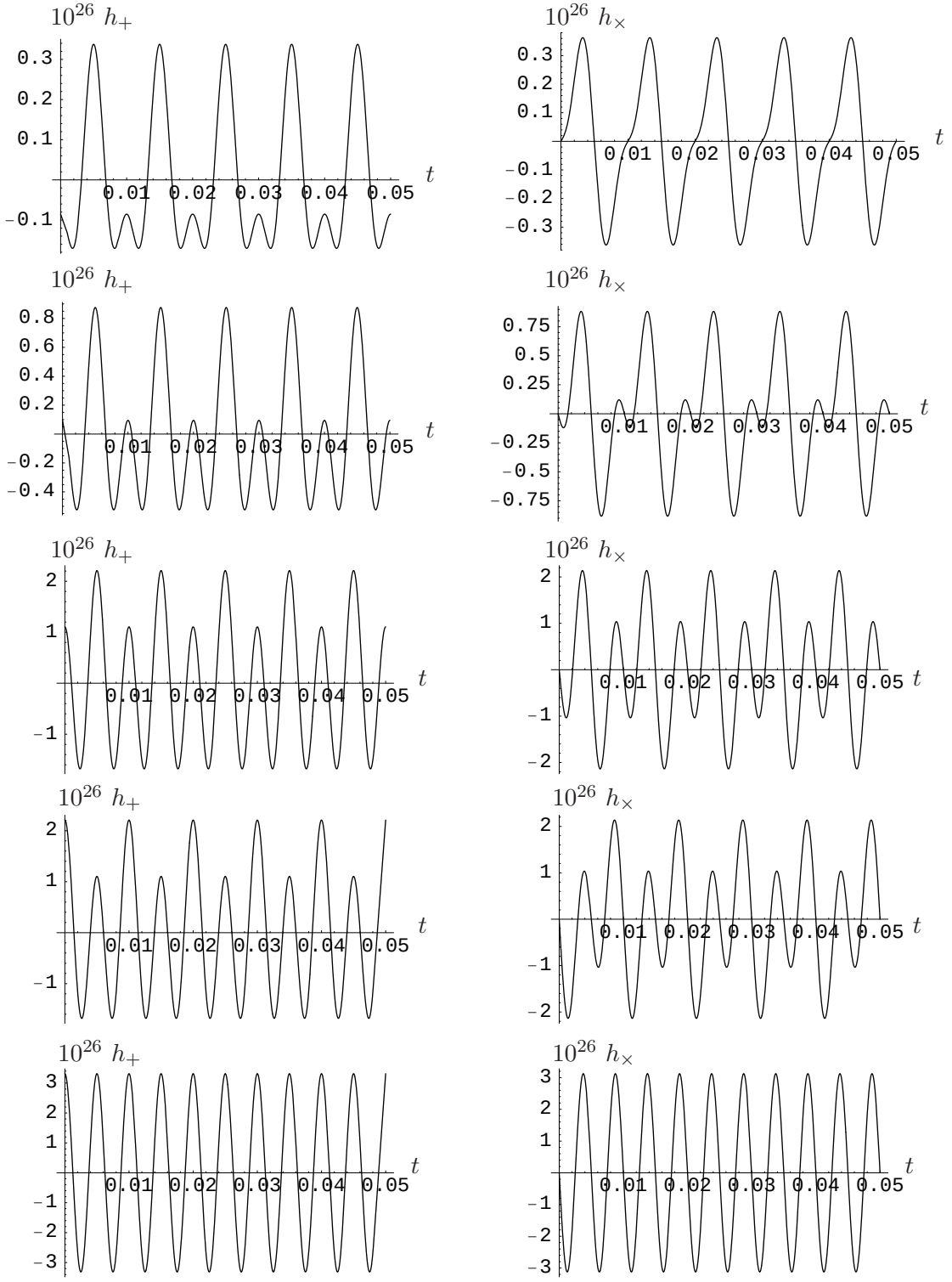


Figure 3.2: Plots of the gravitational waveforms for the $h_+$ (left) and $h_\times$ (right) polarisations against time (in seconds). From top to bottom these plots correspond to values of wobble angle $\theta = \pi/16, \pi/8, \pi/4, 3\pi/4$ and $\pi/2$.

## 3.3 Precession damping

We argued in the introduction that one might expect precession-like dynamics to be generic to neutron stars and in the previous section calculated the gravitational wave emission of such a star. However this precession will not, of course, continue indefinitely but will be subject to damping effects. Here we calculate the kinetic energy of a precessing rigid body and see that the effect of kinetic energy loss may be to reduce the wobble angle and hence damp the precession. It has also been argued that in certain circumstances a body may lose energy by *increasing* its wobble angle until it reaches $\pi/2$ (see, e.g., Cutler [35] and references within). In either scenario, the decrease or increase of wobble angle, one may see how the waveforms should change by referring to figure 3.2.

We work in the body frame, in which the moment-of-inertia tensor takes the diagonal form

$$\mathbf{I} = \begin{pmatrix} I_1 & 0 & 0 \\ 0 & I_1 & 0 \\ 0 & 0 & I_3 \end{pmatrix}. \tag{3.3.1}$$

Now defining an average moment of inertia $I_0 = (2I_1 + I_3)/3$ and a 'difference piece' $\Delta I = I_3 - I_1$, we note that $I_1 = I_2 = I_0 - \Delta I/3$ and $I_3 = I_0 + 2\Delta I/3$. So the moment-of-inertia tensor may be rewritten in a useful form as the sum of a 'spherical piece' and a 'non-spherical piece':

$$\mathbf{I} = I_0\boldsymbol{\delta} + \Delta I(\mathbf{n}_3 \otimes \mathbf{n}_3 - \tfrac{1}{3}\boldsymbol{\delta}). \tag{3.3.2}$$

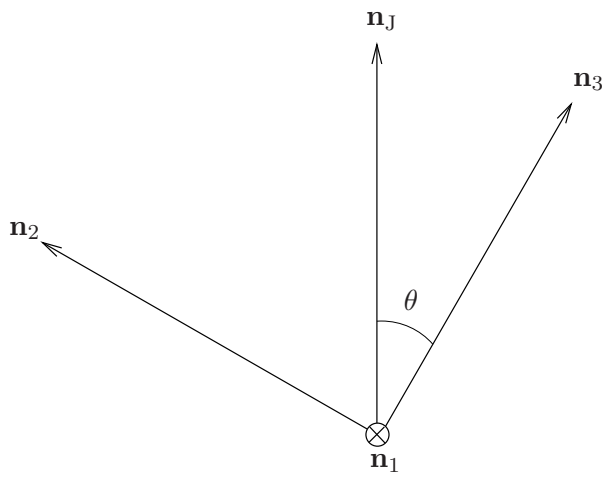


Figure 3.3: The orthogonal triad $(\mathbf{n}_1, \mathbf{n}_2, \mathbf{n}_3)$ and the angular momentum unit vector $\mathbf{n}_J$.

We next decompose the angular velocity vector $\mathbf{\Omega}$ using Euler angles (see the diagram above), picking for simplicity the instant when $\Omega_1 = 0$:

$$\begin{aligned} \mathbf{\Omega} &= \dot{\phi}\mathbf{n}_{\mathrm{J}} + \dot{\psi}\mathbf{n}_3 \\ &= \dot{\phi}\begin{pmatrix} 0 \\ \sin\theta \\ \cos\theta \end{pmatrix} + \dot{\psi}\begin{pmatrix} 0 \\ 0 \\ 1 \end{pmatrix}. \end{aligned} \tag{3.3.3}$$

Now

$$\mathbf{J} = J\mathbf{n}_{\mathrm{J}} = J\begin{pmatrix} 0 \\ \sin\theta \\ \cos\theta \end{pmatrix} \tag{3.3.4}$$

and we may also write the angular momentum vector $\mathbf{J}$ using the following identity:

$$\mathbf{J} = \mathbf{I\Omega} = \begin{pmatrix} I_1\Omega_1 \\ I_2\Omega_2 \\ I_3\Omega_3 \end{pmatrix} = \begin{pmatrix} 0 \\ I_1\dot{\phi}\sin\theta \\ I_3\dot{\phi}\cos\theta + \dot{\psi}I_3 \end{pmatrix}. \tag{3.3.5}$$

Comparing (3.3.4) and (3.3.5) gives:

$$J\sin\theta = I_1\dot{\phi}\sin\theta \;\Rightarrow\; \dot{\phi} = \frac{J}{I_1} \tag{3.3.6}$$

and similarly

$$\dot{\psi} = -\frac{\dot{\phi}\cos\theta\Delta I}{I_3}. \tag{3.3.7}$$

We now substitute these two Euler angle relations into the expression (3.3.3) for $\mathbf{\Omega}$, giving

$$\mathbf{\Omega} = \begin{pmatrix} 0 \\ \frac{J}{I_1}\sin\theta \\ \frac{J}{I_1}\left(1 - \frac{\Delta I}{I_3}\right)\cos\theta \end{pmatrix}. \tag{3.3.8}$$

By using the diagonal form (3.3.1) for the moment of inertia tensor together with (3.3.8), we can now calculate the kinetic energy of a freely precessing rigid body:

$$\begin{aligned} E_K &= \tfrac{1}{2}\mathbf{\Omega I\Omega}^T \\ &= \frac{J^2}{2I_1}\left(1 - \frac{\Delta I}{I_3}\cos^2\theta\right). \end{aligned} \tag{3.3.9}$$

The kinetic energy from the precession itself will then be the difference between $E_K$ evaluated for a wobble angle $\theta$ and the kinetic energy when this wobble angle is zero,

at *fixed* angular momentum:

$$E_{prec} = E_K(\theta) - E_K(0) = \frac{J^2}{2I_1}\left(1 - \frac{\Delta I}{I_3}(\cos^2\theta + 1)\right). \tag{3.3.10}$$

Equation (3.3.10), then, gives the energy decrease if the wobble angle $\theta \to 0$, i.e. $E_{prec}$ is the energy lost in alignment of the body $\mathbf{n}_3$-axis and the angular momentum axis $\mathbf{n}_\mathrm{J}$. Any non-rigidity in the object could thus damp precession without removing angular momentum from the star.

## 3.4 Perturbations in a rotating, magnetised fluid ball

Up until this point we have discussed rigid-body precession, but a neutron star is predominantly a fluid body; it is not obvious, therefore, whether one should expect to find precessing neutron stars. In this section we model a neutron star as a magnetised fluid ball and discuss what effects should contribute to its dynamics. In particular, we explore the idea that a magnetised fluid body should be dynamically analogous to a rigid body.

It was originally suggested by Spitzer [129] that a magnetic field threading a fluid ball could provide some 'rigidity' to the body and allow it to maintain an off-rotation axis distortion. In analogy with the rigid-body situation, one would then expect the motion of this fluid to resemble (in some sense) precession. Mestel [100, 99] used this idea to find a relation between the two primary frequencies characterising the precession, implicitly making a rigid-body ansatz. However, one would not expect the fluid to actually react in a strictly rigid manner to these superimposed rotations. To account for this, Mestel defines a displacement field $\boldsymbol{\xi}$ to describe the deviation of fluid elements from strict precession.

Rigid-body precession and the internal $\boldsymbol{\xi}$-motions should, therefore, give a description of the dynamics of a magnetised fluid with misaligned rotation and magnetic axes. This would be very useful for modelling of many classes of star; in particular, Mestel was concerned with how $\boldsymbol{\xi}$-motions could cause a star to become an aligned or orthogonal rotator (i.e. the rotation and magnetic axes are aligned or orthogonal). As seen in the previous section, 3.3, a star can conserve angular momentum during this transition by dissipation of the precessional energy. In neutron stars, the orthogonal configuration would be optimal for gravitational-wave emission [35]. Whilst the magnetised fluid-ball model of a neutron star is rather simplistic, a

better understanding of the dynamics of this model could help elucidate aspects of the dynamics of real neutron stars — like the apparent rarity of precession in them.

Since rigid-body precession is well understood, it is the $\boldsymbol{\xi}$-motions that require study. In this section we provide a critique of Mestel's work on this topic, concluding that his approach contains certain inconsistencies, which cast doubt on the validity of his $\boldsymbol{\xi}$-motion solutions. In this section we discuss what is needed to patch up Mestel's analytic approach and hence get a better description of the behaviour of the $\boldsymbol{\xi}$ motions. An alternative, numerical, approach to the problem of precession in a magnetised fluid body is suggested in chapter 8.

### 3.4.1 Precession-like fluid motion

In this subsection we follow the perturbative argument of Mestel to establish a relation between the two characteristic frequencies of a rotating magnetised fluid, showing that the leading-order correction to the ordinary rotation is a nutation effect, as for rigid-body free precession. We model a star as a uniformly rotating fluid ball with a frozen-in magnetic field symmetric about some axis $\mathbf{p}$. This axis is inclined at some obliquity angle $\chi$ to the invariant angular momentum vector, whose direction we denote $\mathbf{k}$. We form right-handed triads $(\mathbf{i}, \mathbf{l}, \mathbf{p})$ and $(\mathbf{i}, \mathbf{j}, \mathbf{k})$ associated with these magnetic and rotational axes, and denote the spherical polar coordinate system referred to the $\mathbf{p}$-triad by $(r, \theta, \lambda)$; for the rest of this section we shall work exclusively in this coordinate system.

A stationary, unmagnetised ball of homogeneous fluid would have a spherically symmetric density field $\rho_0(r)$. Including rotation alone adds on a small extra term $\rho_\alpha(r, \theta, \lambda)$ for the effect of the centrifugal bulge on this density distribution; similarly, the density for a non-rotating magnetised fluid ball could be written as $\rho(r, \theta) = \rho_0(r) + \rho_B(r, \theta)$ to take account of magnetic distortions $\rho_B$ to the density. Hence, for a rotating, magnetised star we may write the density of an element at the point $(r, \theta, \lambda)$ as

$$\rho(r, \theta, \lambda) = \rho_0(r) + \rho_B(r, \theta) + \rho_\alpha(r, \theta, \lambda), \tag{3.4.1}$$

where we have neglected cross-terms $\mathcal{O}(\rho_\alpha \rho_B)$ as higher-order than the other density components.

The density field of a star rotating with angular velocity $\alpha\mathbf{k}$ has the angular

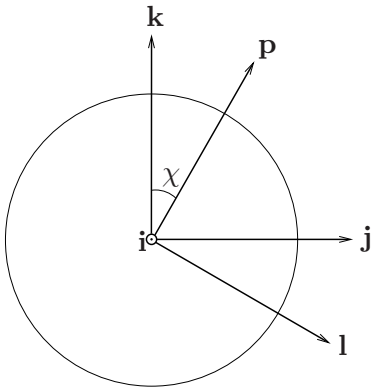


Figure 3.4: The magnetic and rotational triads; we assume **j**, **k**, **l** and **p** are coplanar.

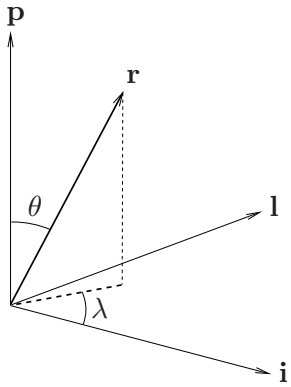


Figure 3.5: The **p**-triad and its spherical polar coordinate system.

momentum vector

$$\mathbf{J}_\alpha = \int \rho \mathbf{r} \times (\alpha \mathbf{k} \times \mathbf{r}) \, \mathrm{d}V. \tag{3.4.2}$$

However this alone does not give an invariant angular momentum orientated along the **k** direction, as the **j**-component of (3.4.2) is non-zero:

$$\mathbf{J}_\alpha \cdot \mathbf{j} = -\alpha \int (\mathbf{j} \cdot \mathbf{r})(\mathbf{k} \cdot \mathbf{r}) \rho_B \, \mathrm{d}V \tag{3.4.3}$$

where the contributions from $\rho_0$ and $\rho_\alpha$ vanish by symmetry. To yield an invariant angular momentum we require an additional rotation $\omega$ (an Eulerian nutation) about the magnetic axis **p** with an associated angular momentum $\mathbf{J}_B$ such that $(\mathbf{J}_\alpha + \mathbf{J}_B) \cdot \mathbf{j} = 0$, i.e.

$$0 = -\alpha \int (\mathbf{j} \cdot \mathbf{r})(\mathbf{k} \cdot \mathbf{r}) \rho_B \, \mathrm{d}V + \int \rho \mathbf{r} \times (\omega \mathbf{p} \times \mathbf{r}) \cdot \mathbf{j} \, \mathrm{d}V. \tag{3.4.4}$$

We assume that **j**, **k**, **l** and **p** are instantaneously coplanar and work in spherical polars with $\mathbf{r} = r(\sin\theta\cos\lambda\ \mathbf{i} + \sin\theta\sin\lambda\ \mathbf{l} + \cos\theta\ \mathbf{p})$. Writing $\mathbf{j} = \cos\chi\ \mathbf{l} + \sin\chi\ \mathbf{p}$, $\mathbf{k} = -\sin\chi\ \mathbf{l} + \cos\chi\ \mathbf{p}$ and $\mathrm{d}V = r^2 \sin\theta\ \mathrm{d}r\mathrm{d}\theta\mathrm{d}\lambda$, we now evaluate the integral (3.4.3) in the $(\mathbf{i}, \mathbf{l}, \mathbf{p})$ triad to give

$$\begin{aligned} \mathbf{J}_\alpha \cdot \mathbf{j} &= -\alpha \int (\mathbf{j} \cdot \mathbf{r})(\mathbf{k} \cdot \mathbf{r}) \rho_B \, \mathrm{d}V \\ &= 2\pi\alpha \sin\chi\cos\chi \iint \rho_B \mathrm{P}_2(\mu) r^4 \, \mathrm{d}r\mathrm{d}\mu. \end{aligned} \tag{3.4.5}$$

Here $\mu \equiv \cos\theta$ and $\mathrm{P}_2(\mu) = \frac{1}{2}(3\mu^2 - 1)$ is the $l = 2$ Legendre polynomial. We evaluate the **j**-component of $\mathbf{J}_B$ in a similar fashion to give

$$\begin{aligned} \mathbf{J}_B \cdot \mathbf{j} &= \int \rho \mathbf{r} \times (\omega \mathbf{p} \times \mathbf{r}) \cdot \mathbf{j} \, \mathrm{d}V \\ &= I_0 \omega \sin\chi \end{aligned} \tag{3.4.6}$$

where $I_0 \equiv \frac{8\pi}{3} \int \rho_0 r^4 \, \mathrm{d}r$ is the moment of inertia of the spherically symmetric density field $\rho_0$; here the two density perturbations are regarded as negligible parts of $\rho$ in comparison with $\rho_0$. We now use equations (3.4.5), (3.4.6) and the requirement $(\mathbf{J}_\alpha + \mathbf{J}_B) \cdot \mathbf{j} = 0$ to find the nutation frequency

$$\omega = -\frac{2\pi\alpha\cos\chi}{I_0} \iint \rho_B \mathrm{P}_2(\mu) r^4 \, \mathrm{d}r\mathrm{d}\mu. \tag{3.4.7}$$

This result may be expressed in a more familiar form by comparing it with the difference in moments of inertia of the **p**-axis and the **i**-axis due to the magnetic distortion:

$$I_{pp} - I_{ii} = \int \rho_B (r^2 - p^2) \, \mathrm{d}V - \int \rho_B (r^2 - i^2) \, \mathrm{d}V = \int \rho_B (i^2 - p^2) \, \mathrm{d}V.$$

In spherical coordinates $(r, \mu \equiv \cos\theta, \lambda)$ we then have

$$\begin{aligned} I_{pp} - I_{ii} &= \int \rho_B \left( (1-\mu^2)\cos^2\lambda - \mu^2 \right) r^4 \, \mathrm{d}r\mathrm{d}\mu\mathrm{d}\lambda \\ &= 2\pi \int \rho_B \left( \frac{1-\mu^2}{2} - \mu^2 \right) r^4 \, \mathrm{d}r\mathrm{d}\mu \\ &= -2\pi \int \rho_B \mathrm{P}_2(\mu) r^4 \, \mathrm{d}r\mathrm{d}\mu. \end{aligned} \tag{3.4.8}$$

We may now compare this result with (3.4.7) to see that

$$\omega = \alpha \cos\chi \, \frac{I_{pp} - I_{ii}}{I_0}. \tag{3.4.9}$$

This is the usual rigid-body result; see for example the classical mechanics text by Landau and Lifshitz [83].

### 3.4.2 Deviation from rigid-body precession in a rotating magnetised fluid

The result at the end of the previous subsection suggests that the macroscopic dynamics of a rotating magnetised fluid body should resemble free precession; however

the fluid is clearly not a rigid body. This presents a question as to what degree the magnetised fluid *can* be regarded as rigid and hence how similar the motion of a magnetised fluid is to 'conventional' rigid-body precession. Mestel sought to answer this by considering the microscopic dynamics — the motion of individual fluid elements. The aim of this subsection is twofold: to elucidate Mestel's original work on fluid precession, and to highlight what we believe are its shortcomings.

The notation used in here is as in the rest of this section, with a couple of additions. Since we will need to distinguish between different frames of reference, we define for brevity the '$\alpha$-frame' to be the one comoving with the star's primary rotation (at frequency $\alpha$) and the '$\omega$-frame' to be the co-precessing frame — i.e. the rigid-body precession frame characterised by the superimposed rotations $\alpha$ and $\omega$.

Let us first recall the two conventional ways of describing perturbations. An *Eulerian* perturbation, denoted $\delta$, is the change in a quantity at a fixed point in space whilst a *Lagrangian* perturbation $\Delta$ is the change in a quantity moving with the fluid. We denote the change in position of a fluid element $\Delta\mathbf{x} \equiv \boldsymbol{\xi}(\mathbf{x}, t)$, called the *Lagrangian displacement*; a fluid element initially located at $\mathbf{x}$ is moved to a new location $\mathbf{x} + \boldsymbol{\xi}(\mathbf{x}, t)$ by the perturbations. From this, it may be seen that the Eulerian and Lagrangian perturbations in (say) the density are related by

$$\Delta\rho = \delta\rho + \boldsymbol{\xi} \cdot \nabla\rho. \tag{3.4.10}$$

We wish to investigate the deviation of a rotating magnetised fluid star from free precession. The rigid-body free precession of the fluid may be described as a density perturbation, whose form is given by (3.4.7); if the fluid precisely obeyed this motion then each fluid element would be stationary as viewed by the co-precessing observer in the $\omega$-frame. Since we do not expect exact rigid-body precession here, let us define the Lagrangian displacement $\boldsymbol{\xi}$ to be the change in position of a fluid element in the co-precessing frame, with its time derivative $\dot{\boldsymbol{\xi}}$ giving the velocity of the element as viewed from the $\omega$-frame. On viewing the star in the inertial frame, we will then see that the motion of a fluid element is a vector sum of *three* characteristic velocities: the normal stellar rotation $\alpha$ about the rotation axis; the slower nutation $\omega$ about the magnetic axis; and the extra velocity field $\dot{\boldsymbol{\xi}}$.

In a rigid body, free precession precisely describes the motion of an element and so by definition $\boldsymbol{\xi} = \mathbf{0}$. However, a fluid is clearly not rigid; it is only able to sustain a time-varying distortion by virtue of the rigidity bestowed by the magnetic field.

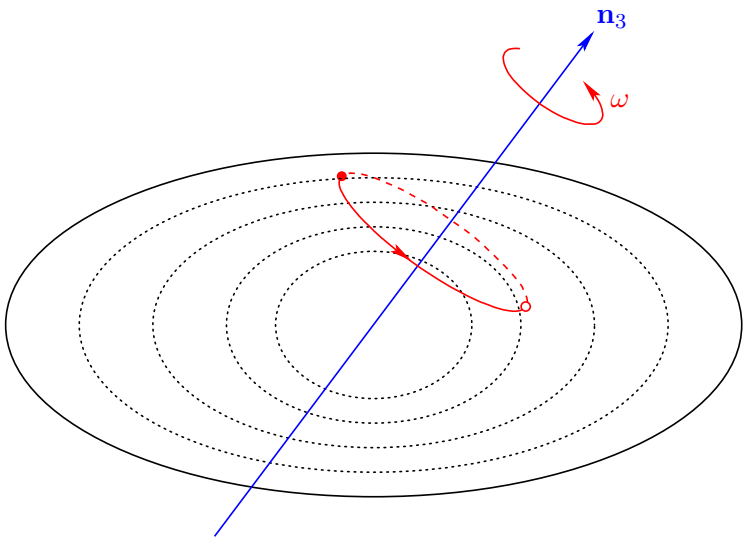


Figure 3.6: Dynamics in the $\alpha$-frame, i.e. the frame rigidly rotating with rate $\alpha$. The centrifugal contribution to the distortion is assumed to dominate, so that the stellar surface (the solid black line) and the isopycnic surfaces (the dashed black lines) are spheroidal. Without a magnetic field, a fluid element will be stationary in this frame; however the magnetic field induces a slow precessional motion, superimposed on the normal stellar rotation. This motion will cause a fluid element (the filled red circle) in the $\alpha$-frame to rotate about the magnetic axis $\mathbf{n}_3$ with period $2\pi/\omega$. Over one period it travels through regions of varying density — it crosses density contours — because of the nonspherical centrifugal distortion.

It is helpful to consider the motion of a fluid element in the $\alpha$-frame; see figure 3.6. In the unmagnetised case the element undergoes only the primary rotation $\alpha$ and so is stationary in the corotating frame. From section 3.4.1 we anticipate that the addition of a misaligned magnetic field will cause the star to precess, and a fluid element in the $\alpha$-frame will therefore undergo a slow rotation or *nutation* (with frequency $\omega$) about the magnetic axis. In doing so, however, the fluid element will be moved through regions of differing density. Since the background density $\rho_0$ is spherical and the magnetic distortion $\rho_B$ is symmetric about its axis, the density difference will be entirely due to the centrifugal bulge $\rho_\alpha$.

This leads us on to a justification of why there should be $\boldsymbol{\xi}$-motions, on the grounds of microscopic physics. Whilst fluid elements will be able to sustain small density variations, those changes which would be experienced by a typical element

in one precession period (see figure 3.6) are likely to be larger than this. For this reason there will be a restoring force on each fluid element that acts to return the element to its original density; hence fluid precession is not rigid, and in general $\boldsymbol{\xi} \neq \mathbf{0}$ (only elements along the magnetic axis will have $\boldsymbol{\xi} = \mathbf{0}$, because they do not experience the nutation in the first place).

There is also a need for $\boldsymbol{\xi}$-motions on macroscopic grounds (i.e. considering the motion of the whole star). Imposing rigid-body precession on a fluid would result in the nutation of the centrifugal bulge about the $\mathbf{n}_3$ axis, potentially taking the fluid well away from its equilibrium configuration; the global effect of the internal $\boldsymbol{\xi}$-motions should then be to restore the star to its stationary equilibrium.

Having described why there should be deviations from rigid-body precession in the magnetised fluid model considered here, we now investigate the nature of these $\boldsymbol{\xi}$-motions. We work in the co-precessing $\omega$-frame unless otherwise stated. First recall that at some initial time $t_0$ we may write the density of a fluid element using (3.4.1). After a time $\delta t$ the element will be rotated through an angle $\delta\lambda = \omega\delta t$; the change in density will be

$$\delta\rho \equiv \rho(t_0 + \delta t) - \rho(t_0) = \rho_\alpha(r, \theta, \lambda + \delta\lambda) - \rho_\alpha(r, \theta, \lambda) = \omega\delta t \frac{\partial \rho_\alpha}{\partial \lambda} \tag{3.4.11}$$

with a similar equation for pressure variation $P_\alpha$,

$$\delta P = P_\alpha(r, \theta, \lambda + \delta\lambda) - P_\alpha(r, \theta, \lambda) = \omega\delta t \frac{\partial P_\alpha}{\partial \lambda}. \tag{3.4.12}$$

We define the Lagrangian displacement $\boldsymbol{\xi}$ to be that change in position which is sourced by the density perturbation $\delta\rho$ (Eulerian in the co-precessing frame); i.e. the displacement field $\boldsymbol{\xi}$ acts to restore fluid elements to their stationary equilibrium state. Then the continuity equation yields

$$\delta\rho = -\nabla \cdot (\rho\boldsymbol{\xi}) \approx -\nabla \cdot (\rho_0\boldsymbol{\xi}) = -\boldsymbol{\xi} \cdot \nabla\rho_0 - \rho_0 \nabla \cdot \boldsymbol{\xi}. \tag{3.4.13}$$

Now expanding this equation in components of $\boldsymbol{\xi}$, we see that

$$\delta\rho = -\xi_r \frac{\mathrm{d}\rho_0}{\mathrm{d}r} - \rho_0 \left( \frac{1}{r^2} \frac{\partial}{\partial r}(r^2 \xi_r) + \frac{1}{r \sin\theta} \frac{\partial}{\partial \theta}(\xi_\theta \sin\theta) + \frac{1}{r \sin\theta} \frac{\partial \xi_\lambda}{\partial \lambda} \right). \tag{3.4.14}$$

From (3.4.11) we know the left-hand side of this equation, but turning to the right-hand side we see that the problem of solving for a displacement field $\boldsymbol{\xi} = (\xi_r, \xi_\theta, \xi_\lambda)$ is, so far, underdetermined: the only equation containing $\boldsymbol{\xi}$ is the continuity equation,

but it contains *three* unknown components of $\boldsymbol{\xi}$. If one does not include any extra physics then there are no other equations to constrain $\boldsymbol{\xi}$ — and hence there is a whole class of solutions (let us call them $\{\boldsymbol{\xi}_{\text{fluid}}\}$) to the problem.

We note, however, that in (3.4.11) and (3.4.13) the magnetic field is conspicuous by its absence. Since the star is only able to precess by virtue of this field, it seems natural that magnetic effects should pick out some particular solution $\boldsymbol{\xi}_{\text{mag}}$ from the class $\{\boldsymbol{\xi}_{\text{fluid}}\}$. Mestel claims that such magnetic terms are all of higher order than the basic perturbations, however, and hence may be ignored.

With no magnetic effects entering his equations, Mestel needs a different approach to resolve the indeterminacy of the problem — he argues that in certain zones of a *main-sequence* star, the $\boldsymbol{\xi}$-motions will be divergence-free. He does however acknowledge that this simplification may not be valid for the whole star — and it is a crude approximation if one is concerned with neutron stars. We repeat his argument for the field being divergence-free here.

We begin with the adiabatic relation between the Lagrangian variations, $\Delta p/p = \gamma\Delta\rho/\rho$; this is the equation of state for the *precessional perturbations*. Substituting the definitions of the variations (3.4.10) and using the continuity equation gives

$$\delta P + \boldsymbol{\xi}\cdot\nabla p = \frac{\gamma p}{\rho}(\delta\rho + \boldsymbol{\xi}\cdot\nabla\rho) = \frac{\gamma p}{\rho}(-\rho\nabla\cdot\boldsymbol{\xi}). \tag{3.4.15}$$

Neglecting $P_\alpha$ and $P_B$ components of the pressure then gives

$$\delta P \approx -\boldsymbol{\xi}\cdot\nabla P_0 - \gamma P_0\nabla\cdot\boldsymbol{\xi} = \omega\delta t\frac{\partial P_\alpha}{\partial\lambda}. \tag{3.4.16}$$

In a uniformly rotating star we have the *background* equation of state, $P_\alpha = \rho_\alpha(\mathrm{d}P_0/\mathrm{d}\rho_0) + \mathcal{O}(\rho_\alpha^2)$, and equation (3.4.16) becomes

$$\boldsymbol{\xi}\cdot\nabla\rho_0 + \frac{\gamma P_0}{\mathrm{d}P_0/\mathrm{d}\rho_0}\nabla\cdot\boldsymbol{\xi} = -\omega\delta t\frac{\partial\rho_\alpha}{\partial\lambda}. \tag{3.4.17}$$

Now combining (3.4.11), (3.4.13) and (3.4.17):

$$-\omega\delta t\frac{\partial\rho_\alpha}{\partial\lambda} = \boldsymbol{\xi}\cdot\nabla\rho_0 + \frac{\gamma P_0}{\mathrm{d}P_0/\mathrm{d}\rho_0}\nabla\cdot\boldsymbol{\xi} = \boldsymbol{\xi}\cdot\nabla\rho_0 + \rho_0\nabla\cdot\boldsymbol{\xi} \tag{3.4.18}$$

which can be rearranged to give the condition

$$\left(\frac{\gamma P_0}{\rho_0(\mathrm{d}P_0/\mathrm{d}\rho_0)} - 1\right)\nabla\cdot\boldsymbol{\xi} = 0. \tag{3.4.19}$$

Mestel now assumes the following relation, which he states is valid in a certain zone of a main-sequence star:

$$\frac{\gamma P_0}{\rho_0(\mathrm{d}P_0/\mathrm{d}\rho_0)} \neq 1 \tag{3.4.20}$$

in which case (3.4.19) implies that the $\boldsymbol{\xi}$-motions are divergence-free:

$$\nabla \cdot \boldsymbol{\xi} = 0. \tag{3.4.21}$$

This condition (3.4.21) implies that the fluid elements move at constant density, $\Delta\rho$, since

$$\Delta\rho = \delta\rho + \boldsymbol{\xi} \cdot \nabla\rho = \delta\rho + \nabla \cdot (\rho\boldsymbol{\xi}) - \rho\nabla \cdot \boldsymbol{\xi} = -\rho\nabla \cdot \boldsymbol{\xi} \tag{3.4.22}$$

where we have used the definition of the Lagrangian perturbation $\Delta\rho$ and the continuity equation.

We are now able to find an expression for the radial component of the velocity field $\dot{\xi}_r$. By combining (3.4.17) with the divergence-free condition (3.4.21) and taking the limit $\delta t \to 0$, we have $\xi_r/\delta t \to \dot{\xi}_r$ and hence

$$\dot{\xi}_r = -\omega \frac{\partial \rho_\alpha}{\partial \lambda} \Big/ \frac{\mathrm{d}\rho_0}{\mathrm{d}r} \tag{3.4.23}$$

Whilst (3.4.23) is a solution for $\dot{\xi}_r$, a third and final constraint is needed to find $\dot{\xi}_\theta$ and $\dot{\xi}_\lambda$ uniquely. Mestel has approached this problem in two ways: in his first paper on the subject he considers the 'simplest' $\boldsymbol{\xi}$-field, where $\xi_\lambda = 0$ [100], but in his second paper seeks the solution which minimises the energy of the $\boldsymbol{\xi}$-motions [99].

The crucial step in the above argument for $\nabla \cdot \boldsymbol{\xi} = 0$ is the condition (3.4.20). This relation is equivalent to the statement that the background and perturbations are governed by different equations of state:

$$\gamma_{back} \equiv \frac{\rho_0}{P_0}\frac{\mathrm{d}P_0}{\mathrm{d}\rho_0} \neq \gamma_{pert}. \tag{3.4.24}$$

Assessing the applicability of this to a main-sequence star is beyond the scope of this thesis, but we do not expect it to be valid for the bulk of a neutron star. In any case, it represents an extra piece of physics being added to the problem. Doing so then gives a class of divergence-free $\boldsymbol{\xi}$-motions, whilst we expect the actual solution for fluid neutron star matter will not have this restriction.

Having argued that Mestel has calculated $\boldsymbol{\xi}$-motions by including extra physics, not applicable to neutron stars, we return to the physics which we believe is missing from the problem: the role of the magnetic field. Examining each term in the perturbed Euler equation, in the $\omega$-frame, Mestel concludes that each one is of higher order than the perturbations he is considering and so all may be neglected. Among these, the perturbed Lorentz force and the nutational Coriolis force have the same order, $\mathcal{O}(\alpha^2 B^2)$, lower than the other perturbed force terms. That is, to lowest order the perturbed Euler equation is a balance between these two terms.

Rather than separately neglecting these two forces, we believe that they should be thought of as a restriction on possible $\boldsymbol{\xi}$-motions. Regarding them in this way, the only acceptable solution to the problem is the one $\boldsymbol{\xi}_{\rm mag}$ that induces a perturbed Lorentz force equal to the nutational Coriolis force. This is then a well-posed problem, which obviates the need to consider $\xi_\lambda = 0$ solutions or 'minimal-energy' solutions.

This system of equations may be solved for very simplistic field geometries, but the general magnetised fluid problem is unlikely to be analytically tractable. In chapter 8 we formulate the problem in a way that allows it to be studied through time evolutions of the perturbation equations of MHD; the idea is that if one finds a precession-like oscillation mode, its frequency can be compared with that mode frequency a precessing rigid body would have. The discrepancy between predicted and observed modes would then provide an answer to the question that motivates this section: how similar are the motion of a magnetised rotating fluid star and a freely precessing rigid body? To date, however, we have been unable to find such precessional modes numerically; we suggest reasons for this in section 8.4.

# Chapter 4

# Rotating and magnetic equilibria: analytic work

One major aim of this thesis is to understand equilibrium configurations of magnetised neutron stars. Neutron stars are believed to be composed predominantly of fluid matter, which can be approximated reasonably well by an $N = 1$ polytrope. Since some neutron stars rotate extremely rapidly and others have very strong magnetic fields, we would like to calculate their equilibria in a non-linear fashion, rather than by using perturbation theory. To accomplish all of this we need to approach the problem numerically; this is described in chapter 6. In this chapter, however, we investigate neutron star equilibria analytically. As well as providing an understanding of the limitations of this approach, our results will provide a check of later numerical work.

Before looking at the problem of magnetically deformed stars, we turn to the simpler problem of distortions of rotating stars. Although a neutron star will have other sources of distortion too, its centrifugal bulge will typically be the largest asphericity. As mentioned before, a uniformly rotating star with no other distortions will be in a stationary state and so not a candidate for precession or gravitational wave emission. However the perturbative calculation here is helpful for understanding the problem of precessional fluid dynamics described in section 3.4.2 and also provides an analytic check of our numerical results in the slow rotation limit.

After the perturbation calculation we present a derivation of the virial theorem, which is valid in the non-linear regime of strong magnetic fields and fast rotation;

we will later use this theorem to test the numerical accuracy of our code. Finally, this chapter contains a calculation for the ellipticities of a rotating magnetised star in terms of components of tensor energy quantities. The major restriction here is that we need to specialise to incompressible fluids, but the results will still give us an indication of the nature of the distortions we should expect in the numerical configurations described in chapter 6.

## 4.1 Distortions of a rotating polytrope

We wish to find an expression for the Eulerian density perturbation $\delta\rho$ at a point in a fluid star consequent on adding a (slow) rotation term. From this expression we will then be able to find the surface shape of a slowly rotating polytrope. We perform the calculation both with and without the Cowling approximation, to see how much this simplification affects the result.

### 4.1.1 Perturbing hydrostatic equilibrium

We begin by supplementing the equations of hydrostatic equilibrium with a rotation term:

$$\frac{1}{\rho}\nabla P + \nabla\Phi + \mathbf{\Omega}\times(\mathbf{\Omega}\times\mathbf{r}) = 0. \tag{4.1.1}$$

where the angular velocity is along the $z$-axis: $\mathbf{\Omega} = \Omega\mathbf{e}_z = \Omega(\cos\theta\mathbf{e}_r - \sin\theta\mathbf{e}_\theta)$. The problem has axial symmetry, so in spherical polars the $\phi$-components are zero. Then $\nabla = \mathbf{e}_r\frac{\partial}{\partial r} + \mathbf{e}_\theta\frac{1}{r}\frac{\partial}{\partial\theta}$ and equation (4.1.1) becomes the pair

$$\frac{\partial P}{\partial r} = -\rho\frac{\partial\Phi}{\partial r} + \rho\Omega^2 r\sin^2\theta \tag{4.1.2}$$

$$\frac{\partial P}{\partial\theta} = -\rho\frac{\partial\Phi}{\partial\theta} + \rho\Omega^2 r^2\sin\theta\cos\theta. \tag{4.1.3}$$

Poisson's equation in these coordinates is

$$\nabla^2\Phi = \frac{1}{r^2}\frac{\partial}{\partial r}\left(r^2\frac{\partial\Phi}{\partial r}\right) + \frac{1}{r^2\sin\theta}\frac{\partial}{\partial\theta}\left(\sin\theta\frac{\partial\Phi}{\partial\theta}\right) = 4\pi G\rho \tag{4.1.4}$$

and assuming a polytropic equation of state gives

$$P = k\rho^\gamma. \tag{4.1.5}$$

Note that $\gamma$ is often replaced with the *polytropic index* $N$, where $1 + \frac{1}{N} = \gamma$. By assuming slow rotation (i.e. that $\Omega^2$ is a small term) we can write, to first order,

each of $\rho$, $P$ and $\Phi$ as a background piece plus a small Eulerian perturbation, e.g. $P = P_0 + \delta P$. We first perturb (4.1.2):

$$\begin{aligned}\frac{\partial P}{\partial r} &= \frac{\partial P_0}{\partial r} + \frac{\partial \delta P}{\partial r} \\ &= (\rho_0 + \delta\rho)\Omega^2 r \sin^2\theta - (\rho_0 + \delta\rho)\left(\frac{\partial \Phi_0}{\partial r} + \frac{\partial \delta\Phi}{\partial r}\right) \\ &= \rho_0\Omega^2 r\sin^2\theta - \rho_0\frac{\partial\Phi_0}{\partial r} - \rho_0\frac{\partial\delta\Phi}{\partial r} - \delta\rho\frac{\partial\Phi_0}{\partial r} \qquad (4.1.6)\end{aligned}$$

where we have neglected the higher-order terms $\delta\rho\ \Omega^2 r\sin^2\theta$ and $\delta\rho\frac{\partial\delta\Phi}{\partial r}$. Clearly hydrostatic equilibrium should be satisfied for the static background configuration (without rotation), so we can split (4.1.6) into background and perturbation equations:

$$\frac{\partial P_0}{\partial r} = -\rho_0\frac{\partial\Phi_0}{\partial r} \qquad (4.1.7)$$

$$\frac{\partial \delta P}{\partial r} = \rho_0\Omega^2 r\sin^2\theta - \rho_0\frac{\partial\delta\Phi}{\partial r} - \delta\rho\frac{\partial\Phi_0}{\partial r}. \qquad (4.1.8)$$

Similarly, perturbing (4.1.3) gives

$$\frac{\partial P_0}{\partial\theta} = -\rho_0\frac{\partial\Phi_0}{\partial\theta} = 0 \qquad (4.1.9)$$

$$\frac{\partial\delta P}{\partial\theta} = \rho_0\Omega^2 r^2\sin\theta\cos\theta - \rho_0\frac{\partial\delta\Phi}{\partial\theta} \qquad (4.1.10)$$

where the $\theta$-derivative term from the first equation vanishes since $\frac{\partial\Phi_0}{\partial\theta} = 0$; the background star is spherically symmetric and therefore $\Phi_0 = \Phi_0(r)$ with no angular dependence.

We next perturb Poisson's equation, yielding background and perturbation equations:

$$4\pi G\rho_0 = \frac{1}{r^2}\frac{\mathrm{d}}{\mathrm{d}r}\left(r^2\frac{\mathrm{d}\Phi_0}{\mathrm{d}r}\right) \qquad (4.1.11)$$

$$4\pi G\delta\rho = \frac{1}{r^2}\frac{\partial}{\partial r}\left(r^2\frac{\partial\delta\Phi}{\partial r}\right) + \frac{1}{r^2\sin\theta}\frac{\partial}{\partial\theta}\left(\sin\theta\frac{\partial\delta\Phi}{\partial\theta}\right). \qquad (4.1.12)$$

Finally, turning to the polytropic relation we have:

$$P = P_0 + \delta P = k(\rho_0 + \delta\rho)^\gamma = k\rho_0^\gamma + \gamma k\rho_0^{\gamma-1}\delta\rho + \mathcal{O}(\delta\rho^2) \qquad (4.1.13)$$

and so

$$P_0 = k\rho_0^\gamma \qquad (4.1.14)$$

$$\delta P = \gamma k\rho_0^{\gamma-1}\delta\rho. \qquad (4.1.15)$$

The same result can be obtained using the relation between Lagrangian variations

$$\frac{\Delta P}{P_0} = \gamma \frac{\Delta \rho}{\rho_0}. \tag{4.1.16}$$

Using the definition of the Lagrangian variation $\Delta = \delta + \boldsymbol{\xi} \cdot \nabla$ into (4.1.16) gives

$$\frac{\delta P + \boldsymbol{\xi} \cdot \nabla P_0}{P_0} = \gamma \frac{\delta \rho + \boldsymbol{\xi} \cdot \nabla \rho_0}{\rho_0} \tag{4.1.17}$$

which with the polytropic assumption on the background $P_0 = k\rho_0^\gamma$ becomes:

$$\begin{aligned} \delta P &= \gamma k \rho_0^{\gamma-1}(\delta\rho + \boldsymbol{\xi} \cdot \nabla \rho_0) - \boldsymbol{\xi} \cdot \nabla(k\rho_0^\gamma) \\ &= \gamma k \rho_0^{\gamma-1} \delta\rho \end{aligned} \tag{4.1.18}$$

as before[1]. This is not surprising: we have simply plugged the polytropic relation for the background relation into that of the Lagrangian variations.

### 4.1.2 Solving the background equations

We first want to find the density distribution of the background, non-rotating star; this means solving the background system of equations

$$\frac{\mathrm{d}P_0}{\mathrm{d}r} = -\rho \frac{\mathrm{d}\Phi_0}{\mathrm{d}r} \tag{4.1.19}$$

$$\frac{1}{r^2}\frac{\mathrm{d}}{\mathrm{d}r}\left(r^2 \frac{\mathrm{d}\Phi_0}{\mathrm{d}r}\right) = 4\pi G \rho_0 \tag{4.1.20}$$

$$P_0 = k\rho_0^\gamma. \tag{4.1.21}$$

We begin by replacing the $\Phi_0$ derivative in (4.1.20) using (4.1.19):

$$\frac{1}{r^2}\frac{\mathrm{d}}{\mathrm{d}r}\left(-\frac{r^2}{\rho_0}\frac{\mathrm{d}P_0}{\mathrm{d}r}\right) = 4\pi G \rho_0. \tag{4.1.22}$$

Now substituting (4.1.21) into (4.1.22) we find, after some algebra, that

$$-4\pi G \rho_0 = k\gamma \rho_0^{\gamma-2}\left(\frac{2}{r}\frac{\mathrm{d}\rho_0}{\mathrm{d}r} + (\gamma-2)\rho_0^{-1}\left(\frac{\mathrm{d}\rho_0}{\mathrm{d}r}\right)^2 + \frac{\mathrm{d}^2\rho_0}{\mathrm{d}r^2}\right). \tag{4.1.23}$$

This equation is clearly greatly simplified for the case $\gamma = 2$, which also happens to be a reasonable approximation for a neutron star (see section 1.1.3). In this case (4.1.23) becomes:

$$\frac{\mathrm{d}^2\rho_0}{\mathrm{d}r^2} + \frac{2}{r}\frac{\mathrm{d}\rho_0}{\mathrm{d}r} + \frac{2\pi G}{k}\rho_0 = 0. \tag{4.1.24}$$

[1] assuming that the $\gamma$ in the Lagrangian relation (4.1.16) is the same as the $\gamma$ of the background polytropic relation.

Solving this equation with the boundary condition of a constant central density $\rho_0(0) = \rho_c$, we find the density distribution:

$$\rho_0(r) = \rho_c \frac{\sin\sqrt{\frac{2\pi G}{k}}r}{\sqrt{\frac{2\pi G}{k}}r}. \tag{4.1.25}$$

### 4.1.3 Cowling solution

We now turn to the second set of equations from our perturbation analysis, for the Eulerian variations $\delta P$ and $\delta\rho$ sourced by the rotation. As a simplest first case, we also make the Cowling approximation: that derivatives of $\delta\Phi$ may be regarded as negligible. This reduces the perturbation equations to the set:

$$\frac{\partial \delta P}{\partial r} = \rho_0\Omega^2 r\sin^2\theta - \delta\rho\frac{\partial\Phi_0}{\partial r} \tag{4.1.26}$$

$$\frac{\partial \delta P}{\partial \theta} = \rho_0\Omega^2 r^2\sin\theta\cos\theta \tag{4.1.27}$$

$$\delta P = 2k\rho_0\delta\rho. \tag{4.1.28}$$

Note that there is no perturbed Poisson equation in this case, as the Cowling approximation is inconsistent with it (the two together imply, incorrectly, that $4\pi G\delta\rho = 0$). Now, for our $\gamma = 2$ polytrope

$$\frac{\mathrm{d}\Phi_0}{\mathrm{d}r} = -\frac{1}{\rho_0}\frac{\mathrm{d}P_0}{\mathrm{d}r} = -\frac{1}{\rho_0}\frac{\mathrm{d}}{\mathrm{d}r}(k\rho_0^2) = -2k\frac{\mathrm{d}\rho_0}{\mathrm{d}r}; \tag{4.1.29}$$

using this result in (4.1.26) gives

$$\frac{\partial \delta P}{\partial r} = \rho_0\Omega^2 r\sin^2\theta + 2k\delta\rho\frac{\mathrm{d}\rho_0}{\mathrm{d}r}. \tag{4.1.30}$$

Now, using (4.1.28) we see that

$$\frac{\partial \delta P}{\partial r} = \frac{\partial}{\partial r}(2k\rho_0\delta\rho) = 2k\rho_0\frac{\partial\delta\rho}{\partial r} + 2k\delta\rho\frac{\mathrm{d}\rho_0}{\mathrm{d}r}; \tag{4.1.31}$$

comparing this with (4.1.30) yields

$$\frac{\partial\delta\rho}{\partial r} = \frac{\Omega^2 r\sin^2\theta}{2k} \tag{4.1.32}$$

which we integrate to give

$$\delta\rho = \frac{\Omega^2 r^2\sin^2\theta}{4k} + \mathcal{A}(\theta) + \mathcal{C}_1 \tag{4.1.33}$$

for some arbitrary function $\mathcal{A}(\theta)$ and integration constant $\mathcal{C}_1$.

Similarly we use (4.1.28) and find that

$$\frac{\partial \delta P}{\partial \theta} = \frac{\partial}{\partial \theta}(2k\rho_0 \delta\rho) = 2k\rho_0 \frac{\partial \delta\rho}{\partial \theta} \tag{4.1.34}$$

since $\frac{\partial \rho_0}{\partial \theta} = 0$; now comparing (4.1.34) with (4.1.28) we see that

$$\frac{\partial \delta\rho}{\partial \theta} = \frac{\Omega^2 r^2 \sin\theta\cos\theta}{2k} \tag{4.1.35}$$

which integrates to give

$$\delta\rho = \frac{\Omega^2 r^2 \sin^2\theta}{4k} + \mathcal{B}(r) + \mathcal{C}_2 \tag{4.1.36}$$

where $\mathcal{B}(r)$ is an arbitrary purely radial function and $\mathcal{C}_2$ some constant.

Now we compare the two perturbation solutions (4.1.33) and (4.1.36), noting that for consistency we require $\mathcal{A}(\theta) = \mathcal{B}(r) = 0$ and $\mathcal{C}_1 = \mathcal{C}_2 \equiv \mathcal{C}$, and find that:

$$\begin{aligned} \delta\rho &= \frac{\Omega^2 r^2 \sin^2\theta}{4k} + \mathcal{C} \\ &\equiv \frac{\Omega^2 (r^2 \sin^2\theta - \mathcal{D})}{4k} \end{aligned} \tag{4.1.37}$$

where on the last line we have rewritten the integration constant as $\mathcal{D} = -4k\mathcal{C}/\Omega^2$ to reflect the requirement that in the limit $\Omega \to 0$ we should recover the background solution, i.e. $\delta\rho = 0$.

To complete the solution we need to find the integration constant $\mathcal{D}$. We begin by finding the radius of the star, which to first order is equal to the radius of the background configuration. The surface of the polytrope is the first zero of the function $\rho_0(r)$; from (4.1.25) we see that this occurs at

$$r = R \equiv \sqrt{\frac{\pi k}{2G}}. \tag{4.1.38}$$

We can extend the continuity equation for a fluid element

$$\delta\rho + \nabla \cdot (\rho_0 \boldsymbol{\xi}) = 0 \tag{4.1.39}$$

to the whole star by integrating it over the star's volume, finding that

$$\int_V \delta\rho \, \mathrm{d}V = -\int_V \nabla \cdot (\rho_0 \boldsymbol{\xi}) \, \mathrm{d}V = -\int_S \rho_0 \boldsymbol{\xi} \cdot \mathrm{d}\mathbf{S} = 0. \tag{4.1.40}$$

We now use this condition and the expression for $\delta\rho$ given by (4.1.37) to determine the constant $\mathcal{D}$:

$$\begin{aligned} 0 = \int_V \delta\rho \; dV &= \int_0^{\phi=2\pi} \int_0^{\theta=\pi} \int_0^{r=R} \frac{\Omega^2(r^2\sin^2\theta - \mathcal{D})}{4k} \; r^2 \sin\theta \; \mathrm{d}r \, \mathrm{d}\theta \, \mathrm{d}\phi \\ &= \frac{\Omega^2\pi^2}{30G^2}\sqrt{\frac{\pi k}{2G}}\left(\frac{\pi k}{5G} - \mathcal{D}\right) \end{aligned} \tag{4.1.41}$$

and hence $\mathcal{D} = \frac{\pi k}{5G}$. Our final expression for the Eulerian density perturbation in a slowly-rotating $\gamma = 2$ polytrope is therefore

$$\delta\rho = \frac{\Omega^2(r^2\sin^2\theta - \frac{\pi k}{5G})}{4k}. \tag{4.1.42}$$

For comparison with the following non-Cowling work we rewrite this result using $\mu = \cos\theta$ and the Legendre polynomial $\mathrm{P}_2(\mu)$:

$$\delta\rho = \frac{\Omega^2(r^2 - \frac{3\pi k}{10G})}{6k} - \frac{\Omega^2 r^2 \mathrm{P}_2(\mu)}{6k}. \tag{4.1.43}$$

### 4.1.4 Non-Cowling solution

#### Perturbation equations

We now return to the original perturbation equations, but this time do not make the Cowling approximation. For a slowly-rotating $\gamma = 2$ polytrope the equations are now:

$$\frac{\partial\delta P}{\partial r} = \rho_0\Omega^2 r\sin^2\theta - \delta\rho\frac{\partial\Phi_0}{\partial r} - \rho_0\frac{\partial\delta\Phi}{\partial r} \tag{4.1.44}$$

$$\frac{\partial\delta P}{\partial\theta} = \rho_0\Omega^2 r^2\sin\theta\cos\theta - \rho_0\frac{\partial\delta\Phi}{\partial\theta} \tag{4.1.45}$$

$$4\pi G\delta\rho = \frac{1}{r^2}\frac{\partial}{\partial r}\left(r^2\frac{\partial\delta\Phi}{\partial r}\right) + \frac{1}{r^2\sin\theta}\frac{\partial}{\partial\theta}\left(\sin\theta\frac{\partial\delta\Phi}{\partial\theta}\right) \tag{4.1.46}$$

$$\delta P = 2k\rho_0\delta\rho. \tag{4.1.47}$$

We wish to re-express the perturbed force balance equations (4.1.44) and (4.1.45) in terms of $\delta\rho$. We first note that the background equation $\frac{\partial\Phi_0}{\partial r} = -\frac{1}{\rho}\frac{\partial P_0}{\partial r}$ allows us to eliminate $\Phi_0$ from (4.1.44), then replace $\delta P$ using (4.1.47). This leaves a perturbed force balance equation in the Eulerian density and gravitational potential variations:

$$\frac{\partial\delta\rho}{\partial r} = \frac{\Omega^2 r\sin^2\theta}{2k} - \frac{1}{2k}\frac{\partial\delta\Phi}{\partial r}. \tag{4.1.48}$$

Similarly, (4.1.45) becomes

$$\frac{\partial \delta\rho}{\partial \theta} = \frac{\Omega^2 r^2 \sin\theta\cos\theta}{2k} - \frac{1}{2k}\frac{\partial \delta\Phi}{\partial \theta}. \tag{4.1.49}$$

Directly integrating (4.1.48) and (4.1.49) shows that the only integration constant $\mathcal{D}$ has to be independent of $r$ and $\theta$. Thus

$$\delta\rho = \frac{\Omega^2(r^2\sin^2\theta - \mathcal{D})}{4k} - \frac{1}{2k}\delta\Phi. \tag{4.1.50}$$

Finally we turn to the perturbed Poisson equation (4.1.46) and use (4.1.50) to write it entirely in terms of $\delta\Phi$:

$$\nabla^2\delta\Phi = 4\pi G\delta\rho = -\frac{2\pi G}{k}\delta\Phi + \frac{G\pi\Omega^2}{k}(r^2\sin^2\theta - \mathcal{D}). \tag{4.1.51}$$

Defining $m \equiv \sqrt{2\pi G/k}$, (4.1.51) is manifestly a Helmholtz equation with a rotational source term:

$$(\nabla^2 + m^2)\delta\Phi = \frac{G\pi\Omega^2}{k}(r^2\sin^2\theta - \mathcal{D}). \tag{4.1.52}$$

**Solving the Poisson equation**

To solve (4.1.52) we first consider the $\Omega = 0$ case — the homogeneous Helmholtz equation

$$(\nabla^2 + m^2)\delta\Phi = 0. \tag{4.1.53}$$

Our problem is one of axial rotation, so we expect $\delta\Phi = \delta\Phi(r,\theta)$ for the homogeneous problem too. We attempt to solve this by separation of variables and so make the ansatz $\delta\Phi = R(r)\Theta(\theta)$. Under this ansatz (4.1.53) becomes

$$\frac{\Theta}{r^2}\frac{\mathrm{d}}{\mathrm{d}r}\left(r^2\frac{\mathrm{d}R}{\mathrm{d}r}\right) + \frac{R}{r^2\sin\theta}\frac{\mathrm{d}}{\mathrm{d}\theta}\left(\sin\theta\frac{\mathrm{d}\Theta}{\mathrm{d}\theta}\right) = -m^2R\Theta; \tag{4.1.54}$$

multiplying through by $r^2/(R\Theta)$ then gives

$$m^2r^2 + \frac{1}{R}\frac{\mathrm{d}}{\mathrm{d}r}\left(r^2\frac{\mathrm{d}R}{\mathrm{d}r}\right) = -\frac{1}{\Theta\sin\theta}\frac{\mathrm{d}}{\mathrm{d}\theta}\left(\sin\theta\frac{\mathrm{d}\Theta}{\mathrm{d}\theta}\right). \tag{4.1.55}$$

Since the left hand side is a function of $r$ and the right a function of $\theta$ we may set both sides equal to some constant $l(l+1)$ (this choice will prove useful) to effect the separation of variables into two equations, one in $r$ and one in $\theta$. The equation in $r$

$$\frac{1}{r^2}\frac{\mathrm{d}}{\mathrm{d}r}\left(r^2\frac{\mathrm{d}R}{\mathrm{d}r}\right) + \left(m^2 - \frac{l(l+1)}{r^2}\right)R = 0 \tag{4.1.56}$$

is a rescaled Bessel equation whose solution for each $l$ is a half-integer Bessel function

$$R(r) = \frac{1}{\sqrt{r}} J_{l+\frac{1}{2}}(mr). \tag{4.1.57}$$

Mathematically, the $Y_{l+\frac{1}{2}}$ Bessel functions are also admissable as solutions, but since these diverge at the origin we discard them as unphysical. Next, we turn to the equation in $\theta$:

$$\frac{1}{\sin\theta}\frac{\mathrm{d}}{\mathrm{d}\theta}\left(\sin\theta\frac{\mathrm{d}\Theta}{\mathrm{d}\theta}\right) + l(l+1)\Theta = 0. \tag{4.1.58}$$

By inspection, this is simply Legendre's equation whose solution is the Legendre polynomial $P_l(\cos\theta)$. The general solution would also include the Legendre $Q_l$ functions, but since these have nondifferentiable points we discard them. Our full solution to (4.1.53), with a set of arbitrary constants $\{\beta_l\}$, is thus

$$\delta\Phi_{homog} = R(r)\Theta(\theta) = \frac{1}{\sqrt{r}}\sum_{l=0}^{\infty}\beta_l\ J_{l+\frac{1}{2}}\left(\sqrt{\tfrac{2\pi G}{k}}r\right)P_l(\cos\theta). \tag{4.1.59}$$

We now seek a particular solution of (4.1.52). We may rewrite the right-hand side of this equation as a sum of the Legendre polynomials $\mathrm{P}_0(\cos\theta) = 1$ and $\mathrm{P}_2(\cos\theta) = \frac{1}{2}(3\cos^2\theta - 1)$:

$$\frac{G\pi\Omega^2}{k}(r^2\sin^2\theta - \mathcal{D}) = \frac{G\pi\Omega^2}{3k}\left(-2r^2\mathrm{P}_2(\cos\theta) + 2r^2 - 3\mathcal{D}\right), \tag{4.1.60}$$

which suggests that we make the ansatz $\delta\Phi = \delta\Phi_0(r) + \delta\Phi_2(r)\mathrm{P}_2(\cos\theta)$ for our particular solution and use this to determine the functions $\delta\Phi_0$ and $\delta\Phi_2$. We first note that, for a purely radial function $f(r)$ and a purely angular one $g(\theta)$,

$$\nabla^2(fg) = g\nabla^2 f + f\nabla^2 g \tag{4.1.61}$$

since the cross-term $2\nabla f\cdot\nabla g$ is zero by orthogonality. Given this, the left-hand side of (4.1.52) under our ansatz $\delta\Phi = \delta\Phi_0 + \delta\Phi_2\mathrm{P}_2$ is:

$$\nabla^2\delta\Phi + \frac{2\pi G}{k}\delta\Phi = \delta\Phi_0'' + \frac{2}{r}\delta\Phi_0' + \frac{2\pi G}{k}\delta\Phi + \left(\delta\Phi_2'' + \frac{2}{r}\delta\Phi_2 + \left(\frac{2\pi G}{k} - \frac{6}{r^2}\right)\delta\Phi_2\right)\mathrm{P}_2 \tag{4.1.62}$$

where a prime denotes a derivative with respect to $r$. We now seek a solution to (4.1.52) by equating the coefficients of $\mathrm{P}_0$ and $\mathrm{P}_2$ for the left and right-hand sides, equations (4.1.62) and (4.1.60) respectively. Equating the $\mathrm{P}_0$ coefficients first leaves the equation

$$\delta\Phi_0'' + \frac{2}{r}\delta\Phi_0' + \frac{2\pi G}{k}\delta\Phi_0 = \frac{G\pi\Omega^2}{k}\left(\frac{2r^2}{3} - \mathcal{D}\right) \tag{4.1.63}$$

which we solve to find that

$$\delta\Phi_0 = \frac{\Omega^2}{6}\left(2r^2 - 3\mathcal{D} - \frac{6k}{\pi G}\right). \tag{4.1.64}$$

We now equate the $\mathrm{P}_2$ coefficients, leading to the equation

$$\delta\Phi_2'' + \frac{2}{r}\delta\Phi_2' + \left(\frac{2\pi G}{k} - \frac{6}{r^2}\right)\delta\Phi_2 = -\frac{2G\pi\Omega^2 r^2}{3k} \tag{4.1.65}$$

whose solution is

$$\delta\Phi_2 = -\frac{\Omega^2 r^2}{3}. \tag{4.1.66}$$

Our particular solution is therefore

$$\delta\Phi_{PS} = \delta\Phi_0 + \delta\Phi_2\mathrm{P}_2 = \frac{\Omega^2}{6}\left(2r^2 - 3\mathcal{D} - \frac{6k}{\pi G}\right) - \frac{\Omega^2 r^2}{3}\mathrm{P}_2. \tag{4.1.67}$$

**External field perturbations**

Outside the star $\delta\rho = 0$ and Poisson's equation is

$$\nabla^2\delta\Phi = 0. \tag{4.1.68}$$

We may perform a separation of variables in a similar fashion as for the homogeneous problem; under the ansatz $\delta\Phi = R(r)\Theta(\theta)$, (4.1.68) becomes the pair of equations

$$\frac{\mathrm{d}}{\mathrm{d}r}\left(r^2\frac{\mathrm{d}R}{\mathrm{d}r}\right) - l(l+1)R = 0 \tag{4.1.69}$$

$$\frac{1}{\sin\theta}\frac{\mathrm{d}}{\mathrm{d}\theta}\left(\sin\theta\frac{\mathrm{d}\Theta}{\mathrm{d}\theta}\right) + l(l+1)\Theta = 0. \tag{4.1.70}$$

The latter equation we have solved already, giving $\Theta = P_l(\cos\theta)$ for a particular $l$. The former equation may be solved to find

$$R = r^{-l-1} \tag{4.1.71}$$

for some particular $l$. We see from this that the perturbation in the external potential is given by an infinite sum over $l$ of each $R\Theta$; however, matching this to an internal field with $\mathrm{P}_0$ and $\mathrm{P}_2$ components only enforces the same structure for the exterior solution, that is

$$\delta\Phi_{ext} = \frac{\alpha_0}{r} + \frac{\alpha_2}{r^3}\mathrm{P}_2 \tag{4.1.72}$$

for some constants $\alpha_0, \alpha_2$.

### Boundary conditions

Our physical boundary conditions for a star are the requirements that both the gravitational potential $\Phi$ and its gradient vector $\nabla\Phi$ are continuous at the star's surface. This condition is automatically satisfied for the background spherically-symmetric field $\Phi_0$, so since $\Phi = \Phi_0 + \delta\Phi$ we require it to be satisfied separately for the perturbation $\delta\Phi$.

From equations (4.1.59) and (4.1.67) we see that inside the star the perturbations in the gravitational potential are of the form

$$\delta\Phi_{int} = \delta\Phi_{homog} + \delta\Phi_{PS} = \frac{\beta_0 J_{\frac{1}{2}}}{\sqrt{r}} + \frac{\Omega^2}{6}\left(2r^2 - 3\mathcal{D} - \frac{6k}{\pi G}\right) + \left(\frac{\beta_0 J_{\frac{5}{2}}}{\sqrt{r}} - \frac{\Omega^2 r^2}{3}\right)\mathrm{P}_2. \tag{4.1.73}$$

For brevity we have not shown the dependence of the Bessel functions $J_{\frac{n}{2}} = J_{\frac{n}{2}}\left(\frac{2\pi G}{k}r\right)$ in the above expression. Now, since $\delta\Phi_{PS}$ has only $\mathrm{P}_0$ and $\mathrm{P}_2$ coefficients we expect the same structure for $\delta\Phi_{homog}$ and have dropped all terms in the sum (4.1.59) except those for $l = 0$ and $l = 2$.

In order to satisfy the boundary conditions, we need to find values of the constants $\alpha_0, \alpha_2$ and $\beta_0, \beta_2$ so that at the surface of the star the internal and external fields, and their gradients, match. As for the Cowling case, the star's radius is $R = \sqrt{\frac{\pi k}{2G}}$.

We begin with the requirement that the $\mathrm{P}_0$ coefficients of $\delta\Phi_{int}$ and $\delta\Phi_{ext}$ should be equal at the surface, radius $R$. Solving this for $\alpha_0$ we find that

$$\alpha_0 = \Omega^2\left(\frac{k(\pi^2 - 6)}{6G} - \frac{\pi\mathcal{D}}{2}\right)\sqrt{\frac{k}{2\pi G}}. \tag{4.1.74}$$

Next, equating the $\mathrm{P}_2$ components of $\delta\Phi_{int}$ and $\delta\Phi_{ext}$ at $r = R$ yields an expression for $\alpha_2$ in terms of $\beta_2$:

$$\alpha_2(\beta_2) = 3\beta_2\sqrt[4]{\frac{k^5}{8\pi^3 G^5}} - \frac{k^2\pi^3\Omega^2}{12G^2}\sqrt{\frac{k}{2\pi G}}. \tag{4.1.75}$$

We now turn to the matching of $\nabla\delta\Phi_{int,ext}$. First note that for some field $f = f_0(r) + f_2(r)\mathrm{P}_2(\cos\theta)$:

$$\nabla f = \frac{\partial}{\partial r}(f_0 + f_2\mathrm{P}_2)\hat{\mathbf{r}} + \frac{1}{r}\frac{\partial}{\partial\theta}(f_0 + f_2\mathrm{P}_2)\hat{\boldsymbol{\theta}} \tag{4.1.76}$$

$$= \left(\frac{\partial f_0}{\partial r} + \frac{\partial f_2}{\partial r}\mathrm{P}_2\right)\hat{\mathbf{r}} + \frac{1}{r}\left(f_2\frac{\partial \mathrm{P}_2}{\partial\theta}\right)\hat{\boldsymbol{\theta}}. \tag{4.1.77}$$

This means that matching the $\hat{\boldsymbol{\theta}}$ components of $\nabla\delta\Phi_{int,ext}$ is equivalent to matching the $\mathrm{P}_2$ components of $\delta\Phi_{int,ext}$, yielding no new information. We see then, that explicit determination of the four constants $\alpha_{0,2}, \beta_{0,2}$ should come from consideration of the $\hat{\mathbf{r}}$ components of $\nabla\delta\Phi_{int,ext}$ at $r = R$. We begin by performing this matching for the $\mathrm{P}_0$ components, which yields an explicit expression for $\beta_0$:

$$\beta_0 = \frac{\Omega^2(\pi^2-2)}{2}\sqrt[4]{\frac{k^5}{8\pi^3G^5}} - \frac{\Omega^2\mathcal{D}}{4}\sqrt[4]{\frac{2\pi k}{G}}. \tag{4.1.78}$$

Next equating the $\mathrm{P}_2$ components, we find explicit expressions for $\alpha_2$ and $\beta_2$:

$$\alpha_2 = -\frac{\Omega^2(\pi^2-15)}{12}\sqrt{\frac{\pi k^5}{2G^5}} \tag{4.1.79}$$

$$\beta_2 = \frac{5\pi k\Omega^2}{12G}\sqrt[4]{\frac{2\pi k}{G}}. \tag{4.1.80}$$

**Final result**

Substituting our expressions for $\beta_0$ and $\beta_2$ into (4.1.73) gives us an explicit solution $\delta\Phi_{int}$ to the perturbed Poisson equation (4.1.52), which satisfies the boundary conditions; all that remains is to determine the constant $\mathcal{D}$. To this end, we now substitute the solution $\delta\Phi_{int}$ back into (4.1.50), in place of $\delta\Phi$, to yield an expression for $\delta\rho$. As for the Cowling case we may integrate the continuity equation to give the condition

$$\int_V \delta\rho \, \mathrm{d}V = 0. \tag{4.1.81}$$

With this requirement we may integrate our expression for $\delta\rho$ to fix $\mathcal{D}$, finding that

$$\mathcal{D} = \frac{(\pi^2-6)k}{3\pi G}. \tag{4.1.82}$$

Finally, by substituting this value for $\mathcal{D}$ back into the expression for $\delta\rho$, (and recalling that $m \equiv \sqrt{2\pi G/k}$) we are able to write down an expression for density perturbations in a $\gamma = 2$ polytropic star:

$$\delta\rho = \frac{\Omega^2}{2G}\left(\frac{1}{\pi} - \frac{\pi}{3mr}\sin mr\right) + \frac{5\Omega^2}{8Gr}\left(\frac{k}{Gr}\cos mr + \frac{2\pi}{m}\left(\frac{1}{3} - \frac{1}{m^2r^2}\right)\sin mr\right)\mathrm{P}_2(\mu). \tag{4.1.83}$$

### 4.1.5 Surface shape of a rotating polytrope

Having found an expression for $\delta\rho$ we are now able to calculate the surface distortion of the star due to the rotation. At the surface of the star the Lagrangian density perturbations are zero:

$$0 = \Delta\rho(R) \equiv \delta\rho(R) + \boldsymbol{\xi} \cdot \nabla\rho|_{r=R} \tag{4.1.84}$$

where we have used the relation between Lagrangian and Eulerian perturbations; next we note that to first order $\rho = \rho_0$ and that $\nabla\rho_0 = \frac{\partial\rho_0}{\partial r}$, thus (4.1.84) gives

$$\xi_R = -\frac{\delta\rho(R)}{\frac{\partial\rho_0}{\partial r}(R)}. \tag{4.1.85}$$

Now evaluating (4.1.83) and differentiating (4.1.25), both at $r = R = \sqrt{\frac{\pi k}{2G}}$, we find that the surface displacement (i.e. the surface distortion) is given by

$$\xi_R(\mu) = \Omega^2 \, \frac{(2 - 5\mathrm{P}_2)}{4\rho_c G^2} \sqrt{\frac{kG}{2\pi}} \tag{4.1.86}$$

and the star's boundary radius at some angle $\mu = \cos\theta$ is just $R + \xi_R(\mu)$. If we now define a rescaled dimensionless velocity $v$ and dimensionless radius $\mathfrak{r}$ by

$$v \equiv \frac{\Omega^2}{2\pi\rho_c G} \tag{4.1.87}$$

$$\mathfrak{r} \equiv mr = \sqrt{\frac{2\pi G}{k}}\, r \tag{4.1.88}$$

then the star's boundary $\mathfrak{r}_0(\mu)$ is given by

$$\mathfrak{r}_0(\mu) = \pi + \pi v \left(1 - \frac{5}{2}\mathrm{P}_2(\mu)\right), \tag{4.1.89}$$

in agreement with the numerical results of Chandrasekhar[21] (equation 55) where the boundary is denoted $\xi_0$. We will later use these analytic results as a check of our stationary equilibrium code; see chapter 6.

Similarly, the fractional distortion is

$$\mathfrak{d}(\mu) = \frac{\xi_R(\mu)}{R} = \left(1 - \frac{5}{2}\mathrm{P}_2(\mu)\right) v \tag{4.1.90}$$

giving an increase in equatorial radius of $\frac{9}{4}v$ and a decrease of polar radius of $\frac{3}{2}v$.

Note that we were able to calculate the surface displacement of the star because of the boundary condition $\Delta\rho(R) = 0$. We have no similar condition for the interior

of the star, so the problem of calculating the displacement field there is underdetermined; we find a similar indeterminacy in the precessing-fluid problem of section 3.4.2. In both problems we conclude that there is no single solution for displacements in a rotating fluid unless there are additional constraints on its motion (for example elasticity or magnetic fields).

We conclude this section with plots (see figure 4.1) of rotating star surfaces calculated using (4.1.89) and the equivalent Cowling formula (calculated using (4.1.85) and (4.1.43)):

$$\mathfrak{r}_0^{cow}(\mu) = \pi + \frac{\pi^3 v}{15}\left(1 - \frac{5}{2}\mathrm{P}_2(\mu)\right). \tag{4.1.91}$$

We see that the Cowling approximation considerably underestimates the surface distortion of a rotating star. The discrepancy is not too surprising: the Cowling approximation is best for high values of azimuthal index $m$, whilst we are dealing with $m = 0$ configurations here. This issue is discussed again in chapter 8, where we find that using the Cowling approximation for $m = 1$ oscillations leads to the appearance of a spurious oscillation mode, which is not present in the full non-Cowling problem.

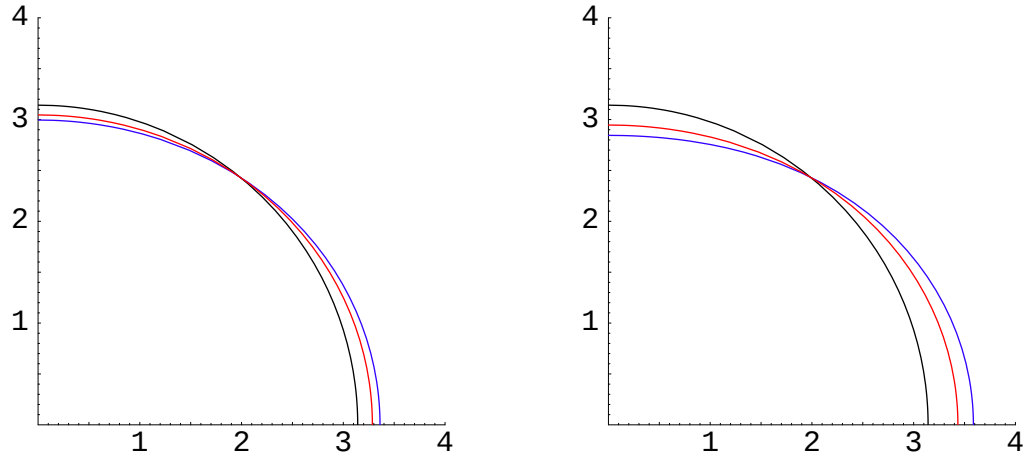


Figure 4.1: Surface distortions of (one $x - z$ quadrant of) a $\gamma = 2$ polytrope due to rotation. For each plot the black curve is the background spherical star, whilst the red and blue curves are for rotating stars calculated with the Cowling approximation (red) and without (blue). The left-hand plot is for $v = 0.01R$ and the right-hand plot $v = 0.02R$. We see that the Cowling approximation underestimates the degree of rotational distortion.

## 4.2 Derivation of the tensor virial equations

The virial theorem dictates the balance which must be satisfied between the various energy quantities in a fluid body at equilibrium; it is a universal criterion which holds in strong-field regimes as well as in the perturbative limit. The *scalar* virial equation is the usual energy balance equation of this theorem. The *tensor* virial equations are a generalisation of the scalar equation and provide the stronger result that individual tensor energy quantities must all satisfy a particular balance criterion. The tensor virial theorem was first discussed by Lord Rayleigh [115] in 1900, but was only widely exploited to understand problems in stellar physics some decades later (see, for example, Chandrasekhar [23]). Here we derive the tensor form of the virial theorem; the scalar theorem is a corollary which follows by contracting the indices of the tensor equations.

The virial theorem will be used on a couple of occasions within this thesis. Firstly, in section 4.3 we follow the working of Ostriker and Gunn [106] to determine the ellipticities of an 'orthogonal rotator' — a star with orthogonal rotational and magnetic axes. We also look at the nonrotating case, to give a simple proof (with certain caveats) of the result that poloidal magnetic fields induce oblate distortions, whilst toroidal fields induce prolate ones. As expected, the nature of magnetic-field distortions in mixed-field stars depends on the ratio of poloidal to toroidal components. Studying magnetic distortions analytically is difficult, so we specialise to considering incompressible stars (i.e. $N = 0$ polytropes) only.

Secondly, since the virial theorem states that a certain combination of energy quantities is equal to the acceleration of the mass distribution, we may use it to test how close a system is to stationarity (i.e. zero acceleration of the mass distribution). We do so in chapter 6, to give a test of the accuracy of our code for generating stationary MHD equilibria.

### 4.2.1 Preliminaries

#### Tensor generalisations of energies

We first define tensor generalisations of the energies we shall use in our derivation, where each tensor contracts to give the corresponding scalar energy quantity[2]. These are the kinetic energy tensor

$$T_{ik} \equiv \frac{1}{2} \int_V \rho u_i u_k \, \mathrm{d}\mathbf{x} \tag{4.2.1}$$

where $u_i$ is the fluid velocity; the magnetic energy tensor

$$M_{ik} \equiv \frac{1}{8\pi} \int_V B_i B_k \, \mathrm{d}\mathbf{x} \tag{4.2.2}$$

the gravitational potential energy tensor

$$W_{ik} \equiv -\int_V \rho(\mathbf{x}) x_k \frac{\partial \Phi}{\partial x_i} \, \mathrm{d}\mathbf{x} \tag{4.2.3}$$

and an energy term from the pressure $p$

$$P_{ik} \equiv \delta_{ik} \int_V p \, \mathrm{d}\mathbf{x}. \tag{4.2.4}$$

We denote each associated energy with the same letter but no indices, for example magnetic energy is written $M \equiv M_{ii} = \frac{1}{8\pi} \int_V |\mathbf{B}|^2 \, \mathrm{d}\mathbf{x}$. We will also require the definition of the quadrupole moment tensor

$$I_{ik} = \int_V \rho x_i x_k \, \mathrm{d}\mathbf{x}. \tag{4.2.5}$$

Here we assume that the pressure is isotropic, allowing us to express the generalised term $P_{ik}$ in terms of the internal energy per unit volume $U$. Many early studies using the tensor virial theorem considered anisotropic pressure, but the only change is that the diagonal tensor $\delta_{ik}p$ is replaced with a more general form $p_{ik}$. The virial theorem in this case is identical, except that the $U$ term is replaced by $P_{ik}$.

[2]except that the convention we follow here means that $P_{ik}$ contracts to give $3(\gamma - 1)$ times the internal energy.

In this subsection we derive two useful results: the expression of $P_{ik}$ in terms of $U$ and the proof that the tensor $W_{ik}$ defined above is symmetric. With these we then proceed, in the next subsection, to the actual derivation of the tensor virial theorem.

**Expressing $P$ in terms of $U$**

For an adiabatic process we can write the First Law of Thermodynamics as $dU = -p\ dV$. We assume a polytropic form of the pressure $p = k\rho^\gamma$ and integrate the First Law to give

$$U_{tot} = -\int k\rho^\gamma \ \mathrm{d}V. \tag{4.2.6}$$

where $U_{tot}$ is the total internal energy. We now use that mass $\mathcal{M} = \rho V$ and change the variable of integration from $V$ to $\rho$:

$$U_{tot} = \int \mathcal{M} k\rho^{\gamma-2} \ \mathrm{d}\rho \tag{4.2.7}$$

which integrates to give

$$U_{tot} = \frac{\mathcal{M}k\rho^{\gamma-1}}{\gamma-1} = \frac{Vp}{\gamma-1} \tag{4.2.8}$$

Now dividing through by $V$ and writing the internal energy as $U = \int \frac{U_{tot}}{V}\ \mathrm{d}\mathbf{x}$ we find

$$U = \frac{1}{\gamma-1}\int_V p\ \mathrm{d}\mathbf{x} = \frac{P}{\gamma-1}. \tag{4.2.9}$$

**Proof that $W_{ik}$ is symmetric**

We wish to show that $W_{ik}$ can be written in a manifestly symmetric form, viz.:

$$W_{ik} \equiv -\int_V \rho(\mathbf{x}) x_k \frac{\partial\Phi}{\partial x_i}\ \mathrm{d}\mathbf{x} \tag{4.2.10}$$

$$= -\frac{G}{2}\int_V\int_{V'} \frac{\rho(\mathbf{x})\rho(\mathbf{x}')(x_i - x_i')(x_k - x_k')}{|\mathbf{x}-\mathbf{x}'|^3}\ \mathrm{d}\mathbf{x}'\ \mathrm{d}\mathbf{x}. \tag{4.2.11}$$

We first note that $\frac{\partial}{\partial x_i}|\mathbf{x}-\mathbf{x}'| = (x_i - x_i')|\mathbf{x}-\mathbf{x}'|^{-1}$, so that

$$\frac{\partial}{\partial x_i}\frac{\rho(\mathbf{x}')}{|\mathbf{x}-\mathbf{x}'|} = \frac{|\mathbf{x}-\mathbf{x}'|\frac{\partial\rho(\mathbf{x}')}{\partial x_i} - \rho(\mathbf{x}')(x_i - x_i')|\mathbf{x}-\mathbf{x}'|^{-1}}{|\mathbf{x}-\mathbf{x}'|^2}$$

$$= -\rho(\mathbf{x}')(x_i - x_i')|\mathbf{x}-\mathbf{x}'|^{-3} \tag{4.2.12}$$

where we have used $\frac{\partial\rho(\mathbf{x}')}{\partial x_i} = 0$ — which is true because $\rho$ has only $\mathbf{x}'$ dependence and not $\mathbf{x}$ dependence. Now, using (4.2.12):

$$\begin{aligned} W_{ik} &\equiv -\int_V \rho(\mathbf{x}) x_k \frac{\partial\Phi}{\partial x_i}\,\mathrm{d}\mathbf{x} \\ &= -\int_V \rho(\mathbf{x}) x_k \frac{\partial}{\partial x_i}\left[-G\int_{V'}\frac{\rho(\mathbf{x}')}{|\mathbf{x}-\mathbf{x}'|}\,\mathrm{d}\mathbf{x}'\right]\,\mathrm{d}\mathbf{x} \\ &= -G\int_V\int_{V'}\frac{\rho(\mathbf{x})\rho(\mathbf{x}')x_k(x_i-x_i')}{|\mathbf{x}-\mathbf{x}'|^3}\,\mathrm{d}\mathbf{x}'\,\mathrm{d}\mathbf{x}. \end{aligned} \tag{4.2.13}$$

We may transpose the two sets of dummy variables in (4.2.13) above, $\mathbf{x} \to \mathbf{x}'$ and $\mathbf{x}' \to \mathbf{x}$, to give

$$+G\int_V\int_{V'}\frac{\rho(\mathbf{x})\rho(\mathbf{x}')x_k'(x_i-x_i')}{|\mathbf{x}-\mathbf{x}'|^3}\,\mathrm{d}\mathbf{x}'\,\mathrm{d}\mathbf{x}. \tag{4.2.14}$$

So $W_{ik}$ is equal to both the expression in (4.2.13) and (4.2.14), so we may write $W_{ik} = \frac{1}{2}[(4.2.13)+(4.2.14)]$. The required result follows from this:

$$W_{ik} = -\frac{G}{2}\int_V\int_{V'}\frac{\rho(\mathbf{x})\rho(\mathbf{x}')(x_i-x_i')(x_k-x_k')}{|\mathbf{x}-\mathbf{x}'|^3}\,\mathrm{d}\mathbf{x}'\,\mathrm{d}\mathbf{x}. \tag{4.2.15}$$

Rewritten in this form, $W_{ik}$ explicitly contracts to give a standard form for gravitational potential energy $W$.

### 4.2.2 Derivation

Consider an inviscid fluid with infinite electrical conductivity and a magnetic field $\mathbf{H}(\mathbf{x})$; we set the permeability $\mu$ to unity so that $\mathbf{H}(\mathbf{x}) = \mu\mathbf{B}(\mathbf{x}) = \mathbf{B}(\mathbf{x})$. Let us consider a perfect fluid with polytropic index $\gamma$. Suppose further that the only forces acting on the fluid are the pressure, magnetic field, and the fluid's self-gravity. Then by the Euler equation (simply Newton's second law) the equation of motion for the fluid is

$$\rho\frac{\mathrm{d}u_i}{\mathrm{d}t} = -\frac{\partial}{\partial x_i}\left(p + \frac{|\mathbf{B}|^2}{8\pi}\right) - \rho\frac{\partial\Phi}{\partial x_i} + \frac{1}{4\pi}\frac{\partial}{\partial x_j}B_iB_j \tag{4.2.16}$$

where $\dfrac{\mathrm{d}}{\mathrm{d}t} = \dfrac{\partial}{\partial t} + u_j \dfrac{\partial}{\partial x_j}$. Now multiply (4.2.16) by $x_k$ and integrate over the entire volume $V$ in which the fluid and fields can pervade. The left hand side becomes

$$\begin{aligned}
\int_V \rho x_k \frac{\mathrm{d}u_i}{\mathrm{d}t}\ \mathrm{d}\mathbf{x} &= \int_V \rho x_k \frac{\mathrm{d}^2 x_i}{\mathrm{d}t^2}\ \mathrm{d}\mathbf{x} \\
&= \int_V \rho \frac{\mathrm{d}}{\mathrm{d}t}\left(x_k \frac{\mathrm{d}x_i}{\mathrm{d}t}\right)\ \mathrm{d}\mathbf{x} - \int_V \rho \frac{\mathrm{d}x_k}{\mathrm{d}t}\frac{\mathrm{d}x_i}{\mathrm{d}t}\ \mathrm{d}\mathbf{x} \\
&= \int_V \rho \frac{\mathrm{d}}{\mathrm{d}t}\left(x_k \frac{\mathrm{d}x_i}{\mathrm{d}t}\right)\ \mathrm{d}\mathbf{x} - 2T_{ik} \qquad (4.2.17)
\end{aligned}$$

where we have used the product rule in the second line. We now treat the terms on the right hand side of (4.2.16) in the same manner. Firstly:

$$\begin{aligned}
-\int_V x_k \frac{\partial}{\partial x_i}\left(p + \frac{|\mathbf{B}|^2}{8\pi}\right)\ \mathrm{d}\mathbf{x} &= -\int_S \left(p + \frac{|\mathbf{B}|^2}{8\pi}\right) x_k\ \mathrm{d}S_i + \delta_{ik}\int_V \left(p + \frac{|\mathbf{B}|^2}{8\pi}\right)\ \mathrm{d}\mathbf{x} \\
&= -\int_S \left(p + \frac{|\mathbf{B}|^2}{8\pi}\right) x_k\ \mathrm{d}S_i + \delta_{ik}[(\gamma-1)U + M] \qquad (4.2.18)
\end{aligned}$$

where we have used the divergence theorem; secondly

$$-\int_V \rho x_k \frac{\partial \Phi}{\partial x_i}\ \mathrm{d}\mathbf{x} \equiv W_{ik} \qquad (4.2.19)$$

and finally

$$\begin{aligned}
\frac{1}{4\pi}\int_V x_k \frac{\partial}{\partial x_j} B_i B_j\ \mathrm{d}\mathbf{x} &= \frac{1}{4\pi}\int_S x_k B_i B_j\ \mathrm{d}S_j - \frac{1}{4\pi}\int_V B_i B_k\ \mathrm{d}\mathbf{x} \\
&= \frac{1}{4\pi}\int_S x_k B_i B_j\ \mathrm{d}S_j - 2M_{ik}. \qquad (4.2.20)
\end{aligned}$$

We now combine (4.2.17), (4.2.18), (4.2.19) and (4.2.20) to give

$$\begin{aligned}
\int_V \rho \frac{\mathrm{d}}{\mathrm{d}t}\left(x_k \frac{\mathrm{d}x_i}{\mathrm{d}t}\right)\ \mathrm{d}\mathbf{x} &= 2T_{ik} + \delta_{ik}[(\gamma-1)U + M] + W_{ik} - 2M_{ik} \\
&+ \frac{1}{8\pi}\int_S x_k(2B_i B_j\ \mathrm{d}S_j - |\mathbf{B}|^2\ \mathrm{d}S_i) - \int_S p x_k\ \mathrm{d}S_i. \qquad (4.2.21)
\end{aligned}$$

Since $p$, $\rho$ and $\mathbf{B}$ all vanish on $S$ (the consequence of requiring that $V$ contains the whole system), we have:

$$\int_V \rho \frac{\mathrm{d}}{\mathrm{d}t}\left(x_k \frac{\mathrm{d}x_i}{\mathrm{d}t}\right)\,\mathrm{d}\mathbf{x} = 2T_{ik} - 2M_{ik} + W_{ik} + \delta_{ik}[(\gamma-1)U + M]. \tag{4.2.22}$$

All of the tensor quantities on the right hand side of (4.2.22) above are symmetric, so the left hand side must be symmetric too. Therefore

$$\int_V \rho \frac{\mathrm{d}}{\mathrm{d}t}\left(x_k \frac{\mathrm{d}x_i}{\mathrm{d}t}\right)\,\mathrm{d}\mathbf{x} = \int_V \rho \frac{\mathrm{d}}{\mathrm{d}t}\left(x_i \frac{\mathrm{d}x_k}{\mathrm{d}t}\right)\,\mathrm{d}\mathbf{x}. \tag{4.2.23}$$

Using this fact and the continuity equation (in the form $\int_V \rho\,\mathrm{d}\mathbf{x}$=constant),

$$\int_V \rho \frac{\mathrm{d}}{\mathrm{d}t}\left(x_k \frac{\mathrm{d}x_i}{\mathrm{d}t} - x_i \frac{\mathrm{d}x_k}{\mathrm{d}t}\right)\,\mathrm{d}\mathbf{x} = \frac{\mathrm{d}}{\mathrm{d}t}\int_V \rho\left(x_k \frac{\mathrm{d}x_i}{\mathrm{d}t} - x_i \frac{\mathrm{d}x_k}{\mathrm{d}t}\right)\,\mathrm{d}\mathbf{x} = 0. \tag{4.2.24}$$

This is a statement of conservation of total angular momentum $\mathbf{L}_{tot}$, since $\mathbf{L}_{tot} = \int_V \mathbf{x}\times\rho\mathbf{u}\,\mathrm{d}\mathbf{x} = \int_V \rho(x_k u_i - x_i u_k)\,\mathrm{d}\mathbf{x}$. Now by (4.2.23) we may replace the left hand side of (4.2.22) with

$$\frac{1}{2}\int_V \rho \frac{\mathrm{d}}{\mathrm{d}t}\left(x_k \frac{\mathrm{d}x_i}{\mathrm{d}t} + x_i \frac{\mathrm{d}x_k}{\mathrm{d}t}\right)\,\mathrm{d}\mathbf{x} = \frac{1}{2}\frac{\mathrm{d}^2}{\mathrm{d}t^2}\int_V \rho x_i x_k\,\mathrm{d}\mathbf{x} = \frac{1}{2}\frac{\mathrm{d}^2 I_{ik}}{\mathrm{d}t^2}. \tag{4.2.25}$$

Using this in (4.2.22) we arrive at the tensor virial equations:

$$\frac{1}{2}\frac{\mathrm{d}^2 I_{ik}}{\mathrm{d}t^2} = 2T_{ik} - 2M_{ik} + W_{ik} + \delta_{ik}[(\gamma-1)U + M]. \tag{4.2.26}$$

If we relax the assumption that pressure is isotropic then the tensor virial equations take their more general form:

$$\frac{1}{2}\frac{\mathrm{d}^2 I_{ik}}{\mathrm{d}t^2} = 2T_{ik} - 2M_{ik} + W_{ik} + P_{ik} + \delta_{ik}M. \tag{4.2.27}$$

We use the tensor virial equations in the next section to calculate the shape of a rotating magnetised fluid star. In addition, we will use the scalar virial theorem (the contraction of the tensor equations) as a test of our MHD equilibrium code in chapter 6.

## 4.3 The shape of a rotating magnetised fluid star

In this section we model a neutron star as a rotating magnetised body composed of incompressible fluid and use the tensor virial equations derived above to determine the ellipticities generated in the star by the effects of rotation and a magnetic field[3]. In particular, we look at the case of an orthogonal rotator — a star with orthogonal rotational and magnetic axes. Looking at the zero-rotation limit, we then show that (under certain simplifications) poloidal magnetic fields generate oblate deformations, whilst toroidal fields generate prolate deformations.

We denote the (orthogonal) magnetic and rotational axes by indices 1 and 3 respectively. We first rewrite $\ddot{I}_{ik}$:

$$\begin{aligned} \ddot{I}_{ik} &= 2\int \rho \dot{x}_i \dot{x}_k \, \mathrm{d}\mathbf{x} + \int \rho(\ddot{x}_i x_k + x_i \ddot{x}_k) \, \mathrm{d}\mathbf{x} \\ &= 4T_{ik} + \int \rho(\ddot{x}_i x_k + x_i \ddot{x}_k) \, \mathrm{d}\mathbf{x}. \end{aligned} \tag{4.3.1}$$

To simplify $\ddot{I}_{ik}$ we assume the fluid is a rigidly rotating triaxial body. Now $\dot{\mathbf{x}} = \boldsymbol{\Omega} \times \mathbf{x}$ and so $\ddot{\mathbf{x}} = \boldsymbol{\Omega} \times (\boldsymbol{\Omega} \times \mathbf{x})$, where $\boldsymbol{\Omega}$ is the angular velocity vector. By assumption $\boldsymbol{\Omega} = \Omega \mathbf{e}_3$, so we have $\ddot{\mathbf{x}} = \Omega^2 \mathbf{e}_3 \times (\mathbf{e}_3 \times \mathbf{x})$. Evaluating this expression gives

$$\ddot{\mathbf{x}} = -\Omega^2 \begin{pmatrix} x_1 \\ x_2 \\ 0 \end{pmatrix}. \tag{4.3.2}$$

We now use this to evaluate (4.3.1) for the diagonal components of $\ddot{I}_{ik}$:

$$\begin{aligned} \ddot{I}_{11} &= 4T_{11} + 2\int \rho \ddot{x}_1 x_1 \, \mathrm{d}\mathbf{x} \\ &= 4T_{11} - 2\Omega^2 \int \rho x_1^2 \, \mathrm{d}\mathbf{x} \\ &= 4T_{11} - 2\Omega^2 I_{11} \end{aligned} \tag{4.3.3}$$

and similarly

$$\ddot{I}_{22} = 4T_{22} - 2\Omega^2 I_{22} \tag{4.3.4}$$

$$\ddot{I}_{33} = 4T_{33}. \tag{4.3.5}$$

[3]Up until the ellipticity formulae (4.3.16), (4.3.17), (4.3.18), this section follows the working of Appendix A of Ostriker and Gunn [106].

The diagonal components of the tensor virial equations are then

$$\begin{aligned} I_{11}\Omega^2 + P_{11} - 2M_{11} + M + W_{11} &= 0 \\ I_{22}\Omega^2 + P_{22} - 2M_{22} + M + W_{22} &= 0 \\ P_{33} - 2M_{33} + M + W_{33} &= 0. \end{aligned} \tag{4.3.6}$$

We assume the pressure anisotropy has the same symmetry as the magnetic field, then as a first-order approximation neglect the quantities $(M_{22} - M_{33})$, $(P_{22} - P_{33})$, $(I_{11} - I_{22})\Omega^2$ and $(I_{33} - I_{22})\Omega^2$. Then to first order, equations (4.3.6) become

$$W_{11} - W_{22} = 2(M_{11} - M_{22}) - (P_{11} - P_{22}) \tag{4.3.7}$$

$$W_{33} - W_{22} = I_{22}\Omega^2 = \tfrac{1}{3}I\Omega^2 \tag{4.3.8}$$

where $I = \mathrm{Tr}(I_{ij})$. We proceed using the following result from Chandrasekhar and Lebovitz [27] for a homogeneous ellipsoid (no sum over the indices):

$$W_{(ii)} = -\tfrac{3}{10}G\mathcal{M}^2 a_i A_i \tag{4.3.9}$$

where

$$A_i = \int_0^\infty \frac{\mathrm{d}u}{(a_i^2 + u)\sqrt{(a_1^2 + u)(a_2^2 + u)(a_3^2 + u)}} \tag{4.3.10}$$

and $a_i$ are the semiaxes. Now define

$$\epsilon_i = \frac{a_i - a}{a} \tag{4.3.11}$$

where $a^3 \equiv a_1 a_2 a_3$; so to linear order in $\epsilon_i$ we find that

$$\epsilon_1 + \epsilon_2 + \epsilon_3 = 0. \tag{4.3.12}$$

Evaluating the integral (4.3.10) and linearising by neglecting products and sums in $\epsilon_i$ gives

$$A_i = \frac{2}{3a^3}(1 - \tfrac{6}{5}\epsilon_i). \tag{4.3.13}$$

Now equation (4.3.9) together with (4.3.12) and (4.3.13) gives

$$W_{(ii)} - W_{(jj)} = \tfrac{4}{15}W(\epsilon_i - \epsilon_j) \tag{4.3.14}$$

with

$$W \equiv \mathrm{Tr}(W_{ij}) = -\frac{3G\mathcal{M}^2}{5a}. \tag{4.3.15}$$

Substituting equations (4.3.15) and (4.3.14) into equations (4.3.7) and (4.3.8) enables us to obtain expressions for the ellipticities $\epsilon_i$ for a rotating, magnetised fluid body:

$$\epsilon_1 = \frac{5}{4W}[4(M_{11} - M_{22}) - 2(P_{11} - P_{22}) - \tfrac{1}{3}I\Omega^2] \tag{4.3.16}$$

$$\epsilon_2 = \frac{5}{4W}[-2(M_{11} - M_{22}) + (P_{11} - P_{22}) - \tfrac{1}{3}I\Omega^2] \tag{4.3.17}$$

$$\epsilon_3 = \frac{5}{4W}[-2(M_{11} - M_{22}) + (P_{11} - P_{22}) + \tfrac{2}{3}I\Omega^2]. \tag{4.3.18}$$

Note that if the stellar pressure is isotropic then $P_{11} = P_{22}$ and the ellipticities have a simpler form.

We conclude by considering two special cases: deformations due purely to rotation and to magnetic effects. In the case of a rotating body with no magnetic field or pressure anisotropies, we have

$$\epsilon_1 = \epsilon_2 = \frac{5}{12|W|}I\Omega^2 \tag{4.3.19}$$

$$\epsilon_3 = -\frac{5}{6|W|}I\Omega^2 \tag{4.3.20}$$

— we have made the sign of each ellipticity explicit by noting that the gravitational energy $W$ is always negative, so that $W = -|W|$. Since the rotation axis is the body axis $\mathbf{x}_3$ we see that, as expected, a centrifugal force generates an oblate configuration. This was established for an $N = 1$ polytrope in section 4.1.5; we find the result is qualitatively the same for the $N = 0$ fluid considered here.

We next turn to ellipticities generated solely by a magnetic field. In this case we have

$$\epsilon_1 = \frac{5}{|W|}(M_{22} - M_{11}) \tag{4.3.21}$$

$$\epsilon_2 = \epsilon_3 = -\frac{5}{2|W|}(M_{22} - M_{11}). \tag{4.3.22}$$

Using the same notation as before, the symmetry axis of the problem is now the body axis $\mathbf{x}_1$. Working in cylindrical polar coordinates, we regard this as the $z$ axis. Hence

$$M_{11} = \frac{1}{8\pi}\int_V B_1^2 \ \mathrm{d}\mathbf{x} = \frac{1}{8\pi}\int_V B_z^2 \ \mathrm{d}\mathbf{x}. \tag{4.3.23}$$

Also, since $M = M_{11} + M_{22} + M_{33} = M_{11} + 2M_{22}$ and

$$M = \frac{1}{8\pi}\int_V B_\varpi^2 + B_\phi^2 + B_z^2 \ \mathrm{d}\mathbf{x} \tag{4.3.24}$$

we conclude that

$$M_{22} = \frac{1}{16\pi}\int_V B_\varpi^2 + B_\phi^2 \ \mathrm{d}\mathbf{x} \tag{4.3.25}$$

and hence that

$$M_{22} - M_{11} = \frac{1}{8\pi}\int_V \frac{1}{2}B_\phi^2 + \frac{1}{2}B_\varpi^2 - B_z^2 \ \mathrm{d}\mathbf{x}. \tag{4.3.26}$$

Now, a poloidal field consists of $B_\varpi$ and $B_z$ components; in a realistic field configuration one would not expect either to dominate, so let us suppose that $B_\varpi^2 \approx B_z^2$. In this case we may write $\frac{1}{2}B_\varpi^2 - B_z^2 \approx -\frac{1}{2}B_z^2 \approx -\frac{1}{4}(B_\varpi^2 + B_z^2)$ and

$$M_{22} - M_{11} \approx \frac{1}{8\pi}\int_V \left(\tfrac{1}{2}B_{tor}^2 - \tfrac{1}{4}B_{pol}^2\right) \ \mathrm{d}\mathbf{x} = \frac{1}{2}\mathcal{E}_{tor} - \tfrac{1}{4}\mathcal{E}_{pol}. \tag{4.3.27}$$

This gives

$$\epsilon_1 - \epsilon_2 \approx \frac{5}{4|W|}\left(\mathcal{E}_{tor} - \frac{1}{2}\mathcal{E}_{pol}\right). \tag{4.3.28}$$

We now note that if $\epsilon_1 - \epsilon_2 > 0$ the star is prolate, and if $\epsilon_1 - \epsilon_2 < 0$ it is oblate; so from (4.3.28) we see that if more than (approximately) one third of the magnetic energy is in the toroidal field then the star will be prolate, whilst if the poloidal energy is more than double the toroidal energy the star will be oblate. We will find in chapter 6 that this general result, of poloidal fields generating oblate stars and toroidal fields prolate stars, also seems to apply to compressible stars and strong magnetic fields.

# Chapter 5

# Oscillation modes: introduction and analytic work

## 5.1 Introduction

To zeroth order, stars are stationary objects, with large-scale evolution happening over very long timescales. On smaller scales however, they have rich dynamics; in particular, they are subject to various kinds of oscillation. Different physical effects manifest themselves as oscillation modes of different frequency, so observations of stellar oscillations give us valuable information about the physics that governs them. Unstable modes are of particular interest in the context of this thesis, since they could result in sufficiently large disturbances in the mass distribution to produce detectable gravitational radiation.

In this chapter calculations for two oscillation mode frequencies are presented, as basic examples of analytic mode solutions. From these analytic results, we also have a point of reference when looking at the mode spectrum of stars with rotation and magnetic fields. In both mode derivations given here, the star is assumed to have no magnetic field. Although there are some analytic calculations for modes of a magnetised star, they are not only rather involved, but also rely on many simplifying assumptions. However, some order-of-magnitude estimates for the effect of magnetic fields on stellar oscillations are given in chapter 7, in addition to numerical results for oscillations of magnetised stars.

### 5.1.1 Classes of oscillation mode

Oscillation modes are induced by fluctuations in the various forces present in the background star; these are called *restoring forces* and they determine the frequency of the mode. It is natural, then, to classify a mode based on its restoring force. We may further distinguish between different modes based on their parity. Using spherical polar coordinates, a general perturbation may be decomposed with respect to the basis $(Y_{lm}\mathbf{e}_r, \nabla Y_{lm}, \mathbf{e}_r \times \nabla Y_{lm})$, where $Y_{lm} = Y_{lm}(\theta, \phi)$ are the usual spherical harmonics. The first two of these terms transform by multiplication by $(-1)^l$ under parity inversion $\mathbf{r} \mapsto -\mathbf{r}$, with the latter one transforming as $(-1)^{l+1}$. Modes whose sign is given by $(-1)^l$ under parity interchange are termed *polar* modes, whilst those transforming as $(-1)^{l+1}$ are called *axial* modes[1]. Hybrid modes, consisting of a sum of axial and polar pieces, are termed axial-led or polar-led based on whether the lowest-$l$ (i.e. $l=m$) term of the mode is axial or polar, respectively.

The simplest model of a fluid star is hydrostatic equilibrium — a balance of the gravitational and pressure forces. Surfaces of constant density are concentric spheres in this case and the only modes present are the pressure or $p$-modes. The lowest-order $p$-mode (i.e. the one with a nodeless eigenfunction) in each series is termed the fundamental mode, or $f$-mode. The $f$-mode frequency is also the frequency of the only mode of oscillation of a homogeneous incompressible sphere; in this context it is known as the Kelvin mode, as it was first studied by Lord Kelvin [77]. The frequency of this mode is derived in section 5.2. The non-axisymmetric $p$-modes in a compressible star are degenerate in the absence of rotation and magnetic fields; each $p$-mode has the same frequency for fixed $m$. These modes are polar in nature.

If a fluid star has thermal or chemical gradients, a new class of modes arises [98, 116, 44]. To understand these, it is easiest to consider the case when these gradients result in stratification of the star; that is, the appearance of surfaces over which the stellar density changes discontinuously. The star's self-gravity will then act to oppose these differences, providing the restoring force for these new modes, called gravity or $g$-modes. Along with the $p$-modes, $g$-modes were first studied by Cowling [33].

With a rotating background star, a Coriolis force term enters the equations

[1]Polar modes are also known as *spheroidal* modes and axial modes as *toroidal* modes. In this thesis we will always use the terms 'axial' and 'polar', however.

governing the perturbations, which removes the $m$-degeneracy in the $p$-modes. The Coriolis term is the restoring force for a new class of modes: the inertial modes, which we term $i$-modes. These modes were first studied in incompressible fluids by Bryan [18]. In general $i$-modes are mixed axial and polar even in the slow-rotation limit, but one class of them are purely axial in this limit: the Rossby or $r$-modes. With the barotropic equation of state we employ here, the only $r$-modes which exist are those with $l = m$. The $r$-mode frequency of a slowly-rotating star is derived in section 5.3.

Other inertial modes have more complicated eigenfunctions than the $r$-mode. For fixed $m$, Lockitch and Friedman [93] found that inertial modes are not characterised by a single $l$, but have an angular dependence consisting of a sum of spherical harmonics $Y_{lm}(\theta, \phi)$. However, in all cases they found there was some threshold value $l_0$, such that the amplitude of $Y_{lm}$ contributions for $l > l_0$ was found to drop off rapidly. Following their work, we label modes using the notation ${}^{l_0}_{m}i_k$, where $k$ distinguishes between different modes with the same $l_0$.

Finally, magnetic fields also induce a class of oscillation mode, restored by the Lorentz force. We term them the Alfvén modes, or $a$-modes. In addition to generating a new class of modes, the Lorentz force can lift degeneracies of nonradial oscillations, causing a splitting in mode frequencies [34]. The addition of the Lorentz force term in the Euler equation for the perturbations should produce shifts in the frequencies of the $p, r$ and $i$ modes from their unmagnetised values. Much of chapter 7 is dedicated to investigating the effect of magnetic fields on a star's oscillation spectrum.

## 5.2 The Kelvin mode

The simplest physical model of a star is the incompressible sphere, which has only one type of oscillation mode; in this section we find its frequency. As well as providing an example of a mode calculation, the resulting frequency has a similar form to that of the $f$-mode of compressible stars [24] and hence is of more general interest within the context of this thesis.

We begin with the governing equations for the system:

$$\rho \frac{\mathrm{d}\mathbf{v}}{\mathrm{d}t} = -\nabla P - \rho \nabla \Phi \tag{5.2.1}$$

$$\nabla^2\Phi = 4\pi G\rho \tag{5.2.2}$$

$$\nabla\cdot(\rho\mathbf{v}) = \mathbf{v}\cdot\nabla\rho + \rho\nabla\cdot\mathbf{v} = 0 \tag{5.2.3}$$

where $\rho_0$ is a constant; since the star is incompressible, the density is uniform throughout the stellar interior: $\rho = \rho_0$. The background equations are

$$-\nabla P_0 - \rho_0\nabla\Phi_0 = 0 \tag{5.2.4}$$

$$\nabla^2\Phi_0 = 4\pi G\rho_0 \tag{5.2.5}$$

and the (first order) perturbations are governed by

$$\rho_0\frac{\mathrm{d}\mathbf{v}}{\mathrm{d}t} = -\nabla\delta P - \rho_0\nabla\delta\Phi - \delta\rho\nabla\Phi_0 \tag{5.2.6}$$

$$\nabla^2\delta\Phi = 4\pi G\delta\rho \tag{5.2.7}$$

$$\rho_0\nabla\cdot\mathbf{v} = -\mathbf{v}\cdot\nabla\rho_0. \tag{5.2.8}$$

We begin by solving the background equations. Since the background star is spherically symmetric all quantities are dependent on $r$ alone. The Euler equation is therefore

$$\frac{\mathrm{d}\Phi_0}{\mathrm{d}r} = -\frac{1}{\rho_0}\frac{\mathrm{d}P_0}{\mathrm{d}r}, \tag{5.2.9}$$

which may be directly integrated to give

$$\Phi_0 = -\frac{P_0}{\rho_0} + K. \tag{5.2.10}$$

Similarly, direct integration of the Poisson equation

$$\frac{1}{r^2}\frac{\mathrm{d}}{\mathrm{d}r}\left(r^2\frac{\mathrm{d}\Phi_0}{\mathrm{d}r}\right) = 4\pi G\rho_0 \tag{5.2.11}$$

yields

$$\Phi_0 = \frac{2\pi G\rho_0 r^2}{3} - \frac{C}{r} + D. \tag{5.2.12}$$

Imposing regularity at the origin gives $C = 0$, whilst $D$ is fixed through the boundary conditions:

$$\Phi_0^{int}(r=R) = \Phi_0^{ext}(r=R) \tag{5.2.13}$$

$$\frac{\mathrm{d}\Phi_0^{int}}{\mathrm{d}r}(r=R) = \frac{\mathrm{d}\Phi_0^{ext}}{\mathrm{d}t}(r=R) \tag{5.2.14}$$

where $R$ is the stellar radius. For the external field

$$\nabla^2\Phi_0 = \frac{1}{r^2}\frac{\mathrm{d}}{\mathrm{d}r}\left(r^2\frac{\mathrm{d}\Phi_0}{\mathrm{d}r}\right) = 0 \tag{5.2.15}$$

and hence

$$\Phi = \frac{\alpha}{r}. \tag{5.2.16}$$

Now (5.2.13) gives

$$D = \frac{\alpha}{r} - \frac{2\pi G\rho_0 R^2}{3} \tag{5.2.17}$$

whilst (5.2.14) gives

$$\alpha = -\frac{4\pi G\rho_0 R^3}{3} \tag{5.2.18}$$

— note that since the stellar mass $M = 4\pi\rho R^3/3$ this last equation gives the external potential as $\Phi = -GM/r$, as expected.

From these two equations we find that

$$D = -2\pi G\rho_0 R^2 \tag{5.2.19}$$

and hence the internal field is given by

$$\Phi_0 = \frac{2\pi G\rho_0(r^2 - 3R^2)}{3}. \tag{5.2.20}$$

Now

$$P_0 = \rho_0(K - \Phi_0) = \rho_0 K + \frac{2\pi G\rho_0^2(3R^2 - r^2)}{3} \tag{5.2.21}$$

so to ensure $P_0$ goes to zero smoothly at the surface we fix $K$ so that

$$P_0 = \frac{2\pi G\rho_0^2(R^2 - r^2)}{3}. \tag{5.2.22}$$

Next we turn to the perturbation equations. Because the star is incompressible, the variation in density at a particular point near the surface will either be $\delta\rho = 0$ (if the point is inside the star both before and after the perturbation) or $\delta\rho = \pm\rho_0$ (if a point out/inside the star ends up in/outside the star after the perturbation). We deal with this odd behaviour by setting $\delta\rho = 0$ in the perturbation equations (true for all points away from the surface) and incorporate the $\delta\rho \neq 0$ behaviour into the boundary conditions. Hence our perturbation equations are now

$$\rho_0\frac{\mathrm{d}\mathbf{v}}{\mathrm{d}t} = -\nabla\delta P - \rho_0\nabla\delta\Phi \tag{5.2.23}$$

$$\nabla^2\delta\Phi = 0 \tag{5.2.24}$$

$$\nabla\cdot\mathbf{v} = 0. \tag{5.2.25}$$

Taking the divergence of (5.2.23) and using the other two equations reduces our set of perturbation equations to a pair of Laplace equations in $\delta P$ and $\delta\Phi$,

$$\nabla^2\delta P = \nabla^2\delta\Phi = 0. \tag{5.2.26}$$

The general solution for $\delta P$ is thus given by

$$\delta P = \sum_{l,m} \hat{C}_{lm} Y_{lm}(Ar^l + Br^{-l-1}). \tag{5.2.27}$$

Regularity at the origin $r = 0$ requires $B = 0$; defining $C_{lm} \equiv A\hat{C}_{lm}$ gives

$$\delta P = \sum_{l,m} C_{lm} Y_{lm} r^l. \tag{5.2.28}$$

At the surface $r = R$ we have the boundary condition

$$\Delta P \equiv \delta P + \boldsymbol{\xi} \cdot \nabla P \tag{5.2.29}$$

which to leading order is

$$\left[\delta P + \xi_r \frac{\mathrm{d}P_0}{\mathrm{d}r}\right](r = R) = 0. \tag{5.2.30}$$

Now using the background solution for $P_0$ and defining $\xi_R \equiv \xi_r(r = R, \theta, \phi)$ we find

$$\xi_R = \frac{3\delta P}{4\pi G\rho_0^2 R}. \tag{5.2.31}$$

With the general solution for $\delta P$ and the above expression for $\xi_R$, we now turn to $\delta\Phi$. The boundary conditions on $\delta\Phi$ for an $N = 0$ polytrope are different from the familiar ones, and in this case they are the only point at which the matter distribution is linked to the other perturbed quantities (since $\delta\rho = 0$ in the equations).

### 5.2.1 Boundary conditions

Consider a small volume element $\delta V$ which passes through the surface of the star, from radius $R - \varepsilon$ to $R + \varepsilon$. Now we integrate the perturbed Poisson equation over this small volume:

$$\int_{\delta V} \nabla^2\delta\Phi \ \mathrm{d}V = 4\pi G \int_{\delta V} \delta\rho \ \mathrm{d}V. \tag{5.2.32}$$

Using the divergence theorem on the left-hand side of this equation and the boundary condition $\Delta\rho \equiv \delta\rho + \boldsymbol{\xi} = 0$ on the right-hand side, we see that

$$\int_{R-\varepsilon}^{R+\varepsilon} \nabla\delta\Phi \cdot \mathrm{d}\mathbf{S} = -4\pi G \int_{R-\varepsilon}^{R+\varepsilon} \boldsymbol{\xi} \cdot \nabla\rho \; \mathrm{d}V. \tag{5.2.33}$$

Now,

$$\int_{R-\varepsilon}^{R+\varepsilon} \frac{\mathrm{d}\rho}{\mathrm{d}r} \; \mathrm{d}r = [\rho]_{R-\varepsilon}^{R+\varepsilon} = -\rho_0 \tag{5.2.34}$$

from which we deduce that $\frac{\mathrm{d}\rho}{\mathrm{d}r} = -\rho_0\delta(r-R)$ and hence that

$$\int_{R-\varepsilon}^{R+\varepsilon} \boldsymbol{\xi} \cdot \nabla\rho \; \mathrm{d}V = -\rho_0 \int_{R-\varepsilon}^{R+\varepsilon} \xi_r\delta(r-R) \; \mathrm{d}V = -\rho_0\xi_R. \tag{5.2.35}$$

Next we note that neither integrand in (5.2.33) has angular dependence (since we are considering an infinitesimal volume, over which the stellar surface is flat), so the angular integrations on each side produce equal contributions which may be cancelled. On performing the remaining, radial, integration we find that

$$\frac{\partial\delta\Phi}{\partial r}(r = R+\varepsilon) - \frac{\partial\delta\Phi}{\partial r}(r = R-\varepsilon) = 4\pi G\rho_0\xi_R. \tag{5.2.36}$$

A second radial integration then yields

$$\delta\Phi(r = R+\varepsilon) - \delta\Phi(r = R-\varepsilon) = 8\pi G\rho_0\xi_R\varepsilon. \tag{5.2.37}$$

Finally we take the limit $\varepsilon \to 0$ in equations (5.2.36) and (5.2.37) to yield the boundary conditions on $\delta\Phi$:

$$\frac{\partial\delta\Phi^{ext}}{\partial r}(r=R) = \frac{\partial\delta\Phi^{int}}{\partial r}(r=R) + 4\pi G\rho_0\xi_R \tag{5.2.38}$$

$$\delta\Phi^{ext}(r=R) = \delta\Phi^{int}(r=R). \tag{5.2.39}$$

### 5.2.2 Final solution

The general solution to $\nabla^2\delta\Phi = 0$ is

$$\delta\Phi = \sum_{l,m} (D_{lm}r^l + E_{lm}r^{-l-1})Y_{lm} \tag{5.2.40}$$

Note that $r^l \to \infty$ as $r \to \infty$ whilst $r^{-l-1} \to \infty$ as $r \to 0$; hence for the interior solution $E_{lm} = 0$ whilst for the exterior solution $D_{lm} = 0$, for all $l, m$. Let us pick some particular $l, m$. Now by the boundary condition (5.2.39):

$$\frac{D_{lm}}{E_{lm}} = R^{-2l-1}. \tag{5.2.41}$$

Now applying the other boundary condition (5.2.38) we find that

$$lR^{l-1}D_{lm}Y_{lm} = -(l+1)R^{-l-2}E_{lm}Y_{lm} - 4\pi G\rho_0\xi_R. \tag{5.2.42}$$

We remove $E_{lm}$ from this equation using (5.2.41), and replace $\xi_R$ in favour of $\delta P$, using equation (5.2.31). The result is

$$Y_{lm}D_{lm} = -\frac{3\delta P(R)}{(2l+1)\rho_0 R^l}. \tag{5.2.43}$$

Now since $\delta P(R) = R^l C_{lm}Y_{lm}$, we see that

$$D_{lm} = -\frac{3}{(2l+1)\rho_0}C_{lm}. \tag{5.2.44}$$

Finally we return to our perturbed Euler equation (5.2.23):

$$\rho_0\dot{\mathbf{v}} = -\nabla\delta P - \rho_0\nabla\delta\Phi. \tag{5.2.45}$$

Now, $\mathbf{v} = \dot{\boldsymbol{\xi}}$ by definition. Since we are looking for oscillatory solutions we make the ansatz $\boldsymbol{\xi} = ke^{i\sigma t}$. Hence $\mathbf{v} = \dot{\boldsymbol{\xi}} = i\sigma\boldsymbol{\xi}$ and $\dot{\mathbf{v}} = \ddot{\boldsymbol{\xi}} = -\sigma^2\boldsymbol{\xi} = i\sigma\mathbf{v}$; hence the perturbed Euler equation becomes

$$i\sigma\rho_0\mathbf{v} = -\nabla\delta P - \rho_0\nabla\delta\Phi. \tag{5.2.46}$$

The radial component of this is

$$v_r = -\frac{1}{i\sigma\rho_0}\left(\frac{\partial\delta P}{\partial r} + \rho_0\frac{\partial\delta\Phi}{\partial r}\right). \tag{5.2.47}$$

We return to equation (5.2.31), making the replacement $\xi_R = v_R/(i\sigma)$:

$$v_R = \frac{3i\sigma\delta P}{4\pi G\rho_0^2 R} \tag{5.2.48}$$

and equate this result with equation (5.2.47) evaluated at the surface:

$$v_R = \frac{3i\sigma\delta P}{4\pi G\rho_0^2 R} = -\frac{1}{i\sigma\rho_0}\left(\frac{\partial\delta P}{\partial r}(R) + \rho_0\frac{\partial\delta\Phi}{\partial r}(R)\right). \tag{5.2.49}$$

Rearranging this gives

$$\sigma^2 = \frac{4\pi G\rho_0 R}{3\delta P}\left(\frac{\partial \delta P}{\partial r}(R) + \rho_0 \frac{\partial \delta\Phi}{\partial r}(R)\right). \tag{5.2.50}$$

Now plugging in the solutions

$$\delta P = C_{lm} Y_{lm} r^l \tag{5.2.51}$$

$$\delta\Phi = D_{lm} Y_{lm} r^l = -\frac{3}{(2l+1)\rho_0} C_{lm} Y_{lm} r^l \tag{5.2.52}$$

to equation (5.2.50) we find, after some algebra, that

$$\sigma^2 = \frac{4\pi G\rho_0}{3}\frac{2l(l-1)}{(2l+1)}. \tag{5.2.53}$$

Finally, we may define a dimensionless frequency $\Omega$ by

$$\Omega^2 \equiv \frac{\sigma^2 R^3}{GM} = \frac{3\sigma^2}{4\pi G\rho_0}. \tag{5.2.54}$$

In terms of this quantity we find that the mode frequency is given by

$$\Omega^2 = \frac{2l(l-1)}{(2l+1)}, \tag{5.2.55}$$

in agreement with Kelvin [77]. As mentioned at the beginning of this section, this incompressible-fluid result is still of interest in the context of neutron stars (which are compressible), since the $f$-mode of compressible stars is closely related to the Kelvin mode derived here [34, 24].

## 5.3 First-order $r$-mode calculation

The $f$-mode and $p$-modes are polar in nature; in a fluid nonrotating star the axial oscillation modes are all zero-frequency solutions. The qualitative change in a rotating star is that axial oscillations no longer have this trivial nature [109, 122]. Having already calculated the Kelvin mode, which is similar to the $f$-mode of compressible stars, we now present a calculation of the $r$-mode, as an example of an axial mode. In chapter 7 we investigate how this mode changes in the presence of a toroidal magnetic field.

### 5.3.1 Dynamics in a rotating frame

In an inertial frame the Euler equation for a rotating fluid star is

$$\frac{\mathrm{d}\mathbf{v}_I}{\mathrm{d}t_I} = -\frac{1}{\rho}\nabla P - \nabla\Phi \tag{5.3.1}$$

where the acceleration is the rate of change of inertial velocity $\mathbf{v}_I$ in the inertial frame $(\mathrm{d}/\mathrm{d}t_I)$. We wish to investigate how quantities are changed when we move from the inertial frame to a frame rotating rigidly with angular velocity $\mathbf{\Omega}$; we shall denote quantities in this frame with the subscript $R$. Firstly, the two velocities $\mathbf{v}_I$ and $\mathbf{v}_R$ are related by

$$\mathbf{v}_I = \mathbf{\Omega}\times\mathbf{r} + \mathbf{v}_R \tag{5.3.2}$$

— that is, $\mathbf{v}_R$ is the piece of the velocity which is *not* rotating rigidly with angular velocity $\mathbf{\Omega}$ in the inertial frame. Hence we have

$$\frac{\mathrm{d}\mathbf{v}_I}{\mathrm{d}t_I} = \frac{\mathrm{d}\mathbf{v}_I}{\mathrm{d}t_R} + \mathbf{\Omega}\times\mathbf{v}_I \tag{5.3.3}$$

— note that this equation is valid for $\mathbf{v}_R$ too.

We replace $\mathbf{v}_I$ in equation (5.3.3) using (5.3.2):

$$\frac{\mathrm{d}\mathbf{v}_I}{\mathrm{d}t_I} = \frac{\mathrm{d}}{\mathrm{d}t_R}\left(\mathbf{\Omega}\times\mathbf{r}+\mathbf{v}_R\right) + \mathbf{\Omega}\times\left(\mathbf{\Omega}\times\mathbf{r}+\mathbf{v}_R\right) \tag{5.3.4}$$

$$= 2\mathbf{\Omega}\times\mathbf{v}_R + \mathbf{\Omega}\times\left(\mathbf{\Omega}\times\mathbf{r}\right) + \frac{\mathrm{d}\mathbf{v}_R}{\mathrm{d}t_R} \tag{5.3.5}$$

since $\mathrm{d}\mathbf{r}/\mathrm{d}t_R = \mathbf{v}_R$ by definition. Now recall that the convective derivative is given by

$$\frac{\mathrm{d}\mathbf{v}}{\mathrm{d}t} = \frac{\partial\mathbf{v}}{\partial t} + (\mathbf{v}\cdot\nabla)\mathbf{v} \tag{5.3.6}$$

whence the Euler equation in a rotating frame is

$$\frac{\partial\mathbf{v}_R}{\partial t_R} + (\mathbf{v}_R\cdot\nabla)\mathbf{v}_R + 2\mathbf{\Omega}\times\mathbf{v}_R + \mathbf{\Omega}\times(\mathbf{\Omega}\times\mathbf{r}) = -\frac{1}{\rho}\nabla P - \nabla\Phi. \tag{5.3.7}$$

Working to first order in the perturbations $\mathbf{v}_R$, $\delta P$, $\delta\rho$ and $\delta\Phi$ our perturbed Euler equation is:

$$\frac{\partial\mathbf{v}_R}{\partial t_R} + 2\mathbf{\Omega}\times\mathbf{v}_R = \frac{\delta\rho}{\rho_0^2}\nabla P_0 - \frac{1}{\rho_0}\nabla\delta P - \nabla\delta\Phi. \tag{5.3.8}$$

From now on we will drop the $R$ subscripts on $\mathbf{v}$ and $t$, with the understanding that these quantities will always refer to the rotating frame. The other perturbation equations — the continuity equation, equation of state and Poisson's equation — are the same in the rotating frame as in the inertial frame.

### 5.3.2 $r$-mode calculation

We are looking for the oscillation frequency $\sigma$ of an axial mode in a slowly rotating star, and so make the ansatz that our velocity field scales linearly with the stellar rotation with nonspherical effects being of higher order. Formally, this means that $\mathbf{v}_R, \sigma \propto \mathcal{O}(\Omega)$, whilst $\delta\rho, \delta P, \delta\Phi \propto \mathcal{O}(\Omega^3)$. Now if we take the curl of equation (5.3.8) and discard the higher-order terms described above, we are left with the equation

$$\frac{\partial}{\partial t}(\nabla \times \mathbf{v}) \; + \; 2\, \nabla \times (\mathbf{\Omega} \times \mathbf{v}) = 0. \tag{5.3.9}$$

Since our velocity field is non-radial by assumption, its general form is

$$\mathbf{v} = f(r)\mathbf{r} \times \nabla Y_{lm}, \tag{5.3.10}$$

and with the ansatz that it is also oscillatory we have $\dot{\mathbf{v}} = i\sigma\mathbf{v}$. With these, equation (5.3.9) becomes

$$\nabla \times \left\{ i\sigma \nabla \times (\mathbf{r} \times \nabla Y_{lm}) + 2\, \nabla \times (\mathbf{\Omega} \times (\mathbf{r} \times \nabla Y_{lm})) \right\} = 0. \tag{5.3.11}$$

Now $\mathbf{\Omega} = \Omega(\cos\theta \mathbf{e}_r - \sin\theta \mathbf{e}_\theta)$, so

$$\mathbf{\Omega} \times (\mathbf{r} \times \nabla Y) = -\Omega(r\cos\theta \nabla Y + \sin\theta(\mathbf{e}_\theta \cdot \nabla Y)\mathbf{r}) \tag{5.3.12}$$

where we are suppressing the $l, m$ indices of $Y_{lm}$ for brevity. We also have

$$\mathbf{r} \times \nabla Y = -\mathbf{e}_\theta r(\nabla Y \cdot \mathbf{e}_\phi) + \mathbf{e}_\phi r(\nabla Y \cdot \mathbf{e}_\theta). \tag{5.3.13}$$

With these identities (5.3.11) becomes

$$\nabla \times \left\{ i\sigma(-\mathbf{e}_\theta r(\nabla Y \cdot \mathbf{e}_\phi) + \mathbf{e}_\phi r(\nabla Y \cdot \mathbf{e}_\theta)) - 2\, \Omega(r\cos\theta \nabla Y + \sin\theta(\mathbf{e}_\theta \cdot \nabla Y)\mathbf{r}) \right\} = 0. \tag{5.3.14}$$

We now recall the vector identity $\nabla \times f\mathbf{A} = (\nabla f) \times \mathbf{A} + f \nabla \times \mathbf{A}$ and apply it to all relevant terms in the previous equation. Together with the identities

$$\nabla \times \mathbf{e}_r = \mathbf{0} \tag{5.3.15}$$

$$\nabla \times \mathbf{e}_\theta = \frac{1}{r}\mathbf{e}_\phi \tag{5.3.16}$$

$$\nabla \times \mathbf{e}_\phi = \frac{1}{r\tan\theta}\mathbf{e}_r + \frac{1}{r}\mathbf{e}_\theta \tag{5.3.17}$$

$$\nabla Y = \frac{e^{im\phi}}{r}\left(\frac{\mathrm{d}P_{lm}}{\mathrm{d}\theta}\mathbf{e}_\theta + \frac{imP_{lm}}{\sin\theta}\mathbf{e}_\phi\right) \tag{5.3.18}$$

$$\nabla \times (\cos\theta \nabla Y) = -\frac{imP_{lm}e^{im\phi}}{r^2}\mathbf{e}_r, \tag{5.3.19}$$

equation (5.3.11) becomes

$$\frac{2\Omega i m e^{im\phi} P_{lm}}{r^2} = i\sigma \left\{ \nabla \left( \frac{im P_{lm} e^{im\phi}}{r \sin\theta} \right) \times \mathbf{e}_\theta - \frac{e^{im\phi} P_{lm,\theta}}{r^2 \tan\theta} - \nabla \left( \frac{e^{im\phi} P_{lm,\theta}}{r} \right) \times \mathbf{e}_\phi \right\}. \tag{5.3.20}$$

Evaluating the $\nabla(...)$ terms and taking the $r$-component of equation (5.3.20) we obtain

$$2\Omega m P_{lm} = \sigma \left( \frac{m^2 P_{lm}}{\sin^2\theta} - \frac{P_{lm,\theta}}{\tan\theta} - P_{lm,\theta\theta} \right). \tag{5.3.21}$$

Finally we recall the associated Legendre equation (whose solutions are the $P_{lm}$ functions, see Arfken and Weber [6]):

$$\frac{1}{\sin\theta} \frac{\mathrm{d}}{\mathrm{d}\theta} \left( \sin\theta \frac{\mathrm{d}P_{lm}}{\mathrm{d}\theta} \right) + \left( l(l+1) - \frac{m^2}{\sin^2\theta} \right) P_{lm} = 0 \tag{5.3.22}$$

which we use in (5.3.21) to find the $r$-mode frequency

$$\sigma = \frac{2\Omega m}{l(l+1)}. \tag{5.3.23}$$

In conclusion, we have established that there are indeed axial modes in a rotating star, with frequencies scaling linearly with the rotational frequency (at least for slow rotation). This was our ansatz, but it would have led to a zero-frequency mode frequency if there had been no such non-trivial mode. The formula (5.3.23) will enable us to identify the $r$-mode from the results of the time-evolution code discussed in chapter 7; with this code we are also able to investigate the effect of strong magnetic fields on the $r$-mode, which is not an analytically tractable problem.

# Chapter 6

# Stationary magnetic equilibria: numerical work

As discussed earlier in this thesis, magnetic distortions of a neutron star are interesting for their potential to produce detectable gravitational radiation (see section 1.2.3) and because of the possibility that they may allow the star to undergo precession-like motion (chapter 3). In chapter 4 we were able to establish some results for MHD equilibria analytically, but to study compressible stars in the fast-rotation and strong-field regimes, we need a numerical approach. The equilibrium configurations we produce using the code described in this chapter are not only interesting in their own right: we will also use them as background configurations about which to perturb. Perturbations and oscillation modes of these stars will be discussed in chapters 7 and 8.

In this chapter we derive the equations of axisymmetric MHD and solve them numerically to find equilibrium solutions for rotating magnetised polytropic stars. We begin with a full derivation for general polytropes in the mixed poloidal-toroidal field case, leading to the Grad-Shafranov equation [60, 124]. These equations were also derived by Chandrasekhar and Prendergast [29, 112], but only for incompressible stars (polytropic index $N = 0$). Purely poloidal fields follow as a special case of the mixed-field equations; the result for purely toroidal fields is established separately, but using a similar method to the mixed-field derivation.

The work reported here is closely related to that of Tomimura and Eriguchi [137], but we study a wider range of aspects of neutron star physics (including the

relative strengths of the poloidal and toroidal field components, the ratio of internal to external field, and ellipticities). This chapter is summarised in Lander and Jones [84].

We begin the chapter with an overview of the fundamental equations of magneto-hydrodynamics. We then present the derivations of the magnetic equations needed for the code. After discussing details of the numerical techiques used, we then present results for stationary equilibria of neutron stars with rotation and magnetic fields.

## 6.1 Magnetohydrodynamics

We begin by recalling Maxwell's equations for electrodynamics:

$$\nabla \times \mathbf{B} = \mu\epsilon\frac{\partial \mathbf{E}}{\partial t} + \mu\mathbf{j} \tag{6.1.1}$$

$$\nabla \cdot \mathbf{B} = 0 \tag{6.1.2}$$

$$\nabla \times \mathbf{E} = -\frac{\partial \mathbf{B}}{\partial t} \tag{6.1.3}$$

$$\nabla \cdot \mathbf{E} = \frac{\rho_e}{\epsilon} \tag{6.1.4}$$

where $\mathbf{B}$ is the magnetic field, $\mathbf{E}$ the electric field, $\mathbf{j}$ the current, $\rho_e$ the charge density and $\epsilon, \mu$ are the permittivity and permeability of the medium, respectively. These last two quantities (in free space) are related to the speed of light $c$: $\epsilon_0\mu_0 = 1/c^2$; if not in free space then the same relation connects $\epsilon, \mu$ to the speed of light in the medium. Note that the values of these constants depend on the system of units used, and $\epsilon$ is defined through its relation to $\mu$ and $c$. *Electromagnetic units* are based on the cgs (centimetre-gram-second) system used in astronomy, with $\mu = 4\pi$ and $c = 2.998 \times 10^{10}$ cm s$^{-1}$; *SI* units are based on the metre, kilogram and second, with $\mu = 4\pi \times 10^{-7}$ and $c = 2.998 \times 10^{8}$ m s$^{-1}$. For comparison with the bulk of the astronomical literature, we have consistently used electromagnetic units for derivations in this work.

For nonrelativistic applications, the charge density $\rho_e$ and displacement current $\epsilon\frac{\partial \mathbf{E}}{\partial t}$ terms will be negligible (see, for example, Davidson [37]); for this reason we

only require the reduced form of Maxwell's equations:

$$\nabla \times \mathbf{B} = \mu \mathbf{j} \tag{6.1.5}$$

$$\nabla \cdot \mathbf{B} = 0 \tag{6.1.6}$$

$$\nabla \times \mathbf{E} = -\frac{\partial \mathbf{B}}{\partial t} \tag{6.1.7}$$

$$\nabla \cdot \mathbf{E} = 0. \tag{6.1.8}$$

In addition to these, we have (reduced) expressions for the current $\mathbf{j}$ (known as Ohm's law) and the Lorentz force $\boldsymbol{\mathcal{L}}$:

$$\mathbf{j} = \sigma(\mathbf{E} + \mathbf{v} \times \mathbf{B}) \tag{6.1.9}$$

$$\boldsymbol{\mathcal{L}} = \mathbf{j} \times \mathbf{B} \tag{6.1.10}$$

where $\mathbf{v}$ is the velocity of the magnetised fluid.

Having discussed the governing magnetic equations, we now turn to the fluid. Newton's second law for an inviscid fluid is the Euler equation:

$$\frac{\mathrm{d}\mathbf{v}}{\mathrm{d}t} = -\frac{\nabla P}{\rho} - \nabla \Phi. \tag{6.1.11}$$

To generalise this to the case of a rigidly rotating fluid with a magnetic field, we need to add on terms corresponding to the centrifugal force and the Lorentz force, giving us the MHD equilibrium equation

$$\boldsymbol{\Omega} \times (\boldsymbol{\Omega} \times \mathbf{r}) = -\frac{\nabla P}{\rho} - \nabla \Phi + \frac{\boldsymbol{\mathcal{L}}}{\rho}. \tag{6.1.12}$$

where $P$ is fluid pressure, $\rho$ density of fluid, $\Phi$ gravitational potential and $\boldsymbol{\Omega}$ angular velocity. The equation may be generalised to an arbitrary rotation law by replacing $\boldsymbol{\Omega} \times (\boldsymbol{\Omega} \times \mathbf{r})$ with the gradient of some centrifugal potential, $\nabla \Phi_r$.

In all of the work in this thesis we make the perfect MHD approximation — that the conductivity $\sigma$ of the fluid is infinite — and in this chapter we are concerned with stationary configurations and so additionally have $\partial/\partial t = 0$. In this case the MHD equations reduce to

$$\nabla \times \mathbf{B} = \mu \mathbf{j} \tag{6.1.13}$$

$$\nabla \cdot \mathbf{B} = 0 \tag{6.1.14}$$

$$\boldsymbol{\mathcal{L}} = \mathbf{j} \times \mathbf{B} \tag{6.1.15}$$

$$0 = -\frac{\nabla P}{\rho} - \nabla \Phi - \boldsymbol{\Omega} \times (\boldsymbol{\Omega} \times \mathbf{r}) + \frac{\boldsymbol{\mathcal{L}}}{\rho}. \tag{6.1.16}$$

## 6.2 The equations of axisymmetric MHD

### 6.2.1 General forms for magnetic field and current

We wish to see how the assumption of axisymmetry constrains the geometry of the magnetic field and the current; and hence also the form of the Lorentz force. This is done following the work of Grad and Rubin [60] and Shafranov [124]. Working in cylindrical polar coordinates, we begin with the equilibrium equation for a magnetised rotating fluid:

$$-\nabla H - \nabla\Phi + \nabla\left(\frac{\Omega^2\varpi^2}{2}\right) + \frac{\boldsymbol{\mathcal{L}}}{\rho} = 0 \tag{6.2.1}$$

where we have rewritten (6.1.16) above by replacing the usual $\nabla P/\rho$ term with the gradient of the enthalpy $H = \int_0^P d\hat{P}/\rho(\hat{P})$ and also explicitly written the centrifugal term as the gradient of a scalar.

If we now take the curl of (6.2.1) then by the vector identity $\nabla \times \nabla f = 0$ (for any scalar field $f$) we see that

$$\nabla \times \left(\frac{\boldsymbol{\mathcal{L}}}{\rho}\right) = 0, \tag{6.2.2}$$

implying that $\boldsymbol{\mathcal{L}}/\rho$ is also the gradient of some scalar $M$. Note that $\nabla M \cdot \mathbf{B} = 0$, i.e. $M$ is constant along field lines.

Next we write $\mathbf{B}$ in terms of a streamfunction $u$, defined through the relations

$$B_\varpi = -\frac{1}{\varpi}\frac{\partial u}{\partial z}\ ,\ B_z = \frac{1}{\varpi}\frac{\partial u}{\partial \varpi} \tag{6.2.3}$$

— note that these components give a solenoidal magnetic field, $\nabla \cdot \mathbf{B} = 0$, by construction. Hence

$$\mathbf{B} = -\frac{1}{\varpi}\frac{\partial u}{\partial z}\mathbf{e}_\varpi + B_\phi \mathbf{e}_\phi + \frac{1}{\varpi}\frac{\partial u}{\partial \varpi}\mathbf{e}_z. \tag{6.2.4}$$

Now comparing the equation with

$$\nabla u \times \mathbf{e}_\phi = -\frac{\partial u}{\partial z}\mathbf{e}_\varpi + \frac{\partial u}{\partial \varpi}\mathbf{e}_z, \tag{6.2.5}$$

we see that $\mathbf{B}$ may be written as

$$\mathbf{B} = \frac{1}{\varpi}\nabla u \times \mathbf{e}_\phi + B_\phi \mathbf{e}_\phi. \tag{6.2.6}$$

Note that this implies $\mathbf{B}\cdot\nabla u = 0$, i.e. $u$ is constant along field lines. Recalling that $M$ also has this property, we deduce that

$$M = M(u). \tag{6.2.7}$$

Next we turn to Ampère's law in axisymmetry:

$$4\pi\mathbf{j} = \nabla\times\mathbf{B} = -\frac{\partial B_\phi}{\partial z}\mathbf{e}_\varpi + \left(\frac{\partial B_\varpi}{\partial z} - \frac{\partial B_z}{\partial \varpi}\right)\mathbf{e}_\phi + \frac{1}{\varpi}\frac{\partial}{\partial\varpi}(\varpi B_\phi)\mathbf{e}_z. \tag{6.2.8}$$

Now by comparing the poloidal part of the current

$$\mathbf{j}_{pol} = -\frac{1}{4\pi\varpi}\frac{\partial}{\partial z}(\varpi B_\phi)\mathbf{e}_\varpi + \frac{1}{4\pi\varpi}\frac{\partial}{\partial\varpi}(\varpi B_\phi)\mathbf{e}_z \tag{6.2.9}$$

with the quantity

$$\nabla(\varpi B_\phi)\times\mathbf{e}_\phi = -\frac{\partial}{\partial z}(\varpi B_\phi)\mathbf{e}_\varpi + \frac{\partial}{\partial\varpi}(\varpi B_\phi)\mathbf{e}_z, \tag{6.2.10}$$

we see that

$$\mathbf{j}_{pol} = \frac{1}{4\pi\varpi}\nabla(\varpi B_\phi)\times\mathbf{e}_\phi. \tag{6.2.11}$$

Next we consider the toroidal part of the current $\mathbf{j}_{tor} = j_\phi\mathbf{e}_\phi$ and rewrite $j_\phi$ using the definition of the streamfunction $u$:

$$4\pi j_\phi = \frac{\partial B_\varpi}{\partial z} - \frac{\partial B_z}{\partial\varpi} = -\frac{1}{\varpi}\left(\varpi\frac{\partial}{\partial\varpi}\left(\frac{1}{\varpi}\frac{\partial u}{\partial\varpi}\right) + \frac{\partial^2 u}{\partial z^2}\right). \tag{6.2.12}$$

For brevity we define a differential operator $\Delta_*$ by

$$\Delta_* \equiv \frac{\partial^2}{\partial\varpi^2} - \frac{1}{\varpi}\frac{\partial}{\partial\varpi} + \frac{\partial^2}{\partial z^2}. \tag{6.2.13}$$

Now using this definition together with (6.2.11) and (6.2.12) we see that the current may be written as

$$4\pi\mathbf{j} = \frac{1}{\varpi}\nabla(\varpi B_\phi)\times\mathbf{e}_\phi - \frac{1}{\varpi}\Delta_* u\ \mathbf{e}_\phi. \tag{6.2.14}$$

Our two key results from this section so far are the expressions (6.2.6) and (6.2.14) for the general form of an axisymmetric magnetic field and current, respectively. Next we consider the form of the Lorentz force arising from these two quantities. We see that in general

$$\begin{aligned}\boldsymbol{\mathcal{L}} = \mathbf{j}\times\mathbf{B} &= (\mathbf{j}_{pol} + j_\phi\mathbf{e}_\phi)\times(\mathbf{B}_{pol} + B_\phi\mathbf{e}_\phi)\\ &= \underbrace{\mathbf{j}_{pol}\times\mathbf{B}_{pol}}_{\boldsymbol{\mathcal{L}}_{tor}} + \underbrace{j_\phi\mathbf{e}_\phi\times\mathbf{B}_{pol} + B_\phi\mathbf{j}_{pol}\times\mathbf{e}_\phi}_{\boldsymbol{\mathcal{L}}_{pol}}.\end{aligned} \tag{6.2.15}$$

Returning to our original force balance equation (6.2.1) we note that the pressure, gravitational and centrifugal forces are axisymmetric (i.e. no $\phi$-dependence); therefore $\boldsymbol{\mathcal{L}}$ is also axisymmetric and its toroidal component must vanish:

$$\boldsymbol{\mathcal{L}}_{tor} = \mathbf{j}_{pol} \times \mathbf{B}_{pol} = 0. \tag{6.2.16}$$

At this point there are two ways to proceed: either $\mathbf{B}_{pol}$ is non-zero, in which case $\mathbf{B}_{pol}$ and $\mathbf{j}_{pol}$ are parallel; or $\mathbf{B}_{pol} = 0$. We shall consider these cases separately in the next two subsections.

### 6.2.2 Mixed poloidal and toroidal fields; the Grad-Shafranov equation

We have shown that the requirement (6.2.16) follows from the axisymmetry of our problem. In this subsection we consider the case where $\mathbf{B}_{pol}$ and $\mathbf{j}_{pol}$ are parallel, corresponding to a magnetic field with both poloidal and toroidal components. We will see that the case of purely poloidal magnetic fields may be found as a particular limit of the general mixed-field configuration.

Recall from (6.2.6) and (6.2.11) that

$$\begin{aligned} \mathbf{B}_{pol} &= \frac{1}{\varpi}\nabla u \times \mathbf{e}_\phi \\ \mathbf{j}_{pol} &= \frac{1}{4\pi\varpi}\nabla(\varpi B_\phi) \times \mathbf{e}_\phi. \end{aligned}$$

Knowing that these two quantities are parallel we see that $u$ and $\varpi B_\phi$ must be related by some function $f$:

$$\varpi B_\phi = f(u). \tag{6.2.17}$$

Next we evaluate the non-zero Lorentz force components, i.e. $\boldsymbol{\mathcal{L}}_{pol}$ from (6.2.15). Using the pair of equations at the start of this subsection, we find that

$$\mathbf{e}_\phi \times \mathbf{B}_{pol} = \mathbf{e}_\phi \times \left(\frac{1}{\varpi}\nabla u \times \mathbf{e}_\phi\right) = \frac{1}{\varpi}\left(\nabla u - \mathbf{e}_\phi(\mathbf{e}_\phi \cdot \nabla u)\right) = \frac{1}{\varpi}\nabla u \tag{6.2.18}$$

and similarly

$$\mathbf{j}_{pol} \times \mathbf{e}_\phi = -\frac{1}{4\pi\varpi}\nabla(\varpi B_\phi). \tag{6.2.19}$$

Now using these expressions in (6.2.15), together with the relation $j_\phi = -\frac{1}{4\pi\varpi}\Delta_* u$ from (6.2.14), we find that

$$\boldsymbol{\mathcal{L}} = -\frac{1}{4\pi\varpi^2}\Delta_* u \; \nabla u - \frac{1}{4\pi\varpi} B_\phi \nabla(\varpi B_\phi) \tag{6.2.20}$$

which, recalling the definitions $\nabla M = \boldsymbol{\mathcal{L}}/\rho$ and $f(u) = \varpi B_\phi$, becomes

$$4\pi\rho\nabla M = -\frac{1}{\varpi^2}\Delta_* u\ \nabla u - \frac{1}{\varpi^2} f(u)\nabla f(u). \tag{6.2.21}$$

Since $M$ and $f$ are both functions of $u$ alone we are able to rewrite $\nabla M(u)$ and $\nabla f(u)$ using the chain rule, to give

$$-4\pi\rho\frac{\mathrm{d}M}{\mathrm{d}u}\nabla u = \frac{1}{\varpi^2}\Delta_* u\ \nabla u + \frac{f(u)}{\varpi^2}\frac{\mathrm{d}f}{\mathrm{d}u}\nabla u. \tag{6.2.22}$$

Now provided $\nabla u \neq 0$ we have

$$4\pi\rho\frac{\mathrm{d}M}{\mathrm{d}u} = -\frac{1}{\varpi^2}\left(\Delta_* u + f(u)\frac{\mathrm{d}f}{\mathrm{d}u}\right), \tag{6.2.23}$$

which is the Grad-Shafranov equation [60, 124].

We now return to the general form of an axisymmetric current (6.2.14), replacing $\varpi B_\phi$ with $f(u)$ and using the chain rule to give:

$$4\pi\mathbf{j} = \frac{1}{\varpi}\frac{\mathrm{d}f}{\mathrm{d}u}\nabla u \times \mathbf{e}_\phi - \frac{1}{\varpi}\Delta_* u\mathbf{e}_\phi. \tag{6.2.24}$$

We now use (6.2.6) to make the replacement $\frac{1}{\varpi}\nabla u \times \mathbf{e}_\phi = \mathbf{B}_{pol}$ and the Grad-Shafranov equation (6.2.23) to eliminate $\Delta_* u$ from (6.2.24):

$$4\pi\mathbf{j} = \frac{\mathrm{d}f}{\mathrm{d}u}\mathbf{B}_{pol} + \frac{1}{\varpi}\left(4\pi\varpi^2\rho\frac{\mathrm{d}M}{\mathrm{d}u} + f(u)\frac{\mathrm{d}f}{\mathrm{d}u}\right)\mathbf{e}_\phi. \tag{6.2.25}$$

Finally we use the definition $f = \varpi B_\phi$ and $\mathbf{B} = \mathbf{B}_{pol} + B_\phi\mathbf{e}_\phi$ to yield an expression for the current in terms of the magnetic field and the derivatives of the functions $M(u)$ and $f(u)$:

$$4\pi\mathbf{j} = \frac{\mathrm{d}f}{\mathrm{d}u}\mathbf{B} + 4\pi\rho\varpi\frac{\mathrm{d}M}{\mathrm{d}u}\mathbf{e}_\phi. \tag{6.2.26}$$

### 6.2.3 Purely poloidal field

Having arrived at an expression for an axisymmetric current associated with a mixed poloidal-toroidal field (6.2.26), we may straightforwardly specialise to purely poloidal magnetic fields by choosing $f(u)$ as a constant. Then $\frac{\mathrm{d}f}{\mathrm{d}u} = 0$ and the mixed term vanishes from the expression for $\mathbf{j}$, leaving only a toroidal current

$$\mathbf{j} = \rho\varpi\frac{\mathrm{d}M}{\mathrm{d}u}\mathbf{e}_\phi \tag{6.2.27}$$

and hence a purely *poloidal* field, by Ampère's law.

### 6.2.4 Purely toroidal field

In the previous subsection we showed that (6.2.26) may be trivially reduced to the poloidal-field case. However it is clear from the form of (6.2.26) that there is no choice of $f$ and $M$ which yields a poloidal current (or equivalently a toroidal field). Setting $M(u)$ to be a constant, for example, results in the general expression for a force-free field

$$4\pi\mathbf{j} = \frac{\mathrm{d}f}{\mathrm{d}u}\mathbf{B}, \tag{6.2.28}$$

which is of less interest to us, as we aim to study distortions caused by magnetic fields.

It is clear that the derivation used for mixed fields does not hold in the toroidal-field case. Previously we were able to use (6.2.16) to simplify the current-field relation, but no such constraint is provided for a toroidal field, where $\mathbf{B}_{pol} = 0$. Accordingly we must return to subsection 6.2.1 where we found that

$$\begin{aligned} \mathbf{B}_{pol} &= \frac{1}{\varpi}\nabla u \times \mathbf{e}_\phi \\ \mathbf{j}_{pol} &= \frac{1}{4\pi\varpi}\nabla(\varpi B_\phi) \times \mathbf{e}_\phi \end{aligned}$$

(from equations (6.2.6) and (6.2.11)). Since $\mathbf{B}_{pol} = 0$ we no longer require $\varpi B_\phi$ to be a function of $u$; indeed the streamfunction $u$ will not even enter our final solution. We also recall that the general form of an axisymmetric Lorentz force is given by (6.2.15), which in the case of $\mathbf{B}_{pol} = 0$ reduces to

$$\boldsymbol{\mathcal{L}} = B_\phi \mathbf{j}_{pol} \times \mathbf{e}_\phi. \tag{6.2.29}$$

Using (6.2.11) to replace $\mathbf{j}_{pol}$ in this expression then gives

$$\boldsymbol{\mathcal{L}} = \frac{B_\phi}{4\pi\varpi}\left(\nabla(\varpi B_\phi) \times \mathbf{e}_\phi\right) \times \mathbf{e}_\phi = -\frac{B_\phi}{4\pi\varpi}\nabla(\varpi B_\phi). \tag{6.2.30}$$

Again recalling previous work in this section, we note that taking the curl of (6.2.1) shows that $\nabla \times (\boldsymbol{\mathcal{L}}/\rho) = 0$. We use this fact together with the vector identity $\nabla \times (f\nabla g) = \nabla f \times \nabla g$ to rewrite (6.2.30) as

$$\nabla\left(\frac{B_\phi}{\rho\varpi}\right) \times \nabla(\varpi B_\phi) = 0. \tag{6.2.31}$$

If we write $\frac{B_\phi}{\rho\varpi}$ in the above expression as $\frac{1}{\rho\varpi^2}\varpi B_\phi$ and use the chain rule, some algebra leads to

$$-\frac{B_\phi}{\rho^2\varpi^3}\nabla(\rho\varpi^2) \times \nabla(\varpi B_\phi) = 0. \tag{6.2.32}$$

Since $B_\phi/\rho^2\varpi^3 \neq 0$ we then deduce that $\nabla(\rho\varpi^2) \times \nabla(\varpi B_\phi) = 0$ and hence that $\rho\varpi^2$ and $\varpi B_\phi$ are related by some function $h$, i.e.

$$\varpi B_\phi = h(\rho\varpi^2). \tag{6.2.33}$$

As before we now define a magnetic function $M$ through $\boldsymbol{\mathcal{L}}/\rho = \nabla M$ (note that here $M$ need not be a function of the streamfunction $u$ of previous sections). From (6.2.30) and (6.2.33) we then find that

$$\nabla M = -\frac{h(\rho\varpi^2)}{4\pi\rho\varpi^2}\nabla h(\rho\varpi^2). \tag{6.2.34}$$

By the chain rule we have $\nabla h(\gamma) = \frac{\mathrm{d}h}{\mathrm{d}\gamma}\nabla\gamma$, where we have introduced the notation $\gamma = \rho\varpi^2$. Given this we have

$$\nabla M = -\frac{h(\gamma)}{4\pi\gamma}\frac{\mathrm{d}h}{\mathrm{d}\gamma}\nabla\gamma \tag{6.2.35}$$

and so

$$M = -\frac{1}{4\pi}\int_0^{\rho\varpi^2} \frac{h}{\gamma}\frac{\mathrm{d}h}{\mathrm{d}\gamma}\,\mathrm{d}\gamma. \tag{6.2.36}$$

### 6.2.5 Notation for the rest of the chapter

For prior sections in this chapter, it was convenient to employ the variables $M$ and $f$ in derivations. Having obtained the required results, we now change notation for consistency with earlier studies: the analytic work on incompressible fluids by Chandrasekhar and Prendergast [29, 112] and the numerical study of Tomimura and Eriguchi [137]. For this, we make the replacements

$$\alpha(u) \equiv \frac{\mathrm{d}f}{\mathrm{d}u} \text{ and } \kappa(u) \equiv 4\pi\frac{\mathrm{d}M}{\mathrm{d}u}. \tag{6.2.37}$$

The relation linking the magnetic current to the field (6.2.26) now becomes

$$4\pi\mathbf{j} = \alpha(u)\mathbf{B} + \varpi\rho\kappa(u)\mathbf{e}_\phi. \tag{6.2.38}$$

## 6.3 Finding integral equations for MHD in a fluid star

### 6.3.1 Basic equations for our stellar model

We model a rotating magnetic neutron star by assuming that it is in a stationary state, axisymmetric with both the magnetic dipole axis and the spin axis aligned,

and composed of infinitely conducting material (the perfect MHD approximation). We work in the electromagnetic units discussed at the start of this chapter. The derivation of the integral equation for $A_\phi$ follows the work of Tomimura and Eriguchi [137].

We begin with the equations of magnetohydrodynamics described earlier. These are the Euler equation describing hydromagnetic equilibrium:

$$-\frac{1}{\rho}\nabla P - \nabla\Phi_g + \nabla\Phi_r + \frac{\boldsymbol{\mathcal{L}}}{\rho} = 0 \tag{6.3.1}$$

where $\boldsymbol{\mathcal{L}} = \mathbf{j} \times \mathbf{B}$ is the Lorentz force; together with Ampère's law:

$$\nabla \times \mathbf{B} = 4\pi\mathbf{j} \tag{6.3.2}$$

and the solenoidal constraint

$$\nabla \cdot \mathbf{B} = 0. \tag{6.3.3}$$

This system of equations is closed with Poisson's equation:

$$\nabla^2\Phi_g = 4\pi G\rho \tag{6.3.4}$$

and the assumption of a barotropic equation of state:

$$P = P(\rho). \tag{6.3.5}$$

In the above equations $P, \rho, \Phi_g, \Phi_r, \mathbf{j}, \mathbf{B}$ and $G$ are the pressure, density, gravitational potential, centrifugal potential, current density, magnetic field and gravitational constant, respectively.

Although the formalism allows for different choices of the centrifugal potential $\Phi_r$ and equation of state $P = P(\rho)$, we will work with a rigidly rotating star:

$$\Phi_r = \frac{\Omega_0^2\varpi^2}{2}, \tag{6.3.6}$$

where the angular velocity $\Omega_0$ is a constant, and a polytropic equation of state:

$$P = k\rho^{1+1/N} \tag{6.3.7}$$

where $k$ is some constant and $N$ the polytropic index.

### 6.3.2 Choices for the magnetic functions

In the previous sections of this chapter we have shown that the equations of perfect MHD reduce to a mixed-field case (section 6.2.2) and a purely toroidal-field case (section 6.2.4). In the former case the equations are rewritten in terms of two magnetic functions $\alpha(u)$ and $\kappa(u)$ of the streamfunction $u$; in the latter case one magnetic function $h(\gamma)$ is employed (where $\gamma = \rho\varpi^2$ as before). Here we outline our chosen forms for these functions, and in the next subsection we describe why many alternative choices are not viable.

In the mixed-field case, the two functions $\alpha(u)$ and $\kappa(u)$ govern different aspects of the magnetic field: firstly, since $\boldsymbol{\mathcal{L}} = \mathbf{j} \times \mathbf{B}$ we have $\boldsymbol{\mathcal{L}} = \varpi\rho\kappa\mathbf{e}_\phi \times \mathbf{B}/4\pi$ (from equation (6.2.38)) — i.e., the Lorentz force is dependent on $\kappa$, and so $\kappa$ governs the relative contributions of the magnetic and centrifugal forces to the overall distortion of the star. The role of $\alpha$ is less clear. From equation (6.2.38) we see that $\alpha = 0$ gives a purely toroidal current and hence poloidal field, whilst increasing $\alpha$ increases the size of the mixed toroidal-poloidal term $\alpha\mathbf{B}$ (and so indirectly increases the toroidal component of the field). However, there is no limit in which the field is purely toroidal in this formalism. We can thus only expect $\alpha$ to have some indirect connection with the relative strengths of the poloidal and toroidal components of the magnetic field.

Following Tomimura and Eriguchi [137], we choose the functional forms of $\alpha(u)$ and $\kappa(u)$ as:

$$\kappa(u) = \kappa_0 = const., \tag{6.3.8}$$

$$\alpha(u) = \begin{cases} a(u - u_{max})^\zeta & \text{if } u > u_{max} \\ 0 & \text{if } u \leq u_{max}, \end{cases} \tag{6.3.9}$$

where $\zeta$ is some constant and $u_{max}$ is the maximum surface value attained by the streamfunction $u$. We find that $u < u_{max}$ for all points outside the star and so the chosen form of $\alpha$ ensures there is no exterior current. Next we combine the definitions $\alpha \equiv \frac{\mathrm{d}f}{\mathrm{d}u}$ and $f(u) \equiv \varpi B_\phi$ to see that

$$\int^u \alpha(u')\ \mathrm{d}u' = \varpi B_\phi \tag{6.3.10}$$

— i.e., we must enforce the continuity of $\int \alpha(u)\ \mathrm{d}u$ to ensure the continuity of $B_\phi$.

We therefore choose the lower limit of the integral of $\alpha$ so that

$$f(u) \equiv \int^{u} \alpha(u')\ \mathrm{d}u' = \begin{cases} \frac{a}{\zeta+1}(u-u_{max})^{\zeta+1} & \text{if } u > u_{max}, \\ 0 & \text{if } u \leq u_{max}. \end{cases} \tag{6.3.11}$$

For our chosen functional forms of $\alpha(u)$ and $\kappa(u)$ we see that for a specific solution we need to choose three constants: $\zeta$, $a$ and $\kappa_0$. We will later drop the zero subscript, with the understanding that $\kappa$ always refers to a constant unless otherwise stated. Tomimura and Eriguchi set $\zeta = 1$, but we have found that a smaller value of $\zeta$ allows for a slightly stronger toroidal-field component; accordingly, we set $\zeta = 0.1$ throughout this chapter, except in comparing our results with previous work (subsection 6.8.2). We have since found that Yoshida and Eriguchi [145] made the same choice as us, also motivated by an attempt to achieve poloidal and toroidal components of similar strength.

For the purely-toroidal field case there is only one magnetic function, $h(\gamma)$. Unlike $\alpha(u)$ of the mixed-field case, $h$ is directly related to the toroidal field. We choose

$$h(\rho\varpi^2) = \lambda\rho\varpi^2 \tag{6.3.12}$$

where $\lambda$ is a constant that governs the field strength. With this choice, we have $B_\phi = \lambda\rho\varpi$.

### 6.3.3 Restrictions on the magnetic functions

Although the magnetic functions discussed above appear to be arbitrary, there are a number of restrictions on their functional forms, on either physical grounds or because they result in trivial solutions.

The functions $\alpha(u)$ and $h(\gamma)$ both govern the toroidal fields, and so both must necessarily vanish outside the star to avoid having exterior currents. Since the streamfunction $u$ in the mixed-field case does not vanish at the star's surface, some care is needed when choosing the functional form of $\alpha(u)$ to ensure the toroidal field is confined within the star. To this end, we define $\alpha(u)$ to have the form shown in equation (6.3.9). There does not appear to be any other functional form for $\alpha$ which vanishes outside the star and is dependent only on $u$, so we conclude that (6.3.9) is the only acceptable choice for $\alpha(u)$. The functional form of $h$, similarly, appears restricted. To vanish outside the star $h(\gamma)$ cannot contain a constant piece, so let

us consider a functional form of $h(\gamma) = \lambda\gamma^{\chi}$ where $\lambda$ and $\chi$ are constants. However, if $\chi < \frac{1}{2}$ then $B_\phi = \lambda\gamma^{\chi}\varpi^{-1} = \lambda\rho^{\chi}\varpi^{2\chi-1}$ will diverge at the origin, so we discard these choices. Additionally, we find that if $\chi > 1$ is chosen, then the field iterates to zero in our numerical scheme, leading us to choose $h(\gamma) = \lambda\gamma$.

Finally, the function $\kappa(u)$ is theoretically allowed to depend on the streamfunction $u$, but if it is chosen as anything other than a constant then, as for $h(\gamma)$, we find that the configuration iterates to a zero-field solution. This may be a limitation of our numerical scheme rather than a physical restriction, but in either case our solutions are limited to those with $\kappa$ being equal to some constant.

We conclude from this that, in fact, the choices made for our functional forms are not specialised ones and (at least within our scheme) do not result in the exclusion of physically valid solutions. Rather, we believe that our results are quite generic to perfectly conducting polytropes in axisymmetry.

### 6.3.4 Integral forms of the basic equations

Here we use the basic equations from the previous section to derive integral equations which can be used in a numerical scheme to find stationary configurations of a rotating magnetised axisymmetric polytrope. For the magnetic integral equation, we follow the work of Tomimura and Eriguchi [137].

Since $\nabla \cdot \mathbf{B} = 0$, we can write $\mathbf{B}$ in terms of a magnetic vector potential $\mathbf{A}$, viz.: $\mathbf{B} = \nabla \times \mathbf{A}$. We use this together with (6.2.38) to reexpress Ampère's law, which in components is now

$$\frac{\partial}{\partial z}\left(\frac{\partial A_z}{\partial \varpi} - \frac{\partial A_\varpi}{\partial z}\right) = -\alpha\frac{\partial A_\phi}{\partial z}, \tag{6.3.13}$$

$$\frac{\partial}{\partial \varpi}\left[\varpi\left(\frac{\partial A_\varpi}{\partial z} - \frac{\partial A_z}{\partial \varpi}\right)\right] = \alpha\frac{\partial \varpi A_\phi}{\partial \varpi}, \tag{6.3.14}$$

$$\frac{\partial}{\partial \varpi}\left(\frac{1}{\varpi}\frac{\partial \varpi A_\phi}{\partial \varpi}\right) + \frac{\partial^2 A_\phi}{\partial z^2} = -\alpha\left(\frac{\partial A_\varpi}{\partial z} - \frac{\partial A_z}{\partial \varpi}\right) - \kappa\rho\varpi. \tag{6.3.15}$$

Note that defining the magnetic field $\mathbf{B}$ through the vector potential $\mathbf{A}$ is equivalent to defining it through the streamfunction $u$; both approaches give a field $\mathbf{B}$ which automatically satisfies the solenoidal constraint. In fact, comparing the $\varpi$ and $z$ components of $\nabla \times \mathbf{A}$ with (6.2.3), we see that

$$u = \varpi A_\phi. \tag{6.3.16}$$

We define $\mathcal{A} \equiv \varpi \left( \frac{\partial A_\varpi}{\partial z} - \frac{\partial A_z}{\partial \varpi} \right)$ and $\mathfrak{A} \equiv \int_0^{\varpi A_\phi} \alpha(u')\ \mathrm{d}u'$; note that $\mathfrak{A} = \mathfrak{A}(u)$. Now, using the chain rule on equations (6.3.13) and (6.3.14), we see that:

$$\frac{\partial \mathcal{A}}{\partial z} = \alpha(u)\frac{\partial u}{\partial z} = \frac{\partial \mathfrak{A}}{\partial z} \tag{6.3.17}$$

$$\frac{\partial \mathcal{A}}{\partial \varpi} = \alpha(u)\frac{\partial u}{\partial \varpi} = \frac{\partial \mathfrak{A}}{\partial \varpi}. \tag{6.3.18}$$

Integrating these two leads to $\mathcal{A} = \mathfrak{A}$, or

$$\frac{\partial A_\varpi}{\partial z} - \frac{\partial A_z}{\partial \varpi} = \frac{1}{\varpi}\int_0^{\varpi A_\phi} \alpha(u')\ \mathrm{d}u'. \tag{6.3.19}$$

Using this relation (6.3.19), equation (6.3.15) can be rewritten as follows:

$$\frac{\partial^2 A_\phi}{\partial \varpi^2} + \frac{1}{\varpi}\frac{\partial A_\phi}{\partial \varpi} - \frac{A_\phi}{\varpi^2} + \frac{\partial^2 A_\phi}{\partial z^2} = -\frac{\alpha}{\varpi}\int_0^{\varpi A_\phi} \alpha(u')\ \mathrm{d}u' - \kappa\rho\varpi. \tag{6.3.20}$$

By multiplying equation (6.3.20) by $\sin\phi$ we see that it may be rewritten as

$$\Delta(A_\phi \sin\phi) = -\left[\frac{\alpha}{\varpi}\int_0^{\varpi A_\phi} \alpha(u')\ \mathrm{d}u' + \kappa\rho\varpi\right]\sin\phi \tag{6.3.21}$$

Next we rewrite the Lorentz force term from (6.3.1):

$$\begin{aligned}
\frac{1}{\rho}(\mathbf{j}\times\mathbf{B}) &= \frac{1}{4\pi}\kappa\varpi\mathbf{e}_\phi \times (\nabla\times\mathbf{A}) \\
&= \frac{1}{4\pi}\kappa \begin{pmatrix} (\varpi A_\phi)_{,\varpi} \\ 0 \\ \varpi A_{\phi,z} \end{pmatrix} \\
&= \frac{1}{4\pi}\kappa(\varpi A_\phi)\nabla(\varpi A_\phi)
\end{aligned} \tag{6.3.22}$$

and the equation of hydromagnetic equilibrium now becomes

$$-\frac{1}{\rho}\nabla P - \nabla\Phi_g + \nabla\Phi_r + \frac{1}{4\pi}\kappa(\varpi A_\phi)\nabla(\varpi A_\phi) = 0. \tag{6.3.23}$$

For the purposes of numerics we seek integral equations; the integral form of (6.3.23) is

$$H = C - \Phi_g + \Phi_r + \frac{1}{4\pi}\int_0^{\varpi A_\phi} \kappa(u')\ \mathrm{d}u' \tag{6.3.24}$$

where $C$ is an integration constant and

$$H(\mathbf{r}) = \int_0^{P(\mathbf{r})} \frac{\mathrm{d}P'}{\rho(P')} \tag{6.3.25}$$

is the enthalpy. The integral form of Poisson's equation (6.3.4) is:

$$\Phi_g(\mathbf{r}) = -G \int \frac{\rho(\mathbf{r}')}{|\mathbf{r}-\mathbf{r}'|}\, \mathrm{d}\mathbf{r}'. \tag{6.3.26}$$

Finally, the integral form for (6.3.21) uses the same Green's function as for Poisson's equation; the result is

$$A_\phi(\mathbf{r})\sin\phi = \frac{1}{4\pi}\int \frac{\frac{\alpha(\varpi' A'_\phi)}{\varpi'}\int_0^{\varpi' A'_\phi}\alpha(u)\, du + \kappa\rho\varpi'}{|\mathbf{r}-\mathbf{r}'|}\sin\phi'\, \mathrm{d}\mathbf{r}'. \tag{6.3.27}$$

With the three equations (6.3.24), (6.3.26) and (6.3.27) it is possible to calculate stationary configurations of magnetised rotating stars (together with various specified functions like $\alpha(u)$ and $\kappa(u)$).

### 6.3.5 Spherical harmonic expansions of the two potential integrals

At this point we switch from cylindrical $(\varpi, \phi_c, z)$ to the spherical $(r, \mu, \phi_s)$ polar coordinates used in the code. The conversions are:

$$\varpi = r\sqrt{1-\mu^2} \tag{6.3.28}$$

$$z = r\mu \tag{6.3.29}$$

$$\phi_c = \phi_s. \tag{6.3.30}$$

The subscripts $c$ and $s$ on $\phi$ are used here for identification, but dropped everywhere else.

We need to rewrite Poisson's equation (6.3.26) as a sum for numerical integration. For this, we expand $\frac{1}{|\mathbf{r}-\mathbf{r}'|}$ in terms of spherical harmonics:

$$\frac{1}{|\mathbf{r}-\mathbf{r}'|} = 4\pi\sum_{l=0}^{\infty}\sum_{m=-l}^{l}\frac{1}{2l+1}\frac{r_<^l}{r_>^{l+1}}Y_l^m(\mu,\phi)Y_l^{m*}(\mu',\phi') \tag{6.3.31}$$

$$= \sum_{l=0}^{\infty}\sum_{m=-l}^{l}\frac{r_<^l}{r_>^{l+1}}\frac{(l-m)!}{(l+m)!}P_l^m(\mu)P_l^m(\mu')e^{im(\phi-\phi')} \tag{6.3.32}$$

where $\mu = \cos\theta$. Now, the density $\rho$ is reflection symmetric and hence an even function of $\mu$, whilst the polynomials $P_l(\mu)$ are even in $\mu$ when $l$ is even and odd when $l$ is odd. So for odd $l$ the integrand of $\Phi_g$ is odd and thus vanishes under integration, leaving only the even-$l$ terms:

$$\Phi_g = -2G\int_0^\infty\int_0^1\int_0^{2\pi}\left[\sum_{l=0}^{\infty}\sum_{m=-l}^{l} f_{2l}(r',r)\frac{(2(l-m))!}{(2(l+m))!}P_{2l}^{2m}P_{2l}^{2m\prime}e^{2im(\phi-\phi')}\right] \rho(r',\mu')\, \mathrm{d}\phi'\mathrm{d}\mu'\mathrm{d}r'. \tag{6.3.33}$$

The radial function $f_{2l}$ is defined as

$$f_{2l}(r',r) = \frac{r_<^{2l}}{r_>^{2l+1}} r'^2 = \begin{cases} \frac{r'^{2l+2}}{r^{2l+1}} & \text{if } r' < r \\ \frac{r^{2l}}{r'^{2l-1}} & \text{if } r' > r. \end{cases} \tag{6.3.34}$$

We now split the sum over $m$ up into an $m = 0$ piece and an $m \neq 0$ sum. Each term in the $m \neq 0$ sum will, after integration, contain a term of the form

$$\int_0^{2\pi} e^{im(\phi-\phi')} \, \mathrm{d}\phi' = 0 \tag{6.3.35}$$

since the exponential term contains the only $\phi'$ dependence in the sum. It follows that all terms except the one with $m = 0$ vanish under integration. Given this, (6.3.33) reduces to

$$\Phi_g = -4\pi G \int_0^\infty \mathrm{d}r' \int_0^1 \mathrm{d}\mu' \; \rho(r',\mu') \sum_{l=0}^{\infty} f_{2l}(r',r) P_{2l}(\mu) P_{2l}(\mu'). \tag{6.3.36}$$

In a similar way, we can rewrite the equation for the magnetic potential (6.3.27). We use the decomposition (6.3.32) as before, which for $A_\phi \sin\phi$ is:

$$A_\phi \sin\phi = \frac{1}{4\pi} \int \left[ \sum_{l=0}^{\infty} \sum_{m=-l}^{l} \frac{(l-m)!}{(l+m)!} f_l(r',r) P_l^m(\mu) P_l^m(\mu') e^{im(\phi-\phi')} \right] \mathcal{M}(r',\mu') \sin\phi' \; \mathrm{d}\mathbf{r}' \tag{6.3.37}$$

where we have defined

$$\mathcal{M}(r',\mu') = \frac{\alpha(\varpi' A'_\phi)}{\varpi'} \int_0^{\varpi' A'_\phi} \alpha(u) \; \mathrm{d}u + \kappa\rho\varpi' \tag{6.3.38}$$

and

$$f_l(r',r) = \frac{r_<^l r'^2}{r_>^{l+1}} = \begin{cases} \frac{r'^{l+2}}{r^{l+1}} & \text{if } r' < r \\ \frac{r^l}{r'^{l-1}} & \text{if } r' > r. \end{cases} \tag{6.3.39}$$

Writing the $\sin\phi'$ term in its exponential form we may absorb it into the other exponential term in the sum:

$$\sin\phi' e^{im(\phi-\phi')} = \frac{e^{im\phi}}{2i} (e^{i\phi'(1-m)} - e^{-i\phi'(1+m)}). \tag{6.3.40}$$

On integrating the above expression with respect to $\phi'$, all terms vanish except when $m = \pm 1$. Hence (6.3.37) reduces to

$$A_\phi \sin\phi = \int_0^\infty \int_{-1}^1 \left[ \sum_{l=0}^\infty \frac{f_l(r,r')}{4i} \left( \frac{(l-1)!}{(l+1)!} P_l^1 P_l^{1\prime} e^{i\phi} - \frac{(l+1)!}{(l-1)!} P_l^{-1} P_l^{-1\prime} e^{-i\phi} \right) \right] \mathcal{M}(r',\mu')\, \mathrm{d}\mu' \mathrm{d}r'$$

$$= \int_0^\infty \mathrm{d}r' \int_0^1 \mathrm{d}\mu'\, \mathcal{M}(r',\mu') \sum_{l=0}^\infty \frac{f_l(r,r')}{l(l+1)} P_l^1 P_l^{1\prime} \sin\phi \qquad (6.3.41)$$

where we have integrated over $\phi'$ and used the following relation for associated Legendre functions:

$$P_l^{-m} = (-1)^m \frac{(l-m)!}{(l+m)!} P_l^m. \qquad (6.3.42)$$

Now cancelling the $\sin\phi$ terms on the LHS and RHS of equation (6.3.41), we have a relation for $A_\phi$ alone which can be numerically integrated:

$$A_\phi(\mathbf{r}) = \int_0^\infty \mathrm{d}r' \int_0^1 \mathrm{d}\mu'\, \mathcal{M}(r',\mu') \sum_{l=0}^\infty \frac{f_l(r,r')}{l(l+1)} P_l^1(\mu) P_l^1(\mu'). \qquad (6.3.43)$$

Finally, the quantity $\mathcal{M}$ is an even function of $\mu$, so as for the gravitational potential we will lose all odd terms after integration. For the gravitational potential that meant keeping the $P_{2l}$ terms; for the magnetic potential it means keeping the $P_l^1$ terms with *odd* $l$, as it is these functions which are even in $\mu$; $P_{2l}^1$ is odd in $\mu$. This leaves us with the following expression for $A_\phi$:

$$A_\phi(\mathbf{r}) = \int_0^\infty \mathrm{d}r' \int_0^1 \mathrm{d}\mu'\, \mathcal{M}(r',\mu') \sum_{l=0}^\infty \frac{f_{2l-1}(r,r')}{2l(2l-1)} P_{2l-1}^1(\mu) P_{2l-1}^1(\mu'). \qquad (6.3.44)$$

### 6.3.6 Numerical integration

In the previous subsection we derived expressions for the two potential integrals (6.3.26) and (6.3.27) in terms of Legendre functions:

$$\Phi_g(\mathbf{r}) = -4\pi G \int_0^\infty \mathrm{d}r' \int_0^1 \mathrm{d}\mu'\, \rho(r',\mu') \sum_{l=0}^\infty f_{2l}(r',r) P_{2l}(\mu) P_{2l}(\mu') \qquad (6.3.45)$$

$$A_\phi(\mathbf{r}) = \int_0^\infty \mathrm{d}r' \int_0^1 \mathrm{d}\mu'\, \mathcal{M}(r',\mu') \sum_{l=1}^\infty \frac{f_{2l-1}(r,r')}{2l(2l-1)} P_{2l-1}^1(\mu) P_{2l-1}^1(\mu'). \qquad (6.3.46)$$

Note that these expansions are exactly equal to the original integrals. We now use Simpson's three-point formula to approximate these as sums; the resulting expressions will be accurate up to some factor dependent on the step size $h$ and the fourth

derivative of the integrand:

$$\int_{x_1}^{x_3} f(x)\ \mathrm{d}x = \frac{h}{3}\left[f(x_1) + 4f(x_2) + f(x_3)\right] + \mathcal{O}(h^5 f^{(4)}). \tag{6.3.47}$$

In the code we will integrate on a $\mu$ vs. $r$ grid with $k_{div}$ points in the $\mu$-direction and $l_{div}$ points in the $r$-direction, with grid points in the ranges $0 \leq \mu \leq 1$ and $0 \leq r \leq r_{max}$. Hence

$$r_j = r_{max}\ \frac{j-1}{l_{div}-1} \tag{6.3.48}$$

and

$$\mu_i = \frac{i-1}{k_{div}-1}. \tag{6.3.49}$$

For the rest of this section we label the unprimed quantity $r$ with the index $j$, whilst $k$ labels $r'$ and $l$ labels $P_l'$.

We now integrate the $\mu'$-dependent quantities of an arbitrary element in the sum (6.3.45) over $\mu'$ using Simpson's rule:

$$\begin{aligned} V_{k,l} &= \int_0^1 \rho(r',\mu')P_{2l}(\mu')\ d\mu' \\ &= \sum_{i=1,i\ odd}^{k_{div}-2} \frac{1}{3(k_{div}-1)}\left[P_{2l}(\mu_i)\rho_{i,k} + 4P_{2l}(\mu_{i+1})\rho_{i+1,k} + P_{2l}(\mu_{i+2})\rho_{i+2,k}\right]. \end{aligned} \tag{6.3.50}$$

Note that the sum is over odd $i$ up to $k_{div}-2$ (typically we set $k_{div} = 257$ in the code; in any case it must be an odd number) since

$$\int_1^{k_{div}} = \int_1^3 + \int_3^5 + ... + \int_{k_{div}-2}^{k_{div}}. \tag{6.3.51}$$

Next we integrate over $r'$ to find the quantity

$$\begin{aligned} \mathfrak{V}_{l,j} &= \int_0^{r_{max}} \int_0^1 \rho(r',\mu')P_{2l}(\mu')f_{2l}(r',r_j)\ \mathrm{d}\mu'\mathrm{d}r' \\ &= \int_0^{r_{max}} V_{k,l} f_{2l}(r',r_j)\ \mathrm{d}r' \\ &= \sum_{k=1,k\ odd}^{l_{div}-2} \frac{r_{max}}{3(l_{div}-1)}[f_{2l}(r_k,r_j)V_{k,l} + 4f_{2l}(r_{k+1},r_j)V_{k+1,l} \\ &\qquad + f_{2l}(r_{k+2},r_j)V_{k+2,l}]. \end{aligned} \tag{6.3.52}$$

Finally, we see that the gravitational potential at the grid point $(\mu_i, r_j)$ is given by

$$(\Phi_g)_{i,j} = -4\pi G \sum_{l=0}^{\infty} \mathfrak{V}_{l,j} P_{2l}(\mu_i). \tag{6.3.53}$$

The derivation for the magnetic potential is very similar, with the quantity $\mathcal{M}(r',\mu') = \frac{\alpha(\varpi' A'_\phi)}{\varpi'} \int_0^{\varpi' A'_\phi} \alpha(u)\ \mathrm{d}u + \kappa\rho\varpi'$ replacing the $\rho(r',\mu')$ in the working above. Given this, we may use (6.3.46) to write down

$$(A_\phi)_{i,j} = \sum_{l=1}^{\infty} \frac{1}{2l(2l-1)} \mathfrak{W}_{l,j} P^1_{2l-1}(\mu_i) \tag{6.3.54}$$

where, in analogy with the previous derivation, $\mathfrak{W}_{l,j}$ is related to the quantity $W_{k,l}$ which in turn is related to $\mathcal{M}$:

$$\begin{aligned} \mathfrak{W}_{l,j} &= \sum_{k=1,k\ odd}^{l_{div}-2} \frac{r_{max}}{3(l_{div}-1)} [f_{2l-1}(r_k,r_j)W_{k,l} + 4f_{2l-1}(r_{k+1},r_j)W_{k+1,l} \\ &\qquad + f_{2l-1}(r_{k+2},r_j)W_{k+2,l}] \end{aligned} \tag{6.3.55}$$

$$\begin{aligned} W_{k,l} &= \sum_{i=1,i\ odd}^{k_{div}-2} \frac{1}{3(k_{div}-1)} [P^1_{2l-1}(\mu_i)\mathcal{M}_{i,k} + 4P^1_{2l-1}(\mu_{i+1})\mathcal{M}_{i+1,k} \\ &\qquad + P^1_{2l-1}(\mu_{i+2})\mathcal{M}_{i+2,k}]. \end{aligned} \tag{6.3.56}$$

In practice one cannot perform the infinite $l$-sums shown in equations (6.3.53) and (6.3.54), so we terminate them at some finite $l_{max}$. We choose $l_{max} = 16$ for the code; we find that terms of higher $l$ than this produce a negligible contribution to the sum.

## 6.4 Details of the code

### 6.4.1 Non-dimensionalising

For the purposes of numerics it is convenient to work with dimensionless variables of order unity. We nondimensionalise all variables using $G$, the maximum density $\rho_{max}$ and the equatorial radius $r_{eq}$. The variables used in the code are then:

$$\hat{\rho} = \frac{\rho}{\rho_{max}}, \tag{6.4.1}$$

$$\hat{\varpi} = \frac{\varpi}{r_{eq}}, \tag{6.4.2}$$

$$\hat{\Omega}^2 = \frac{\Omega^2}{G\rho_{max}}, \tag{6.4.3}$$

$$\hat{\kappa} = \frac{\kappa}{\sqrt{G}/r_{eq}}, \tag{6.4.4}$$

$$\hat{\alpha} = \frac{\alpha}{1/r_{eq}}, \tag{6.4.5}$$

$$\hat{A}_\phi = \frac{A_\phi}{r_{eq}^2 \rho_{max} \sqrt{G}}. \tag{6.4.6}$$

All the magnetic rescalings above may be found by starting from the units of the Lorentz force, plus $\nabla \times \mathbf{B} = 4\pi\mathbf{j}$, $\nabla \times \mathbf{A} = \mathbf{B}$ and equation (6.2.38).

### 6.4.2 Enthalpy

Since the enthalpy is given by $H = (1+N)P/\rho$, we may use this formula together with (6.3.7) to give a relation between density and enthalpy:

$$\rho = \left( \frac{H}{k(1+N)} \right)^N. \tag{6.4.7}$$

### 6.4.3 Enthalpy boundary condition

Recall that the first integral of the Euler equation is

$$H = C - \Phi_g + \frac{\Omega^2 \varpi^2}{2} + \frac{1}{4\pi} \int_0^{\varpi A_\phi} \kappa(u') \, \mathrm{d}u'. \tag{6.4.8}$$

The boundary condition on the enthalpy $H$ is that it must vanish at the surface. We call the equatorial radius $r_{eq}$ and the polar radius $r_p$, and rescale the radial coordinate by dividing by $r_{eq}$. Evaluating the boundary condition on the enthalpy at the equator and at the poles gives

$$H(r_{eq}) = 0 = C - \Phi(r_{eq}) + \frac{\Omega_0^2 r_{eq}^2}{2} + \frac{\kappa_0 r_{eq} A_\phi(r_{eq})}{4\pi} \tag{6.4.9}$$

$$H(r_p) = 0 = C - \Phi(r_p). \tag{6.4.10}$$

Rearranging these in rescaled variables where $r_{eq} = 1$ we see that

$$\Omega_0^2 = 2 \left( \Phi(r_{eq}) - \Phi(r_p) - \frac{\kappa_0 A_\phi(r_{eq})}{4\pi} \right) \tag{6.4.11}$$

and

$$C = \Phi(r_{eq}) - \frac{\Omega_0^2}{2} - \frac{\kappa_0 A_\phi(r_{eq})}{4\pi}. \tag{6.4.12}$$

### 6.4.4 Numerical scheme

Our code uses the Hachisu self-consistent field (HSCF) method [61] to iteratively find a stationary solution to the hydromagnetic equilibrium equation (6.3.1). Specifically, the user specifies a polytropic index $N$, magnetic functions $\alpha(u)$ and $\kappa(u)$ and a deformation (i.e. axis ratio) $r_p/r_{eq}$ and the code determines the angular velocity, density distribution and other quantities consistent with the user's input parameters. The code we use is based on a code for rotating stars written by Nikolaos Stergioulas, extended here to include magnetic fields.

The original HSCF method was a numerical scheme for calculating the stationary equilibrium configurations of an unmagnetised rotating star. We now generalise it to include axisymmetric magnetic fields; the steps in this modified scheme are:

1. Make an initial guess of $\rho$=const
2. Find $\Phi_g$ from Poisson's equation (6.3.53)
3. Guess $A_\phi$=const
4. Find an improved, space-dependent form of $A_\phi(\mathbf{r})$ from equation (6.3.54) and the guesses for $\rho$ and $A_\phi$ (this is the iterative step for $A_\phi$)
5. Find $\Omega_0^2$ and $C$ from (6.4.11) and (6.4.12), using the potentials $\Phi_g$ and $A_\phi$ found earlier and given a user-specified axis ratio $r_p/r_{eq}$
6. We now know all right-hand side terms in (6.3.24); use the equation to determine the enthalpy at all points in the star
7. Find the new (improved) estimate for the density distribution using $\rho_{new}(r,\mu) = \left(\frac{H(r,\mu)}{H_{max}}\right)^N$ where $N$ is the polytropic index and $H_{max}$ the maximum value of enthalpy attained in the star[1]
8. As the iterative step, return to step 1 but use $\rho = \rho_{new}$ instead of the earlier density distribution ($\rho$=const for the first cycle). At step 3 in the new cycle, use the 'new' form of $A_\phi$ calculated in step 4 of the previous cycle.

This sequence of steps is repeated until the code has converged satisfactorily, i.e.

[1]The expression here comes from (6.4.7)

until all the quantities

$$|(H_{max})_{n+1} - (H_{max})_n|, \tag{6.4.13}$$

$$|(\Omega_0^2)_{n+1} - (\Omega_0^2)_n|, \tag{6.4.14}$$

$$|C_{n+1} - C_n| \tag{6.4.15}$$

are less than some small value $\delta$. The subscript $n$ here represents the value of a quantity at the $n$-th iterative step.

## 6.5 Formulation for a purely toroidal field

The Grad-Shafranov equation (or equivalently equation 6.2.38 for the current) allows for purely poloidal fields and mixed toroidal-poloidal fields. For a purely toroidal field a different formalism is needed; this was derived in section 6.2.4. Recall that one may define a scalar potential $M$ through

$$\nabla M = \frac{\mathbf{j} \times \mathbf{B}}{\rho}. \tag{6.5.1}$$

For a purely toroidal field we have $\mathbf{B} = B_\phi \mathbf{e}_\phi$. In section 3 we found that

$$B_\phi = \frac{1}{\varpi} h(\gamma) \tag{6.5.2}$$

$$M = -\frac{1}{4\pi} \int_0^{\rho\varpi^2} \frac{h}{\gamma} \frac{\mathrm{d}h}{\mathrm{d}\gamma} \, \mathrm{d}\gamma \tag{6.5.3}$$

where $h$ is an arbitrary function of $\gamma = \rho\varpi^2$. For simplicity we choose $h(\rho\varpi^2) = \lambda\rho\varpi^2$ where $\lambda$ is a constant specified by the user of the code. With this choice of $h$ we then have

$$M = -\int_0^{\rho\varpi^2} \frac{h(\gamma)}{\gamma} \frac{\mathrm{d}h}{\mathrm{d}\gamma} \, \mathrm{d}\gamma = -\int_0^{\rho\varpi^2} \frac{\lambda\gamma}{\gamma} \lambda \, \mathrm{d}\gamma = -\lambda^2 \rho\varpi^2. \tag{6.5.4}$$

The first integral of the Euler equation becomes:

$$H = C - \Phi + \tfrac{1}{2}\Omega^2\varpi^2 + M \tag{6.5.5}$$

$$= C - \Phi + \tfrac{1}{2}\Omega^2\varpi^2 - \lambda^2\rho\varpi^2. \tag{6.5.6}$$

Also for this choice of $h$ we have $B_\phi = \lambda\rho\varpi$. Note that since $\rho$ is zero at the surface, the equations which give $\Omega^2$ and $C$ in terms of the axis ratio do not feature any

magnetic term and are just those for a rotating unmagnetised fluid:

$$\Omega_0^2 = 2\left(\Phi(r_{eq}) - \Phi(r_p)\right) \tag{6.5.7}$$

$$C = \Phi(r_{eq}) - \frac{\Omega_0^2}{2} \tag{6.5.8}$$

i.e. (6.4.11) and (6.4.12) with $\kappa = 0$. The numerical scheme is simpler than that for the mixed case as the magnetic term only enters in the Euler equation (6.5.6). The steps of the code are:

1. Make an initial guess of $\rho$=const
2. Find $\Phi_g$ from Poisson's equation (6.3.53)
3. Find $\Omega_0^2$ and $C$ from (6.4.11) and (6.4.12), using the gravitational potential $\Phi_g$ and given a user-specified axis ratio $r_p/r_{eq}$,
4. Evaluate the magnetic term $M$ using the density distribution $\rho$ and given a user-specified Lorentz force strength parameter $\lambda$,
5. We now know all right-hand side terms in (6.3.24); use the equation to determine the enthalpy at all points in the star
6. Find the new (improved) estimate for the density distribution using $\rho_{new}(r,\mu) = \left(\frac{H(r,\mu)}{H_{max}}\right)^N$ where $N$ is the polytropic index and $H_{max}$ the maximum value of enthalpy attained in the star
7. As the iterative step, return to step 1 but use $\rho = \rho_{new}$ instead of the earlier density distribution ($\rho$=const for the first cycle).

As before this sequence is iterated until the code has achieved satisfactory convergence; the quantities

$$|(H_{max})_{n+1} - (H_{max})_n|, \tag{6.5.9}$$

$$|(\Omega_0^2)_{n+1} - (\Omega_0^2)_n|, \tag{6.5.10}$$

$$|C_{n+1} - C_n| \tag{6.5.11}$$

should all be less than some small value $\delta$. The subscript $n$ here represents the value of a quantity at the $n$-th iterative step.

## 6.6 Code-calculated quantities

### 6.6.1 The magnetic energy

We will wish to calculate the magnetic energy $\mathcal{E}_{mag}$ of the star in the code, to compare with kinetic energy and also to calculate a virial test (see next section). The familiar definition of $\mathcal{E}_{mag}$ is

$$\mathcal{E}_{mag} = \int_{\text{all space}} \frac{B^2}{8\pi} \ \mathrm{d}\mathbf{r}, \tag{6.6.1}$$

but this is not suited to numerical evaluation, since the integrand only decays at infinite distance; numerical integration would necessarily be over a finite radius and so introduce truncation error. However some vector identities show that an equivalent definition for $\mathcal{E}_{mag}$, more useful here, is

$$\mathcal{E}_{mag} = \int_{\text{all space}} \mathbf{r} \cdot \boldsymbol{\mathcal{L}} \ \mathrm{d}\mathbf{r} \tag{6.6.2}$$

— see section 4.2 for details. Now since $\boldsymbol{\mathcal{L}} = \mathbf{j} \times \mathbf{B}$, where the current $\mathbf{j}$ is zero outside the star (see equation (6.2.38)), it is clear that $\boldsymbol{\mathcal{L}}$ is also zero outside the star. The integrand in (6.6.2) will therefore also vanish outside the star, so the integration need only be performed within the star. We wish to express $\mathcal{E}_{mag}$ in terms of the quantity $A_\phi$ which the code calculates. Firstly, since $\mathbf{B} = \nabla \times \mathbf{A}$ we have:

$$B_\varpi = -A_{\phi,z} \tag{6.6.3}$$

$$B_\phi = A_{\varpi,z} - A_{z,\varpi} \tag{6.6.4}$$

$$B_z = A_{\phi,\varpi} + \frac{1}{\varpi} A_\phi \tag{6.6.5}$$

and hence the Lorentz force is:

$$\boldsymbol{\mathcal{L}} = \mathbf{j} \times \mathbf{B} = \frac{1}{4\pi} \varpi \rho \kappa \mathbf{e}_\phi \times \mathbf{B} \tag{6.6.6}$$

$$= \frac{1}{4\pi} \varpi \rho \kappa \begin{pmatrix} A_{\phi,\varpi} + \frac{1}{\varpi} A_\phi \\ 0 \\ A_{\phi,z} \end{pmatrix}. \tag{6.6.7}$$

The integrand is then given by

$$\mathbf{r} \cdot \boldsymbol{\mathcal{L}} = \frac{1}{4\pi} \varpi \rho \kappa (\varpi A_{\phi,\varpi} + A_\phi + z A_{\phi,z}). \tag{6.6.8}$$

The code uses a spherical polar grid based on $r$ and $\mu = \cos\theta$, whereas the above expression is in terms of cylindrical polars; we therefore wish to rewrite it.

We recall from earlier the coordinate transformations from cylindrical to spherical polars:

$$\varpi = r\sqrt{1-\mu^2} \tag{6.6.9}$$

$$z = r\mu \tag{6.6.10}$$

(one may see this by writing the cylindrical coordinates as Cartesians as an intermediate step: $\varpi = x_{Cart}$ and $z = z_{Cart}$). Now using the chain rule we have:

$$\frac{\partial}{\partial r} = \frac{\partial \varpi}{\partial r}\frac{\partial}{\partial \varpi} + \frac{\partial z}{\partial r}\frac{\partial}{\partial z} = \sqrt{1-\mu^2}\frac{\partial}{\partial \varpi} + \mu\frac{\partial}{\partial z} \tag{6.6.11}$$

$$\frac{\partial}{\partial \mu} = \frac{\partial \varpi}{\partial \mu}\frac{\partial}{\partial \varpi} + \frac{\partial z}{\partial \mu}\frac{\partial}{\partial z} = -\frac{\mu r}{\sqrt{1-\mu^2}}\frac{\partial}{\partial \varpi} + r\frac{\partial}{\partial z}. \tag{6.6.12}$$

Rearranging these we see that

$$\frac{\partial}{\partial \varpi} = \sqrt{1-\mu^2}\frac{\partial}{\partial r} - \frac{\mu\sqrt{1-\mu^2}}{r}\frac{\partial}{\partial \mu} \tag{6.6.13}$$

$$\frac{\partial}{\partial z} = \mu\frac{\partial}{\partial r} + \frac{(1-\mu^2)}{r}\frac{\partial}{\partial \mu}. \tag{6.6.14}$$

We now know the transformations for the coordinates and the derivatives; after some algebra we find that the integrand (6.6.8) may be reexpressed in terms of spherical polars as:

$$\frac{1}{4\pi}\rho\kappa r\sqrt{1-\mu^2}(rA_{\phi,r} + A_\phi). \tag{6.6.15}$$

At last we are able to write the magnetic energy as a spherical polar integral in terms of $A_\phi$:

$$\mathcal{E}_{mag} = \int_0^{2\pi}\int_1^{-1}\int_0^{\infty} \frac{1}{4\pi}\rho\kappa r\sqrt{1-\mu^2}(rA_{\phi,r} + A_\phi)\; r^2 \;\mathrm{d}r\mathrm{d}\mu\mathrm{d}\phi \tag{6.6.16}$$

$$= \int_0^1\int_0^R \rho\kappa r^3\sqrt{1-\mu^2}(rA_{\phi,r} + A_\phi)\;\mathrm{d}r\mathrm{d}\mu, \tag{6.6.17}$$

using the symmetry of the $\mu$-integral, integrating over $\phi$ and noting that the integrand is zero outside the surface radius $R$ of the star (by virtue of the $\rho$ term in the integrand).

### 6.6.2 Virial test

We may use the virial theorem as a test of convergence for the code. First take the trace of the tensor virial equations (4.2.26) (further details are found in section 4.2) to yield the scalar virial theorem:

$$\frac{1}{2}\frac{\mathrm{d}^2 I}{\mathrm{d}t^2} = 2T + \mathcal{E}_{mag} + 3(\gamma - 1)U + W \tag{6.6.18}$$

where $I$ is the moment of inertia and $T, \mathcal{E}_{mag}, U$ and $W$ the kinetic, magnetic, internal and gravitational energies, respectively. For our stationary star $I$ has no time variation so the first term is zero, whilst the internal energy term may be rewritten using $\Pi \equiv \int p \; d\mathbf{r} = (\gamma - 1)U$. Given this, we expect the various energies for our star to satisfy

$$2T + \mathcal{E}_{mag} + 3\Pi + W = 0. \tag{6.6.19}$$

Calculating the quantity on the left-hand side of the above equation tells us the absolute deviation from zero, but we need to know the relative error. A value of $2T + \mathcal{E}_{mag} + 3\Pi + W = 10^{-5}$ would appear to indicate acceptable accuracy, but if the individual energies are of order $10^{-4}$ then the relative error is unacceptable: around 10%. For this reason we normalise by dividing through by $W$ and define our virial test result $VC$ as

$$VC \equiv \frac{|2T + \mathcal{E}_{mag} + 3\Pi + W|}{|W|}; \tag{6.6.20}$$

the smaller the value of $VC$, the greater the code's accuracy. In particular, in the limit $VC \to 0$ the calculated configuration is an exact stationary equilibrium solution.

### 6.6.3 Toroidal and poloidal energies for the mixed case

The code variables $\kappa$ and $\alpha$ are related to the ratio of toroidal to poloidal field strength, but in a very nontrivial manner. To get a more intuitive, physical, measure of their respective strengths we would like to know the part of the magnetic energy contained in the poloidal and toroidal fields, $\mathcal{E}_{pol}$ and $\mathcal{E}_{tor}$, respectively.

Since the total magnetic energy is given by

$$\mathcal{E}_{mag} = \frac{1}{8\pi}\int \mathbf{B}\cdot\mathbf{B}\; \mathrm{d}V = \frac{1}{8\pi}\int B_\varpi^2 + B_\phi^2 + B_z^2 \; \mathrm{d}V \tag{6.6.21}$$

we define

$$\mathcal{E}_{pol} = \frac{1}{8\pi}\int B_\varpi^2 + B_z^2 \,\mathrm{d}V \tag{6.6.22}$$

$$\mathcal{E}_{tor} = \frac{1}{8\pi}\int B_\phi^2 \,\mathrm{d}V. \tag{6.6.23}$$

As in other places, the integrands have no $\phi$-dependence so the integration over $\phi$ may be done immediately to give $2\pi$, whilst converting from $\theta$ to $\mu$ and using reflection symmetry changes the angular integral from $\int_0^\pi ... \sin\theta \,\mathrm{d}\theta$ to $2\int_0^1 ...\mathrm{d}\mu$. Hence our magnetic energy integrals become

$$\mathcal{E}_{pol} = \frac{1}{2}\int_0^1\int_0^\infty B_\varpi^2 + B_z^2 \,\mathrm{d}r\mathrm{d}\mu \tag{6.6.24}$$

$$\mathcal{E}_{tor} = \frac{1}{2}\int_0^1\int_0^\infty B_\phi^2 \,\mathrm{d}r\mathrm{d}\mu. \tag{6.6.25}$$

We recall the conversions between $(\varpi, z, \partial_\varpi, \partial_z)$ and $(r, \mu, \partial_r, \partial_\mu)$ from before; with these we can rewrite the cylindrical-polar components of $\mathbf{B}$ in terms of spherical polars:

$$B_\varpi = -A_{\phi,z} = -\mu A_{\phi,r} - \frac{(1-\mu^2)}{r}A_{\phi,\mu} \tag{6.6.26}$$

$$B_z = \frac{A_\phi}{\varpi} + A_{\phi,\varpi} = \frac{A_\phi}{r\sqrt{1-\mu^2}} + \sqrt{1-\mu^2}A_{\phi,r} - \frac{\mu\sqrt{1-\mu^2}}{r}A_{\phi,\mu} \tag{6.6.27}$$

$$B_\phi = \frac{1}{r\sqrt{1-\mu^2}}\int^{r\sqrt{1-\mu^2}A_\phi} \alpha(u)\,\mathrm{d}u. \tag{6.6.28}$$

We recall here that whilst the upper limit for the integral of $\alpha$ is fixed, the lower limit is not; we choose it so that there is no constant after integration and hence no jump in $B_\phi$.

The integral for $\mathcal{E}_{tor}$ may now be straightforwardly evaluated, since its integrand $B_\phi$ is confined to the star; however the integral for $\mathcal{E}_{pol}$ does not have compact support. We can get around this by using the fact that $\mathcal{E}_{mag} = \mathcal{E}_{pol} + \mathcal{E}_{tor}$ and so define $\mathcal{E}_{pol}$ in terms of the other two integrals $\mathcal{E}_{pol} \equiv \mathcal{E}_{mag} - \mathcal{E}_{tor}$; in this manner we can evaluate the poloidal energy through quantities which extend only over the star. For a consistency check on our work, we compare this compact-support expression for $\mathcal{E}_{pol}$ with the standard infinite-integral form by plotting the quantity

$$\mathfrak{P} \equiv \frac{\frac{1}{2}\int_0^1\int_0^R (B_\varpi^2 + B_z^2)\; dr d\mu}{\mathcal{E}_{mag} - \mathcal{E}_{tor}} \tag{6.6.29}$$

for increasing integration radius $R$; see figure 6.1 below. We see from the figure that $\mathfrak{P} \to 1$ as $R \to \infty$, confirming that $\mathcal{E}_{mag} - \mathcal{E}_{tor}$ does indeed give the poloidal-field energy.

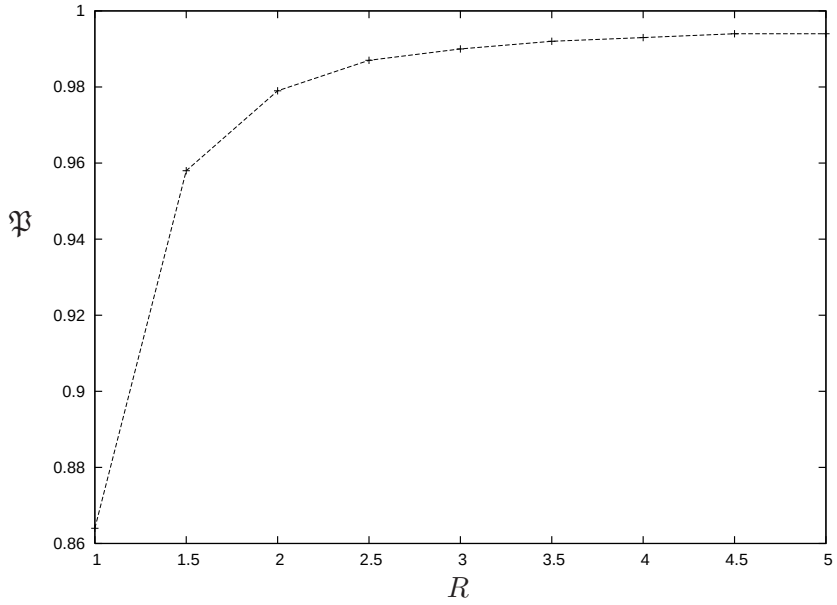


Figure 6.1: Confirming the veracity of our compact-support definition for $\mathcal{E}_{pol}$. The values on the plot are for a star of axis ratio $r_p = 0.5$ and $\kappa = 17$, purely poloidal field. The convergence also occurs if a toroidal field is included.

### 6.6.4 Keplerian velocity

The Keplerian (or break-up) velocity $\Omega_K$ is defined to be the velocity at which the centrifugal force matches the gravitational force. If a star's velocity exceeds $\Omega_K$, then it will begin to shed mass. The criterion for mass shedding is therefore $\Omega = \Omega_K$. With a view to determining $\Omega_K$, we first define a different velocity $\Omega_c$ through the relation

$$\Omega_c^2 \equiv \frac{1}{r_{eq}} \frac{\partial \Phi}{\partial r}, \tag{6.6.30}$$

which in dimensionless form is simply

$$\hat{\Omega}_c^2 \equiv \hat{\Phi}_{,r}. \tag{6.6.31}$$

We are able to find this quantity by differentiating the equilibrium equation (6.3.24) in dimensionless form:

$$\Phi_{,r} = -H_{,r} + \Omega^2 r(1-\mu^2) + \frac{\kappa}{4\pi}\sqrt{1-\mu^2}(A_\phi + rA_{\phi,r}). \tag{6.6.32}$$

We evaluate this at the equator (i.e. $\mu = 0$), where the centrifugal force is greatest and hence where mass shedding will occur first. This gives

$$\Omega_c^2 = \Phi_{,r}|_{eq} = -H_{,r} + \Omega^2 + \frac{\kappa}{4\pi}(A_\phi + A_{\phi,r}). \tag{6.6.33}$$

In general $\Omega_c$ as defined above is *not* the Keplerian velocity — the two are only equal as the star reaches the mass-shedding limit. When this limit is reached $\Omega = \Omega_c = \Omega_K$, so $\Omega_c$ is a test of whether the star has reached its mass-shedding limit.

### 6.6.5 Ellipticity

Recall that the quadrupole moment tensor $I_{jk}$ is defined as

$$I_{jk} = \int \rho x_j x_k \, \mathrm{d}V. \tag{6.6.34}$$

Since our star is axisymmetric we have

$$I_{eq} \equiv I_{xx} = I_{yy} \tag{6.6.35}$$

$$I_{pol} \equiv I_{zz}. \tag{6.6.36}$$

Now

$$\begin{aligned} I_{eq} &= \int \rho x^2 \, \mathrm{d}V \\ &= \int \rho(r,\mu)\ r^2(1-\mu^2)\cos^2\phi\ r^2 \mathrm{d}r\mathrm{d}\mu\mathrm{d}\phi \\ &= 2\pi \int_0^1 \int_0^R \rho r^4(1-\mu^2)\ \mathrm{d}r\mathrm{d}\mu \qquad (6.6.37) \\ I_p &= \int \rho z^2 \, \mathrm{d}V \\ &= 4\pi \int_0^1 \int_0^R \rho r^4 \mu^2 \ \mathrm{d}r\mathrm{d}\mu \qquad (6.6.38) \end{aligned}$$

There are various ways of defining the ellipticity $\epsilon$, but one is to use these unreduced quadrupole moments:

$$\epsilon \equiv \frac{I_{eq} - I_p}{I_{eq}}. \tag{6.6.39}$$

## 6.7 Constructing physical sequences of stars

For numerical purposes, we work with dimensionless variables. However, to understand these results in the context of physical neutron stars we need to redimensionalise them. Making a meaningful study of a group of different equilibrium configurations entails ensuring that we always compare the effects of magnetic fields and rotation in the same physical star: we do this by ensuring that we work with sequences of constant (physical) mass and the same equation of state.

For the former requirement, we need to use the relation

$$\hat{M} = \frac{M}{\rho_{max} r_{eq}^3}. \tag{6.7.1}$$

Maintaining a constant mass, then, enforces the above relation between the maximum density $\rho_{max}$ and $r_{eq}$. Secondly, we need to ensure we compare stars with the same equation of state, i.e. the relation $P = k\rho^{1+1/N}$: this means always using the same polytropic index $N$ *and* polytropic constant $k$. The former is specified when the code is run and is not a dimensional quantity; for the latter we need to redimensionalise. Using dimensional analysis as before, we find that the nondimensional code $\hat{k}$ is related to the physical $k$ by

$$\hat{k} = \frac{k}{G r_{eq}^2 \rho_{max}^{1-1/N}}. \tag{6.7.2}$$

Now our nondimensional polytropic relation is $\hat{P} = \hat{k}\hat{\rho}^{1+1/N}$, but since the maximum density is normalised to unity in the code, we have simply

$$\hat{k} = \hat{P}_{max}, \tag{6.7.3}$$

the maximum (code) pressure in the star. From the two equations (6.7.1) and (6.7.2) (replacing $\hat{k}$ with $\hat{P}_{max}$) we are then able to fix the real mass and equation of state; this allows us to find the values of $\rho_{max}$ and $r_{eq}$. We use (6.7.1) to find that

$$r_{eq} = \sqrt[3]{\frac{M}{\rho_{max}\hat{M}}} \tag{6.7.4}$$

and use this to replace $r_{eq}$ in equation (6.7.2), giving

$$\hat{P}_{max} = \frac{k}{G\hat{M}^{-2/3} M^{2/3} \rho_{max}^{1/3-1/N}}. \tag{6.7.5}$$

We now fix our neutron star mass as $M = 1.4M_\odot = 2.8 \times 10^{33}$ g (we are working in cgs units) and our polytropic constant as $k = 4.25 \times 10^4$ cm$^5$g$^{-1}$s$^{-2}$; the latter coming from rearranging $r_{eq} = \sqrt{\pi k/2G}$ given an equatorial radius for the spherical 'background' star[2] of 10 km. See Chandrasekhar [22] for details of polytropic relations. This gives

$$\rho_{max} = \left(\frac{k}{G\hat{M}^{-2/3}M^{2/3}\hat{P}_{max}}\right)^{3N/(N-3)} \text{ g cm}^{-3} \tag{6.7.6}$$

$$= 5.48 \times 10^{15}\ \hat{M}^{-1}\hat{P}_{max}^{3/2} \text{ g cm}^{-3} \text{ for an } N{=}1 \text{ polytrope.} \tag{6.7.7}$$

Having found $\rho_{max}$ for each star we then find the corresponding equatorial radius $r_{eq}$ using the mass relation (6.7.4). For an $N = 1$ polytrope this is

$$r_{eq} = 7.98 \times 10^5\ \hat{P}_{max}^{-1/2}\ \text{ cm} = 7.98\ \hat{P}_{max}^{-1/2}\ \text{ km.} \tag{6.7.8}$$

For an axis ratio of unity we find that $\hat{P}_{max} = 0.637$; substituting this back into the equation above we recover the background radius of 10 km, as required. With these two quantities we are now able to redimensionalise any code quantities; in particular the physical values of magnetic field strengths and rotation rates which generate a specified axis ratio.

For a measure of the magnetic field strength in the star, we define a volume-averaged magnetic field $\bar{B}$ through

$$\bar{B}^2 = \frac{1}{V}\int B^2\ \mathrm{d}V = \frac{8\pi\mathcal{E}_{mag}}{V} \tag{6.7.9}$$

The relation between the physical $\bar{B}$ and the nondimensional code version $\hat{\bar{B}}$ is

$$\bar{B} = r_{eq}\rho_{max}\sqrt{G}\hat{\bar{B}} = 1.13 \times 10^{18}\ \hat{P}_m\hat{M}^{-1}\hat{\bar{B}} \text{ gauss} \tag{6.7.10}$$

$$= r_{eq}\rho_{max}\sqrt{G}\ \sqrt{\frac{8\pi\hat{\mathcal{E}}_{mag}}{\hat{V}}} = 5.66 \times 10^{18}\ \hat{P}_m\hat{M}^{-1}\hat{\mathcal{E}}_{mag}^{1/2}\hat{V}^{-1/2} \text{ gauss.} \tag{6.7.11}$$

The physical rotation rate is simpler to find, being given by

$$\Omega = \sqrt{G\rho_{max}}\hat{\Omega} \tag{6.7.12}$$

$$= 1.91 \times 10^4\ \hat{M}^{-1/2}\hat{P}_m^{3/4}\hat{\Omega} \text{ rad s}^{-1} \tag{6.7.13}$$

$$= 3.04 \times 10^3\ \hat{M}^{-1/2}\hat{P}_m^{3/4}\hat{\Omega} \text{ Hz.} \tag{6.7.14}$$

[2]Note that in the context of this chapter, 'background' refers to the hydrostatic equilibrium configuration, with no magnetic fields or rotation. This is completely distinct from the perturbation-theory connotations of 'background'.

The physical values quoted later in this chapter are calculated from the equations (6.7.9) and (6.7.12). The process of redimensionalising for other polytropic indices is very similar to the one described here.

## 6.8 Testing the code

### 6.8.1 Convergence plots

We begin by demonstrating that both the mixed-field code and the purely toroidal-field code converge satisfactorily; i.e. that the numerical error decreases as the grid resolution increases. As a test of this numerical error we evaluate the quantity $VC$ from (6.6.20):

$$VC = \frac{|2T + \mathcal{E}_{mag} + 3\Pi + W|}{|W|} \tag{6.8.1}$$

since this is zero for a physical stationary configuration, by the virial theorem. We find that both codes are second-order convergent as required; see figure 6.2.

### 6.8.2 Comparison with previous work

We are able to confirm the results produced by the code in various regimes. Firstly, we compare rotating unmagnetised configurations generated numerically with the analytic result for the fractional distortion (4.1.90) from chapter 4:

$$\mathfrak{d}(\mu) = \frac{\xi_R(\mu)}{R} = \left(1 - \frac{5}{2}P_2(\mu)\right) v. \tag{6.8.2}$$

Here $v$ is a nondimensional velocity, $v \equiv \Omega^2/2\pi\rho_c G$. We use a different definition of nondimensional velocity (called $\hat{\Omega}^2$) in the code of this chapter, but the two are related through:

$$v \equiv \frac{\Omega^2}{2\pi\rho_c G} = \frac{\hat{\Omega}^2}{2\pi}. \tag{6.8.3}$$

Note that the central and maximum densities are equal in this case: $\rho_c = \rho_{max}$. We may now work out the perturbative analytic result for the axis ratio of a slowly rotating $N = 1$ polytrope:

$$\frac{r_p}{r_{eq}} = \frac{1 + \mathfrak{d}(0)}{1 + \mathfrak{d}(1)} = \frac{1 - \frac{3}{4\pi}\hat{\Omega}^2}{1 + \frac{9}{8\pi}\hat{\Omega}^2}. \tag{6.8.4}$$

Table 6.1: Comparing numerically-generated rotating stars with results from analytic work.

| $\hat{\Omega}^2$ | $1-\frac{r_p}{r_{eq}}$ (code) | $1-\frac{r_p}{r_{eq}}$ (analytic) |
|---|---|---|
| 6.964e-3 | 4.17e-3 | 4.15e-3 |
| 1.393e-2 | 8.33e-3 | 8.27e-3 |
| 3.470e-2 | 2.08e-2 | 2.05e-2 |
| 8.254e-2 | 5.00e-2 | 4.78e-2 |
| 1.622e-1 | 1.00e-1 | 9.15e-2 |

The analytic result is only valid in the slow rotation, small distortion limit, so we compare the code and analytic results in this regime, for a few values of $\hat{\Omega}^2$; see table 6.1.

We are also able to make both qualitative and quantitative comparisons with work on magnetised stars. Qualitatively, it has long been predicted that poloidal magnetic fields generate oblate configurations, whilst toroidal fields induce prolate distortions. A simple analytic indication of this is given by the formula (4.3.28), derived from early work on magnetised stars in section 4.3. Given the opposing effects of poloidal and toroidal fields, one would expect a mixed-field magnetic distortion to depend on the relative strengths of the two field components. For our mixed-field code, however, we are only able to generate oblate stars; we believe this is due to the weak nature of toroidal fields within our mixed-field formalism, where the toroidal-field energy $\mathcal{E}_{tor}$ is always less than 7% of the total magnetic energy $\mathcal{E}_{mag}$.

As a quantitative confirmation of our results, we compare with table 4 from Tomimura and Eriguchi [137]. Their results are nondimensionalised by dividing by appropriate powers of $\rho_{max}$, $r_{eq}$ and $4\pi G$ and these dimensionless quantities are denoted by a hat; for example

$$\hat{\Omega}^2 = \frac{\Omega^2}{4\pi G \rho_{max}}. \tag{6.8.5}$$

For comparison with their results we must also use $\zeta = 1$ instead of $\zeta = 0.1$ as the exponent in the functional form of $\alpha$ from (6.3.9). Taking this into account we find that for a $N = 1.5$ polytrope, with $\hat{\kappa} = 0.4$ and $\hat{a} = 200$, we have the sequence of configurations given in table 6.2.

Table 6.2: Comparison between our results and those of Tomimura and Eriguchi. We present dimensionless energy quantities for a sequence of rotating magnetised equilibrium configurations with $N = 1.5, \hat{\kappa} = 0.4, \hat{a} = 200$ and $\zeta = 1$. The numerical values are our results; the percentages show the differences from Tomimura and Eriguchi.

| $r_p/r_{eq}$ | $\mathcal{E}_{mag}/\lvert W\rvert$ | $U/\lvert W\rvert$ | $T/\lvert W\rvert$ | $\lvert\hat{W}\rvert$ | $VC$ |
|---|---|---|---|---|---|
| 0.588 | 0.144 | 0.284 | 1.21e-3 | 0.0481 | 2.97e-5 |
| 0.55 | 0.151 (0.7%) | 0.276 (0.0%) | 0.0111 (4.7%) | 0.0459 (0.4%) | 3.10e-5 |
| 0.50 | 0.165 (0.6%) | 0.264 (0.0%) | 0.0211 (2.9%) | 0.0432 (0.5%) | 3.33e-5 |
| 0.45 | 0.189 (0.5%) | 0.255 (0.4%) | 0.0227 (3.2%) | 0.0401 (0.2%) | 3.63e-5 |
| 0.40 | 0.222 (0.0%) | 0.252 (0.0%) | 0.0119 (8.2%) | 0.0358 (0.3%) | 4.02e-5 |
| 0.371 | 0.242 | 0.252 | 1.10e-3 | 0.0331 | 4.32e-5 |

Our highest and lowest axis ratios (0.588 and 0.371) differ slightly from those of Tomimura and Eriguchi [137] (who have 0.589 and 0.372), so we cannot make a direct comparison for these values. For the other four axis ratios, our values agree with theirs to within 1% for the magnetic, gravitational and internal energy quantities but have discrepancies of around $3 - 8\%$ in the kinetic energy. Since our virial tests show smaller relative errors than those of Tomimura and Eriguchi, we suggest that the discrepancies may simply be due to us having used higher-resolution results.

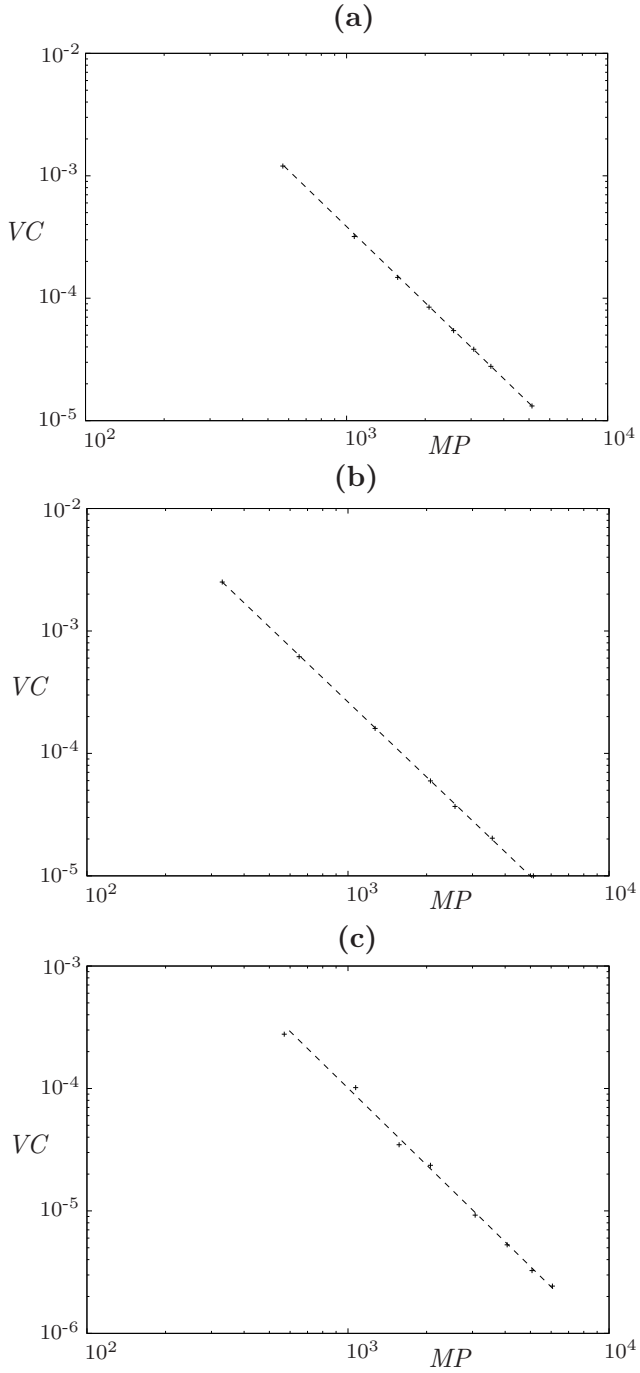


Figure 6.2: Logarithmic-scaled plots of the virial test $VC$ against the number of mesh points $MP$. The data points are plotted together with a line of gradient two; we note that this is a good fit to the points and conclude that both codes are second-order convergent. The plots are for: (a) mixed-field code run with purely poloidal field, $\Omega = 0$ and axis ratio 0.2; (b) mixed-field code run with a mixed field with $\alpha(u) = 10(u - u_{max})^{0.1}$, $\Omega = 0$ and axis ratio 0.2; (c) toroidal-field code run with $\Omega = 0$ and axis ratio 1.05.

## 6.9 Results

### 6.9.1 Magnetic field configurations

With the formalism described earlier in this chapter, we are able to examine field configurations in axisymmetric perfectly conducting polytropes. Since neutron star matter is thought to have high conductivity and be roughly approximated by an $N = 1$ polytrope, the field structures shown here should have some similarity to those in real neutron stars — although the field strengths here are considerably higher than those that have been observed so far. There are, nonetheless, some reasons to consider such strong fields. They provide a demonstration that the code can compute stellar structures in the nonlinear magnetic regime; we also find many common features among all configurations, suggesting that they could also exist for more weakly magnetised stars. In addition, the interior fields of neutron stars could be considerably stronger than their surface values.

The plots in this subsection show the magnetic field strength given by $|\mathbf{B}| = \sqrt{\mathbf{B}\cdot\mathbf{B}}$, and of the poloidal and toroidal components, $|\mathbf{B}_{pol}| = \sqrt{B_\varpi^2 + B_z^2}$ and $|\mathbf{B}_{tor}| = |B_\phi|$. The plots are colour-coded, with the peak field strength represented in yellow, and zero-field regions in black. The stellar surface is represented by the thick white arc which meets the $x$-axis at unity. Finally, since the equatorial radius $r_{eq} = 1$ in code units, we will often denote the axis ratio of the star $r_p/r_{eq}$ simply by the dimensionless polar radius, $r_p$.

All of the magnetic-field results presented here (and discussed in this subsection) are for nonrotating $N = 1$ polytropes, unless otherwise stated. We have not presented extra results for magnetic field configurations in rotating stars, since we find there is no qualitative difference when rotation is included. In addition, we have concentrated mostly on mixed-field configurations, since there are strong indications from both theory [96, 133, 144] and simulations [14, 79, 50] that both purely poloidal and purely toroidal fields are generically unstable.

In figure 6.3 we plot the poloidal and toroidal components of three mixed-field stars. Although the plots show stars with very different levels of deformation (axis ratios of $0.95, 0.5$ and $0.0$), each magnetic configuration is broadly similar. For each plot, the poloidal field pervades most of the interior of the star, as well as extending outside it. This component of the field is highest in the centre except in the extreme $r_p = 0.0$ case (when the shape of the star becomes toroidal, with

zero central density). The poloidal fields only go to zero in a small region towards the edge of the star (seen as the black region on the equator at $x \sim 0.9$); Tayler [96] calls this zero-field point the 'magnetic axis'. By contrast the toroidal field reaches its maximum here, and is only non-zero in a small region dictated by the functional form of $\alpha(u)$ that we use. Whilst the toroidal field energy is always a small proportion of the total magnetic energy — $\mathcal{E}_{tor}/\mathcal{E}_{mag} < 7\%$ — the *maxima* of both field components are comparable in magnitude.

In figure 6.4 we show how the poloidal and toroidal components of the field fit together by showing how the total field strength varies in two mixed-field stars. Despite the very different levels of distortion in the two plots, there are again broad similarities: the field tends to be strongest around the centre (due to its poloidal component) and in a small region around the equator near the surface (due to the toroidal component) which corresponds to a torus in the actual 3D star.

The differences in the toroidal field in a mixed-field star compared with a purely toroidal-field star within our formalism are shown in figure 6.5. The geometry is somewhat similar, since any toroidal field has to vanish along the pole and at the surface, but the field in the pure-toroidal star pervades virtually all of the interior of the star, whereas in the mixed-field case it is confined to a small region. Whilst the maximum field strengths are similar in both cases, the pure-toroidal field shown contains far more energy, by virtue of occupying a larger region of the star.

All of the plots so far have given only half of the information about the magnetic field in these stars — their magnitude. In figure 6.6 we additionally show the direction of a typical poloidal field by plotting contours of the streamfunction $u$. These contours are parallel to magnetic field lines, by the derivation in section 6.2.1. Since a purely toroidal field has direction vector $\mathbf{e}_\phi$, the field lines would go into the page in the $x - z$ plane we employ here; these would form concentric circles in the $x - y$ plane. Mixed-field lines lie in neither plane so we have not shown them here.

Lastly in this subsection, figure 6.7 shows the dependence of the ratio $B_p/\bar{B}$ on the polytropic index $N$; we find that there is an approximately linear relationship between the two, and for all polytropic indices $B_p/\bar{B}$ is of the same order of magnitude. For $N = 1$, $B_p/\bar{B} \approx 0.5$, suggesting that neutron stars (approximated as $N = 1$ polytropes) with purely poloidal fields are likely to have a $\bar{B}$ around double the polar field $B_p$.

Table 6.3: Comparing parameters related to the influence of the toroidal component in a mixed-field star with axis ratio 0.9.

| $a$ | $\mathcal{E}_{tor}/\mathcal{E}_{mag}$ | $\mathcal{E}_{mag}/\lvert W\rvert$ | $\epsilon$ | $B_p/\bar{B}$ |
|---|---|---|---|---|
| 0 | 0.00 | 2.43e-02 | 0.216 | 0.580 |
| 10 | 9.87e-03 | 2.55e-02 | 0.216 | 0.554 |
| 20 | 3.02e-02 | 2.82e-02 | 0.213 | 0.504 |
| 30 | 3.96e-02 | 2.93e-02 | 0.204 | 0.484 |
| 40 | 4.05e-02 | 2.92e-02 | 0.196 | 0.488 |
| 50 | 3.86e-02 | 2.88e-02 | 0.191 | 0.495 |

### 6.9.2 The relationship between $a$ and $\mathcal{E}_{tor}/\mathcal{E}_{mag}$

As mentioned earlier, we can increase the proportion of toroidal field in the mixed-field configurations only indirectly, by varying the code parameter $a$ from equation (6.3.9). In table 6.3 we show the effect of changing this parameter, for a non-rotating star with axis ratio $r_p/r_{eq} = 0.9$. One would expect that increasing $a$ would increase the toroidal portion of the field, which in turn would lead to a decrease in oblateness (since toroidal fields induce prolate distortions); one would also expect a reduction in the ratio $B_p/\bar{B}$ (since more of the field is toroidal and hence does not extend outside the star). Looking at the table, we see all of these effects do occur as the value of $a$ is increased, up until the $a = 40$ configuration. At this point the larger value of $a$ is no longer reflected in stronger toroidal-field effects. In all cases changing $a$ does not strongly affect the value of $\mathcal{E}_{mag}/|W|$, confirming our expectation that it is the variation in the toroidal component which affects ellipticity and $B_p/\bar{B}$, rather than simply a reduction in $\mathcal{E}_{mag}/|W|$. Finally, we note that even for the highest values of $a$, the relative contribution of the toroidal portion of the field is very small — only 4% of the total for the star shown in table 6.3. We shall see later that this is a generic feature of our formalism together with our boundary condition, where poloidal fields extend outside the star but toroidal ones vanish at the surface.

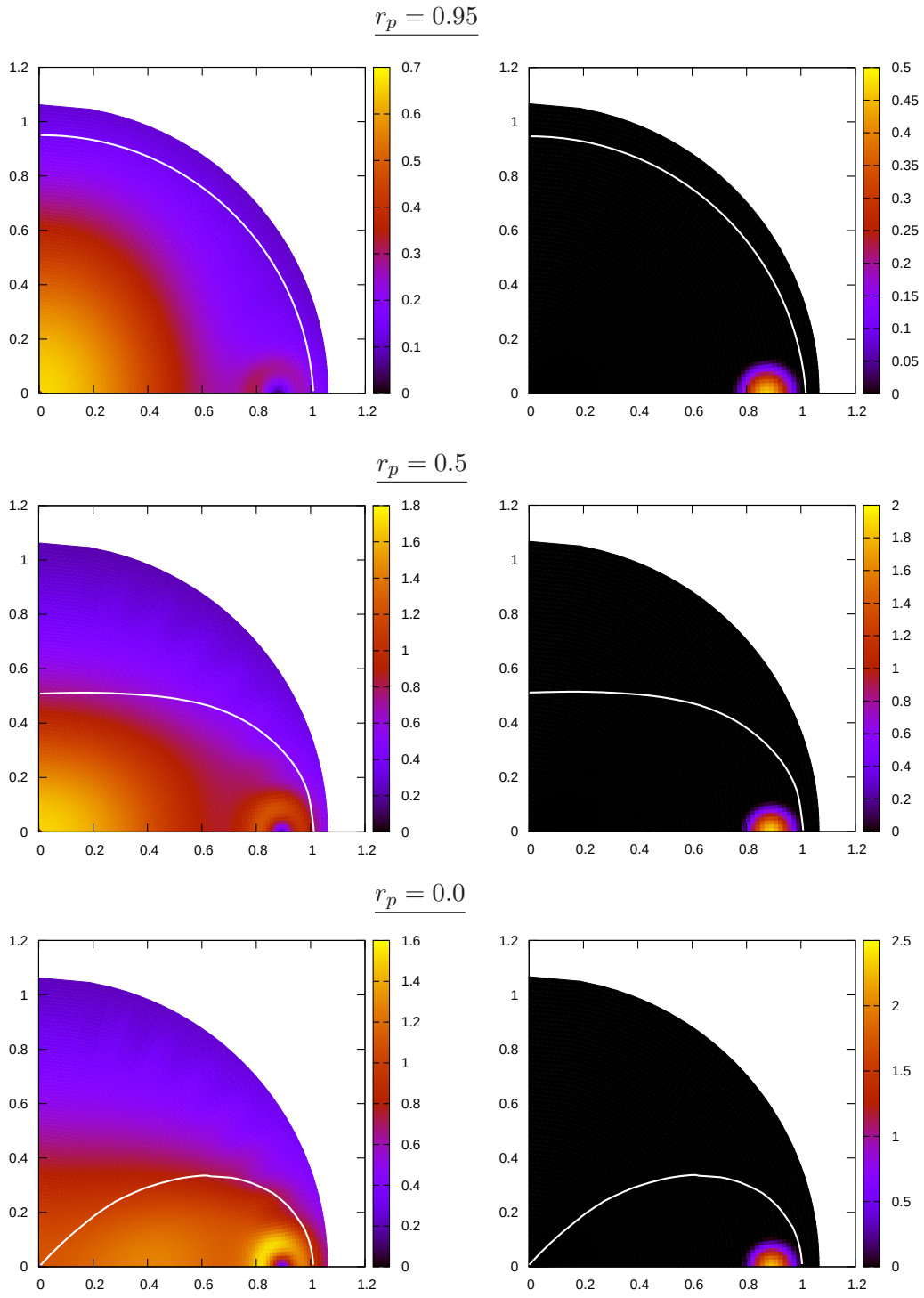


Figure 6.3: Density plots of the magnetic field strength for axis ratios of (top to bottom) $r_p = 0.95$, $r_p = 0.5$, $r_p = 0.0$. All plots are for mixed toroidal and poloidal fields in nonrotating stars, with toroidal-field parameter $a = 30$. This corresponds to toroidal fields of $3.7\%, 5.9\%$ and $6.7\%$ of the total $\mathcal{E}_{mag}$ for $r_p = 0.95, 0.5$ and $0.0$ respectively. We see that the toroidal component is confined to a far smaller region than the poloidal one. See text for further details.

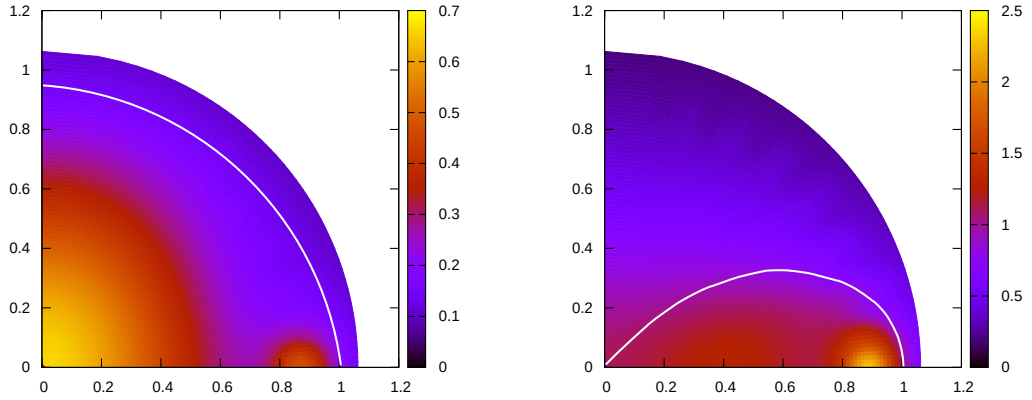


Figure 6.4: Total magnetic field for two mixed-field stars with extremes of axis ratio — $r_p = 0.95$ on the left and $r_p = 0.0$ on the right. They do, nonetheless, have qualitative similarities, with peak field strengths at/near the centre, and another peak near the equatorial surface.

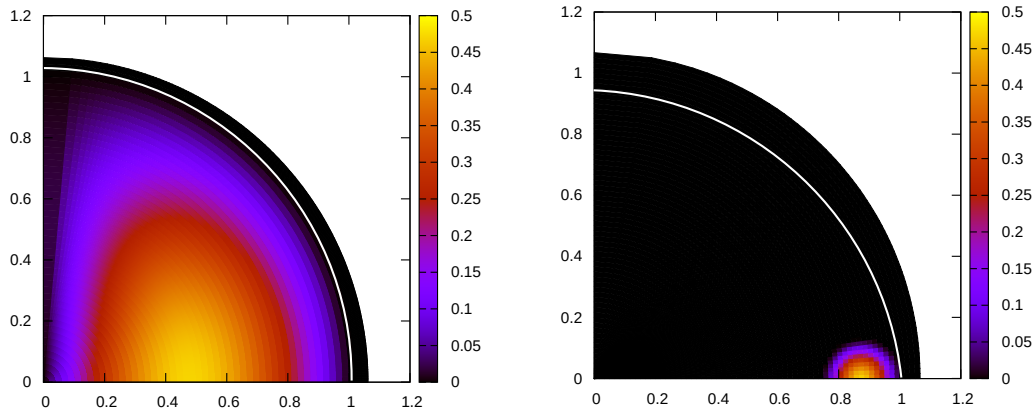


Figure 6.5: Density plots of the toroidal magnetic field strength for a pure-toroidal field star (left) and a mixed-field star (right). In both cases the stars are nonrotating, with maximum field strengths of $2.8 \times 10^{17}$ G. Note that whilst both fields are confined to a torus (this is the geometry of a toroidal field), the pure-toroidal field star has a toroidal field extending over a far larger portion of the interior.

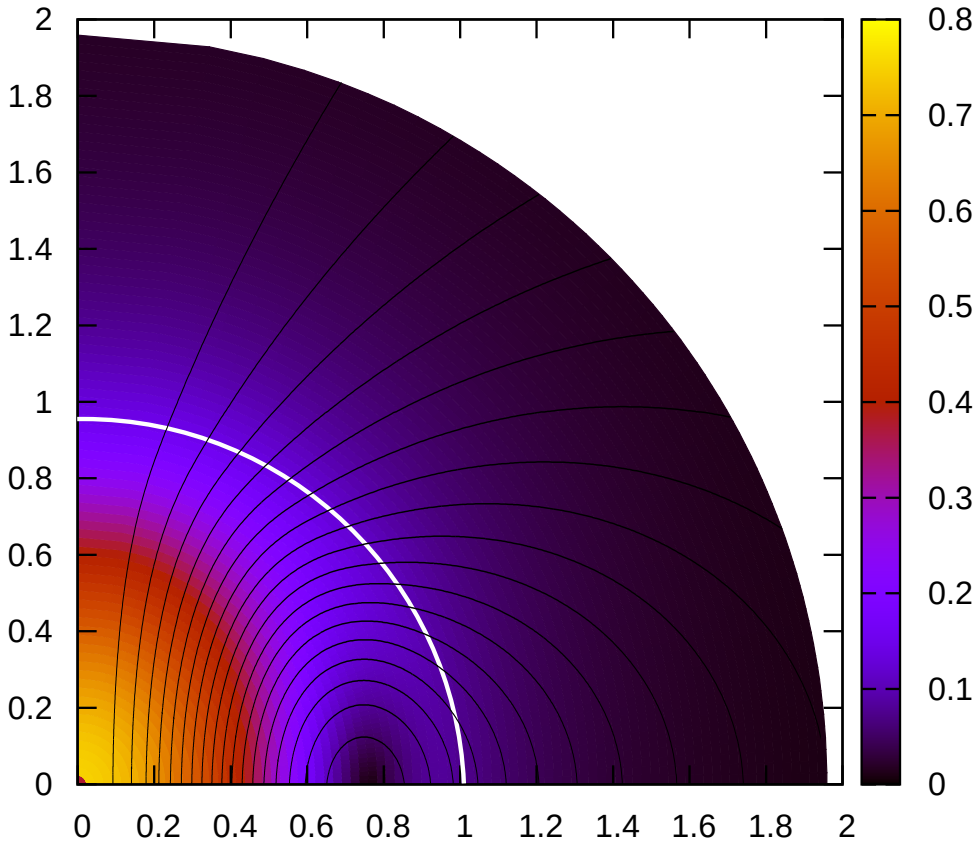


Figure 6.6: A representation of the magnitude and direction of a purely poloidal magnetic field in a nonrotating star. The colours represent the magnetic field strength and the overlaid black lines are field lines. Field lines for the toroidal component of a mixed-field star, or for purely toroidal fields, would go into the page and hence we have not plotted such configurations. The bold white arc represents the surface of the star.

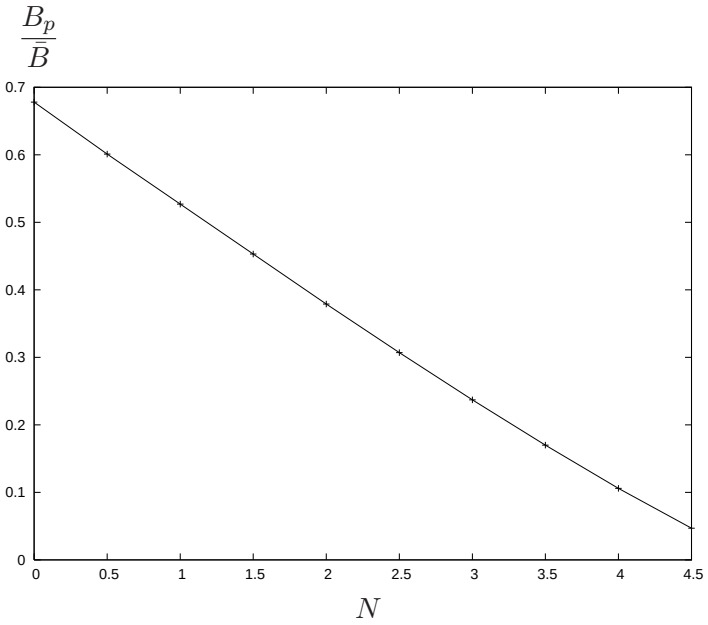


Figure 6.7: The ratio of polar field to volume-averaged field, $B_p/\bar{B}$, as a function of the polytropic index $N$. The plot is for purely poloidal fields in non-rotating stars, all with an axis ratio of 0.996. Note that if the field was purely toroidal then this ratio would be zero, regardless of $N$, since toroidal fields vanish at the stellar surface.

### 6.9.3 Magnetically-induced distortions

Having looked at field configurations, we now turn to the distortions these fields produce in the star's density distribution. The plots in this subsection show plots of the density in contours of $0.1\rho_{max}$, where the maximum density $\rho_{max}$ is normalised to unity.

For later comparison, we begin by looking at the more familiar effect of rotation (figure 6.8); this produces an oblate distortion that becomes larger with increasing rotation rate. The star become more centrally concentrated, in the sense that the region within the innermost contour — where $\rho > 0.9\rho_{max}$ — becomes smaller, and the $0 < \rho < 0.1\rho_{max}$ region grows.

Next we consider purely poloidal fields, confirming the expectation from section 4.3 that these fields induce an oblate distortion; the surface shapes of such stars are thus similar to those of rotationally distorted stars. However, the interior density distributions are very different: unlike a centrifugal force, the Lorentz force acts to pull the point of maximum density away from the centre into a maximum-density ring. In the extreme limit where the ratio $r_p/r_{eq} \to 0$, the star actually becomes a torus (figure 6.9). For mixed fields, the effect of increasing the toroidal component is similar to the effect of adding rotation: it tends to push the maximum density region back to the centre — see figure 6.10. Note that both the mixed-field stars shown are oblate though, due to the dominance of the poloidal component; stronger toroidal fields tend to make stars prolate, but our formalism and boundary condition seem to generate mixed fields with weak toroidal components only (the 5.5%-toroidal field of figure 6.10 plot (c) is relatively strongly toroidal, within this context).

The only situation where we are able to study dominantly toroidal fields is the other limit of our formalism — the pure-toroidal case. In this case we find that, as expected, the resultant density distribution is prolate. Although the surface shapes are very close to spherical in all cases (in contrast with the pure-poloidal and mixed-field cases), the ellipticities may be very large; the innermost density contours become highly prolate (see figure 6.11).

For weak fields and small distortions, perturbation theory results suggest that the ellipticity of a star should depend linearly on $B^2$; see, for example, section 4.3. With our non-linear code we are able to check this, and see how well the perturbative result holds as field strengths are increased; this is plotted for both poloidal and

toroidal fields in figure 6.12. The results depart slowly from the linear regime to begin with, but in the poloidal-field case the field strength required peaks for an ellipticity of $\epsilon \sim 0.8$. This peak seems to correspond to roughly the point at which the maximum density is pulled out into a ring, making the star's density distribution toroidally-shaped. We speculate that for extremely distorted configurations this toroidal density distribution is a lower-energy state than the usual spheroidal one.

In figure 6.11 we found that purely toroidal fields give prolate density distributions, but never induce significant surface distortions. Because rotation gives rise to oblateness in stars, it opposes the effect of a toroidal field in a star, and the two effects can balance to give a rotating magnetised star with zero overall ellipticity. Note that in this case the stars will have oblate surface shapes but a spherical density distribution — see figure 6.13.

Next we look at the effect of magnetic fields on the Keplerian velocity $\Omega_K$ — see figure 6.14. We find that whilst increasing the field strength causes a slight decrease in the velocity needed to cause mass shedding, this effect only becomes noticeable for very strong fields. It seems, therefore, that magnetic fields are unlikely to affect the stability of a star in this manner.

We have generally presented results for an $N = 1$ polytrope, as this is regarded as a reasonable approximation to a neutron star. For our final two figures, however, we briefly investigate the effect of varying the polytropic index $N$, whilst maintaining a mass of $1.4M_\odot$ and equatorial radius of 10 km in the corresponding unmagnetised 'background' polytropic star. In figure 6.15, we plot four stars with the same surface distortion $r_p/r_{eq} = 0.5$ but different $N$. We see that when $N$ is low the density contours are all close to the edge of the star, with a large (slightly off-centre) high-density region; in the limiting case $N = 0$ the star is an incompressible, uniform density configuration, so all contour lines coincide with the star's surface. For higher values of $N$ the high-density region becomes smaller and the low-density outer region becomes larger. We note that the $N = 2$ polytrope shown cannot be a neutron star model, however, as its maximum density of $1.79 \times 10^{14}$ g cm$^{-3}$ is lower than the density of heavy nuclei, $\rho_0 = 2.4 \times 10^{14}$ g cm$^{-3}$.

Finally, in figure 6.16, we look at non-rotating stars with a purely poloidal field and an axis ratio of 0.95. We plot the dependence of the field strength on polytropic index $N$, finding that as $N$ is increased a weaker field is required to support the same surface distortion.

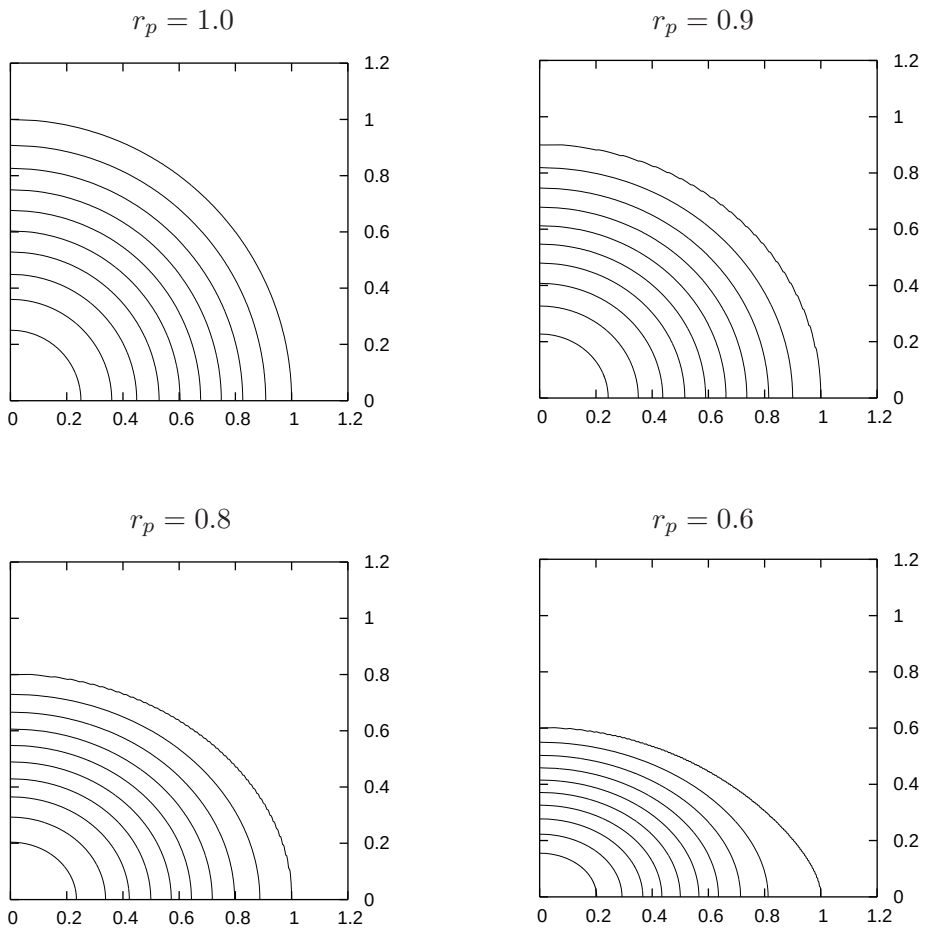


Figure 6.8: Contour plots of the density in rotating unmagnetised $N = 1$ polytropic stars; the axis ratios are labelled above each plot. We see that the density becomes more centrally concentrated in the more highly distorted stars. The rotation rates required to produce axis ratios of $r_p = 1, 0.9, 0.8, 0.6$ are, respectively, $0, 749, 997, 1190$ Hz; the respective equatorial radii are $r_{eq} = 10.0, 10.7, 11.5, 14.4$ km.

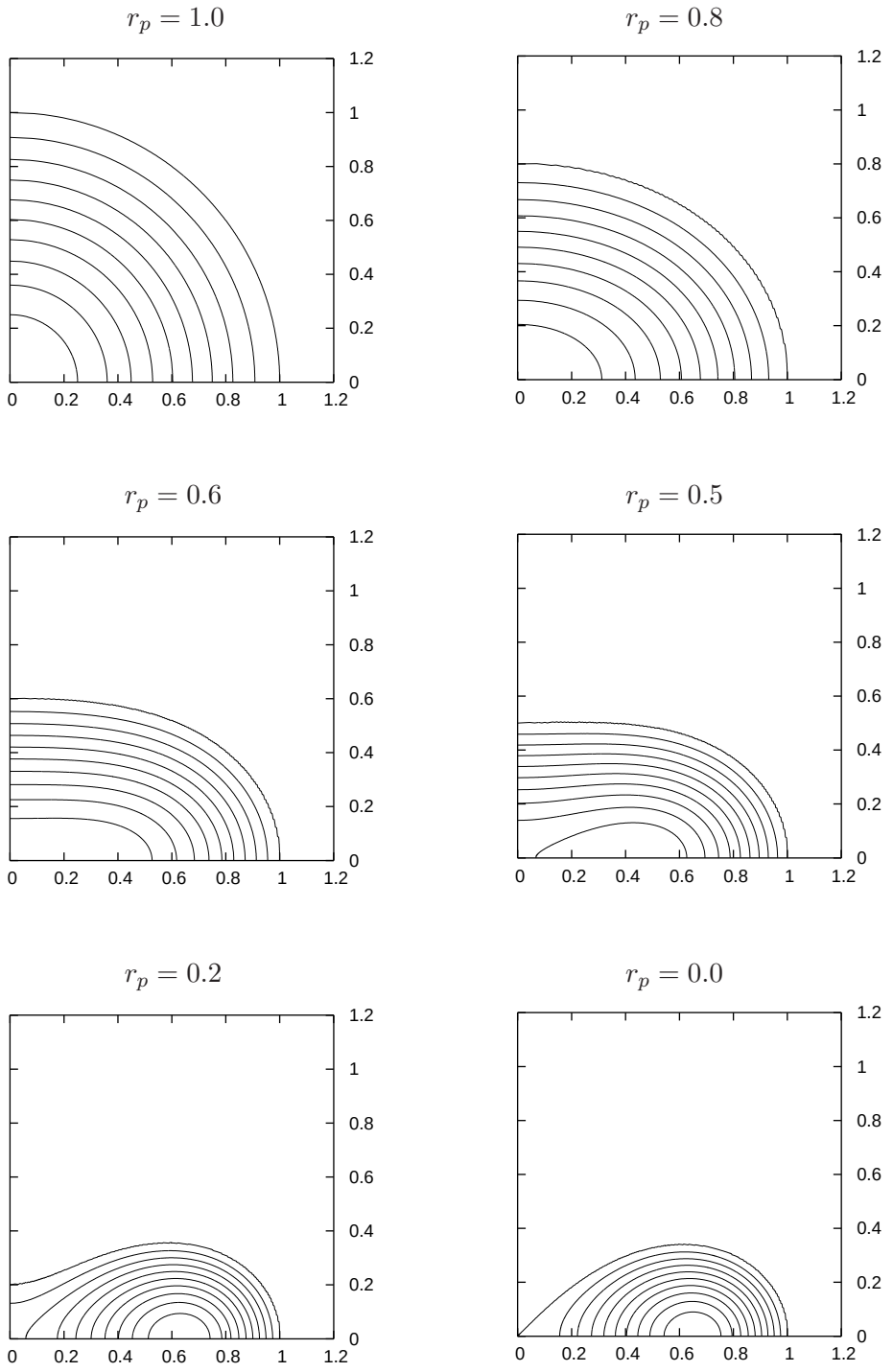


Figure 6.9: Contour plots of the density in nonrotating $N = 1$ polytropic stars, distorted by a purely poloidal field. Note that the maximum density moves away from the centre of the star for the more distorted configurations. The averaged magnetic field strengths for the stars with $r_p = 1, 0.8, 0.6, 0.5, 0.2, 0.0$ are, respectively, $\bar{B} = 0, 3.38, 4.76, 5.15, 4.70, 4.46 \times 10^{17}$ gauss. The equatorial radii are, respectively, $r_{eq} = 10.0, 10.9, 12.1, 12.9, 16.2, 17.0$ km.

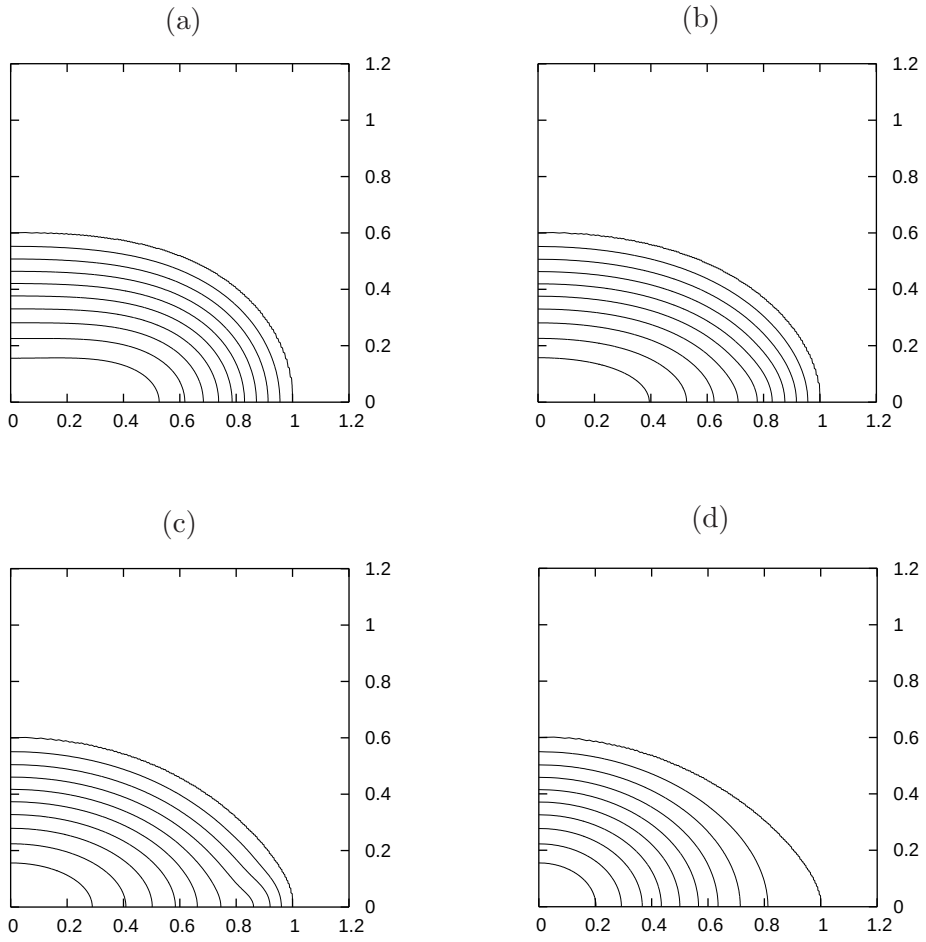


Figure 6.10: Density contours in an $N = 1$ polytropic star with axis ratio of 0.6, with different sources of distortion. Plots (a), (b) and (c) are nonrotating configurations with, respectively: purely poloidal field, mixed-field with 3.4% toroidal field, mixed-field with 5.5% toroidal field. Plot (d) is for a purely rotationally-distorted star with no magnetic field. All stars have the canonical mass of $1.4M_{\odot}$, with equatorial radii of $12.1, 12.5, 13.2, 14.4$ km for stars (a)-(d), respectively. We note that whilst a purely poloidal field tends to push the maximum density away from the centre, both toroidal field components and rotation have the effect of increasing the equatorial radius and making the star more diffuse.

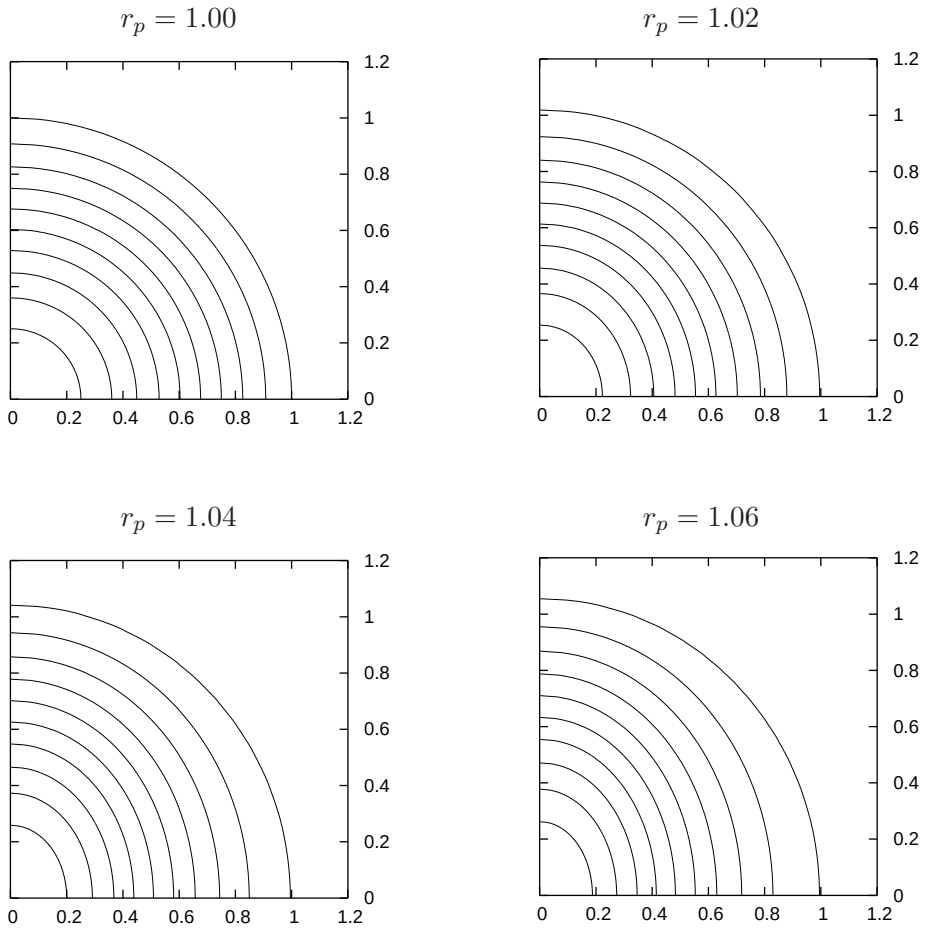


Figure 6.11: Density contour plots for stars with purely toroidal fields. Whilst the surface shapes (i.e. the axis ratios, labelled above each plot) are barely aspherical, one can see from the innermost contours that the density distributions do in fact become highly prolate. In all cases we use an $N = 1$ polytrope with $\Omega = 0$. The magnetic field strengths for $r_p = 1.00, 1.02, 1.04, 1.06$ are $\bar{B} = 0, 1.81, 2.46, 2.82 \times 10^{17}$ gauss, respectively; $r_{eq} = 10.0, 10.1, 10.4, 10.6$ km.

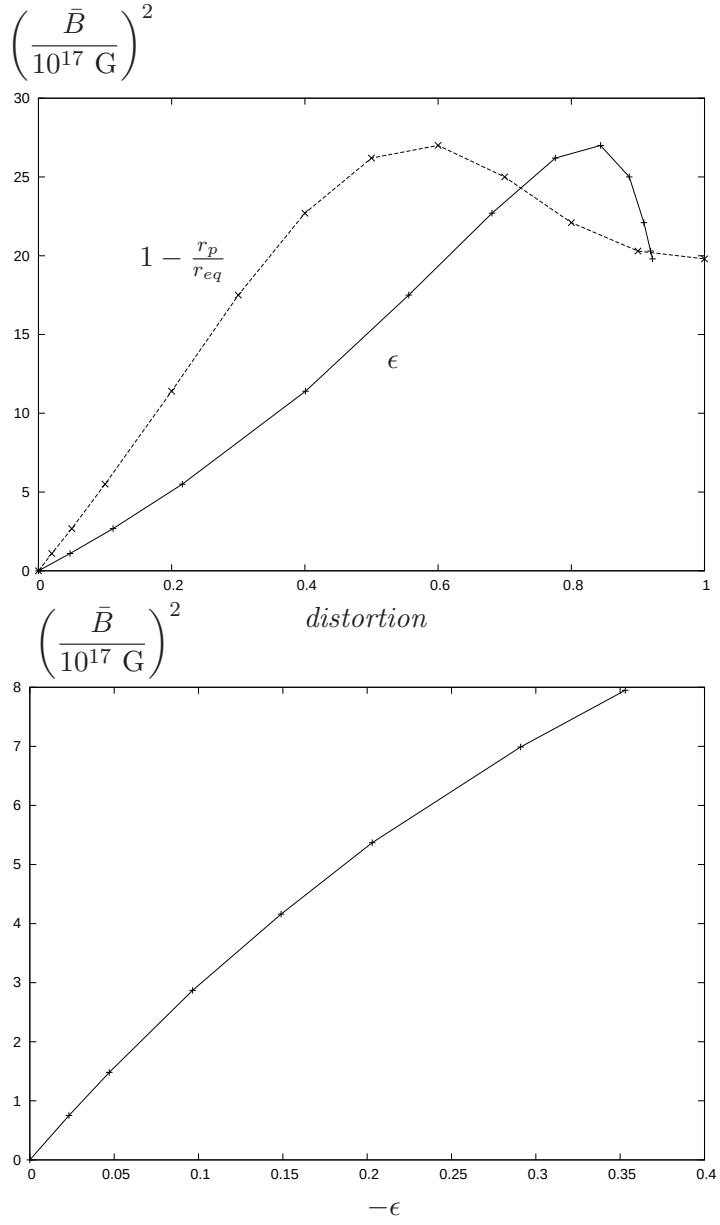


Figure 6.12: Top: a graph showing how (poloidal) magnetic distortions vary with the field strength. $1 - r_p/r_{eq}$ is the surface distortion, whilst $\epsilon$ represents the distortion of the density distribution, as defined in equation (6.6.39). Note that the required field strength peaks for $1 - r_p/r_{eq} \sim 0.6$ or $\epsilon \sim 0.8$ and then drops slightly for more extreme distortions. For small distortions we see that there is a roughly quadratic dependence on the field strength. Bottom: toroidal-field distortions versus $B^2$. In this case we only use $\epsilon$ to gauge the level of distortion, as the surface shapes remain nearly spherical.

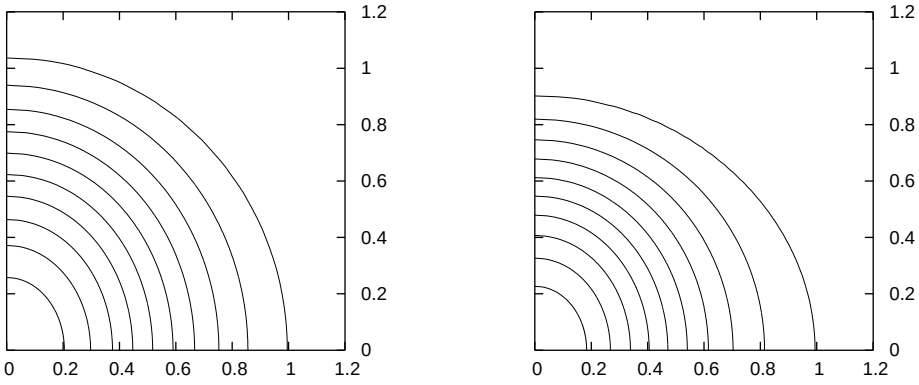


Figure 6.13: Two stars with toroidal magnetic fields. The left-hand configuration is a non-rotating star (and hence has a prolate density distribution), whilst the right-hand one is the same physical star but with rotation added, with an oblate surface shape but an overall ellipticity of zero. The average field strength in both cases is $\bar{B} = 2.4 \times 10^{17}$ G.

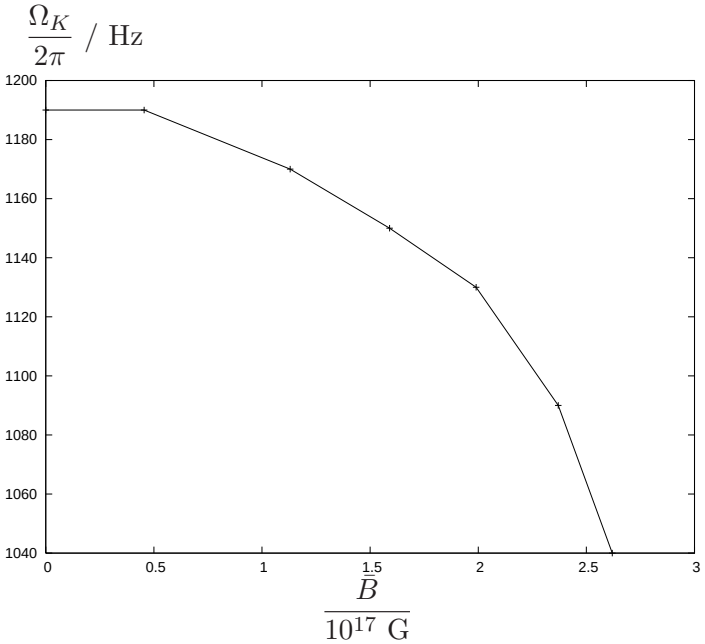


Figure 6.14: The dependence of Keplerian velocity $\Omega_K$ on magnetic field strength $\bar{B}$, for stars with purely poloidal fields. Note that an appreciable decrease in $\Omega_K$ only occurs for very strong fields.

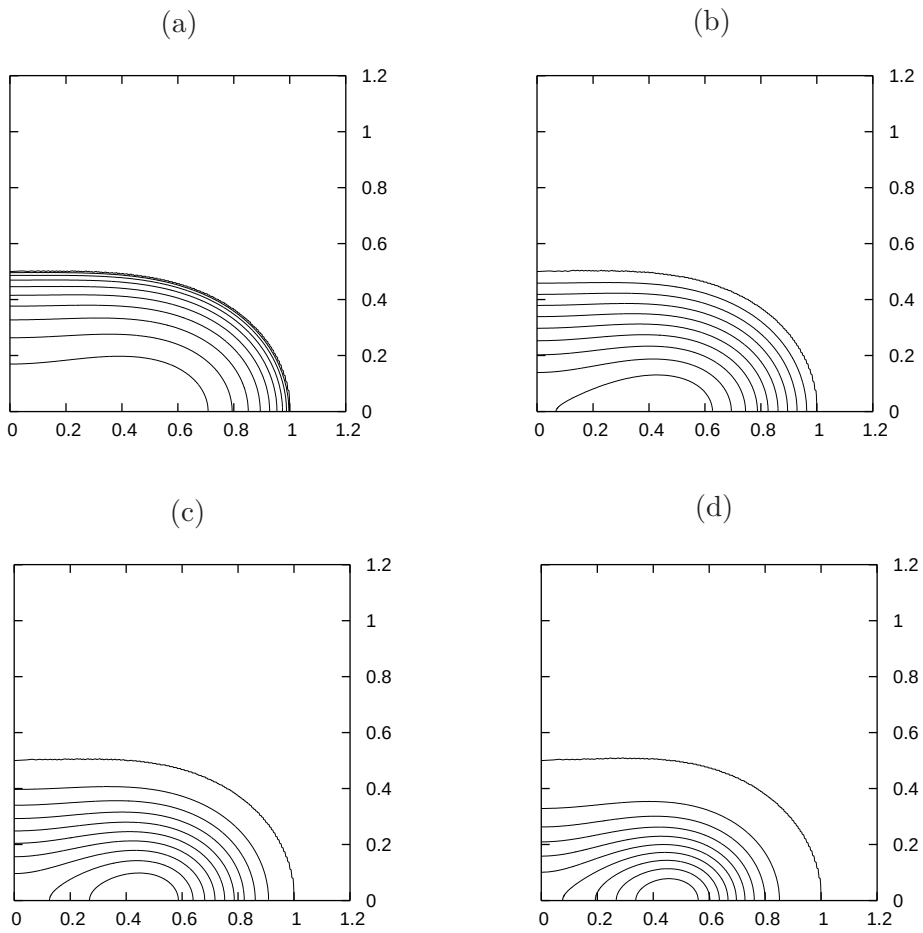


Figure 6.15: Non-rotating configurations, all with a purely poloidal field and an axis ratio of $r_p/r_{eq} = 0.5$. Plots (a) to (d) are for $N = 0.5, 1, 1.5, 2$ polytropes, respectively; the corresponding field strengths are $\bar{B} = 7.62, 4.31, 2.98, 1.13 \times 10^{17}$ G, the maximum densities are $1.67, 1.14, 0.623, 0.179 \times 10^{15}$ g cm$^{-3}$ and the equatorial radii are $r_{eq} = 10.2, 12.9, 17.6, 29.6$ km, respectively.

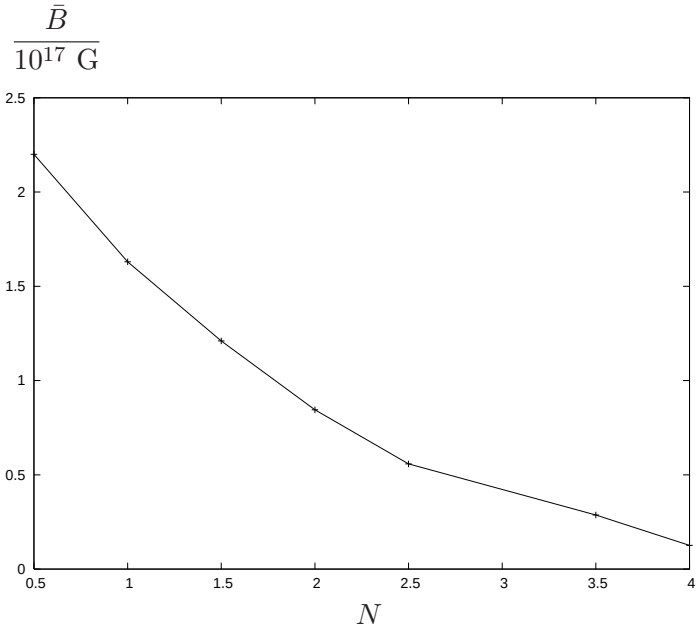


Figure 6.16: The poloidal field strength $\bar{B}$ required to induce a surface distortion of $r_p/r_{eq} = 0.95$, plotted for various polytropic indices. We see that the required field is weaker for higher-$N$ polytropes.

## 6.10 Discussion

To understand how strong magnetic distortions may be in highly magnetised objects like magnetars, realistic models are needed to study the field structure of these stars. The formalism we use in this work comes directly from the assumptions of axisymmetry and perfect conductivity, together with a boundary condition that the poloidal part of the field should only become zero at infinite distance from the star, rather than vanishing at its surface; we anticipate that these conditions provide a reasonable model of a neutron star's magnetic field.

The general formalism of axisymmetric MHD reduces to a mixed-field case and a purely toroidal-field case, with two (mathematically) arbitrary functions in the former case ($\kappa(u)$ and $\alpha(u)$) and one in the latter ($h(\gamma)$). Despite the apparent freedom in choosing these functions, we found that on physical grounds only one functional form was satisfactory for each one; see section 6.3.3. We conclude that the equations we have numerically solved in this work are in fact quite general and that we have not excluded physically valid branches of solutions with our choices.

Perturbative calculations in the weak-field regime have found that $\epsilon$ depends linearly on $\bar{B}^2$. With the use of our nonlinear code we are able to investigate how well this approximation holds for larger fields and ellipticities. We can see graphically that the first few points from both plots in figure 6.12 lie in fairly straight lines and hence we deduce the relations

$$\epsilon_{pol} \sim 5 \times 10^{-4} \left( \frac{\bar{B}}{10^{16}\ \mathrm{G}} \right)^2 \sim 2 \times 10^{-3} \left( \frac{B_p}{10^{16}\ \mathrm{G}} \right)^2 \tag{6.10.1}$$

for the purely poloidal case (the above relation also uses $B_p/\bar{B} \sim 0.5$ from figure 6.7), and

$$\epsilon_{tor} \sim -3 \times 10^{-4} \left( \frac{\bar{B}}{10^{16}\ \mathrm{G}} \right)^2 \tag{6.10.2}$$

for the purely toroidal case; where in both cases we have used a star of mass $1.4 M_\odot$ whose radius would be 10 km if unmagnetised. By comparing these extrapolated linear-regime formulae with our non-linear code results, we can explore how well perturbative results are likely to hold in a strong-field regime. We find that the linear-regime results given by (6.10.1) and (6.10.2) deviate by less than 10% from the actual non-linear code result (shown in figure 6.12) provided that $\bar{B} \lesssim 1.5 \times 10^{17}$ G, or equivalently $\epsilon \lesssim 0.15$. Alternatively, if we allow the linear relation to differ by

up to 30% from the nonlinear result, we may use the linear relation as an 'acceptable' approximation for $\bar{B} \lesssim 3 \times 10^{17}$ G or $\epsilon \lesssim 0.35$ (i.e. it holds for the entire range of ellipticities we can plot in the toroidal-field case).

This suggests that for *all* known neutron star field strengths, $\epsilon$ is likely to be linearly dependent on $\bar{B}^2$, to a good approximation. Hence perturbation theory *could* provide accurate predictions of NS distortions, provided the neutron star model used is also a close approximation to real NS physics.

We are also able to compare our linear-regime formulae with the analytic work of Haskell et al. [64], who also treated pure poloidal fields extending outside the star and pure toroidal fields vanishing at the stellar surface (as for our work). For the same mass, radius and polytropic index their formulae give:

$$\epsilon_{pol} \sim 10^{-2} \left( \frac{B_s}{10^{16}\ \mathrm{G}} \right)^2 \quad \text{and} \quad \epsilon_{tor} \sim -2 \times 10^{-4} \left( \frac{\bar{B}}{10^{16}\ \mathrm{G}} \right)^2 \tag{6.10.3}$$

where $B_s$ is the surface magnetic field strength, which was assumed constant in their calculation; we do not have a constant surface field so have compared with their work using the value of $|\mathbf{B}|$ at the pole instead. Since their field geometries are clearly not identical to ours, and since we had to extrapolate to obtain our formulae, we would not expect precise agreement. Nonetheless, we feel that the similarities show that our work makes sensible contact with perturbative calculations.

From figure 6.12, beginning at an unmagnetised spherical star, we find that in both the poloidal and toroidal-field cases the magnetic field strength required to induce a certain distortion initially increases for increasing distortion — as would be expected from perturbative work. However, in the purely poloidal case the required field strength then *peaks* at $\epsilon \sim 0.8$, dropping slightly as $\epsilon$ is increased further. Around the same point the density distribution becomes toroidal in nature — that is, the point of maximum density moves away from the centre and a high-density torus forms; this leads us to speculate that at $\epsilon \sim 0.8$ it becomes energetically favourable for the density to change from a spheroidal profile (as seen in the weaker-field stars, e.g. the $r_p = 0.8$ plot of figure 6.9) to a toroidal one (e.g. figure 6.9, $r_p = 0.0$ plot). It is clear that if the magnetic field in a star is increased beyond the peak value of $\sim 5 \times 10^{17}$ G shown in the left-hand plot of figure 6.12 then one of our initial assumptions must be violated. Since we cannot investigate the possibilities with our current code, we conclude that a hypothetical star with a field of $\bar{B} > 6 \times 10^{17}$ may either have no stationary equilibrium solution (in which case

it may lose magnetic energy until it is in equilibrium), or that there may be a new triaxial branch of super-magnetised solutions bifurcating from the biaxial curve at $\epsilon \sim 0.8$.

We do not find a similar peaking of the field strength in the purely toroidal case, however. In this case the largest ellipticities we are able to calculate are around $\epsilon \sim 0.35$. Whilst this particular value may represent a limitation of our numerical scheme, we suggest that a limited range of ellipticities is a consequence of the formalism for toroidal fields in axisymmetry, where $\mathbf{B}$ is directly linked to the density $\rho$; in the mixed-field case we have a separate equation to iteratively solve for the magnetic field. Thus restrictions on the field geometry may restrict the size of permissible ellipticities.

Of course, whilst the 'peak field strength' we discuss here is a theoretical upper bound on NS fields, there are very probably other physical effects that place a lower bound than $\sim 5 \times 10^{17}$ G on the maximum field. Certainly, if magnetar surface fields are $\sim 10^{15}$ G one would not expect their volume-averaged fields to exceed $\sim 10^{16}$ G significantly.

We have argued that the equations we solve in this chapter lead to quite general solutions for axisymmetric stars. However, we find that although it is possible to find solutions with purely poloidal or purely toroidal fields, the range of mixed-field solutions is very limited. Using $\mathcal{E}_{tor}/\mathcal{E}_{mag}$ as a gauge of the strength of the toroidal component in a mixed-field star, we find that for all our stars $0 \leq \mathcal{E}_{tor}/\mathcal{E}_{mag} < 0.07$. The other extreme is of course $\mathcal{E}_{tor}/\mathcal{E}_{mag} = 1$ for purely toroidal fields. This means that although the toroidal component does have some influence in a mixed-field star (see table 6.3), it is dominated by the effect of the poloidal field. In particular all our mixed-field stars have oblate density distributions.

Mixed-field configurations with weak toroidal components are not peculiar to our work. Ciolfi et al. [31] studied mixed fields in relativistic stars, with a perturbative approach and minimising energy at fixed magnetic helicity. Although this approach is clearly very different from the non-linear work on Newtonian stars reported in this chapter, a similar result emerges: that the toroidal-field energy is only up to $\sim 10\%$ of the total magnetic energy.

Some studies, similar to ours, have claimed to produce mixed-field configurations with comparable poloidal and toroidal fields; see for example Yoshida and Eriguchi [145]. However, they use a different measure for the relative strength of the field

components: the *maximum magnitude* of each component, rather than the energy contained in each one. In this sense, the results in this chapter also contain configurations with comparable field components. We believe that the ratio of energies is a better measure than the ratio of maxima though: we are interested in magnetic distortions, which are proportional to $B^2$ (or equivalently the magnetic energy), *not* to the maximum field.

Our mixed-field stars have the boundary condition that the toroidal component vanishes at the surface, whilst the poloidal piece only decays at infinity. By contrast, Haskell et al. [64] considered the problem of mixed-field stars where the total field vanished at the surface. This results in an eigenvalue problem, with all (discrete) solutions having prolate density distributions and all having dominantly toroidal fields. Since the chief difference between our work and theirs seems to be the choice of boundary condition, we speculate that our boundary condition favours the poloidal field, whilst that of Haskell et al. favours the toroidal component. We note that this idea seems to be consistent with the recent work of Duez and Mathis [39]. These authors found MHD equilibria with roughly equal toroidal and poloidal-energy components using a semi-analytic approach; but like Haskell et al. they consider only confined fields.

The numerical simulations of Braithwaite [15] suggest that a stable magnetic field will have $0.20 \lesssim \mathcal{E}_{tor}/\mathcal{E}_{mag} \lesssim 0.95$. If this result is directly applicable to our work then it would imply that *none* of the solutions that exist within our axisymmetric formalism are stable. However, for numerical reasons these simulations use a magnetic diffusivity term which is zero within the star and increases through a transition region to a high, constant value in the exterior (see Braithwaite and Nordlund [16] for details). We suggest that this transition region may favour the toroidal component of a mixed-field star; it would be interesting to see if a similar stability result emerges from simulations using a boundary condition more similar to ours.

Although we regard our boundary condition as the most natural for a mixed-field fluid with infinite conductivity, neutron stars are not perfect conductors. In moving from the fluid interior to the crust and magnetosphere, it is clear that the resistivity of the medium increases and hence the boundary condition should be adapted to reflect this. For the poloidal component, this adapted boundary condition should have a damping effect in the outer regions of the star — and hence could resemble a surface treatment somewhere between ours (where the poloidal field is unaffected by

passing through the surface) and that of Haskell et al. [64] (where the poloidal field vanishes at the surface). Since our boundary condition gives a poloidal-dominated field and that of Haskell et al. gives a toroidal-dominated field, we suggest that the inclusion of resistivity would result in configurations where neither component is universally dominant. In particular, we would not expect magnetic distortions in real, mixed-field, neutron stars to be universally oblate or prolate. We conclude that future, more realistic, models of magnetised stars should incorporate a boundary condition like ours, but modified to take account of the increasing resistivity in the outer regions of the neutron star.

# Chapter 7

# Studying magnetic oscillations through time evolutions

## 7.1 Introduction

In chapter 2 we discussed some of the roles magnetic fields may play in neutron stars, including the observation of magnetar QPOs. By improving the modelling of magnetic stellar oscillations, we may be able to use these QPOs as a probe of neutron star physics. Whilst magnetars rotate very slowly, there are many other neutron stars with high angular velocity as well as strong magnetic fields, so it is desirable to be able to study oscillations in stars at both of these extremes. In addition, it will prove easier to see magnetic effects on oscillations by looking at very highly-magnetised configurations. An introduction to stellar oscillation modes, with details of some of the terminology used in this chapter, is given in chapter 5.

The nonlinear code described in chapter 6 allows us to generate stationary MHD equilibrium configurations. In this chapter we use these configurations as a background on which to study perturbations. This is done with a code which evolves perturbations in time; from this the oscillation spectrum of the system can be found.

More specifically, we study linear perturbations of rotating Newtonian neutron stars endowed with purely toroidal magnetic fields, making the Cowling approximation. Since the background configuration may be nonspherical by virtue of rotational and magnetic effects, the perturbations and background are self-consistent. We are also able to track modes up to very high magnetic field strengths ($\sim 10^{17}$ G) and

close to Keplerian velocity. This is in contrast to many previous numerical studies of magnetic oscillations. Whilst we employ a purely toroidal background field, the perturbed field is mixed poloidal-toroidal.

The code described here is based on the nonmagnetic code of Jones et al. [75] and Passamonti et al. [110]; the main work of this chapter has been to extend this work to oscillations of magnetised stars. We begin by discussing the equations required to describe perturbations of a rotating magnetised star, then give details of the boundary conditions and initial data used. We next describe numerical issues and test the accuracy and convergence properties of the code. Finally, we present results for magnetic oscillation modes. A condensed report on the work in this chapter is given in Lander, Jones and Passamonti [85].

## 7.2 Governing equations

This section consists of a full description of the perturbation problem: the evolution equations for the velocity, density and magnetic field, together with the boundary conditions required and the initial data used.

### 7.2.1 Background and perturbation equations

We model a neutron star as a self-gravitating, rotating, magnetised polytropic fluid with infinite conductivity. This system is governed by the equations of perfect magnetohydrodynamics (MHD):

$$\rho\left(\frac{\partial \mathbf{v}}{\partial t}+(\mathbf{v}\cdot\nabla)\mathbf{v}+2\boldsymbol{\Omega}\times\mathbf{v}\right)=-\nabla P-\rho\nabla\Phi-\rho\boldsymbol{\Omega}\times(\boldsymbol{\Omega}\times\mathbf{r})+\frac{1}{4\pi}(\nabla\times\mathbf{B})\times\mathbf{B}, \quad (7.2.1)$$

$$\nabla^2\Phi=4\pi G\rho, \quad (7.2.2)$$

$$\frac{\partial\rho}{\partial t}=-\nabla\cdot(\rho\mathbf{v}), \quad (7.2.3)$$

$$\frac{\partial\mathbf{B}}{\partial t}=\nabla\times(\mathbf{v}\times\mathbf{B}), \quad (7.2.4)$$

$$P=k\rho^{\gamma}, \quad (7.2.5)$$

together with the solenoidal constraint $\nabla\cdot\mathbf{B}=0$ on the magnetic field. Here $\mathbf{v}$ denotes the part of the fluid's velocity field which is not rigid rotation $\boldsymbol{\Omega}$; all other symbols have their usual meanings. Throughout this chapter we work with $\gamma=2$

polytropes exclusively, as a simple approximation to a neutron star equation of state. We consider linear Eulerian perturbations of this system by making the standard ansatz that each physical quantity has a zeroth-order background piece and a first-order perturbed piece; e.g. the density is written as $\rho = \rho_0 + \delta\rho$.

We assume that our background star is stationary and rigidly rotating, so that $\mathbf{\Omega}$ is zeroth-order and $\mathbf{v}$ first-order. Equations (7.2.3) and (7.2.4) become trivial and we are left with

$$0 = -\nabla P_0 - \rho_0 \nabla \Phi_0 - \rho_0 \mathbf{\Omega} \times (\mathbf{\Omega} \times \mathbf{r}) + \frac{1}{4\pi}(\nabla \times \mathbf{B}_0) \times \mathbf{B}_0, \tag{7.2.6}$$

$$\nabla^2 \Phi_0 = 4\pi G \rho_0, \tag{7.2.7}$$

$$P_0 = k\rho_0^\gamma. \tag{7.2.8}$$

Making the additional assumption of axisymmetry one may show that this system of equations splits into two cases: one where the magnetic field is purely toroidal and a second mixed-field case (with pure-poloidal fields as a limiting case). Details of the solution of these equations are given in chapter 6; we use the code described therein to generate the background configurations used here. Here we merely note that our background configurations are fully self-consistent, with rotation, magnetic fields and fluid effects in equilibrium. In contrast to other work on magnetic oscillations, our background star need not be spherical, but may be distorted by rotational or magnetic effects, or a combination thereof.

Working in the frame corotating with the background star, the linearised perturbation equations are:

$$\rho_0 \frac{\partial \mathbf{v}}{\partial t} = -\nabla \delta P - \rho_0 \nabla \delta\Phi - \delta\rho \nabla \Phi_0 + \frac{1}{4\pi}(\nabla \times \mathbf{B}_0) \times \delta\mathbf{B} + \frac{1}{4\pi}(\nabla \times \delta\mathbf{B}) \times \mathbf{B}_0, \tag{7.2.9}$$

$$\nabla^2 \delta\Phi = 4\pi G \delta\rho, \tag{7.2.10}$$

$$\frac{\partial \delta\rho}{\partial t} = -\nabla \cdot (\rho_0 \mathbf{v}), \tag{7.2.11}$$

$$\frac{\partial \delta\mathbf{B}}{\partial t} = \nabla \times (\mathbf{v} \times \mathbf{B}_0), \tag{7.2.12}$$

$$\delta P = k\gamma\rho_0^{\gamma-1}\delta\rho = \frac{\gamma P_0}{\rho_0}\delta\rho. \tag{7.2.13}$$

Here we have assumed that the background and perturbations have the same equation of state, both with polytropic index $\gamma$. Note that, by (7.2.12), $\partial_t(\nabla \cdot \delta\mathbf{B}) = 0$; i.e. if $\nabla \cdot \delta\mathbf{B} = 0$ in the initial data then it will remain zero. Since the background is divergence-free by construction[1], a divergence-free initial perturbation gives $\nabla \cdot \mathbf{B}_{total} = \nabla \cdot \mathbf{B}_0 + \nabla \cdot \delta\mathbf{B} = 0$ for all time.

We now simplify the perturbation equations by making the Cowling approximation, and use (7.2.13) to eliminate $\delta P$ terms from the perturbed Euler equation (7.2.9); the perturbations are then governed by the reduced set of equations

$$\rho_0 \frac{\partial \mathbf{v}}{\partial t} = -\nabla\left(\frac{\gamma P_0 \delta\rho}{\rho_0}\right) - \delta\rho\nabla\Phi_0 + \frac{1}{4\pi}(\nabla \times \mathbf{B}_0) \times \delta\mathbf{B} + \frac{1}{4\pi}(\nabla \times \delta\mathbf{B}) \times \mathbf{B}_0, \quad (7.2.14)$$

$$\frac{\partial \delta\rho}{\partial t} = -\nabla \cdot (\rho_0 \mathbf{v}), \quad (7.2.15)$$

$$\frac{\partial \delta\mathbf{B}}{\partial t} = \nabla \times (\mathbf{v} \times \mathbf{B}_0), \quad (7.2.16)$$

Now using (7.2.6) to replace $\Phi_0$, equation (7.2.9) may be rewritten as

$$\begin{aligned} \frac{\partial \mathbf{f}}{\partial t} &= -\frac{\gamma P_0}{\rho_0}\nabla\delta\rho + \left[(2-\gamma)\nabla P_0 - \frac{1}{4\pi}(\nabla \times \mathbf{B}_0) \times \mathbf{B}_0\right]\frac{\delta\rho}{\rho_0} \\ &\quad + \frac{1}{4\pi}(\nabla \times \mathbf{B}_0) \times \delta\mathbf{B} + \frac{1}{4\pi}(\nabla \times \delta\mathbf{B}) \times \mathbf{B}_0, \quad (7.2.17) \end{aligned}$$

where we have defined $\mathbf{f} \equiv \rho_0 \mathbf{v}$. Working with $\mathbf{f}$ simplifies the boundary conditions; to the same end we define $\boldsymbol{\beta} = \rho_0 \delta\mathbf{B}$. Now

$$\nabla \times \delta\mathbf{B} = \nabla \times \left(\frac{\boldsymbol{\beta}}{\rho_0}\right) = \frac{1}{\rho_0}\nabla \times \boldsymbol{\beta} - \frac{\nabla\rho_0}{\rho_0^2} \times \boldsymbol{\beta} \quad (7.2.18)$$

and

$$\nabla \times (\mathbf{v} \times \mathbf{B}) = \nabla \times \left(\frac{\mathbf{f}}{\rho_0} \times \mathbf{B}_0\right) = \frac{1}{\rho_0}\nabla \times (\mathbf{f} \times \mathbf{B}_0) - \frac{\nabla\rho_0}{\rho_0^2} \times (\mathbf{f} \times \mathbf{B}_0). \quad (7.2.19)$$

Using these relations, together with the identity $\nabla P_0 = \frac{\gamma P_0}{\rho_0}\nabla\rho_0$, we arrive at the final form of our perturbation equations:

[1] In the mixed-field case we employ the vector potential $\mathbf{A}$; in the purely toroidal-field case the divergence $\nabla \cdot \mathbf{B}_{tor} \equiv 0$ since $\partial/\partial\phi \equiv 0$ in axisymmetry

$$\rho_0 \frac{\partial \mathbf{f}}{\partial t} = -\gamma P_0 \nabla \delta\rho + \left( \frac{(2-\gamma)\gamma P_0}{\rho_0} \nabla \rho_0 - \frac{1}{4\pi} (\nabla \times \mathbf{B}_0) \times \mathbf{B}_0 \right) \delta\rho + \frac{1}{4\pi} (\nabla \times \mathbf{B}_0) \times \boldsymbol{\beta} + \frac{1}{4\pi} (\nabla \times \boldsymbol{\beta}) \times \mathbf{B}_0 - \frac{1}{4\pi\rho_0} (\nabla \rho_0 \times \boldsymbol{\beta}) \times \mathbf{B}_0 \tag{7.2.20}$$

$$\frac{\partial \delta\rho}{\partial t} = -\nabla \cdot \mathbf{f}, \tag{7.2.21}$$

$$\frac{\partial \boldsymbol{\beta}}{\partial t} = \nabla \times (\mathbf{f} \times \mathbf{B}_0) - \frac{\nabla \rho_0}{\rho_0} \times (\mathbf{f} \times \mathbf{B}_0). \tag{7.2.22}$$

If we rewrite these equations in terms of $\delta P = \frac{\gamma P_0}{\rho_0} \delta\rho$ and set the magnetic field to zero they reduce to equations (15) and (16) of Passamonti et al. [110] in the unstratified limit.

Writing out our perturbation equations in terms of components leaves us with seven scalar equations governing the evolution of the perturbations. We write these concisely by defining the vector quantities:

$$\boldsymbol{\mathcal{A}} = \frac{1}{4\pi} (\nabla \times \mathbf{B}_0) \times \mathbf{B}_0 \tag{7.2.23}$$

$$\boldsymbol{\mathcal{B}} = \frac{1}{4\pi} (\nabla \times \mathbf{B}_0) \times \boldsymbol{\beta} \tag{7.2.24}$$

$$\boldsymbol{\mathcal{C}} = \frac{1}{4\pi} (\nabla \times \boldsymbol{\beta}) \times \mathbf{B}_0 \tag{7.2.25}$$

$$\boldsymbol{\mathcal{D}} = \frac{1}{4\pi} (\nabla \rho_0 \times \boldsymbol{\beta}) \times \mathbf{B}_0 \tag{7.2.26}$$

$$\boldsymbol{\mathcal{E}} = \nabla \times (\mathbf{f} \times \mathbf{B}_0) \tag{7.2.27}$$

$$\boldsymbol{\mathcal{F}} = \nabla \rho_0 \times (\mathbf{f} \times \mathbf{B}_0). \tag{7.2.28}$$

With these definitions our Euler equation becomes:

$$\rho_0 \partial_t f_r = -\gamma P_0 (\delta\rho)_{,r} + \left( \frac{(2-\gamma)\gamma P_0}{\rho_0} \rho_{0,r} - \mathcal{A}_r \right) \delta\rho + \mathcal{B}_r + \mathcal{C}_r - \frac{1}{\rho_0} \mathcal{D}_r \tag{7.2.29}$$

$$\rho_0 \partial_t f_\theta = -\frac{\gamma P_0}{r} (\delta\rho)_{,\theta} + \left( \frac{(2-\gamma)\gamma P_0}{\rho_0} \rho_{0,\theta} - \mathcal{A}_\theta \right) \delta\rho + \mathcal{B}_\theta + \mathcal{C}_\theta - \frac{1}{\rho_0} \mathcal{D}_\theta \tag{7.2.30}$$

$$\rho_0 \partial_t f_\phi = -\frac{\gamma P_0}{r \sin\theta} (\delta\rho)_{,\phi} - \mathcal{A}_\phi \delta\rho + \mathcal{B}_\phi + \mathcal{C}_\phi - \frac{1}{\rho_0} \mathcal{D}_\phi \tag{7.2.31}$$

whilst the continuity equation is:

$$-\partial_t \delta\rho = \frac{2f_r}{r} + f_{r,r} + \frac{f_\theta}{r\tan\theta} + \frac{f_{\theta,\theta}}{r} + \frac{f_{\phi,\phi}}{r\sin\theta}. \tag{7.2.32}$$

Finally the induction equation in components is:

$$\partial_t \beta_r = \mathcal{E}_r - \frac{1}{\rho_0}\mathcal{F}_r \tag{7.2.33}$$

$$\partial_t \beta_\theta = \mathcal{E}_\theta - \frac{1}{\rho_0}\mathcal{F}_\theta \tag{7.2.34}$$

$$\partial_t \beta_\phi = \mathcal{E}_\phi - \frac{1}{\rho_0}\mathcal{F}_\phi. \tag{7.2.35}$$

We next write all perturbed quantities as:

$$\delta(t,r,\theta,\phi) = \sum_{m=0}^{\infty} \delta_m^+(t,r,\theta)\cos m\phi + \delta_m^-(t,r,\theta)\sin m\phi. \tag{7.2.36}$$

We will drop the $m$ subscripts, with the understanding that the following relations in $\delta^+$ and $\delta^-$ quantities are for a fixed azimuthal index $m$. This decomposition removes the $\phi$ dependence of the perturbations at the expense of doubling the number of equations: we now have 2D evolution equations in 14 perturbations: $f_r^+, f_r^-, f_\theta^+, f_\theta^-, f_\phi^+, f_\phi^-, \delta\rho^+, \delta\rho^-, \beta_r^+, \beta_r^-, \beta_\theta^+, \beta_\theta^-, \beta_\phi^+, \beta_\phi^-$. We demonstrate this decoupling with the unmagnetised version of the $\partial_t f_r$ equation:

$$\rho_0 \partial_t f_r = -\gamma P_0 \frac{\partial \delta\rho}{\partial r} + \frac{(2-\gamma)\gamma P_0}{\rho_0}\frac{\partial \rho_0}{\partial r}\delta\rho. \tag{7.2.37}$$

With the $\phi$ decomposition this becomes

$$\begin{aligned} \rho_0 \partial_t (f_r^+ \cos m\phi \; + \; & f_r^- \sin m\phi) \\ = \; & -\gamma P_0 \frac{\partial}{\partial r}(\delta\rho_r^+ \cos m\phi + \delta\rho_r^- \sin m\phi) \\ & + \frac{(2-\gamma)\gamma P_0}{\rho_0}\frac{\partial \rho_0}{\partial r}(\delta\rho_r^+ \cos m\phi + \delta\rho_r^- \sin m\phi). \end{aligned} \tag{7.2.38}$$

Now equating $\cos m\phi$ and $\sin m\phi$ terms we see that

$$\rho_0 \partial_t f_r^+ = -\gamma P_0 \frac{\partial \delta\rho^+}{\partial r} + \frac{(2-\gamma)\gamma P_0}{\rho_0}\frac{\partial \rho_0}{\partial r}\delta\rho^+. \tag{7.2.39}$$

$$\rho_0 \partial_t f_r^- = -\gamma P_0 \frac{\partial \delta\rho^-}{\partial r} + \frac{(2-\gamma)\gamma P_0}{\rho_0}\frac{\partial \rho_0}{\partial r}\delta\rho^-. \tag{7.2.40}$$

$$\tag{7.2.41}$$

The full, $\phi$-decomposed system of perturbations is given in the appendix, section A.1.

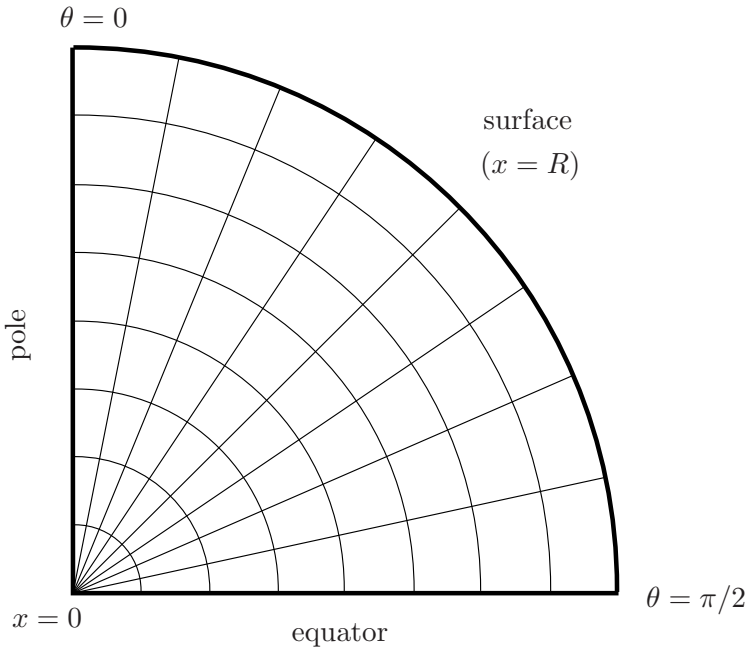


Figure 7.1: The numerical grid used in the code. After decomposing the perturbation variables in $\phi$ only a 2D grid is needed. This is evenly divided in $\theta$ and in the coordinate $x \equiv x(r, \theta)$, which is fitted to isopycnic surfaces of the star. With suitable boundary conditions at the equator and pole, only one quarter of a disc is needed for the evolutions.

### 7.2.2 Boundary conditions

With suitable boundary conditions and the decomposition in $\phi$, we are able to reduce our numerical domain from a sphere to one quadrant of a disc, as shown in figure 7.1. We describe these conditions here.

#### Surface

Rotational and magnetic forces will serve to distort the star's density distribution away from spherical symmetry and hence complicate the treatment of perturbations at the stellar surface. To avoid these complications we replace the radial coordinate $r$ with one fitted to isopycnic surfaces, $x = x(r, \theta)$; even a nonspherical surface will be defined by one value $x = R$. With the background density being a function of $x$

alone, we have $\rho_0(x=R)=0$ and hence

$$\mathbf{f}(x=R)=\boldsymbol{\beta}(x=R)=\mathbf{0}. \tag{7.2.42}$$

Finally, the Lagrangian pressure perturbation $\Delta P$ is zero at the surface by definition. Relating this to the Eulerian perturbation we have

$$\delta P+\boldsymbol{\xi}\cdot\nabla P_0=0 \quad \text{at the surface.} \tag{7.2.43}$$

Using (7.2.6), we see that $\nabla P_0$ may be written as two terms proportional to $\rho_0$ and a term involving the magnetic current $\nabla\times\mathbf{B}/4\pi$. Both density and current are zero at the stellar surface and so $\nabla P_0$ must also vanish there. This yields our last surface boundary condition:

$$\delta P(x=R)=0. \tag{7.2.44}$$

Our boundary conditions allow us to evolve the interior magnetic field perturbations of our star, but not oscillations of the exterior. By contrast, one would expect magnetic perturbations in a physical neutron star to reach the surface and produce electromagnetic radiation extending through the exterior. Whilst our treatment of the surface does not account for this, we believe that it is the most that can be done using the equations of perfect MHD: in an infinitely-conducting polytropic star, a magnetic field that extends to the surface has a corresponding Alfvén speed $c_A\equiv\sqrt{B^2/4\pi\rho}$ which becomes superluminal at some low density and infinite when $\rho=0$ (i.e. the stellar surface and exterior).

Dealing with the surface and exterior thus requires extra physics: a stellar model more sophisticated than a polytropic fluid with perfect electrical conductivity. One could employ a low-density numerical atmosphere for the exterior, or assume that the field is confined or matches to some simplified crust — but these are merely numerical conveniences rather than good models of actual NS physics. In reality, perfect MHD ceases to be a good approximation close to the surface of a NS, where resistive effects become important and the full equations of electromagnetism should be used. The stellar surface is not fluid but an elastic crust; and the exterior will have a magnetosphere region rather than a dilute, uniform 'atmosphere'.

Needless to say, a credible model star which included all these effects would give an oscillation spectrum closer to that of a real neutron star than the one we study here. In lieu of such a model, however, we treat oscillations over the fluid, highly-conductive interior of the star only. With magnetic fields being strongest here and

$\sim 99\%$ of the NS's mass consisting of a fluid interior, we suggest that dynamics in this region could dominate the star's oscillation spectrum; and hence that our treatment is a reasonable first attempt to understand oscillations in real NSs.

### Centre

Next we look at the conditions at the centre of the star. Since we deal with $m > 0$ perturbations in this study, we should enforce a zero-displacement condition:

$$\delta P(x{=}0) = 0 \ , \ \mathbf{f}(x{=}0) = \boldsymbol{\beta}(x{=}0) = \mathbf{0}. \tag{7.2.45}$$

### Equator

The equatorial symmetry properties of the perturbations in a fluid star may be established through analysis of the governing equations. Specifically, one looks at the behaviour of the equations under reflection about the equator: $r \mapsto r, \theta \mapsto \pi - \theta$ (we have already decomposed in $\phi$). In many cases, one finds that the variables may be classed according to their equatorial symmetry — either odd (the perturbation is zero across the equator) or even (its $\theta$-derivative is zero there). That is, certain variables will always have one symmetry class (e.g. even) and the other variables will always have the other symmetry class (odd if the first class are even). If analysis of all the equations places each variable consistently in the same symmetry class, then the system is indeed symmetric about the equator; in this case we are able to reduce our numerical domain to just one 2D quadrant and enforce the perturbation symmetry at the equator as another set of boundary conditions.

Analysing the perturbation equations for the (unmagnetised) rotating fluid problem, one finds that the perturbation variables may be divided into the two symmetry classes $\{f_r^{\pm}, f_\phi^{\pm}, \delta\rho^{\pm}\}$ and $\{f_\theta^{\pm}\}$. In the case of a background star with a pure poloidal field these classes are augmented by magnetic variables, viz. $\{f_r^{\pm}, f_\phi^{\pm}, \delta\rho^{\pm}, \beta_\theta^{\pm}\}$, $\{f_\theta^{\pm}, \beta_r^{\pm}, \beta_\phi^{\pm}\}$. Note that although the background field is pure-poloidal, the perturbed field will still be mixed poloidal-toroidal. For a pure-toroidal background the magnetic perturbations are again mixed, but they fall into *different* symmetry classes from perturbations of a pure-poloidal star: $\{f_r^{\pm}, f_\phi^{\pm}, \delta\rho^{\pm}, \beta_r^{\pm}, \beta_\phi^{\pm}\}$ and $\{f_\theta^{\pm}, \beta_\theta^{\pm}\}$. It follows that whilst we may separately treat perturbations on either a pure-poloidal or pure-toroidal background, the perturbations of a mixed-field background will have no definite equatorial symmetry. Investigating this latter group

of perturbations requires an extended numerical domain consisting of an upper and lower quadrant. For the work reported here we concentrate only on oscillations of stars with purely toroidal background fields.

### Pole

Recall from chapter 5 that a general vector perturbation (the velocity is shown here) can be decomposed as

$$\mathbf{v} = U(r)Y_{lm}\mathbf{e}_r + V(r)\nabla Y_{lm} + W(r)\mathbf{e}_r \times \nabla Y_{lm}, \tag{7.2.46}$$

whilst a scalar perturbation (in this case, the density) will have the form

$$\delta\rho = T(r)Y_{lm}. \tag{7.2.47}$$

From the form of these perturbations, their behaviour at the pole may be deduced. Although we do not decompose in $\theta$ in the code, we will find it convenient to rewrite the spherical harmonics using $Y_{lm}(\theta,\phi) = P_{lm}(\theta)\mathrm{e}^{im\phi}$ (the constants are unimportant; they may be regarded as absorbed into the radial function). The boundary conditions at the pole $\theta = 0$ are then given by the behaviour of the relevant functions of $P_{lm}$ there. Using recurrence relations (see for example Arfken and Weber [6]), one may show that a Legendre function $P_{lm}$ contains a $\sin^m\theta$ term and that its $\theta$-derivative $\mathrm{d}P_{lm}/\mathrm{d}\theta$ contains a $\sin^{m+1}\theta$ term and a $\sin^{m-1}\theta$ term.

By (7.2.47), it is clear that scalar perturbations have $\theta$-dependence given simply by $P_{lm}$; since we are concerned with $m \neq 0$ perturbations our BC at the pole is that a scalar perturbation must vanish there.

For vector perturbations, we first re-express (7.2.46) in terms of spherical polar components:

$$\begin{aligned}
v_r &= U(r)Y_{lm} && (7.2.48)\\
v_\theta &= V(r)\nabla Y_{lm}\cdot\mathbf{e}_\theta + W(r)(\mathbf{e}_r\times\nabla Y_{lm})\cdot\mathbf{e}_\theta \\
&= \frac{\mathrm{e}^{im\phi}}{r}\left(V(r)P_{lm,\theta} - \frac{imW(r)}{\sin\theta}P_{lm}\right) && (7.2.49)\\
v_\phi &= V(r)\nabla Y_{lm}\cdot\mathbf{e}_\phi + W(r)(\mathbf{e}_r\times\nabla Y_{lm})\cdot\mathbf{e}_\phi \\
&= \frac{\mathrm{e}^{im\phi}}{r}\left(V(r)P_{lm,\theta} + \frac{imW(r)}{\sin\theta}P_{lm}\right) && (7.2.50)
\end{aligned}$$

From these, it is clear that $v_r = 0$ at the pole for all $m \neq 0$. $v_\theta$ and $v_\phi$ may be expressed as powers of $\sin\theta$ as described earlier; the lowest power in each case is

$\sin^{m-1}\theta$. We deduce that $v_\theta = v_\phi = 0$ at the pole for $m \geq 2$, whilst for $m = 1$ the boundary condition only requires them to be finite and continuous; in this case the boundary condition is that the $\theta$-derivatives should vanish at the pole.

In summary, then, the boundary conditions at the pole for $\delta\rho, \mathbf{v}$ and $\boldsymbol{\beta}$ are:

$$\begin{aligned} \delta\rho = v_r = \beta_r &= 0 \quad \forall m \neq 0 \\ v_\theta = v_\phi = \beta_\theta = \beta_\phi &= 0 \quad m \geq 2 \\ v_{\theta,\theta} = v_{\phi,\theta} = \beta_{\theta,\theta} = \beta_{\phi,\theta} &= 0 \quad m = 1 \end{aligned}$$

### 7.2.3 Initial data

Let us return again to the general forms of scalar and vector perturbations given by (7.2.47) and (7.2.46):

$$\begin{aligned} \mathbf{v} &= U(r)Y_{lm}\mathbf{e}_r + V(r)\nabla Y_{lm} + W(r)\mathbf{e}_r \times \nabla Y_{lm} \\ \delta\rho &= T(r)Y_{lm} \end{aligned}$$

where the functions $U(r)$ and $V(r)$ are coefficients of the *polar* part and $W(r)$ is the coefficient of the *axial* term in the vector perturbation. The scalar perturbation only has a polar term, with coefficient $T(r)$. It follows that we should choose different initial data for evolutions based on whether we wish to study polar or axial oscillation modes. Considering the nonrotating and unmagnetised case for simplicity, we wish to see what initial data excites axial modes and what excites polar modes. Velocity and density perturbations are discussed separately.

#### Velocity initial data

Assume the initial data is some velocity $\mathbf{v}$. Then by the continuity equation a perturbation will be induced in the density, governed by

$$\frac{\partial\delta\rho}{\partial t} = -\nabla\cdot(\rho_0\mathbf{v}) = -\rho_0\nabla\cdot\mathbf{v} - \nabla\rho_0\cdot\mathbf{v}. \tag{7.2.51}$$

Since $\rho_0$ is spherically symmetric (with no rotation or magnetic field to distort it), we then have

$$\frac{\partial\delta\rho}{\partial t} = -\rho_0\nabla\cdot\mathbf{v} - \frac{\mathrm{d}\rho_0}{\mathrm{d}t}v_r. \tag{7.2.52}$$

Taking the divergence of (7.2.46) gives

$$\nabla\cdot\mathbf{v} = \frac{\mathrm{d}U}{\mathrm{d}r}Y_{lm} + \frac{2}{r}UY_{lm} + V\nabla^2 Y_{lm} + W\nabla\cdot(\mathbf{e}_r\times\nabla Y_{lm}), \tag{7.2.53}$$

where we have used the result that the scalar product of orthogonal vectors is zero. Using Legendre's equation $\nabla^2 Y_{lm} = -l(l+1)Y_{lm}/r^2$ and simplifying then gives

$$\nabla \cdot \mathbf{v} = \left( \frac{\mathrm{d}U}{\mathrm{d}r} + \frac{2}{r}U - \frac{l(l+1)V}{r^2} \right) Y_{lm} + W \nabla \cdot (\mathbf{e}_r \times \nabla Y_{lm}). \tag{7.2.54}$$

Now consider the final term (whose coefficient is the radial function $W(r)$). In spherical polar components we have

$$\mathbf{e}_r \times \nabla Y_{lm} = \begin{pmatrix} 0 \\ \frac{m}{r \sin\theta} Y_{lm} \\ -\frac{1}{r} Y_{lm,\theta} \end{pmatrix}, \tag{7.2.55}$$

the divergence of which is zero — and so the final term in (7.2.54) is zero, and we are left with

$$\nabla \cdot \mathbf{v} = \left( \frac{\mathrm{d}U}{\mathrm{d}r} + \frac{2}{r}U - \frac{l(l+1)V}{r^2} \right) Y_{lm}, \tag{7.2.56}$$

i.e. polar initial data in $\mathbf{v}$ induces a perturbation in $\delta\rho$, but an axial initial $\mathbf{v}$ produces *no* perturbation in the density (for a spherically symmetric background star).

### Density initial data

Using a similar approach, let us start with some initial $\delta\rho$ and find the induced velocity perturbation. In this case we need the Euler equation, which is

$$\frac{\partial \rho_0 \mathbf{v}}{\partial t} = \rho_0 \frac{\partial \mathbf{v}}{\partial t} = -\frac{\gamma P_0}{\rho_0} \nabla \delta\rho + \frac{(2-\gamma)\gamma P_0}{\rho_0} \delta\rho \tag{7.2.57}$$

Since the angular dependence of $\delta\rho$ is given simply by $Y_{lm}$, it is immediately clear that the induced $\mathbf{v}$ consists of a $Y_{lm}$ term and a $\nabla Y_{lm}$ term and hence is a polar perturbation. Therefore, initial data in $\delta\rho$ can only induce a polar velocity perturbation.

### Initial data used in the code

From the above analysis, we see that axial initial data in $\mathbf{v}$ will produce purely axial perturbations and no $\delta\rho$, in the case of a spherically symmetric background. Adding a distorting effect to the background configuration, the resultant modes will still be dominantly axial unless the distortion is very large — i.e. fast rotation or extremely strong magnetic fields. Similarly, an initial $\delta\rho$ will induce only polar

modes in a spherical star; for a non-spherical star the modes will not be purely polar, but polar-led modes should still dominate the oscillation spectrum.

Hence, we excite polar/polar-led modes using initial data given by

$$\delta\rho = \frac{r^m}{R^m} Y_{mm}(\theta) = \left(\frac{r\sin\theta}{R}\right)^m \tag{7.2.58}$$

and axial/axial-led modes with an initial perturbation of the form

$$\mathbf{f} = \rho_0 \mathbf{v} = \rho_0 \mathrm{e}^{(r^m/R^m)} \mathbf{e}_r \times \nabla Y_{mm}, \tag{7.2.59}$$

where $R$ is the stellar radius. Similar choices were used by Jones et al. [75] and Passamonti et al. [110] for oscillations of unmagnetised stars. We find that these forms of initial data also efficiently excite oscillations of magnetised configurations.

## 7.3 Numerics

### 7.3.1 Plan of code

As described above, our numerical domain is one quadrant of a (2D) disc, with $x \in [0, 1]$ and $\theta \in [0, \pi/2]$; by symmetry and through a $\phi$-decomposition this domain is sufficient to investigate behaviour over the whole 3D, potentially nonspherical, star. Upon decomposing in $\phi$, we have a system of fourteen perturbation equations to evolve in time.

The code we use is written in C and C++ and is divided into a number of subroutines, which are shown in figure 7.2. The idea is to first generate the requisite background star, with a chosen rotation rate and magnetic field strength. Initial data is specified: either the $f$-mode file, which excites polar and polar-led modes; or the $r$-mode or inertial-mode file, which both excite the axial class of oscillations. Since we have decomposed in $\phi$, we also need to specify the azimuthal index $m$ for each evolution. Linear perturbation equations are then evolved on this background and with the given initial conditions, subject to the requisite boundary conditions.

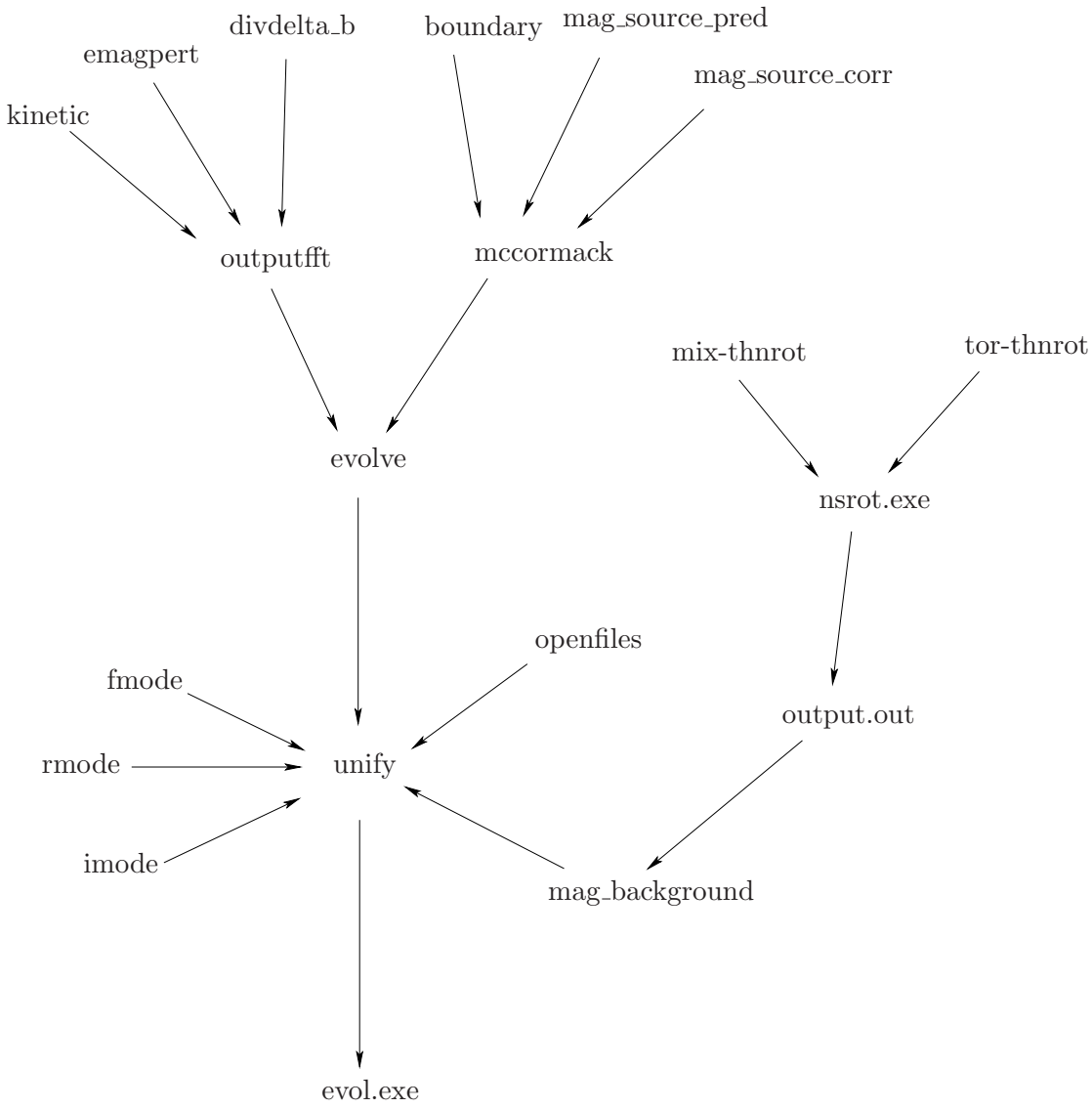


Figure 7.2: Schematic plan of the code. The main routine is unify, and evol.exe is the executable time-evolution code. In addition to the subroutines shown above, the code also employs the header files defs.h, globals.h, proto.h and nrutil.h.

In more detail, the time-evolution code compiles an executable, evol.exe, from a number of subroutines. To generate the background star, one must first make the executable nsrot.exe from either tor-thnrot.c or mix-thnrot.c; the former gives stars with purely toroidal fields, the latter allows for mixed toroidal-poloidal fields with pure poloidal fields as a special case. Next nsrot.exe is run, with user-specified parameters related to rotation rate and magnetic field strength. This generates a large data file output.out containing all background quantities at each grid point. This is scanned by mag_background, a subroutine which imports all this background data into the time-evolution code proper.

Mag_background is in turn called by unify, the highest-level subroutine in the code — unify itself being used to compile the final executable evol.exe. In addition to mag_background, unify calls three other subroutines: openfiles designates files to contain information from the running executable, evolve contains the actual code responsible for evolving the perturbation equations, and finally one of the three initial data files (fmode, rmode or imode) is called, specified in the header file defs.h.

The subroutine evolve calls two lower subroutines itself. One, outputfft, saves data from different timesteps — both direct information about the perturbations $\delta\rho$, $\mathbf{f}$ and $\boldsymbol{\beta}$, and combinations of these variables: the kinetic and magnetic energy in the perturbations, and the divergence of the perturbed field (generated in their own subroutines kinetic, emagpert and divdelta_b respectively). The other subroutine called from evolve is the key one: mccormack. This subroutine uses the McCormack predictor-corrector scheme (see the following subsection) to evolve linear perturbations on the background star. These perturbations are evolved in the interior of the star from sources contained in the subroutines mag_source_pred and mag_source_corr respectively, whilst the boundary conditions are imposed after each timestep using the boundary-condition subroutine boundary.

### 7.3.2 McCormack scheme

To evolve the perturbation equations of our system numerically, we employ the McCormack scheme [97]. This is a 'predictor-corrector' method: starting at some particular timestep $t^n$ (where $n$ is an index, not a power), it begins with an estimate of the values of the variables at the next timestep $t^{n+1}$ (the predictor step) and then uses this estimated value to improve the solution at the new timestep $t^{n+1}$

(the corrector step). Although both the predictor and corrector steps are only first-order, they are combined in a way that gives an overall scheme which is second-order accurate.

More specifically, let us consider the Euler equation. This equation relates the evolution of the fluid velocity $\mathbf{v}$ to quantities involving the background and perturbed density, pressure and magnetic field. For simplicity we group all of these quantities into the source term $\mathbf{S}$; the Euler equation is then

$$\frac{\partial \mathbf{v}}{\partial t} = \mathbf{S}. \tag{7.3.1}$$

We start at timestep $t^n$, with known values of the velocity $\mathbf{v}^n$ and the source term $\mathbf{S}^n$. The predictor step of the McCormack scheme then provides an estimate $\tilde{\mathbf{v}}^{n+1}$ for the velocity at the next timestep:

$$\tilde{\mathbf{v}}_i^{n+1} = \mathbf{v}_i^n - \frac{\Delta t}{\Delta x}\left(\mathbf{S}_i^n - \mathbf{S}_{i-1}^n\right) \tag{7.3.2}$$

where the index $i$ labels a spatial point in the grid, $\Delta t$ is the size of the timestep and $\Delta x$ the grid spacing. The corrector step then combines the predicted $\tilde{\mathbf{v}}^{n+1}$ with the original $\mathbf{v}^n$ into a second-order accurate $\mathbf{v}^{n+1}$:

$$\mathbf{v}_i^{n+1} = \frac{1}{2}\left(\tilde{\mathbf{v}}_i^{n+1} + \mathbf{v}_i^n\right) - \frac{\Delta t}{2\Delta x}\left(\tilde{\mathbf{S}}_{i+1}^{n+1} - \tilde{\mathbf{S}}_i^{n+1}\right) \tag{7.3.3}$$

where $\tilde{\mathbf{S}}^{n+1}$ is the source term evaluated from the predictor-step estimates for quantities at the new timestep.

The continuity equation and the induction equation are evolved in the same manner as described above for the Euler equation. A full derivation of this scheme, together with details of its stability are given by Hirsch [66].

### 7.3.3 Kreiss-Oliger dissipation

Finite difference methods, like the one used for the time evolution code presented here, approximate a continuum problem by a discrete one. Quantities which should be smooth are replaced by approximations to their values over a finite number of points. Because the actual system of PDEs evolved contains this numerical error, one would expect this discretised system to have oscillations dependent on the grid spacing $h$. In particular, there may be solutions of the form $\exp(at/h)$, where $a > 0$. These are unphysical instabilities, not present in the continuum solution, and need to be removed.

To do this, we use *Kreiss-Oliger dissipation*; this is an extra term added to the Euler equation [82]. It has the form of a viscosity, which damps out spurious high-frequency oscillations. This viscosity term is given by some dissipation operator $D_4$ acting on the fluid velocity $v$; its form (shown in 1D for simplicity) is

$$(D_4 v)_i = -\frac{1}{16h}\left(v_{i-2} - 4v_{i-1} + 6v_i - 4v_{i+1} + v_{i+2}\right) \tag{7.3.4}$$

at some gridpoint $i$ [66]. This term is fourth-order in accuracy and so does not affect the overall order of convergence of the (second-order) code. The magnitude of this term is resolution-dependent, so that it vanishes in the infinite-resolution continuum limit.

### 7.3.4 Artificial resistivity

In addition to this dissipation, two further tricks are required to ensure stability and accuracy of magnetic evolutions. To stabilise the numerical evolution of the magnetic field, we first note that if the electrical resistivity $\eta$ is non-zero, the induction equation gains an extra term:

$$\frac{\partial \mathbf{B}}{\partial t} = \nabla \times (\mathbf{v} \times \mathbf{B}) - \eta \nabla \times (\nabla \times \mathbf{B}). \tag{7.3.5}$$

By including this second term (at a small magnitude) we are able to suppress instabilities which arise from evolving the magnetic field. As for the Kreiss-Oliger dissipation, this artificial resistivity is added in a resolution-dependent manner, becoming zero in the continuum limit. We find that a very small value of $\eta$ is sufficient to improve long-term stability, but has negligible physical effect on our evolutions, since it acts over a far longer timescale than any others in our problem.

### 7.3.5 Divergence cleaning

Finally, for the long-term accuracy of the code we need to ensure that the perturbed magnetic field remains solenoidal. This is guaranteed in the continuum limit if the initial data has no monopolar term, since the divergence of the induction equation is

$$\frac{\partial (\nabla \cdot \mathbf{B})}{\partial t} = \nabla \cdot \nabla \times (\mathbf{v} \times \mathbf{B}) \equiv 0, \tag{7.3.6}$$

but in practice numerical error will be introduced from the finite grid resolution. It is important to 'clean' the field of this class of numerical error, since it has been

shown that a numerically-generated monopolar field gives rise to a spurious extra force [13].

There are various approaches to divergence cleaning for numerical schemes. A review of these may be found in Dedner et al. [38], where in addition a new constrained formulation of MHD is proposed, where the condition $\nabla \cdot \mathbf{B} = 0$ is coupled to the induction equation through an auxiliary function; we repeat their argument below.

In the continuum limit the induction equation states that the vector $\partial_t \mathbf{B}$ has a divergence-free part only, whereas a general vector can be decomposed into curl-free and divergence-free parts. Our discretised induction equation will no longer preserve this divergence-free property exactly and accordingly we add a curl-free term $-\nabla\psi$ to the RHS, with $\psi$ being some unknown function. We then couple our augmented induction equation to a relation for $\psi$:

$$\partial_t \mathbf{B} = \nabla \times (\mathbf{v} \times \mathbf{B}) - \nabla\psi \tag{7.3.7}$$

$$\mathcal{D}(\psi) = -\nabla \cdot \mathbf{B} \tag{7.3.8}$$

where $\mathcal{D}$ is some linear differential operator. The Euler equation and the equation of mass conservation are unaffected. We now take the divergence of the first relation and the time derivative of the second:

$$\partial_t(\nabla \cdot \mathbf{B}) = -\nabla^2\psi \tag{7.3.9}$$

$$\partial_t \mathcal{D}(\psi) = -\partial_t(\nabla \cdot \mathbf{B}) \tag{7.3.10}$$

which we combine to see that

$$\partial_t \mathcal{D}(\psi) = \nabla^2\psi. \tag{7.3.11}$$

The choice of $\mathcal{D}$ determines the way in which divergence errors are removed. The three basic types of cleaning are elliptic, parabolic and hyperbolic — so named because they entail solving a Poisson equation, heat equation or wave equation, respectively. Dedner et al. [38] pioneer a mixed hyperbolic-parabolic approach, which they find to be superior to the simpler divergence-cleaning methods since it allows for errors to be propagated out of the star (hyperbolic cleaning) whilst simultaneously being damped (parabolic cleaning). The third method, elliptic cleaning, has

the serious disadvantage that it requires the repeated solution of the (computationally expensive) Poisson equation; the mixed-hyperbolic scheme only adds the modest expense of having to evolve one more quantity — the function $\psi$.

Hyperbolic-parabolic divergence cleaning involves defining $\mathcal{D}$ by

$$\mathcal{D}(\psi) = \frac{1}{c_h^2}\partial_t\psi + \frac{1}{c_p^2}\psi, \tag{7.3.12}$$

which leads to a telegraph (damped-wave) equation for $\psi$:

$$\partial_{tt}\psi = -\frac{c_h^2}{c_p^2}\partial_t\psi + c_h^2\nabla^2\psi. \tag{7.3.13}$$

Within the code, we implement this divergence-cleaning method through the evolution equation

$$\partial_t\psi = -\frac{c_h^2}{c_p^2}\psi - c_h^2\nabla\cdot\mathbf{B} \tag{7.3.14}$$

together with our modified induction equation (7.3.7). Following Price and Monaghan [113] we take $c_h$, the divergence-wave propagation speed, to be related to the sound $c_s$ and Alfvén $c_A$ speeds through the relation:

$$c_h = \sqrt{c_s^2 + c_A^2}. \tag{7.3.15}$$

The other coefficient is physically the inverse of the decay timescale $\tau$ of equation (7.3.13):

$$\frac{c_h^2}{c_p^2} = \frac{1}{\tau} \tag{7.3.16}$$

which Price and Monaghan argue is not universal, but rather should be adapted to suit some lengthscale $\lambda$ specific to the problem, i.e.

$$\frac{c_h^2}{c_p^2} = \frac{1}{\tau} = \frac{\alpha c_h}{\lambda}, \tag{7.3.17}$$

where $\alpha$ is a dimensionless parameter. Using this result, we take $\lambda$ to be the radial grid spacing $\Delta r$ in our code. Finally then, our evolution equation for the function $\psi$ is

$$\partial_t\psi = -\frac{\alpha\sqrt{c_s^2 + c_A^2}}{\Delta r}\psi - (c_s^2 + c_A^2)\nabla\cdot\mathbf{B}. \tag{7.3.18}$$

To close the system we need to give appropriate boundary conditions and initial data. For the latter we simply set $\psi(t = 0) = 0$ — this is reasonable because the

initial data is divergence-free and so the variable $\psi$, associated with the monopole part of the magnetic field, should be zero initially.

For the boundary condition at the surface, we choose the Sommerfeld outgoing-wave condition on $\psi$:

$$\partial_t \psi = -\sqrt{c_s^2 + c_A^2}\,(\partial_r \psi + \psi)\,. \tag{7.3.19}$$

This result is for a spherical surface, but we find it still gives satisfactory cleaning in the case where the background star is spheroidal.

### 7.3.6 Testing the code

Since we already have confidence in the performance of the code in the nonmagnetic limit (see Passamonti et al. [110] for details), we now test its accuracy and convergence properties with the inclusion of magnetic effects. To this end, we wish to monitor the divergence of the magnetic field and the total energy of the system (which should be conserved in the continuum limit). Since the background configurations are stationary their total energy is automatically conserved. In addition, the background magnetic fields are also guaranteed divergence-free: in the purely poloidal/mixed-field case the field is written in terms of the vector potential $\mathbf{A}$, and so

$$\nabla \cdot \mathbf{B} = \nabla \cdot \nabla \times \mathbf{A} \equiv 0; \tag{7.3.20}$$

whilst in the pure-toroidal field case

$$\nabla \cdot \mathbf{B} = \frac{1}{r \sin\theta} \frac{\partial B_\phi}{\partial \phi} \equiv 0 \tag{7.3.21}$$

since $\partial/\partial\phi \equiv 0$ in axisymmetry. Therefore it suffices to check conservation of the perturbed energy and the value of $\nabla \cdot \delta\mathbf{B}$.

#### Divergence of $\delta\mathbf{B}$

Let us first write $\nabla \cdot \delta\mathbf{B}$ in terms of the code variable $\boldsymbol{\beta} = \rho_0 \delta\mathbf{B}$:

$$\nabla \cdot \delta\mathbf{B} = \nabla \cdot \left(\frac{\boldsymbol{\beta}}{\rho_0}\right) = \frac{1}{\rho_0} \nabla \cdot \boldsymbol{\beta} - \frac{1}{\rho_0^2} \nabla\rho_0 \cdot \boldsymbol{\beta}. \tag{7.3.22}$$

Expanding the quantities in the previous equation into components we find that

$$\begin{aligned} \nabla \cdot \boldsymbol{\beta} \;=\; & \left(\beta^+_{r,r} + \frac{2}{r}\beta^+_r + \frac{1}{r}\beta^+_{\theta,\theta} + \frac{1}{r\tan\theta}\beta^+_\theta + \frac{m}{r\sin\theta}\beta^-_\phi\right)\cos m\phi \\ & + \left(\beta^-_{r,r} + \frac{2}{r}\beta^-_r + \frac{1}{r}\beta^-_{\theta,\theta} + \frac{1}{r\tan\theta}\beta^-_\theta - \frac{m}{r\sin\theta}\beta^+_\phi\right)\sin m\phi \end{aligned} \tag{7.3.23}$$

and

$$\nabla\rho_0 \cdot \boldsymbol{\beta} = \frac{\partial\rho_0}{\partial r}\beta_r + \frac{1}{r}\frac{\partial\rho_0}{\partial\theta}\beta_\theta. \tag{7.3.24}$$

It is clear that $\nabla \cdot \delta\mathbf{B}$ consists of a component with $\cos m\phi$ dependence and another with $\sin m\phi$ dependence; we denote these $(\nabla\cdot\delta\mathbf{B})^+$ and $(\nabla\cdot\delta\mathbf{B})^-$ respectively. To test the divergence-cleaning method of section 7.3.5, we evolve initial data containing a large monopolar piece both with and without divergence cleaning (DC); the results are shown in figure 7.3. We choose to use $(\nabla \cdot \delta\mathbf{B})^-$, but the results are the same for $(\nabla\cdot\delta\mathbf{B})^+$. After a short time the initially central monopolar region has been propagated to the edge of the star by the divergence cleaning method; in the non-DC evolution it is virtually unchanged. At late times, there is no trace of the initial monopolar data in the DC evolution and the divergence is low throughout the star. The non-DC evolution, however, illustrates why $\nabla \cdot \mathbf{B} = 0$ must be enforced: an instability has set in at the centre, with the divergence growing to a huge value.

The test in figure 7.3 shows that any divergence in the field is propagated throughout the star and leaves when it reaches the surface. This is laborious to check at all points in the star for each evolution, so we would also like a way of checking the divergence globally. However, one cannot simply use the volume integral of $\nabla \cdot \delta\mathbf{B}$ over the star, since $\nabla \cdot \delta\mathbf{B} = (\nabla \cdot \delta\mathbf{B})^+ \cos m\phi + (\nabla \cdot \delta\mathbf{B})^- \sin m\phi$; both terms are zero after $\phi$-integration. Instead we define a 'monopole energy'

$$\mathfrak{D} \equiv \frac{R^2}{8\pi}\int (\nabla \cdot \delta\mathbf{B})^2 \,\mathrm{d}V \tag{7.3.25}$$

where $R$ is the stellar radius, included to give $\mathfrak{D}$ the dimensions of an energy for a meaningful comparison with the perturbed magnetic energy $\delta M$ (whose explicit form is given in equation (7.3.30)); we need $\mathfrak{D}$ to stay small throughout each evolution.

Using the above expressions for $\nabla \cdot \delta\mathbf{B}$ and recalling that $\sin^2 m\phi$ and $\cos^2 m\phi$ integrate to $\pi$ whilst $\sin m\phi \cos m\phi$ integrates to zero, we find that

$$\begin{aligned}\mathfrak{D} \;=\; & \frac{1}{8}\int \frac{1}{\rho_0^2}\left(\beta^+_{r,r} + \frac{2\beta^+_r}{r} + \frac{\beta^+_{\theta,\theta}}{r} + \frac{\beta^+_\theta}{r\tan\theta} + \frac{m\beta^-_\phi}{r\sin\theta} - \frac{\rho_{0,r}\beta^+_r}{\rho_0} - \frac{\rho_{0,\theta}\beta^+_\theta}{r\rho_0}\right)^2 \\ & + \frac{1}{\rho_0^2}\left(\beta^-_{r,r} + \frac{2}{r}\beta^-_r + \frac{\beta^-_{\theta,\theta}}{r} + \frac{\beta^-_\theta}{r\tan\theta} - \frac{m\beta^+_\phi}{r\sin\theta} - \frac{\rho_{0,r}\beta^-_r}{\rho_0} - \frac{\rho_{0,\theta}\beta^-_\theta}{r\rho_0}\right)^2 \mathrm{d}r\mathrm{d}\theta.\end{aligned} \tag{7.3.26}$$

For the results presented in this thesis, the divergence of $\delta\mathbf{B}$ was monitored through the dimensionless quantity $\mathfrak{D}/\delta M$. This value oscillates over time, but we

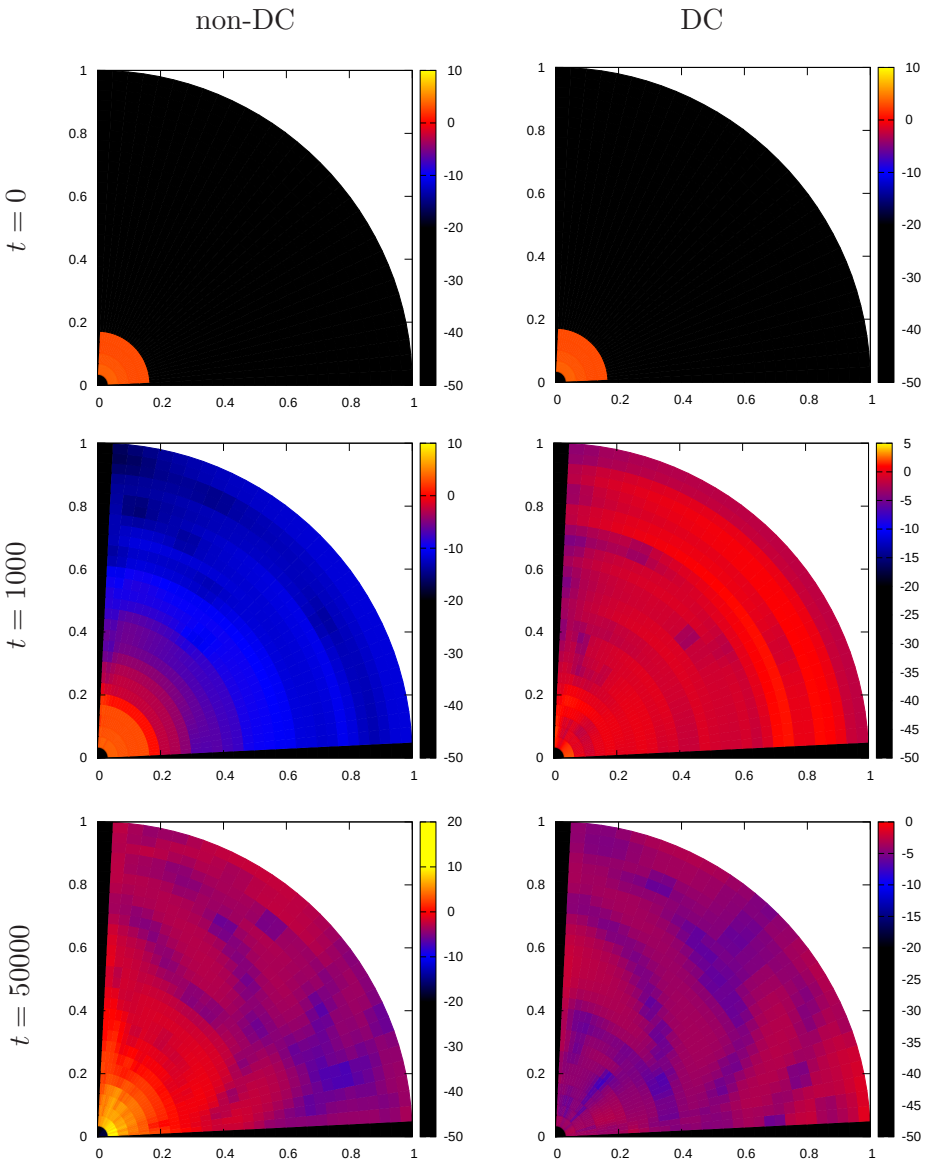


Figure 7.3: Testing the divergence-cleaning method used in the code. Monopolar initial data is evolved without (left column) and with (right column) divergence cleaning; the value of $\log[(\nabla \cdot \delta\mathbf{B})^{-}]$ is shown initially, after 1000 timesteps and after 50000 timesteps (from top to bottom). After 1000 timesteps the monopolar region in the non-DC plot has barely moved from its original location; in the DC plot it has propagated to the edge of the star, where it leaves the numerical grid. After 50000 timesteps the non-DC evolution has become unstable, with the divergence exceeding $10^{10}$ (in code units) near the centre, whilst the DC plot shows low divergence throughout; in particular the original monopolar field at the centre has been completely removed.

find it to be typically of the order $\sim 0.01$. This is comparable with the initial value, suggesting that (with divergence cleaning) the code's evolutions preserve $\partial_t(\nabla \cdot \mathbf{B})$ well.

### Conservation of energy

Next we use conservation of (perturbed) energy to test the order of convergence of our code, using the fact that in the limit of infinite resolution energy should be exactly conserved.

The total energy of the system is the sum of all constituent energies — the kinetic $T$, gravitational $W$, internal $U$ and magnetic $M$:

$$\begin{aligned} \mathfrak{E} &= T + W + U + M \\ &= \int \left( \frac{1}{2}\rho \mathbf{V} \cdot \mathbf{V} - \rho\Phi + \frac{P}{\gamma - 1} + \frac{1}{8\pi}\mathbf{B} \cdot \mathbf{B} \right) \, \mathrm{d}V \end{aligned} \tag{7.3.27}$$

where $\mathbf{V} = \mathbf{\Omega} + \mathbf{v}$ is the sum of the background rotation and the velocity perturbation. On perturbing each energy term we recover the background energy at zeroth order, leaving an expression for $\delta\mathfrak{E}$ which we evaluate to second order in the perturbations, since the first-order terms will be proportional to $\cos m\phi$ or $\sin m\phi$ and hence will integrate to zero. Since we make the Cowling approximation, $\delta\Phi = 0$ and so the second-order perturbation in the gravitational energy is zero:

$$\delta W = -\int \delta\rho\delta\Phi \, \mathrm{d}V = 0 \tag{7.3.28}$$

Next we turn to the perturbed kinetic and magnetic energies, which are straightforwardly expressed:

$$\delta T = \int \frac{1}{2}\rho_0 |\mathbf{v}|^2 \, \mathrm{d}V, \tag{7.3.29}$$

$$\delta M = \int \frac{1}{8\pi} |\delta\mathbf{B}|^2 \, \mathrm{d}V, \tag{7.3.30}$$

but the internal-energy perturbation needs more care. Since we are looking for second-order contributions, when making the perturbative ansatz $P = P_0 + \delta P$ we now take $\delta P$ to mean the *total* perturbation, not simply the first-order piece. We may naturally find the higher-order piece by using the polytropic relation $P = k\rho^\gamma$

in our analysis:

$$\begin{aligned} U &= \frac{1}{\gamma-1}\int k\rho^\gamma \,\mathrm{d}V \\ &= \frac{1}{\gamma-1}\int k(\rho_0+\delta\rho)^\gamma \,\mathrm{d}V \\ &= \frac{1}{\gamma-1}\int k\rho_0^\gamma\left(1+\frac{\delta\rho}{\rho_0}\right)^\gamma \,\mathrm{d}V \\ &= \frac{1}{\gamma-1}\int P_0\left(1+\gamma\frac{\delta\rho}{\rho_0}+\frac{\gamma(\gamma-1)}{2}\left(\frac{\delta\rho}{\rho_0}\right)^2+\mathcal{O}\left(\frac{\delta\rho}{\rho_0}\right)^3\right)\mathrm{d}V. \end{aligned} \tag{7.3.31}$$

Now the zeroth-order piece is the background relation for $U$ and the first-order piece integrates to zero, yielding the second-order expression

$$\delta U = \int \frac{\gamma P_0}{2\rho_0^2}\delta\rho^2 \,\mathrm{d}V. \tag{7.3.32}$$

These energies have a simple form when written in the $\phi$-decomposed variables used in the code. For example, the magnetic energy of a perturbed magnetic field $\delta\mathbf{B}$ is given by

$$\delta M = \frac{1}{8\pi}\int \delta\mathbf{B}\cdot\delta\mathbf{B}\,\mathrm{d}V = \frac{1}{8\pi}\int \frac{\boldsymbol{\beta}\cdot\boldsymbol{\beta}}{\rho_0^2}\,\mathrm{d}V. \tag{7.3.33}$$

Now each component of $\boldsymbol{\beta}$ is decomposed in $\phi$, e.g. $\beta_r = \beta_r^+\cos m\phi + \beta_r^-\sin m\phi$. Taking the square of this gives

$$\beta_r^2 = (\beta_r^+)^2\cos^2 m\phi + (\beta_r^-)^2\sin^2 m\phi + 2\beta_r^+\beta_r^-\cos m\phi\sin m\phi. \tag{7.3.34}$$

On integrating this quantity (or equally $\beta_\theta^2$ or $\beta_\phi^2$) over $\phi\in[0,2\pi]$, the cross-term vanishes and $\cos^2 m\phi$ and $\sin^2 m\phi$ each integrate to $\pi$. Hence,

$$\begin{aligned} \int \boldsymbol{\beta}\cdot\boldsymbol{\beta}\,\mathrm{d}r\mathrm{d}\theta\mathrm{d}\phi &= \int(\beta_r^2+\beta_\theta^2+\beta_\phi^2)\,\mathrm{d}r\mathrm{d}\theta\mathrm{d}\phi \\ &= \pi\int\left((\beta_r^+)^2+(\beta_r^-)^2+...+(\beta_\phi^-)^2\right)\,\mathrm{d}r\mathrm{d}\theta \end{aligned} \tag{7.3.35}$$

and so

$$\delta M = \frac{1}{8}\int\frac{1}{\rho_0^2}\left((\beta_r^+)^2+(\beta_r^-)^2+...+(\beta_\phi^-)^2\right)\,\mathrm{d}r\mathrm{d}\theta. \tag{7.3.36}$$

Since we are making the Cowling approximation, $\delta W = 0$ and we are left with

$$\delta\mathfrak{E} = \delta T + \delta U + \delta M = \int\left(\frac{1}{2}\rho_0|\mathbf{v}|^2+\frac{\gamma p_0}{2\rho_0^2}\delta\rho^2+\frac{1}{8\pi}|\delta\mathbf{B}|^2\right)\,\mathrm{d}V. \tag{7.3.37}$$

This is in agreement with equation (C5) of Friedman and Schutz [46] in the case of adiabatic perturbations within the Cowling approximation, but with an additional magnetic energy term.

To evaluate the convergence ratio, we monitor the evolution of the high-resolution energy $\delta\mathfrak{E}_{64\times60}(t)$ and the medium-resolution energy $\delta\mathfrak{E}_{32\times30}(t)$, comparing these with the initial value of the energy $\delta\mathfrak{E}(0)$. In the continuum limit $\delta\mathfrak{E}$ will have no time-dependence and will be equal to its initial value for all time. Hence we are able to use this exact result to define a convergence ratio:

$$\mathcal{O}_{conv} = \frac{1}{\log 2} \log \left( \frac{\delta\mathfrak{E}_{32\times30}(t) - \delta\mathfrak{E}(0)}{\delta\mathfrak{E}_{64\times60}(t) - \delta\mathfrak{E}(0)} \right). \tag{7.3.38}$$

In figure 7.4 we evaluate $\mathcal{O}_{conv}$ over time, confirming that the code is second-order convergent.

### 7.3.7 Nondimensionalising

Throughout the code we employ variables which have been made dimensionless through division by a suitable combination of powers of gravitational constant $G$, central density $\rho_c$ and equatorial radius $r_{eq}$. For example, a dimensionless mode frequency $\hat{\sigma}$ is related to the physical one $\sigma$ (with units of rad $\mathrm{s}^{-1}$) through the relation $\hat{\sigma} = \sigma/\sqrt{G\rho_c}$; the conversion is the same for rotational frequency $\Omega$. Since dimensionless frequencies of this form are common in oscillation mode literature we use these throughout this work. Dimensionless magnetic field strengths, however, are less likely to be familiar and so we quote these in terms of gauss.

When we use dimensional quantities they are for a neutron star with canonical parameters: an equatorial radius of 10km (in the non-rotating, unmagnetised case) and a mass of $1.4M_\odot$ (where $M_\odot$ is solar mass). The relationship between dimensionless frequencies $\hat{\sigma}$ (equivalently $\hat{\Omega}$) and their physical counterparts is only weakly dependent on $\Omega$ and $\mathbf{B}$ — and hence is roughly linear, with

$$\sigma[\mathrm{Hz}] \approx 1890\hat{\sigma}. \tag{7.3.39}$$

Finally, we note that in our dimensionless units, the Keplerian (break-up) velocity $\Omega_K \approx 0.72$. When we plot sequences of modes in rotating stars, we typically track the modes up to $\Omega/\Omega_K \approx 0.95$; that is, rotation rates 95% of the break-up velocity.

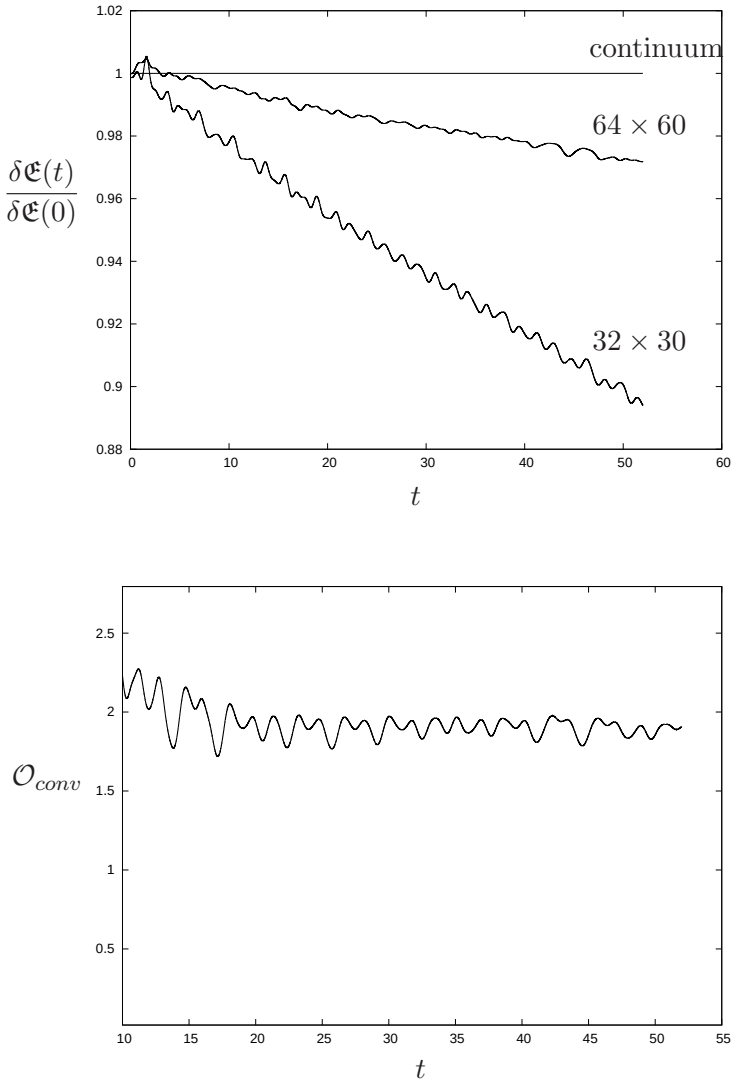


Figure 7.4: We determine the order of convergence of our code by evaluating the total perturbed energy $\delta\mathfrak{E}$ over time; in the exact, continuum limit this quantity will not deviate from its initial value. The upper plot shows the deviation of $\delta\mathfrak{E}$ from its initial value for $(r, \theta)$ grids of $32 \times 30$ and $64 \times 60$ points. From these we confirm that the order of convergence $\mathcal{O}_{conv}$ of the code is equal to 2, as intended (see lower plot). $\mathcal{O}_{conv}$ is only plotted for $t \geq 10$, since at early times the numerical values of $\delta\mathfrak{E}$ cross the continuum value, causing $\mathcal{O}_{conv}$ to oscillate rapidly. The background configuration for these tests was a star with rotation rate $\Omega/\sqrt{G\rho} = 0.238$ and with an average magnetic field strength $\bar{B} = 2.87 \times 10^{16}$ G, evolved for 30 $f$-mode oscillations.

## 7.4 Results

### 7.4.1 Mode spectrum of a nonrotating magnetised star

In this section we present results for nonrotating stars, since the mode spectrum is simpler, leaving rotating stars to the next section. We begin by investigating the new class of modes present with the addition of a magnetic field: the Alfvén modes (termed $a$-modes for brevity). Results are presented for both polar and axial $a$-modes.

Let us begin by considering where in the frequency spectrum these modes could be expected. Now, any mode frequency will be proportional to some characteristic wave speed. For fluid modes like the $f$-mode, the frequency should be proportional to the sound speed $c_s$; similarly the $a$-mode frequencies should be proportional to the Alfvén speed $c_A$. Accordingly the ratio of frequencies should scale as

$$\frac{\sigma_f}{\sigma_a} \sim \left\langle \frac{c_s}{c_A} \right\rangle \tag{7.4.1}$$

where the angle brackets represent a volume average. Now

$$\frac{c_s}{c_A} = \sqrt{\frac{\gamma P}{\rho}} \Big/ \sqrt{\frac{B^2}{4\pi\rho}} \tag{7.4.2}$$

and so

$$\left\langle \frac{c_s}{c_A} \right\rangle = \frac{2\sqrt{\pi\gamma < P >}}{\bar{B}}. \tag{7.4.3}$$

We find from our background code that a nonrotating unmagnetised $\gamma = 2$ polytrope with a mass of $1.4M_\odot$ and radius $R = 10$ km has a volume-averaged pressure $< P >$ of $3.10 \times 10^{34}$ dyn cm$^{-2}$. Using this value and $\bar{B} = 10^{16}$ G to nondimensionalise, we find that

$$\frac{\sigma_f}{\sigma_a} \sim 90 \times \left( \frac{< P >}{3.10 \times 10^{34} \text{ dyn cm}^{-2}} \right)^{1/2} \left( \frac{\bar{B}}{10^{16} \text{ G}} \right)^{-1}. \tag{7.4.4}$$

With the value of $< P >$ varying little with magnetic field strength, let us assume that it is a constant and that $\sigma_f/\sigma_a$ scales only with $\bar{B}$. It then follows that we should expect $\sigma_a$ to be roughly 1/90 of $\sigma_f$ for a $10^{16}$ G field, but 1/9 of $\sigma_f$ for a $10^{17}$ G field. This part of the spectrum may be dominated by inertial modes in the case of unmagnetised rotating stars, but in the absence of rotation we may be confident that any oscillations at lower frequency than the $f$-mode are associated with the magnetic field — see figure 7.5.

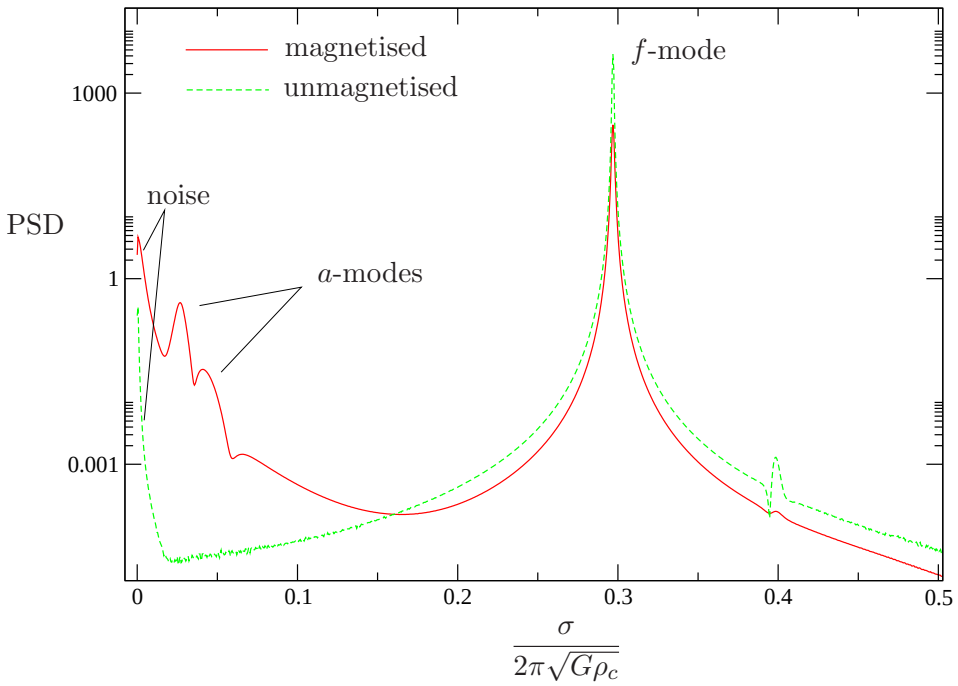


Figure 7.5: Typical FFT results for a pair of nonrotating stars, one magnetised and the other unmagnetised. We plot mode frequency $\sigma$ (in a dimensionless form) against PSD, the power spectral density. We see that the $f$-mode frequencies are very close in each case. With no Coriolis force there are no inertial modes, therefore any peaks at lower frequency than the $f$-mode must be either noise or Alfvén modes. We identify the lowest-frequency spike in the magnetic FFT as noise, since there is a corresponding unphysical peak in the nonmagnetic FFT. The following peaks in the magnetised-star FFT, however, have no analogue in the nonmagnetic FFT and so we identify these as Alfvén modes. The duration of the evolution was sufficient to resolve around 100 Alfvén oscillations.

Now, with $\sigma_a \propto < c_A >$ and $c_A = B/\sqrt{4\pi\rho}$, it follows that $\sigma_a \propto B$, provided that magnetic changes to the density distribution are higher order (which should be true for all but very high field strengths — see chapter 6). To summarise, $a$-modes should scale approximately linearly with field strength and appear as oscillations with lower frequency than the $f$-mode. With these expectations, we now turn to numerical results from our time-evolution code.

In figure 7.6 we track a number of Alfvén mode frequencies up to averaged-field strengths of order $10^{17}$ gauss. For axial initial data and fixed $m$ we find a single $l = m$ mode[2], whilst polar initial data excites two $l_0 = m + 1$ modes for a given $m$. The index $l_0$ refers to the highest-$l$ $Y_{lm}$ that contributes significantly to the mode's eigenfunction; see chapter 5 or Lockitch and Friedman [93] for more details. In all cases, we see that as expected there is a near-linear relationship between $\sigma_a$ and $\bar{B}$. The identification of the $a$-modes is based on analysis of their eigenfunctions, using the numerical method of Stergioulas et al. [131]. The labelling used here anticipates the results of the next section, where we track these modes for increasing rotation rate.

At the start of this section we showed that the $a$-mode frequency should vary linearly with $\bar{B}$, and this appears to be borne out by our results. We now quantify this dependence and the deviation from it. By looking at the weak-field results from our code (where the relationship should be closest to linear), we determine the constants of proportionality in the relationship

$$\frac{{}^{l_0}_{m}(\sigma_a)_k}{\sqrt{G\rho_c}} = {}^{l_0}_{m}c_k \left( \frac{\bar{B}}{10^{16}\ \mathrm{G}} \right), \tag{7.4.5}$$

finding that ${}^{2}_{2}c = 0.033, {}^{3}_{2}c_1 = 0.030, {}^{3}_{2}c_2 = 0.045, {}^{4}_{4}c = 0.086, {}^{5}_{4}c_1 = 0.069, {}^{5}_{4}c_2 = 0.090, {}^{6}_{6}c = 0.146, {}^{7}_{6}c_1 = 0.127, {}^{7}_{6}c_2 = 0.150$. We may use the linear relationship (7.4.5), with the numerically-established constants ${}^{l_0}_{m}c_k$, to test how close our results are to the linear regime. We find that even for strong fields, the deviation from the linear regime is always less than 8% — and in most cases is less than 5%.

Finally in this section, we look at the shift in the frequency of the fundamental mode upon the addition of a magnetic field to the star. This mode is restored by perturbations in the fluid pressure $P$ in the unmagnetised case, so we anticipate that in the magnetic problem the restoring force is perturbations of *total* (fluid

[2]We also find three axial $l_0 = m + 2$ modes, but these are harder to resolve for high $m$ and so do not feature in the plots in this section

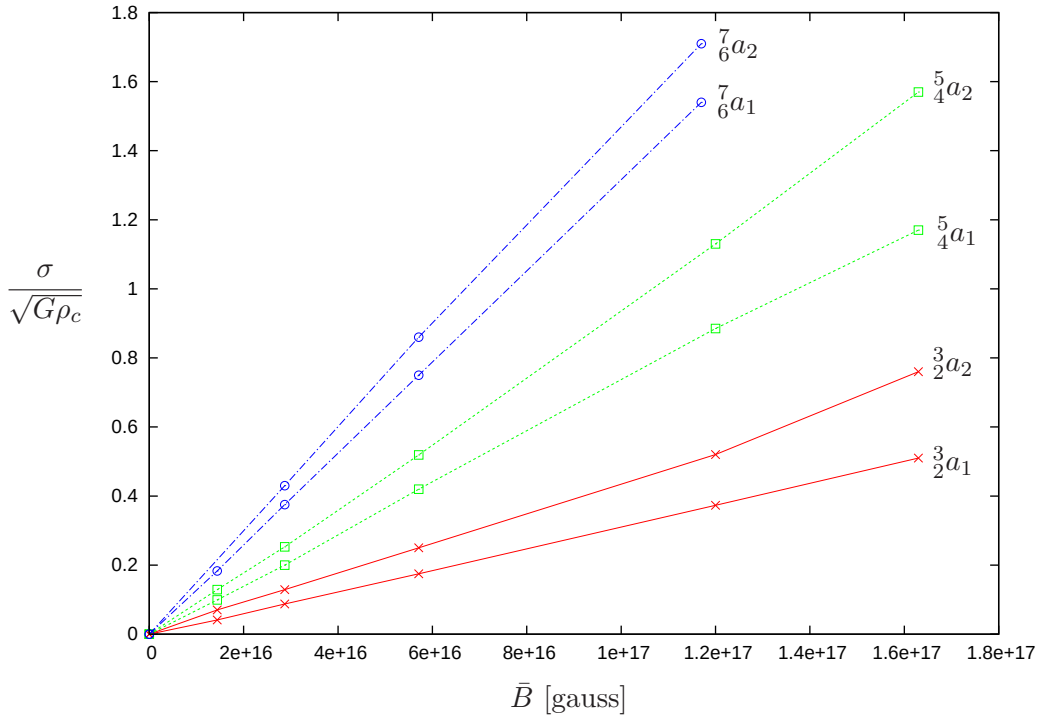


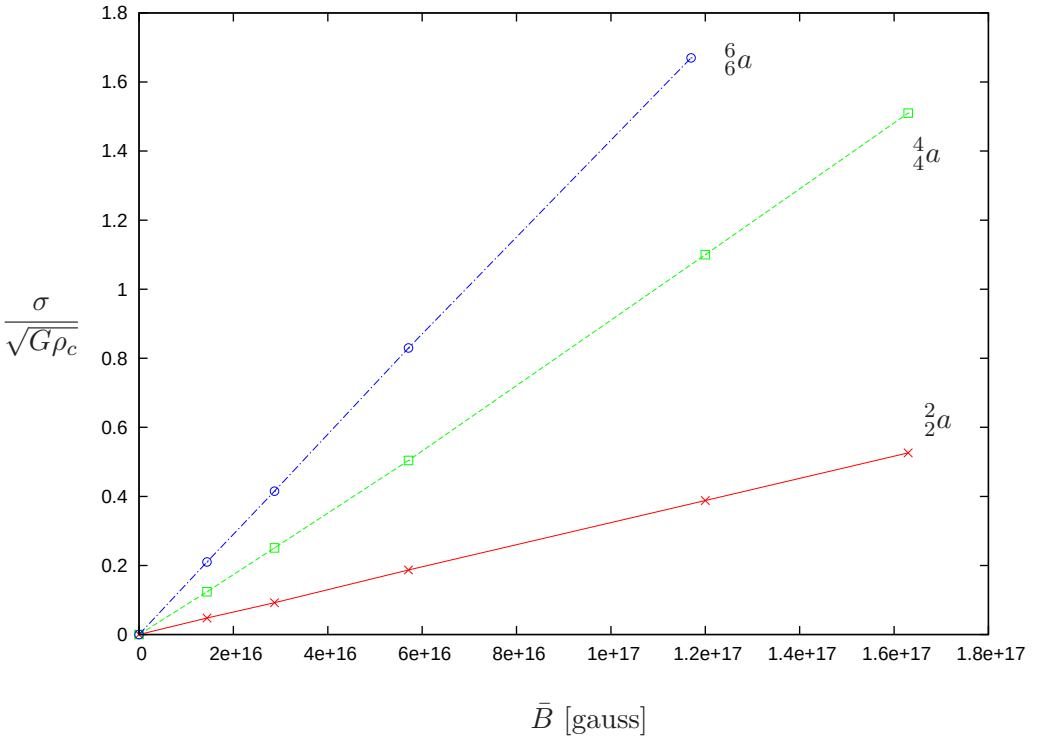


Figure 7.6: Polar $l_0 = m + 1$ Alfvén modes (top) and axial $l = m$ Alfvén modes (bottom), for $m = 2, 4, 6$. Tracking the modes to high field strength, we see that each mode frequency scales linearly with magnetic field strength, as anticipated. These results are for a nonrotating star.

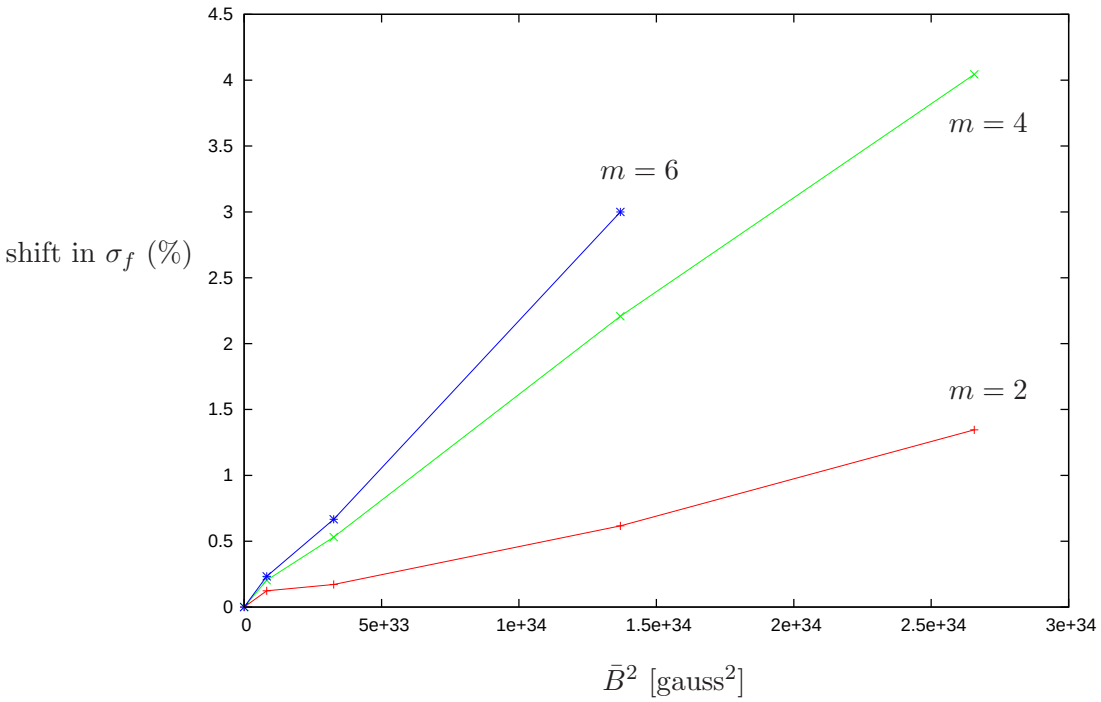


Figure 7.7: The shift in $f$-mode frequency due to magnetic effects (for nonrotating stars), for $m = 2, 4, 6$. On the $y$-axis we plot percentage increase in $\sigma_f$ from its unmagnetised value; we see that this shift appears to depend quadratically on $\bar{B}$. The apparent deviation from this dependence, visible in the weakest-field results, is attributable to numerical errors in these very small frequency shifts.

plus magnetic) pressure, $P + B^2/8\pi$. The magnetic shift in $\sigma_f$, then, should be proportional to $B^2$ — but since magnetic pressure is very modest in magnitude compared with fluid pressure, we expect the frequency shift to be small. For example, using our canonical model star, the magnetic pressure is $\sim 1\%$ of the fluid pressure at $\bar{B} = 10^{17}$ G. We confirm these expectations in figure 7.7. In all cases $\sigma_f$ is increased by the inclusion of magnetic effects, but the shifts are only around a couple of percent even for $\bar{B} \sim 10^{17}$. The relative shift appears to be more pronounced for higher-$m$ oscillations.

### 7.4.2 Mode spectrum of a rotating magnetised star

Armed with knowledge from the previous subsection about the spectrum of magnetised nonrotating stars, we next consider rotating magnetised configurations. The earliest studies of magnetic oscillations (e.g. Chandrasekhar and Limber [28]) suggested that the significance of the magnetic field on the oscillation spectrum should be linked to the ratio $M/|W|$; when additionally including rotational effects we would expect the relative significance of the two effects to be related to $M/T$ [104].

We first consider magnetic shifts in the $f$-mode frequency for rotating stars. Rotation splits the $f$-mode into co- and counter-rotating modes; we expect the frequencies of both branches of the mode to shift with the addition of magnetic fields. At low rotation, the magnetic shift for each piece of the $f$-mode is comparable with the shift in the nonrotating case, but at higher rotation rates the shift becomes less significant — see figure 7.8. This bears out our expectation that the magnetic shift should scale with $M/T$.

We next turn to $a$-modes and $r$-modes of rotating magnetised stars. Based on our experience so far, we have expectations on how each mode should behave. We anticipate a rotational splitting of the $a$-modes into co- and counter-rotating pieces (as seen for the $f$-mode); in addition we expect to see some magnetic shift, scaling with $M/T$, in the $r$-mode. We shall see that both of these effects are combined: the pure $r$- and $a$-modes are replaced by a hybrid magneto-inertial mode, which resembles a magnetically-shifted $r$-mode when rotation is more important, and a rotationally-split $a$-mode when magnetic effects are more significant.

We begin by tracking the axial ${}^2_2a$-mode with increasing rotation, finding that as expected it undergoes rotational splitting (figure 7.9). The lower-frequency branch of this $a$-mode appears to tend to zero with increasing $\Omega$ (or equivalently, as $M/T \to 0$). The higher-frequency branch of the $a$-mode tends to the ${}^2_2r$-mode frequency as $M/T \to 0$. We confirm that the magnetic/inertial character of these hybrid modes depends on $M/T$ by tracking the ${}^2_2a$-mode for three different field strengths, finding that when $\bar{B}$ is higher the hybrid-mode frequency approaches the $r$-mode frequency more slowly. The higher-frequency branch of the ${}^2_2a$ mode is counter-rotating — it is this branch that joins up with the (also counter-rotating) ${}^2_2r$-mode, whilst the lower-frequency ${}^2_2a$ mode corotates with the star.

Having established that the pure ${}^2_2a$ mode and the pure ${}^2_2r$-mode are replaced

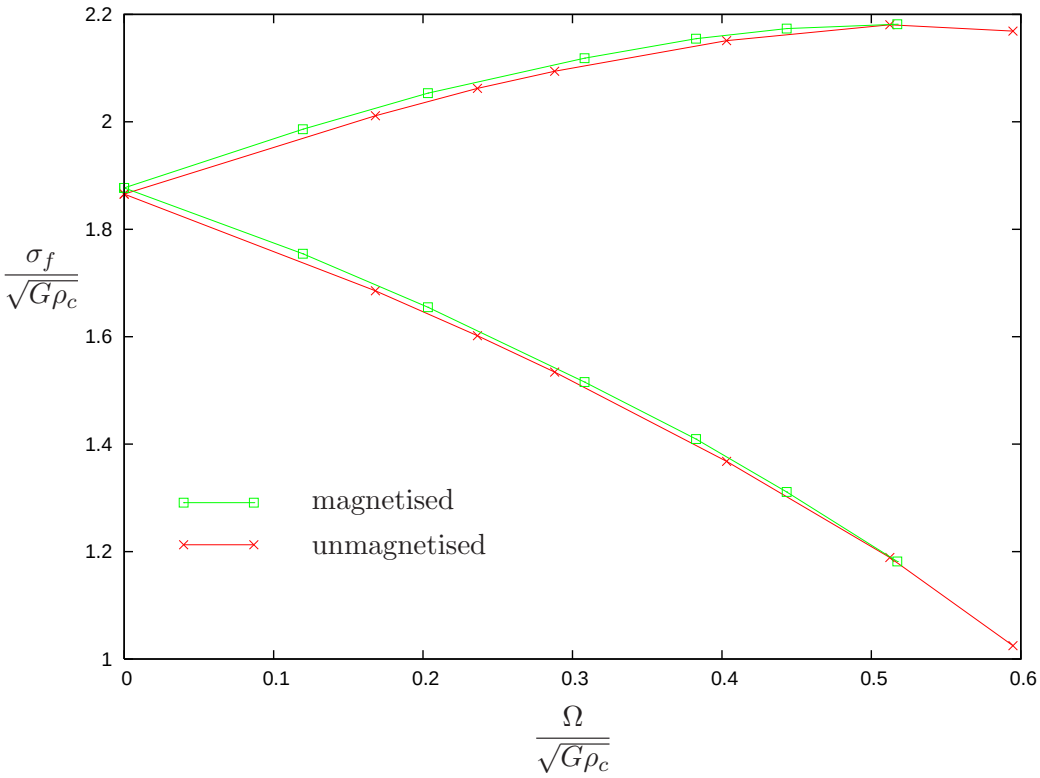


Figure 7.8: Magnetic shift of the $m = 2$ $f$-mode frequency for rotating stars. Since the shift is very small we take a very highly magnetised background star, with $\bar{B} = 1.17 \times 10^{17}$ G, for comparison with the nonmagnetic sequence of results. We find that as the rotation rate $\Omega$ increases, magnetic effects become less significant.

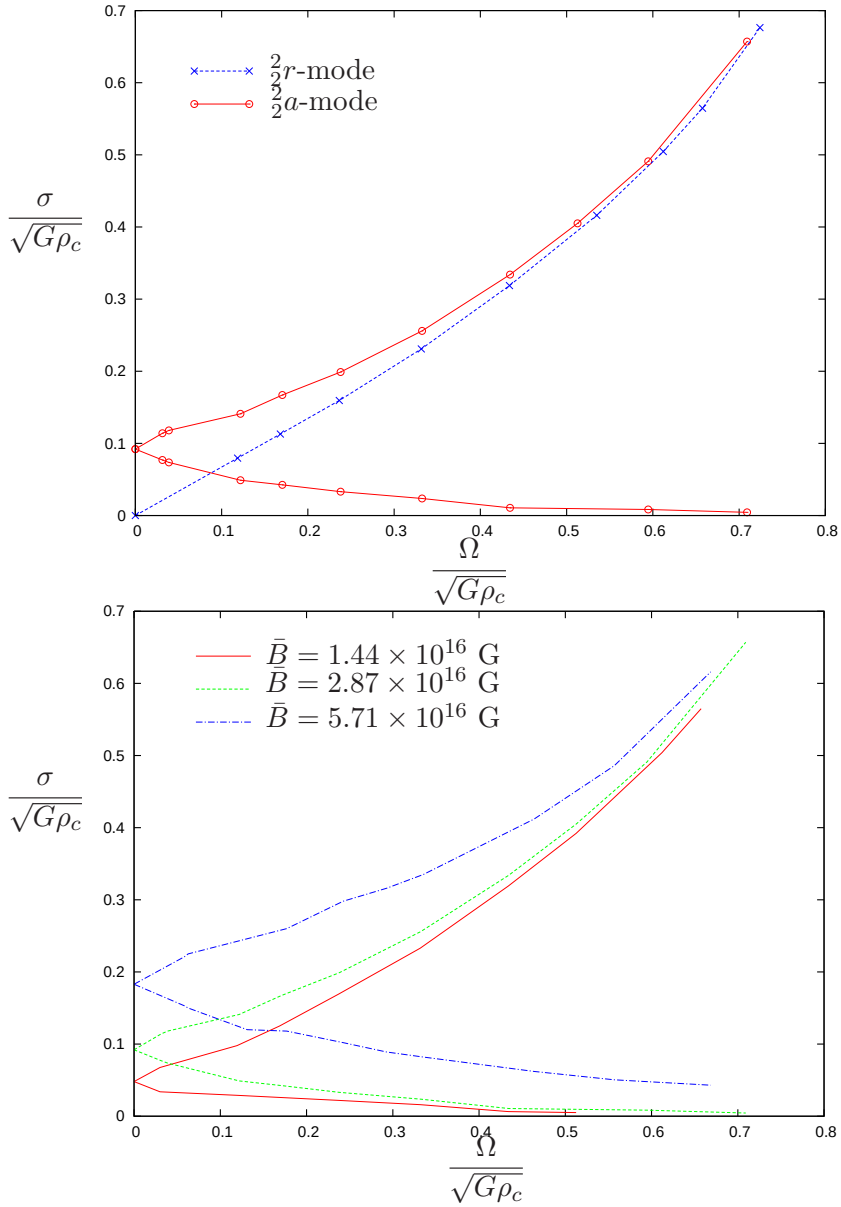


Figure 7.9: Illustrating the hybrid magneto-inertial nature of modes in a rotating magnetised star. When $\Omega = 0$ there is a pure $l = m = 2$ $a$-mode, which is split into co- and counter-rotating modes by the effect of rotation. The counter-rotating mode frequency approaches the nonmagnetic $^2_2r$-mode frequency as $\Omega$ increases, while the corotating branch tends to zero frequency. The upper plot compares the $a$-mode with the $r$-mode, whilst the lower plot shows that the nature of the hybrid mode depends on the ratio $M/T$; when $\bar{B}$ is larger, the $a$-mode frequency approaches the $r$-mode frequency more slowly. Modes are tracked up to $\Omega \approx 0.7$ in dimensionless units, which is over 95% of the break-up velocity. The irregular parts of the curves may correspond to avoided crossings with other magneto-inertial modes.

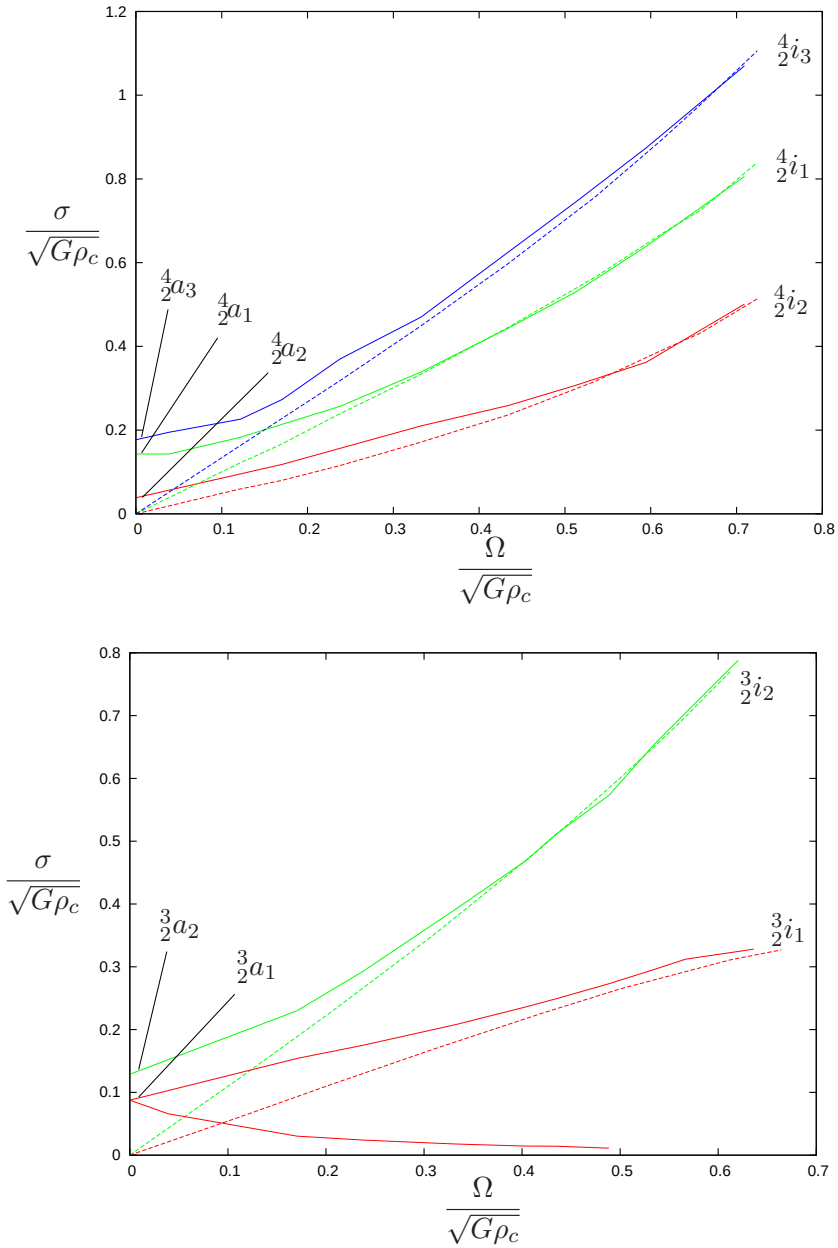


Figure 7.10: The $m = 2, l_0 = 3, 4$ hybrid magneto-inertial modes. Dashed lines represent the pure inertial ($\bar{B} = 0$) modes, whilst solid lines show magneto-inertial modes, which reduce to pure Alfvén modes in the $\Omega \to 0$ limit. The upper plot shows the $l_0 = 4$ (axial) hybrid modes, whilst the lower plot shows $l_0 = 3$ (polar) modes. In each case the upper-frequency branch of a hybrid mode is seen to meet a corresponding $i$-mode as $M/T \to 0$. For the ${}^3_2a_1$ mode, we were also able to track the lower-frequency branch, which appears to reduce to a zero-frequency mode in the $M/T \to 0$ limit.

by a hybrid magneto-inertial mode when both magnetic and rotational restoring forces are present, one would expect to find similar hybrid modes corresponding to other Alfvén/inertial modes; we confirm this expectation in figure 7.10. As before, rotation appears to split each $a$-mode into co- and counter-rotating branches[3]. We are able to track the upper-frequency branches of both polar ${}^3_2a$-modes to their inertial counterparts, and all three ${}^4_2a$-modes to known inertial modes in the $M/T \to 0$ limit. In addition, we are able to track the lower-frequency branch of the ${}^3_2a_1$ mode to high rotation rates; it appears to become a zero-frequency mode in the $M/T \to 0$ limit, as for the lower ${}^2_2a$-mode.

### 7.4.3 The continuous mode spectrum of perfect MHD

The study of oscillation modes of magnetised stars is complicated by the fact that in the perfect-MHD limit, where the resistivity is zero, discrete modes may be replaced by a continuum. In this case one may no longer talk of global modes, since different parts of the star will have different frequencies of oscillation. This phenomenon was first discovered by researchers in plasma physics: see, for example, Grad [59] and references therein. Later research argued that continuous spectra are relevant to astrophysics too [57, 90].

It appears that the continuous parts of the oscillation spectrum are, however, a somewhat pathological effect peculiar to MHD without dissipation. The inclusion of resistive effects or perpendicular thermal conduction each remove some of the continuous spectra, whilst with both effects there are no continua left [70]. Although many astrophysical situations (like the interior of a neutron star) involve matter of very high conductivity, their non-zero (albeit small) resistivity may therefore result in a qualitatively different spectrum from that predicted by perfect MHD: discrete modes rather than a continuum.

We look for behaviour consistent with a continuous spectrum in figure 7.11. Here we plot the Fourier transform of $\beta_r^-$ at three different points in the star, for a nonrotating background configuration with an average magnetic field strength $\bar{B} = 2.87 \times 10^{16}$ G. The evolutions are for azimuthal index $m = 2$, so all modes discussed here are also $m = 2$. The evolution time in each case was sufficient to

[3]Note, however, that we are only able to see the lower-frequency branches clearly for the ${}^2_2a$ and ${}^3_2a_1$ modes; we believe other lower-frequency branches are harder to track because they undergo many avoided crossings.

resolve around 1000 oscillations. The perturbations are not evolved at the pole or equator (boundary conditions are imposed here), but we pick interior angular points close to $\theta = 0$ and $\theta = \pi/2$, and also a central point with $\theta = \pi/4$. In all cases the radial value used was $r = 0.4R_*$. In the plots shown we are able to identify peaks corresponding to the ${}^2a, {}^3a_1, {}^3a_2$ and ${}^4a_1$ modes; these vary by no more than 1% for the three positions. The ${}^4a_2$ and ${}^4a_3$ modes have very weak peaks in this particular figure, but may be identified in the Fourier transforms of other perturbed quantities — it is difficult to resolve all of the higher-$l_0$ $a$-modes from one plot alone. We place brackets around these modes in the figure to stress that we have never identified modes based on such minor peaks in the spectrum.

To summarise: within our work, we find no evidence of continua in the mode spectrum, although we model stars as perfect conductors in MHD. We believe that although we only include dissipative effects (Kreiss-Oliger dissipation and artificial resistivity) for numerical purposes, they may have the side-effect of removing continuous parts of the spectrum, as discussed above. This is not necessarily a weakness of our approach; our aim is to model neutron stars rather than perfectly conducting fluids *per se*, and dissipative effects may act to give a real neutron star a discrete mode spectrum too. Furthermore, we have found that in the presence of rotation $a$-modes become hybrid magneto-inertial modes. With sufficient rotation an $a$-mode has predominantly inertial character and hence should become discrete. Rotation must therefore affect the Alfvén continuum too, perhaps by reducing its width.

### 7.4.4 Mode instabilities

Whilst an unperturbed rotating star cannot emit gravitational radiation — it is a stationary configuration — the various non-axisymmetric oscillations of the star can. This radiation carries angular momentum away from the star, which may drive instabilities in certain oscillation modes. In particular, it was shown by Chandrasekhar [25] and Friedman and Schutz [46, 47] that *all* rotating perfect-fluid stars are unstable. This radiation-driven effect is known as the CFS instability, from the three authors of these early studies.

Very briefly, the CFS mechanism works in the following way: in the comoving frame of a rotating star, there exist both prograde (forward-moving) and retrograde (backward-moving) modes; these modes have, respectively, positive and negative

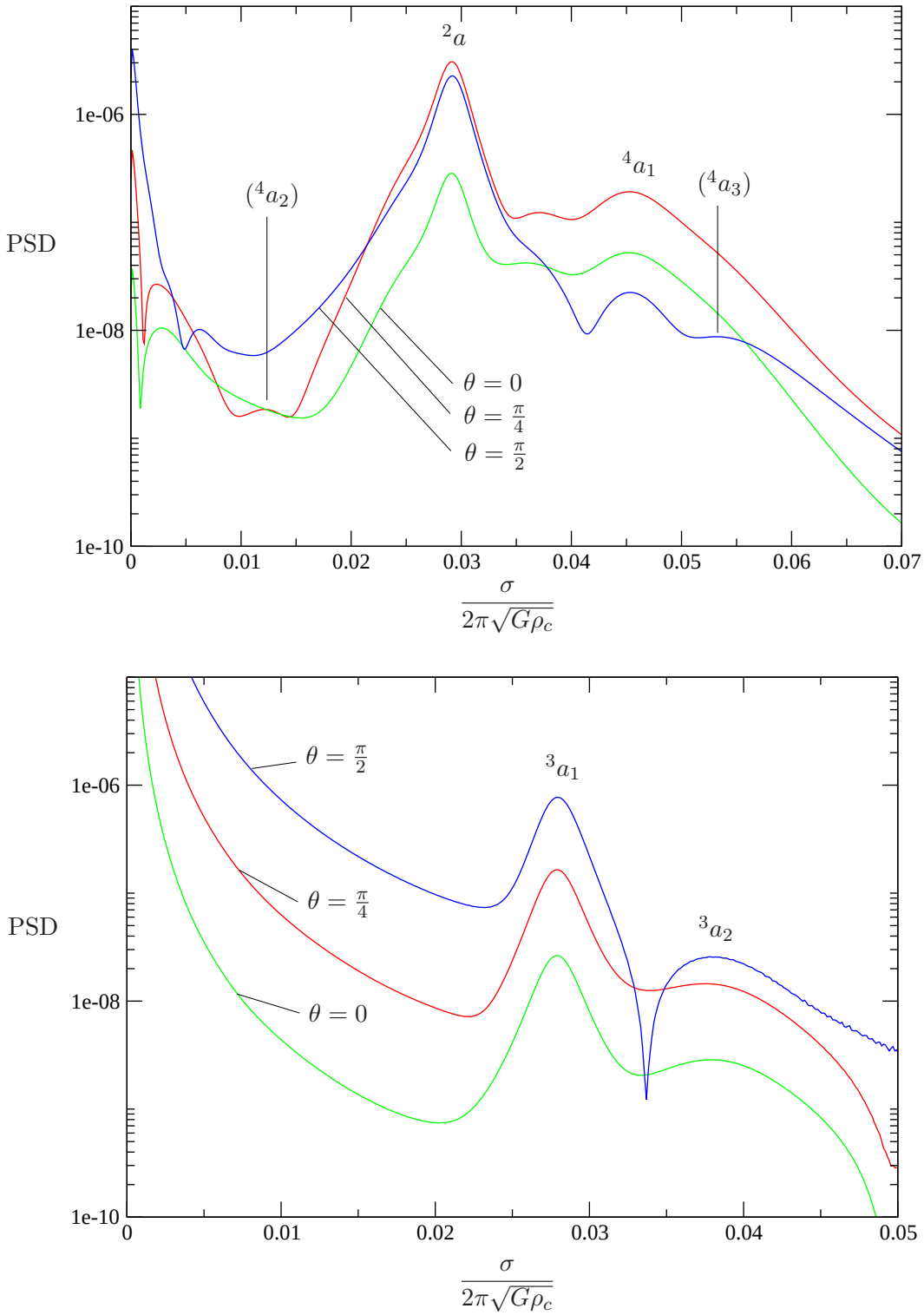


Figure 7.11: Plots showing that the Alfvén mode frequencies in this work are independent of position within the star (and hence do not form a continuum). We present typical Fourier-transformed data from evolutions of axial (top) and polar (bottom) perturbations. The plots show mode frequency $\sigma$ against power spectral density PSD. Further details are given in the text.

angular momentum in this frame. Suppose a mode is retrograde in the rotating frame but moves with a speed which is lower than the stellar rotation rate. Then in the inertial frame it will appear *prograde*. As the star loses angular momentum due to gravitational radiation, this mode will also lose angular momentum as it appears prograde; but in the rotating frame its angular momentum becomes more negative and the mode amplitude grows. At some point this process could induce an oscillation in the mass distribution of the star large enough to produce detectable gravitational waves.

A number of modes are subject to this instability, but in general only become unstable for sufficiently rapid rotation. However, the $r$-modes are unstable even in slowly rotating stars, in the absence of viscosity; see Andersson and Kokkotas [5]. We have already seen that magnetic fields significantly alter the behaviour of the $r$-mode for slow rotation, so we now consider the effect this has on their stability. For a counter-rotating mode with frequency $\sigma$ (positive by convention) in the rotating frame, the instability criterion is

$$\sigma(\sigma - m\Omega) < 0; \tag{7.4.6}$$

this may also be found in Andersson and Kokkotas. It follows immediately that radiative instabilities are entirely suppressed when $\sigma > m\Omega$. In the upper plot of figure 7.12 we show this threshold frequency, together with the nonmagnetic $r$-mode and the hybrid mode that replaces it in the magnetic case. It is clear that whilst the unmagnetised $r$-mode is always in the unstable regime, its magnetic equivalent (the hybrid of the $r$-mode and the axial $l = m$ $a$-mode) *is* stable for sufficiently low rotation rates. The maximum rotational frequency a star can have before its ${}^2_2r$ mode goes unstable is presented in the lower plot, as a function of the stellar magnetic field strength.

Even when magnetic fields are not strong enough to suppress the $r$-mode instability, they may slow down its growth. A full calculation of this effect is beyond the scope of this work, but we may estimate it with some simplifying assumptions. The growth time $\tau_{GR}$ of the $r$-mode instability due to gravitational radiation is given by

$$\frac{1}{\tau_{GR}} = -\frac{1}{2E}\frac{\mathrm{d}E}{\mathrm{d}t} \tag{7.4.7}$$

where $E$ is the energy of the mode in the rotating frame. From this one can show that the growth time $\tau_{GR}$ scales with the rotating-frame mode frequency $\sigma$ in the

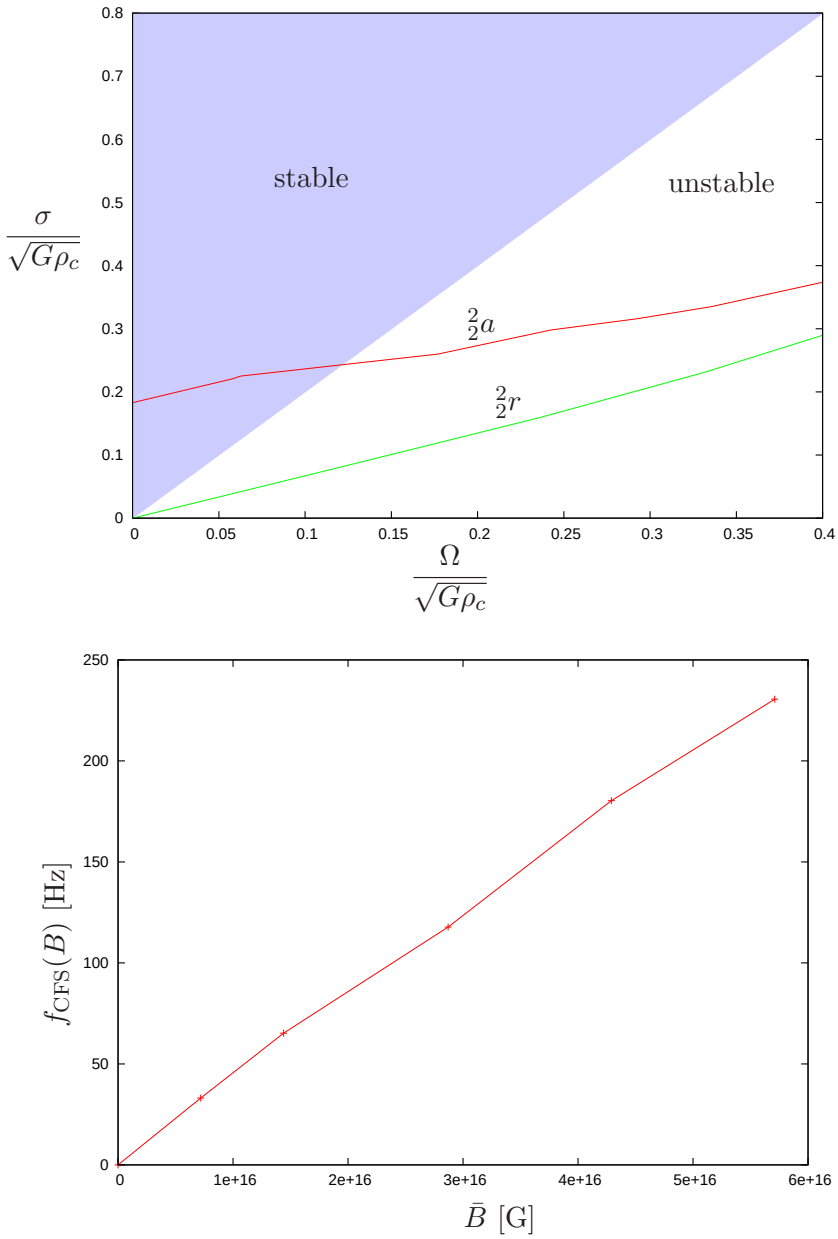


Figure 7.12: In a slowly-rotating magnetised star, the $r$-mode is replaced by the axial $l = m$ $a$-mode. From the upper plot we see that this $a$-mode is not subject to the CFS instability if $\Omega$ is sufficiently small, but at some higher rotational frequency $f_{\rm CFS}$ (a function of the field strength $B$) it crosses into the unstable regime. The lower plot shows the variation of $f_{\rm CFS}$ with average field strength $\bar{B}$.

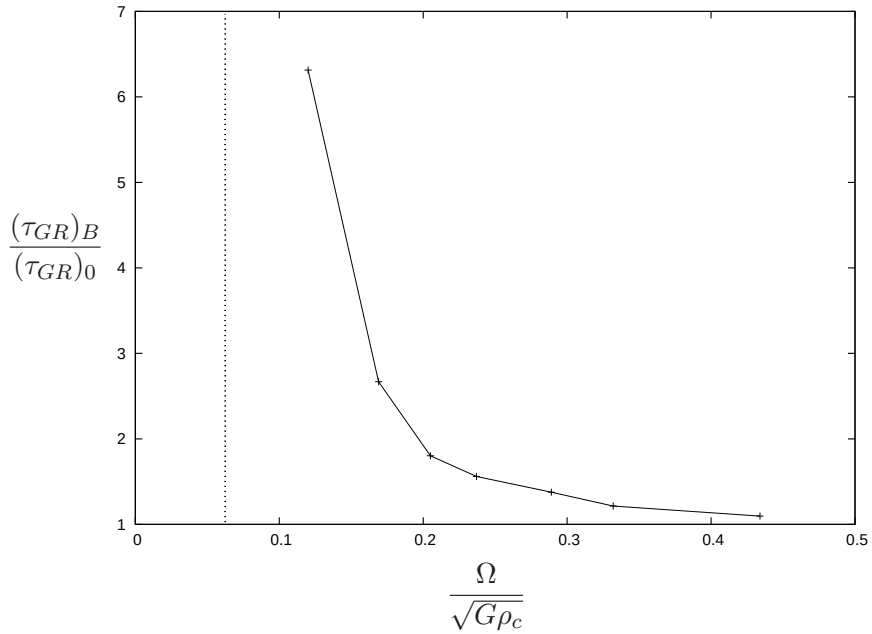


Figure 7.13: A magnetic field changes the growth time of the $r$-mode instability. Here we plot an approximation of the ratio of magnetised $(\tau_{GR})_B$ to unmagnetised $(\tau_{GR})_0$ growth timescales, against dimensionless rotation rate. The dashed vertical line shows where the ratio asymptotes (i.e. when the magnetised mode becomes stable). We see that in all cases the instability growth is slower with magnetic effects, but the effect becomes insignificant for rapid rotation. The magnetic timescales shown here are for a star with a field strength of $2.87 \times 10^{16}$ G.

following manner for an $l = m$ $r$-mode:

$$\frac{1}{\tau_{GR}} \sim \sigma(\sigma - l\Omega)^{2l+1} \tag{7.4.8}$$

— see Andersson and Kokkotas [5] for details. Note that for $l = m = 2$, the growth time scales with the sixth power of $\sigma$.

We wish to estimate how the growth time for the $\frac{2}{2}r$-mode instability changes when magnetic effects are included. Since $\tau_{GR}$ contains a factor of $\sigma^6$, we will assume that this term has the most significant variation when a magnetic field is added. Other terms in the expression of $E$ and its derivative will be approximated as constant. Using the indices 0 and $B$ to denote nonmagnetic and magnetic quantities (respectively), we then see that

$$\frac{(\tau_{GR})_B}{(\tau_{GR})_0} \approx \frac{\sigma_0(\sigma_0 - 2\Omega)^5}{\sigma_B(\sigma_B - 2\Omega)^5}. \tag{7.4.9}$$

In figure 7.13 we plot this dimensionless quantity as a function of the rotation rate, finding that a toroidal magnetic field does indeed slow down the instability's growth. The importance of the effect depends on the rotation rate: at twice the threshold frequency for stability of the magnetised $r$-mode (i.e. when the mode is unstable), its growth time is still a factor of $\sim 6$ longer than in the nonmagnetic $r$-mode case; however, for very rapid rotation the difference in growth times is negligible.

## 7.5 Discussion and conclusions

In this chapter we have investigated oscillation modes of neutron stars with rotation and magnetic fields, specialising to the case of purely toroidal background fields. Our numerical approach allows us to study oscillations of rapidly rotating and highly magnetised stars in a self-consistent manner. We first generate a stationary star in equilibrium to use as the background configuration, using the work of chapter 6; this star may have axisymmetric distortions due to magnetic effects and rotation. We then time-evolve linear perturbations on this background star in order to study its modes of oscillation.

When a magnetic field is added to a star, the most obvious change to its oscillation spectrum is the presence of Alfvén ($a$-) modes, a class of stellar oscillation restored by the Lorentz force. These modes are purely magnetic in nature only for a nonrotating background star.

In a rotating magnetised star, we find that the pure $a$-modes of a nonrotating star (or equivalently, the purely inertial $i$-modes of an unmagnetised star) are replaced by hybrid magneto-inertial modes, whose character is governed by the ratio of the magnetic $M$ and kinetic $T$ energies, as discussed by Morsink and Rezania [104]. Tracking a star at fixed magnetic field from $\Omega = 0$ through increasing rotation rate, we see a rotational splitting of the $a$-modes into co- and counter-rotating modes. The higher-frequency branches of these modes approach known $i$-mode frequencies. In general the lower-frequency branches are harder to track, owing to the dense nature of the oscillation spectrum, but when we are able to identify them we find that they appear to become zero-frequency modes in the $M/T \to 0$ limit.

The presence of these hybrid modes has parallels with other work. The evolutions of Passamonti et al. [110] and Gaertig and Kokkotas [48] found that when tracking $g$-modes (i.e. modes restored by composition gradients within the star) for increasingly rapid rotation, their frequencies approached known $i$-mode frequencies. One key difference between stratified and magnetised stars, however, is the behaviour of the $r$-mode in each case. Being purely axial in the slow-rotation limit, the $r$-modes are unaffected by composition gradients, whereas we have found that the presence of a magnetic field means that in the slow-rotation limit they become the axial $l = m$ $a$-modes.

Our work seems to be consistent with the analysis of Glampedakis and Andersson [51], who found that magnetic fields could act to suppress instabilities driven by gravitational radiation (the CFS instability); and in particular, that purely poloidal or purely toroidal fields should always play a stabilising role in this case. Using $\sigma$ to denote a mode frequency as measured in the rotating frame, it is known that modes satisfying the condition $\sigma(\sigma - m\Omega) < 0$ are susceptible to these radiation-driven instabilities; in particular, this includes the $r$-mode. In the presence of a magnetic field we find that the $r$-mode is replaced by the $l = m$ axial $a$-mode; for sufficiently slow rotation we have $\sigma_a > m\Omega$ and hence the mode is CFS-stable. In the regime where the star is unstable, we use a simple estimate to suggest that the instability's growth will be slower in the presence of a magnetic field.

In addition to the hybrid magneto-inertial modes, there are also magnetic corrections to the $f$-mode frequency. These corrections are very modest ($\sim$1%) even up to field strengths of the order $10^{17}$ gauss. In addition, as for the magneto-inertial modes, the magnetic correction becomes less significant still as $M/T \to 0$. However,

we note that the magnetic correction seems to increase between $m = 2$ and $m = 6$, so although our approach limits us to low $m$ one might expect more appreciable corrections to high-$m$ $f$- and $p$-modes.

Although it would be premature to make a quantitative comparison between our results and observed magnetar QPOs, we note that there are certain similarities in the oscillation spectra. The QPOs observed from SGR 1806-20 include 26 and 30 Hz modes; these cannot be explained as overtones of crustal shear modes because the spacing is too small (they would need to be integer multiples of some fundamental frequency for this). By contrast, it is easy to interpret these frequencies as global modes of a fluid star (i.e. the magnetar's interior), since we see modes at far smaller separation than integer multiples. For example, using our fitted relation (7.4.5) we see that the frequency ratio of the axial ${}^2_2a$ and polar ${}^3_2a_1$ modes is $0.030/0.033 \approx 0.91$ — comparable with the observed ratio of $26/30 \approx 0.87$.

This work adds to the picture of magnetic stellar oscillations built up by a number of other recent numerical studies. The work of Sotani et al. [128] and Cerdá-Durán et al. [19] investigated axial magnetar oscillations, modelling the star's magnetic field as dipolar (and hence purely poloidal). They found two localised families of QPOs, which they related to observed magnetar QPOs. Colaiuda et al. [32] worked on a similar problem, but in the more general case of a mixed poloidal-toroidal background field. Their work complements other studies, but they are also able to identify a third family of QPOs in their model star. Finally, Sotani and Kokkotas [127] find a set of polar oscillations of dipolar fields, agreeing with the work of Lee [89] that a magnetar should have both axial and polar oscillations.

Many of these recent studies have analysed their results in the light of the suggestion that magnetic oscillations of a perfectly-conducting star form a continuum, rather than discrete modes. This was proposed by Levin [90], revisiting earlier work by Goossens [57] and others. Various numerical studies [128, 19, 32] have found results consistent with this proposal, in the case of axial oscillations of a dipole field. However, Sotani and Kokkotas [127] suggest that *polar* oscillations of a dipolar-field star are discrete.

Since our background field is purely toroidal, we cannot make quantitative comparisons with work discussed in the last two paragraphs, since those studies assumed dipolar fields (or mixed poloidal-toroidal fields in the case of Colaiuda et al. [32]). However, we do find broad similarities — in particular, our $a$-mode frequencies are

of the order 100 Hz (for a field of $\sim 10^{16}$ gauss), as found from other magnetic evolutions. With a toroidal field there is less evidence for a continuum of modes, since work on this phenomenon seems to have focussed on fields with a poloidal component. Indeed, all our results have shown discrete mode frequencies, with no dependence on position within the star, up to uncertainties due to resolution and the finite duration of our simulations (in practice, errors of $\lesssim 1\%$). Our polar $a$-modes thus share this property with those of Sotani et al. [128], but our axial $a$-modes are discrete too.

Purely toroidal fields and purely poloidal fields suffer from generic localised instabilities, so in the absence of damping mechanisms are not viable candidates for long-lived stellar magnetic fields [144, 133]. Despite this, we have been able to perform stable evolutions of perturbations about a purely toroidal background for this work. There may be a number of reasons why these analytically-established instabilities have not affected our numerical work. Since we only consider first-order perturbations, higher-order effects are avoided; at the linear level, the greatest instabilities are those for $m = 0$ and $m = 1$, whilst we have only considered $m \geq 2$ oscillations. Finally, we have included artificial viscosity and resistivity to damp numerically-generated instabilities, and it is possible that these have prevented the growth of physical instabilities too.

One way in which pure-poloidal/toroidal fields may be stabilised is through rotation [50, 14, 79], although this effect will be small in the case of the magnetars, whose rotational periods are very long. Relatively small poloidal components may stabilise dominantly toroidal fields [15], but it is difficult to draw general conclusions on the relative strengths of the two components, since other work has found that apparently general constructions of magnetic stars in equilibrium (in both Newtonian and relativistic contexts) result in mixed fields which are dominantly *poloidal*; see chapter 6 and Ciolfi et al. [31].

Given the many uncertainties regarding the nature of stellar magnetic fields, we believe that it is reasonable to study oscillations of purely toroidal fields, even though these may suffer certain instabilities, as we have discussed. Furthermore, a star whose field is dominantly toroidal could be expected to have an oscillation spectrum with similar features to those discussed in this work.

# Chapter 8

# $m = 1$ modes and precession

In literature on neutron star oscillations, the $m = 1$ modes tend to be neglected; this is because those with lowest $l$ (i.e. $l = m = 1$ modes) are dipolar, whereas the lowest-order contributions to gravitational-wave emission are quadrupolar. The primary motivation for this chapter is instead to explore the idea (discussed in section 3.4) that a magnetised fluid star can undergo motion analogous to rigid-body free precession, by looking for oscillation modes at frequencies expected for precession. As we shall show, for small-angle free precession these modes are $m = 1$ to leading order. We describe our approach for exciting precessional modes and suggest reasons why it has so far proved unsuccessful. We additionally present some new results about the nature of $m = 1$ inertial modes in stars approaching break-up frequency, and find some evidence of the unstable nature of purely toroidal fields and the stabilising effect of rotation. We believe that this represents the first evidence of the $m = 1$ Tayler instability from a global analysis ($m = 0$ instabilities were investigated by Kiuchi et al. [79]).

## 8.1 Initial data for precession

Here we consider a precessing configuration as a perturbation away from the stationary background star, and wish to describe this perturbation in terms of the change in the density $\delta\rho$ and velocity field $\mathbf{v}$. We start with an axisymmetric background star which is magnetised and rotating, and hence is distorted by both of these effects; its

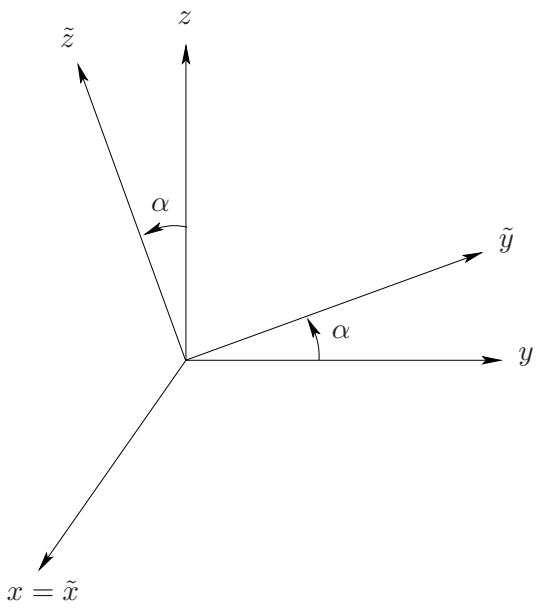


Figure 8.1: The $(x, y, z)$ frame for the unperturbed system and the rotated $(\tilde{x}, \tilde{y}, \tilde{z})$ frame. In the unperturbed configuration the magnetic and rotational distortions are symmetric about $z$; in the perturbed star the magnetic distortion is symmetric about $\tilde{z}$.

density distribution $\rho$ may be written

$$\rho(r, \theta) = \rho_0(r) + \rho_\Omega(r, \theta) + \rho_B(r, \theta) \tag{8.1.1}$$

where $\rho_0$ is the spherical piece of the density distribution, $\rho_\Omega$ the distortion induced by rotation and $\rho_B$ the magnetically-induced distortion. Whilst our numerical method for generating MHD equilibria (see chapter 6) does not allow us to disentangle $\rho_B$ from $\rho_\Omega$, we may look at the variation of $\rho_B$ with field strength $B$ for a *nonrotating* star and assume that the same relation holds to leading order in a rotating star.

Now consider a perturbation about this background $\rho_B$ which has the effect of rotating the magnetic distortion through some angle $\alpha$; the new magnetic density distortion (background plus perturbation) will be denoted by a tilde and is no longer axisymmetric: $\tilde{\rho}_B = \tilde{\rho}_B(r, \theta, \phi)$. Let us work in the Cartesian coordinate system where this perturbative rotation of $\rho_B$ is about the $x$-axis. We emphasise that this rotation is different from the ordinary stellar rotation, whose axis in the unperturbed

star is the original $z$-axis (not $\tilde{z}$). The original and rotated frames are shown in figure 8.1.

Performing the rotation about the $x$-axis, the new rotated axes $\tilde{y}, \tilde{z}$ are related to the original ones $y, z$ by:

$$\begin{aligned} \tilde{y} &= y\cos\alpha + z\sin\alpha \\ \tilde{z} &= z\cos\alpha - y\sin\alpha. \end{aligned}$$

We use $(r, \theta, \phi)$ to denote spherical polar coordinates in the $(x, y, z)$ frame and $(r, \tilde{\theta}, \tilde{\phi})$ for the corresponding coordinates in the $(\tilde{x}, \tilde{y}, \tilde{z})$ frame; note that $r = \tilde{r}$. Now since $r\sin\theta = \sqrt{x^2 + y^2}$, we have

$$r^2 \sin^2\tilde{\theta} = \tilde{x}^2 + \tilde{y}^2. \tag{8.1.2}$$

Using the usual relations between Cartesian and spherical polar coordinates and noting that $\tilde{x} = x$ (since the rotation was about the $x$-axis), we see that the angle transformation is given by

$$\sin^2\tilde{\theta} = (\sin\theta\cos\phi)^2 + (\sin\theta\sin\phi\cos\alpha + \cos\theta\sin\alpha)^2. \tag{8.1.3}$$

To proceed we assume $\alpha \ll 1$ and Taylor expand $\tilde{\rho}_B$:

$$\tilde{\rho}_B(r,\theta,\phi) = \rho_B(r,\tilde{\theta}) = \rho_B(r,\theta) + \frac{\partial\rho_B(r,\theta)}{\partial\theta}(\tilde{\theta}-\theta) + \frac{1}{2!}\frac{\partial^2\rho_B(r,\theta)}{\partial\theta^2}(\tilde{\theta}-\theta)^2 + \dots \tag{8.1.4}$$

Working to linear order, we have

$$\delta\rho = \tilde{\rho}_B(r,\theta,\phi) - \rho_B(r,\theta) = (\tilde{\theta}-\theta)\frac{\partial\rho_B(r,\theta)}{\partial\theta}. \tag{8.1.5}$$

This expression contains both $\theta$ and $\tilde{\theta}$ terms, whereas we want a result referred entirely to the original $(r, \theta, \phi)$ coordinates. However, since $\tilde{\theta} - \theta$ is small we may use a trigonometric identity to write

$$\tilde{\theta} - \theta \approx \sin(\tilde{\theta} - \theta) = \sin\tilde{\theta}\cos\theta - \cos\tilde{\theta}\sin\theta. \tag{8.1.6}$$

We may now use this expression together with (8.1.3) to write our expression for $\delta\rho$ as

$$\begin{aligned} \delta\rho = &\Big[\cos\theta\sqrt{(\sin\theta\cos\phi)^2 + (\sin\theta\sin\phi + \alpha\cos\theta)^2} \\ &- \sin\theta\sqrt{1 - (\sin\theta\cos\phi)^2 - (\sin\theta\sin\phi + \alpha\cos\theta)^2}\Big]\frac{\partial\rho_B}{\partial\theta}, \end{aligned} \tag{8.1.7}$$

where we have made the small-angle approximations $\sin\alpha \approx \alpha$ and $\cos\alpha \approx 1$, and neglected the higher-order $\alpha^2$ terms. The expression may be simplified by using the binomial theorem to expand the square roots; after some algebra we arrive at the result

$$\delta\rho = \alpha \sin\phi \frac{\partial \rho_B}{\partial \theta}. \tag{8.1.8}$$

The $\sin\phi$ factor here tells us that small-angle precession may be regarded as an $m = 1$ perturbation, to leading order.

We now turn to the effect of precession on the velocity field. For the nonprecessing (i.e. rigidly rotating) background star the velocity is $\mathbf{V} = \mathbf{\Omega} \times \mathbf{r}$ and so the precessing configuration has $\tilde{\mathbf{V}} = (\mathbf{\Omega} + \delta\mathbf{\Omega}) \times \mathbf{r}$, where $\delta\mathbf{\Omega}$ is the off-rotation axis perturbation in the angular velocity. The velocity perturbation $\mathbf{v}$ is then simply given by

$$\mathbf{v} = \tilde{\mathbf{V}} - \mathbf{V} = \delta\mathbf{\Omega} \times \mathbf{r}. \tag{8.1.9}$$

Since $\delta\mathbf{\Omega}$ is the piece of the angular velocity that does not have an $\mathbf{e}_z$ component, then by analogy with rigid-body dynamics (see, for example, Jones and Andersson [73]) we have

$$\delta\mathbf{\Omega} = \epsilon_B \alpha \Omega \mathbf{e}_y \tag{8.1.10}$$

to leading order, where $\epsilon_B$ is the (dimensionless) ellipticity induced by the magnetic field. This gives $\mathbf{v} = \epsilon_B \alpha \Omega \mathbf{e}_y \times \mathbf{r}$. Expressing this in terms of spherical polar coordinates we have

$$\mathbf{v} = \epsilon_B \alpha \Omega \begin{pmatrix} 0 \\ r\cos\phi \\ -r\cos\theta\sin\phi \end{pmatrix}. \tag{8.1.11}$$

As for $\delta\rho$, we see that the precession is to leading order an $m = 1$ perturbation. The leading order precessional perturbation in the flux $\mathbf{f} = \rho_0 \mathbf{v}$ is given by

$$\begin{aligned} f_r &= 0 \\ f_\theta &= \epsilon_B \alpha \Omega \rho_0 r \cos\phi \\ f_\phi &= \epsilon_B \alpha \Omega \rho_0 r \cos\theta \sin\phi. \end{aligned} \tag{8.1.12}$$

## 8.2 $m = 1$ modes in an unmagnetised star

Before looking at $m = 1$ oscillations of magnetised stars, we first need to check our code reproduces known results for nonmagnetic modes. Yoshida and Lee [146]

Table 8.1: Comparison between Yoshida-Lee results and those from our time-evolution code run for a dimensionless rotation rate of $\hat{\Omega} = 0.119$. All mode frequencies are made dimensionless through division by $\Omega$ and calculated in the rotating frame of the star. As for the chapter 7 results, our mode labelling is consistent with that of Lockitch and Friedman [93]. In Yoshida and Lee's results, corotating modes are shown with a negative mode frequency, whilst we are only able to find the magnitude. Finally, we were unable to find the ${}^3i_1$ mode, which we believe is due to its proximity in frequency space to the strong $r$-mode peak.

| mode | Yoshida-Lee | time evolution | discrepancy |
|---|---|---|---|
| ${}^1r$ | 1.000 | 1.006 | 0.6% |
| ${}^2i_1$ | -0.4014 | 0.388 | 3.3% |
| ${}^2i_2$ | 1.413 | 1.418 | 0.4% |
| ${}^3i_1$ | -1.032 | - | - |
| ${}^3i_2$ | 0.6906 | 0.684 | 1.0% |
| ${}^3i_3$ | 1.614 | 1.611 | 0.2% |
| ${}^4i_1$ | -1.312 | 1.241 | 5.4% |
| ${}^4i_2$ | -0.1788 | 0.171 | 4.2% |
| ${}^4i_3$ | 1.052 | 1.021 | 2.9% |
| ${}^4i_4$ | 1.726 | 1.738 | 0.7% |

included results for $m = 1$ oscillations in their study of inertial modes of slowly rotating stars. For our code, the rotation rate is specified through the oblateness of the star (see section 6.4) and so the minimum rotation rate is limited by grid spacing; the polar radius needs to be one cell smaller than the equatorial radius. This means we cannot quite study the $\Omega \to 0$ limit. In addition, we work in the Cowling approximation, which Yoshida and Lee do not. This could be expected to cause fairly large errors in some cases, since the Cowling approximation is poorer for low $m$. Notwithstanding these differences of approach, we find convincing agreement with their work; see table 8.1.

One oddity of the $m = 1$ spectrum is that there is no $f$-mode; a dipolar mode with no radial node displaces the centre of mass of the star. The absence of the $f$-mode could be expected by looking at the analogous case for incompressible fluids:

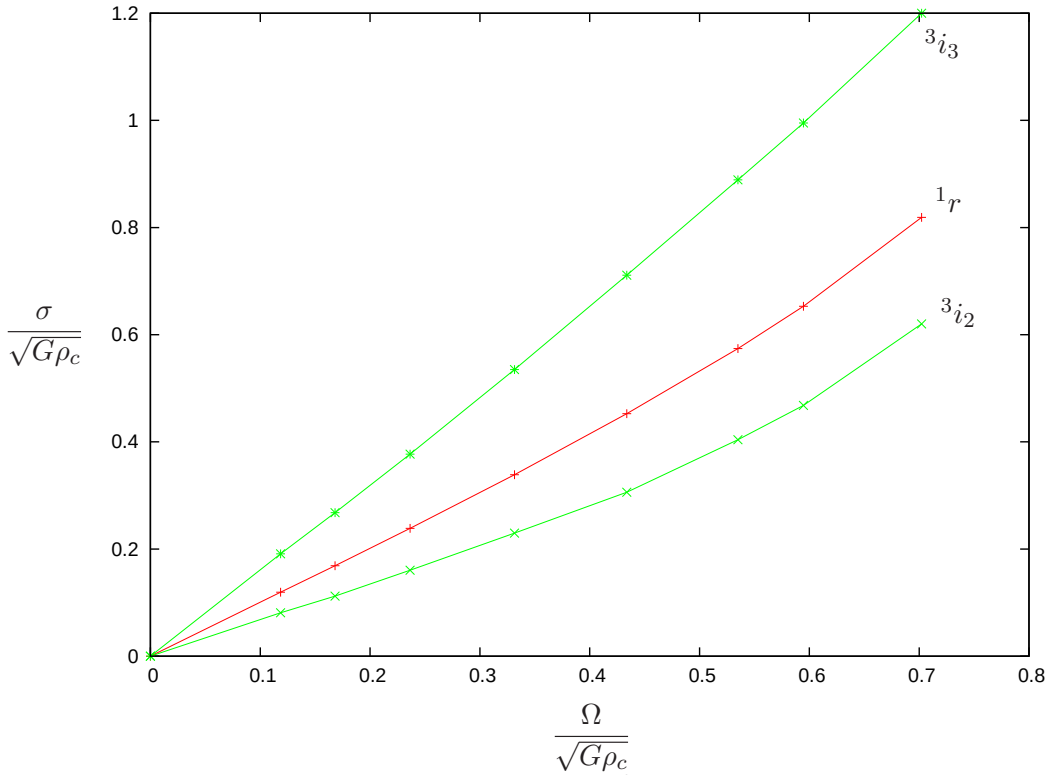


Figure 8.2: Axial-led $m = 1$ inertial modes. The $^3i_1$ mode is missing; it seems to be obscured in the spectrum by the nearby $r$-mode, which has a very strong peak.

the Kelvin mode. It was shown in section 5.2 that this mode has frequency

$$\sigma^2 \propto \frac{2l(l-1)}{(2l+1)}, \tag{8.2.1}$$

which is zero when $l = 1$. However, if one makes the Cowling approximation then an $f$-mode *does* appear in the frequency spectrum, in its usual place between the (pressure) $p$-modes and the (gravity) $g$-modes. This spurious mode shifts to become the lowest-order $g$-mode in the full non-Cowling problem [30].

In addition to finding nine of the ten $m = 1$ inertial modes described by Yoshida and Lee, we also see the spurious $f$-mode described above. Since our background configuration is generated in a nonlinear manner, we are able to track the inertial modes up to break-up velocity, where the results of Yoshida and Lee are no longer valid. We also see avoided crossings between four of the polar inertial modes and the corotating branch of the $f$-mode. These results are shown in figures 8.2 and 8.3.

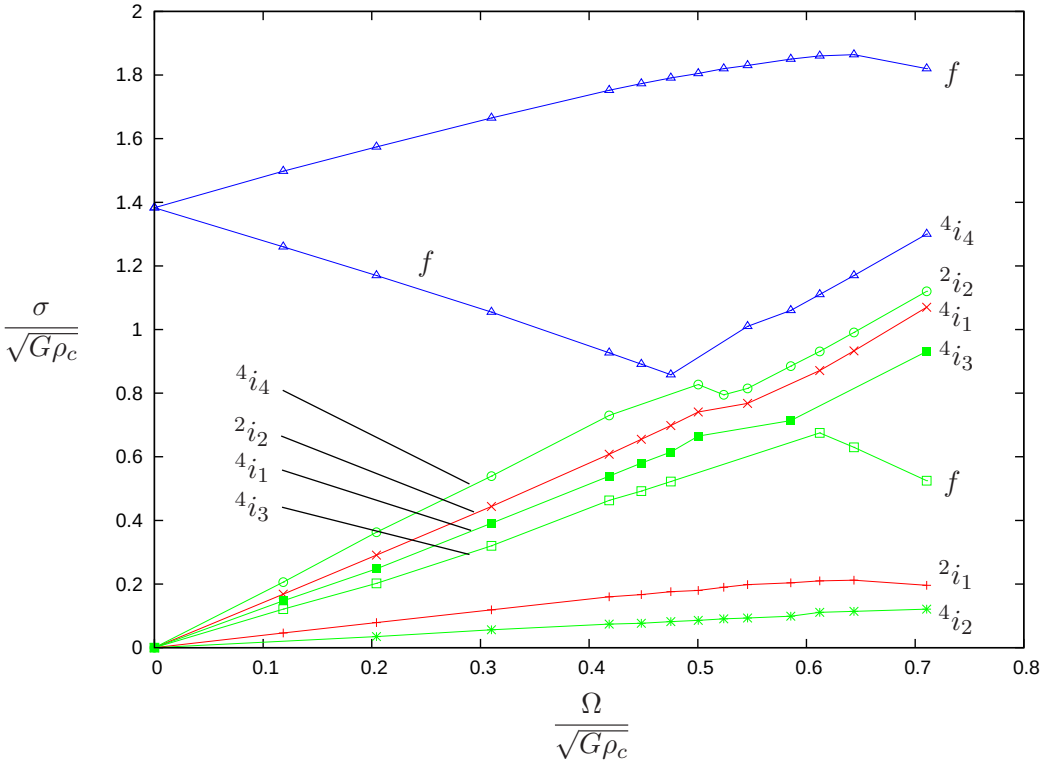


Figure 8.3: Polar-led $m = 1$ inertial modes and the spurious $f$-mode, which has zero frequency in the full problem but appears as an oscillation mode of the Cowling-approximation system of equations. Four of the inertial modes have avoided crossings with the corotating branch of the $f$-mode, where their character changes; note the difference in labelling of these modes before and after the avoided crossings.

## 8.3 Instabilities in purely toroidal fields

In the previous section we established that our time evolution code ran stably for unmagnetised backgrounds with $m = 1$, reproducing known results for inertial modes as well as finding the spurious dipolar $f$-mode that is an artefact of making the Cowling approximation. In order to study magnetic precession, we also need to stably evolve magnetic perturbations. There are, however, additional difficulties here; as well as numerical instabilities associated with the evolution of finite-differenced equations, the magnetic field may suffer genuine physical instabilities.

The stability analysis of Tayler [133] established that a large class of toroidal field configurations suffer localised instabilities; earlier calculations than Tayler's had involved a global analysis and hence did not find evidence of the unstable nature of toroidal fields (see, for example, Roxburgh and Durney [120]). Tayler showed that instabilities tend to occur close to the symmetry axis of the star, with $m = 1$ oscillations appearing to be the most unstable in the linear regime. These instabilities occur over short timescales (of the order of the Alfvén crossing time) and also exist for $m \neq 1$ perturbations [58].

More recently, there have been numerical studies of purely toroidal fields. With a local analysis in a small region around the magnetic axis, Braithwaite [14] confirmed the existence of the Tayler instability for generic toroidal fields and found that rotation has a stabilising effect on these fields. This study was in Newtonian gravity, but the later evolutions of Kiuchi et al. [79] found a similar picture for the stability of relativistic stars.

These studies into toroidal-field instabilities contrast with the work of chapter 7, in which we are able to time-evolve perturbations on a purely toroidal background field over long times without seeing evidence of unstable oscillations. However, our analysis is not a local one about the magnetic axis but an evolution of global modes. We add small-magnitude viscosity and resistivity terms in order to suppress numerical instabilities, but these may also damp out genuine unstable oscillations that are present in the continuum solution. Finally, in the work reported earlier in this thesis we only considered $m \geq 2$ oscillation modes, whereas $m = 1$ perturbations are thought to be the most unstable.

To study precession, however, we have to evolve $m = 1$ magnetic perturbations — precisely those thought to suffer most from the Tayler instability in the toroidal-

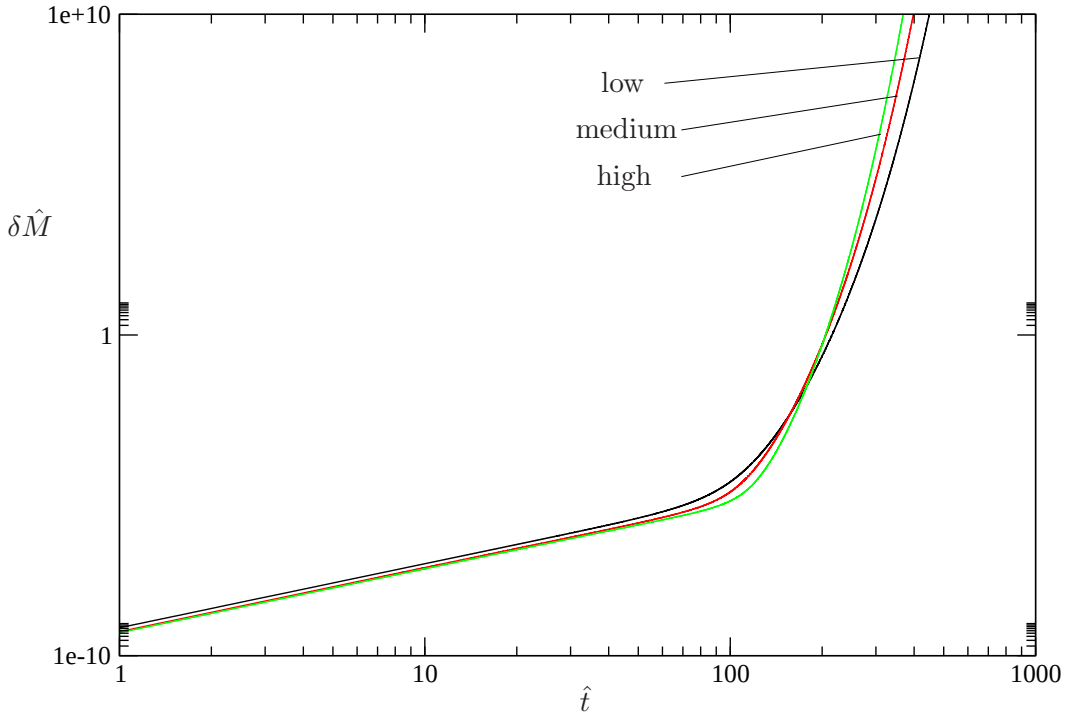


Figure 8.4: The Tayler instability for toroidal magnetic fields in a nonrotating star. We plot the magnetic energy $\delta\hat{M}$ against time $\hat{t}$, both in dimensionless form, for three different grid resolutions. We see that the onset time for the instability is independent of resolution, and its growth rate converges, suggesting that it may indeed be a physical instability. The results are for a star with field strength $\bar{B} = 3.0 \times 10^{16}$ G.

field case. However, it is not clear if we would be better off considering precession in stars with purely poloidal fields instead, since these are also thought to be unstable [96, 144, 50]; neither are all mixed-field configurations likely to be stable [15]. Given this, we choose to continue looking at oscillations of stars with toroidal fields; even if the localised instabilities appear in our evolutions, they should be suppressed by rotation — and in any case, rotation of the background star is required for precession.

Our $m = 1$ evolutions for stars with toroidal fields are consistent with previous work on instabilities. For evolutions with no rotation, we see from the magnetic energy of the perturbations $\delta M$ that the system suffers an instability; see figure 8.4. We compare evolutions for three different grid resolutions: low ($16 \times 15$), medium ($32 \times 30$) and high ($64 \times 60$). In all cases the instability seems to set in at the

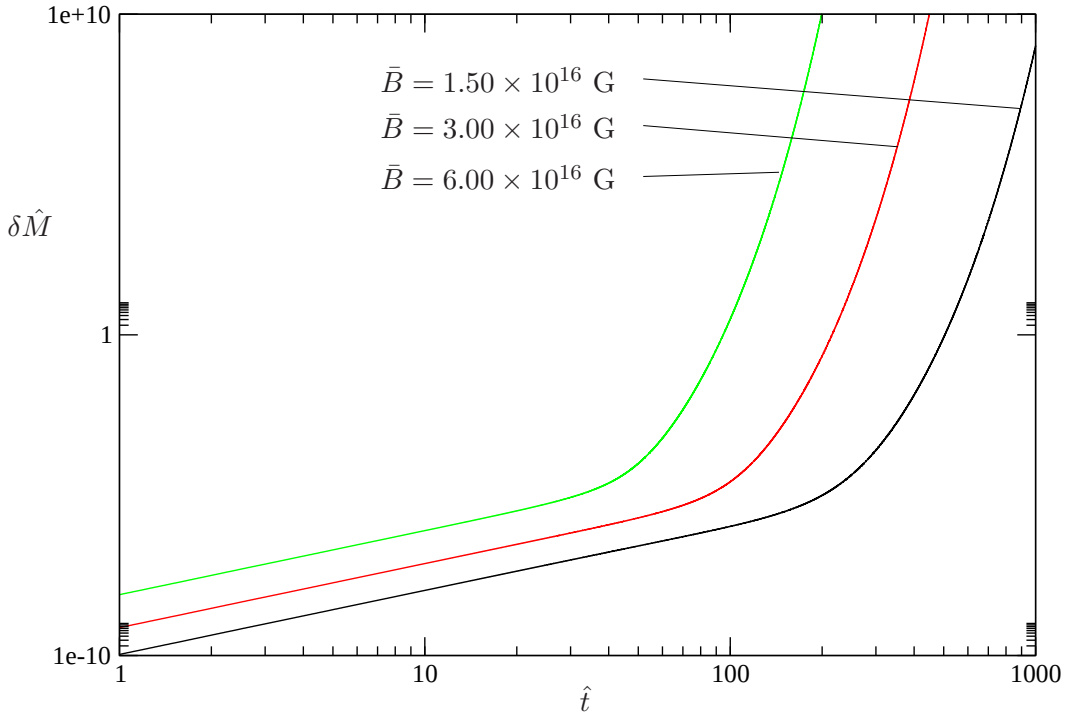


Figure 8.5: Showing that the Tayler instability sets in after one Alfvén crossing time. We plot the magnetic energy against time, as before, and find that the onset of instability happens sooner for higher field strengths; in particular, the observed onset time in each case seems to be close to the Alfvén crossing time: $\hat{\tau}_A \approx 154, 77, 39$ for $\bar{B} = 1.5, 3.0, 6.0 \times 10^{16}$ G respectively.

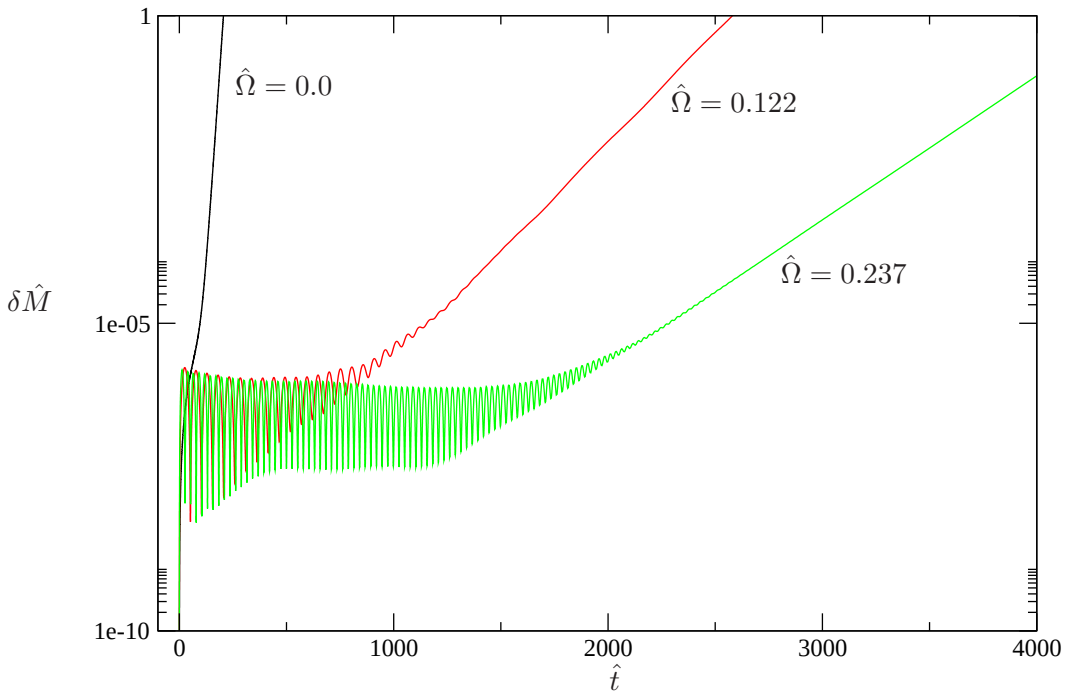


Figure 8.6: The stabilising effect of rotation on purely toroidal magnetic fields. The magnetic energy is plotted against time for three different rotation rates. We see that increasing the rotation rate decreases the growth timescale of the instability; i.e. the gradient of $\delta M$ is reduced in the regime where the instability dominates. As for the previous plot, each configuration has a field strength of $\bar{B} = 3.0 \times 10^{16}$ G.

same point, suggesting it is a physical instability rather than a numerical one. After the onset of instability, it can be seen that the growth rates differ slightly for the different resolutions. By comparing the three gradients, we find that the growth rate converges with resolution at approximately second order (the intended accuracy of the code).

Tayler suggests that the toroidal-field instability uncovered in his work should appear after approximately one Alfvén crossing time, i.e. after

$$\tau_A \approx \frac{2R_*}{<c_A>} = 2R_* \sqrt{\frac{4\pi <\rho>}{\bar{B}^2}}, \tag{8.3.1}$$

using the same notation as in chapter 7. Evaluating this in dimensionless form for a star with field strength $\bar{B} = 3.0 \times 10^{16}$ G gives $\hat{\tau}_A \approx 77$; this is consistent with the results shown in figure 8.4, where $\delta M$ is seen to begin growing rapidly at $\hat{t} \approx 80-100$. To check that this is not a coincidence, we plot the results for three different field strengths in figure 8.5. As expected, in each case the instability appears to set in after one Alfvén crossing time.

Further evidence that we are seeing the Tayler instability is the behaviour of our $m = 1$ toroidal-field evolutions in the presence of rotation. This is expected to reduce the effect of the Tayler instability, which is what we find. In figure 8.6 we compare the behaviour of $\delta M$ in rotating and nonrotating evolutions. We see that the instability becomes visible at considerably later times when the rotation rate of the background star is increased; this is because the growth of the instability has been slowed by rotation. Comparing the gradients of the three lines in the regime when the instability dominates any stable modes, we may estimate the growth timescales. We find that for $\hat{\Omega} = 0.122$ the growth timescale is 14 times that of the nonrotating case; when $\hat{\Omega} = 0.237$ it is 22 times the nonrotating timescale.

In summary then, when numerically evolving $m = 1$ perturbations on a background star with a purely toroidal magnetic field, we find an instability sets in at early times. We have reason to believe that this is a genuine physical effect, rather than just a numerical instability, since it bears many of the hallmarks of the instability described by Tayler [133]. In particular, it sets in after approximately one Alfvén crossing time (independent of numerical resolution), its growth rate seems to be convergent and it is reduced by the effect of rotation.

## 8.4 A numerical approach to magnetised-fluid precession

In the rigid-body precession case, the precession period $T_{prec}$ is related to the rotational period $T_\Omega$ by

$$T_{prec} = \frac{T_\Omega}{\epsilon_B}, \tag{8.4.1}$$

for small wobble angle; see subsection 3.4.1. The precession frequency (in rad $s^{-1}$) is therefore

$$\omega_{prec} = \frac{2\pi\epsilon_B}{T_\Omega}. \tag{8.4.2}$$

Our expectation from the work of section 8.1 is that evolutions of $m = 1$ perturbations on a rotating magnetised background star should show evidence of precession — that is, oscillations whose frequency is approximately given by (8.4.2). The idea is to identify precession-like modes from these evolutions, and compare their frequencies with the rigid-body result (8.4.2); this would then help us understand to what degree the motion of a rotating magnetised fluid star resembles free precession — a problem we discussed with an analytic approach in section 3.4.

Unfortunately, we have been unable to convincingly identify oscillation modes corresponding to magnetised-fluid precession from our evolutions; that is, we have been unable to track low-frequency peaks that scale linearly with $\Omega$ and $\epsilon_B$. This is despite having analytic arguments for the existence of such modes (see section 3.4), as well as a code which we know performs well for nonmagnetic $m = 1$ oscillations (see section 8.2) and magnetic $m \geq 2$ oscillations (see chapter 7).

The chief difficulties in resolving precession modes are related to the fact that the precession frequency is very low — it is proportional to the ellipticity $\epsilon_B$ induced by the magnetic field. Although we are able to evolve perturbations on background fields up to around $\bar{B} \sim 10^{17}$ G, the correponding ellipticity in this maximum case is still only around 0.02; this gives a precession period of $T_{prec} = 50T_\Omega$. To resolve a precession peak reasonably accurately, we need to run the code for several precession periods; let us say 10 is the minimum acceptable number. This means that in the optimal case, we still need an evolution whose duration is 500 rotation periods. Over such long evolutions, the energy of the perturbations decreases to a small fraction of its original value, due to dissipative effects in the code. Hence, any precession-mode peak in Fourier space may be very weak and indistinguishable from noise.

A secondary issue is the inherent instability of $m = 1$ perturbations on purely toroidal-field backgrounds, although we are able to overcome this by looking at rapidly rotating configurations.

Although the topic of precession in a magnetised fluid star is an old one, it is still relevant for our understanding of neutron star dynamics. The fluid interiors of neutron stars seem to have the necessary physics to undergo precession — strong magnetic fields and rotation — but few candidates for precession exist among them (see chapter 3). A better understanding of the internal dynamics of a magnetised fluid could shed light on this issue, and would also be relevant to discussion of other classes of star (magnetised-fluid precession was first studied in the context of main-sequence stars [100, 129]). Although the work reported here and in section 3.4 has not yet borne fruit, we believe it could form the basis of a more thorough study into the problem.

# Chapter 9

# Discussion

Among the many extreme aspects of neutron star physics is the exceptional strength their magnetic fields can reach. In this thesis we have focussed on two particular roles magnetic fields can play in neutron stars: the distortions they induce in the star's equilibrium structure and their effect on the oscillation spectrum. We have also discussed how a fluid star may precess by virtue of its magnetic field.

We begin with two introductory chapters: chapter 1 discusses general aspects of neutron star physics and their potential as gravitational wave sources, whilst chapter 2 is a review of theory and observations related to magnetic effects in neutron stars. These chapters provide two main sources of motivation for studying magnetic fields in neutron stars. Firstly, magnetically-induced distortions in neutron stars may produce gravitational waves of a detectable amplitude; secondly, the inclusion of magnetic effects is likely to be necessary to understand the observed oscillations of magnetars.

A third motivating factor for modelling magnetised neutron stars, related to the other two, is the idea that magnetic distortions could allow a fluid star to undergo motion similar to rigid-body precession. Chapter 3 is predominantly a review of aspects of neutron star precession and some analytic work, beginning with a calculation of the gravitational-wave signal which would be expected from a precessing neutron star. We present the first-order calculation, following the work of Zimmermann [148], but note that it would be more interesting to detect second-order effects in the GW spectrum — from these we should gain direct information about the star's wobble angle and asymmetries [17].

Following the calculation of GWs in a precessing star, we look at the effect of damping the precession. This leads to one of two final outcomes. The first is that the star becomes an aligned rotator, with its axis of distortion (for example, the magnetic axis) aligned with the rotation axis. This is a stationary configuration and hence does not produce gravitational radiation. More interestingly, precession damping may result in an orthogonal rotator — the optimal configuration for gravitational-wave emission.

At the end of chapter 3, we discussed Mestel's work on magnetised-fluid precession [100, 99]. The idea is that a fluid star gains some rigidity from a magnetic field and hence is able to maintain an distortion not aligned with the rotation axis. Such a star might be expected to undergo motion similar to rigid-body precession. However, since the star is not *completely* rigid, the actual motion will deviate from precession. We argue that Mestel's approach to understanding this fluid precession is not fully consistent and relies on assumptions which are not valid in a neutron star. We conclude by suggesting ways to rectify this, to give a better description of the dynamics of the magnetised fluid interior of a neutron star.

We continue with analytic work in chapter 4, where we present calculations of rotational and magnetic distortions. These will give us an indication of what results to expect from the numerical work of chapter 6. We begin with a perturbative calculation for the effect of rotation on the density distribution of a $N = 1$ polytropic star, then use the tensor virial theorem to find formulae for the ellipticities of a rotating magnetised incompressible ($N = 0$) star, following the work of Ostriker and Gunn [106]. We show that these formulae lead to the result that poloidal fields induce oblate distortions and toroidal fields induce prolate ones. Although our work is in the context of incompressible stars, we establish in chapter 6 that the same result holds for compressible-fluid stars too.

Chapter 5, the last of the three chapters of analytic work, is an introduction to stellar oscillation modes. We provide calculations of two mode frequencies: those of the Kelvin mode and the $r$-mode. Although all the results in this chapter are well established, they are helpful for understanding the more complicated problem of modes in a magnetised star; this is studied numerically in chapter 7.

Chapter 6, a numerical study of equilibrium configurations for rotating magnetised stars, is the first chapter of the thesis containing a substantial amount of new material. We begin by looking at the equations of MHD in axisymmetry, showing

that they reduce to two cases: one describing mixed-field configurations and another for purely toroidal fields. The mixed-field case is given by the Grad-Shafranov equation [60, 124] which describes axisymmetric MHD in terms of two scalar functions; setting one of these to zero gives a purely-poloidal field case. The toroidal field case is described with only one scalar function. Although it initially appears that there is considerable freedom in choosing these magnetic functions, we show that virtually all choices are ruled out on physical grounds. In practice, we are left with only one general form for each function.

Next in chapter 6, we describe how to convert the equations of axisymmetric MHD into forms that can be numerically integrated. These are solved iteratively to find stationary equilibrium configurations. For ease of comparison, we present all results for the same physical neutron star model, which has the canonical mass of $1.4M_{\odot}$ and (in the nonrotating, unmagnetised case) a radius of 10 km.

Since our code is non-linear, we are able to look at the realm of validity of the perturbative regime, where the magnetically-induced distortion $\epsilon$ is assumed to depend linearly on $B^2$; we find that this is a good approximation up to $B \sim 10^{17}$ G. This suggests that a good model of the neutron star's field is more important than including $\mathcal{O}(B^4)$ terms for ellipticity calculations. We give approximate linear-regime relations using our work and compare these with the analytic work of Haskell et al. [64].

Starting with a spherical unmagnetised star, we find that in the purely poloidal-field case the ellipticity initially increases with increasing field strength (as expected), but only up to some peak value of $B \sim 5 \times 10^{17}$ G, corresponding to $\epsilon \sim 0.8$. If $\epsilon$ is increased beyond this point, the field strength required actually drops again (though remains of the order of $10^{17}$ G). We believe this behaviour can be explained by looking at the density distribution of the star as the field strength is increased. To begin with the star is distorted into an oblate spheroid, but around the point where $\epsilon \sim 0.8$ the density distribution seems to curve in at the poles. For higher $\epsilon$ the density around the pole is distorted further, leaving the star becoming more torus-shaped. This leads us to speculate that at $\epsilon \sim 0.8$ it becomes energetically favourable for the star to change from a spheroidal to a toroidal profile. Since the peak-field stationary axisymmetric configuration we have found has $B \sim 5 \times 10^{17}$ G, a (hypothetical) configuration with higher $B$ may either have no stationary equilibrium solution or may be non-axisymmetric. For the purely toroidal case, we

do not see a similar peaking when looking at field strength versus ellipticity; however, in this case the greatest distortions we are able to calculate are rather smaller — around $\epsilon \sim 0.35$.

We have argued that the equations solved in chapter 6 should give generic solutions for axisymmetric magnetised stars. However, we find that although it is possible to find solutions with purely poloidal or purely toroidal fields, the range of mixed-field solutions is very limited, with the poloidal component dominating. This result is not peculiar to our work: Ciolfi et al.'s study [31] of mixed fields in relativistic stars, using a perturbative approach and minimal-energy arguments for fixed magnetic helicity, found the toroidal component only reached around 10% of the total magnetic energy.

We suggest, based on the results of our work and a number of other studies [64, 145, 39, 31], that the boundary conditions play an important role in determining the relative strength of the two field components. In particular, when the poloidal component extends outside the star it seems to dominate the total magnetic energy; when it is confined within the star the toroidal component seems larger (in all cases the toroidal field has to be confined to avoid exterior magnetic current).

The numerical simulations of Braithwaite [15] suggest that a stable magnetic field will have a toroidal component between 20% and 95% of the total magnetic energy — suggesting that *none* of the solutions that exist within our axisymmetric formalism are stable. However, these simulations employ a magnetic diffusivity term (added for numerical stability) which is high in the outer part of the star and for the exterior; given this, we believe it is difficult to judge the general validity of Braithwaite's stability criteria.

Although we regard our boundary condition as the most natural for our infinitely-conducting fluid star, real neutron stars are not entirely fluid or perfect conductors. In moving from the fluid interior to the crust and magnetosphere, the resistivity of the medium increases and hence the boundary condition should be adapted to reflect this. If the relative strength of the magnetic field components is influenced by boundary conditions in the way we suggest, then configurations including resistivity may differ greatly from the perfect-MHD models discussed above.

In chapter 7 we investigate oscillation modes of fluid neutron stars with rotation and magnetic fields, specialising to the case of purely toroidal background fields. Using the work of chapter 6 to generate our background configurations means we

are able to study the oscillation spectrum of rapidly rotating and highly magnetised stars in a self-consistent manner. This is done by time-evolving the perturbation equations of the system on these background stars.

When a magnetic field is added to a nonrotating star we find a number of Alfvén ($a$-) modes, a class of stellar oscillation restored by the Lorentz force. These modes are purely magnetic in nature only for a nonrotating background star.

In a rotating magnetised star, we find that the pure $a$-modes of a nonrotating star (or equivalently, the purely inertial modes of an unmagnetised star) are replaced by hybrid magneto-inertial modes, whose character is governed by the ratio of the magnetic and kinetic energies. The presence of these hybrid modes has parallels with other work. The evolutions of Passamonti et al. [110] and Gaertig and Kokkotas [48] found that the pure $g$-modes of stratified nonrotating stars became hybrids with inertial-mode character in the rotating case.

In addition to the hybrid magneto-inertial modes, there are also magnetic corrections to the $f$-mode frequency, although these are very modest ($\sim$1%) even for field strengths up to around $10^{17}$ gauss. We also find evidence that the presence of magnetic fields reduces the effect of the CFS instability, as suggested by Glampedakis and Andersson [51].

One feature of magnetic oscillations we do not see in our work is the continuous mode spectrum of perfect MHD; we find only global, discrete, modes. It is known that the continuum can be broken by resistivity [70], so one possible explanation is that the artificial resistivity we employ for numerical stability is having this unintended effect. However, real neutron stars will also have some (albeit small) level of resistivity, which may give them an entirely discrete oscillation spectrum.

Finally, in chapter 8 we discuss $m = 1$ evolutions; the work of chapter 7 considers only $m \geq 2$ modes. The main motivation for the work reported in this chapter is to try to investigate numerically the problem discussed at the end of chapter 3: how similar magnetised-fluid precession is to the familiar rigid-body form. We begin by showing that to leading order, small-angle precession may be regarded as an $m = 1$ perturbation about a rotating magnetised axisymmetric background. The derived form of the perturbation may then be used as initial data for evolutions, with the hope that this data will efficiently excite precession-like modes. The idea is to first establish that such modes exist — i.e., that a magnetised fluid can undergo precession-like motion — and then evaluate the deviation of the actual mode

frequencies from the rigid-body result. This would then go some way to resolving the problem considered by Mestel.

In practice, we have not seen convincing precessional modes from the results of our evolutions. The main difficulty is probably that any such modes will have very low frequencies — they are proportional to the (small) magnetic distortion — and hence very long evolutions are needed to resolve a useful number (e.g. 10) of precession periods. After such long evolutions, the energy of the perturbations has decreased considerably and this may lead to any precession mode being too weak to find. Alternatively, it may simply be that the actual motion of a magnetised fluid differs too much from precession for it to be seen close to the expected rigid-body frequency.

Despite having no conclusive evidence for precession, the evolutions of chapter 8 have produced other interesting results. Firstly, to confirm that our code performs correctly we compare our $m = 1$ inertial-mode frequencies with those of Yoshida and Lee [146]. We find good agreement for slow rotation, where Yoshida and Lee's work is valid, but are also able to look at the behaviour of these modes for fast rotation — as high as $\sim 95\%$ of the star's break-up velocity. We also find evidence for the $m = 1$ Tayler instability of purely toroidal magnetic fields. We believe this is the first time the instability has been seen from a global analysis; the $m = 0$ instability was investigated by Kiuchi et al. [79]. As expected, we find that the instability sets in after approximately one Alfvén crossing time, is resolution-independent (suggesting that it is not simply a numerical instability) and is stabilised through rotation.

The work reported in this thesis could be extended in a variety of ways. Chapter 6 describes a method for numerically solving the MHD equilibrium equations; the code built on this is nonlinear and hence can find equilibria of stars up to break-up velocity and with extremely strong magnetic fields. In principle, we could also include any extra physics that is expressible in integral form; we believe, for example, that models of superconducting stars could be studied in this manner.

In a similar way, the work of chapter 7 could also be extended. Most obviously, a straightforward modification of the equatorial boundary conditions should allow us to study oscillations of stars with purely poloidal fields; whilst mixed-field stars could be investigated by extending the numerical grid. More advanced work might include time evolutions of magnetised stars with stratification or superfluid effects.

Finally, the work of chapters 3 and 8 could prove the foundation of a more

thorough study into precession-like effects in magnetised fluid stars. This could help our understanding of the dynamics of neutron star interiors, in particular. Of separate interest in chapter 8 is the possibility that we have found the Tayler instability for toroidal fields using a global perturbative study, where most work has only uncovered it from a local analysis.

# Appendix A

# The decomposed MHD perturbation equations

## A.1 The evolution equations

After performing a $\phi$-decomposition of the perturbation equations described in chapter 7, we are left with a system of fourteen equations in the fourteen perturbation variables — the components of the flux $\mathbf{f}$, the density perturbation $\delta\rho$ and the magnetic function $\boldsymbol{\beta}$. These equations are given here for completeness.

$$
\begin{aligned}
\partial_t f_r^+ &= -\frac{1}{\rho^2}(\gamma-2)\gamma P\delta\rho^+\rho_{,r} - \frac{1}{\rho}\gamma P\delta\rho^+_{,r} + 2\Omega\sin\theta f_\phi^+ \\
&\quad -\frac{1}{4\pi r\rho^2}B_\theta\beta_r^+\rho_{,\theta} \;+\; \frac{1}{4\pi\rho^2}\left(B_\theta\beta_\theta^+ + B_\phi\beta_\phi^+\right)\rho_{,r} \\
&\quad +\frac{1}{4\pi r\rho}\Big[B_\theta^2\delta\rho^+ + B_\phi^2\delta\rho^+ + \beta_\theta^+ B_{r,\theta} - r\beta_\theta^+ B_{\theta,r} - r\beta_\phi^+ B_{\phi,r} \\
&\qquad +B_\theta\left(-2\beta_\theta^+ + \beta^+_{r,\theta} + \delta\rho^+\left(-B_{r,\theta} + rB_{\theta,r}\right) - r\beta^+_{\theta,r}\right) \\
&\qquad +B_\phi\left(\frac{m}{\sin\theta}\;\beta_r^- - 2\beta_\phi^+ + r\delta\rho^+ B_{\phi,r} - r\beta^+_{\phi,r}\right)\Big] \qquad \text{(A.1.1)} \\
\partial_t f_r^- &= -\frac{1}{\rho^2}(\gamma-2)\gamma P\delta\rho^-\rho_{,r} - \frac{1}{\rho}\gamma P\delta\rho^-_{,r} + 2\Omega\sin\theta f_\phi^- \\
&\quad -\frac{1}{4\pi r\rho^2}B_\theta\beta_r^-\rho_{,\theta} \;+\; \frac{1}{4\pi\rho^2}\left(B_\theta\beta_\theta^- + B_\phi\beta_\phi^-\right)\rho_{,r} \\
&\quad +\frac{1}{4\pi r\rho}\Big[B_\theta^2\delta\rho^- + B_\phi^2\delta\rho^- + \beta_\theta^- B_{r,\theta} - r\beta_\theta^- B_{\theta,r} - r\beta_\phi^- B_{\phi,r} \\
&\qquad +B_\theta\left(-2\beta_\theta^- + \beta^-_{r,\theta} + \delta\rho^-\left(-B_{r,\theta} + rB_{\theta,r}\right) - r\beta^-_{\theta,r}\right) \\
&\qquad +B_\phi\left(-\frac{m}{\sin\theta}\;\beta_r^+ - 2\beta_\phi^- + r\delta\rho^- B_{\phi,r} - r\beta^-_{\phi,r}\right)\Big] \qquad \text{(A.1.2)} \\
\partial_t f_\theta^+ &= -\frac{1}{r\rho^2}(\gamma-2)\gamma P\delta\rho^+\rho_{,\theta} - \frac{1}{r\rho}\gamma P\delta\rho^+_{,\theta} + 2\Omega\cos\theta f_\phi^+ \\
&\quad -\frac{1}{4\pi\rho^2}B_r\beta_\theta^+\rho_{,r} \;+\; \frac{1}{4\pi r\rho^2}\left(B_r\beta_r^+ + B_\phi\beta_\phi^+\right)\rho_{,\theta} \\
&\quad +\frac{1}{4\pi r\rho}\Big[\frac{1}{\tan\theta}B_\phi^2\delta\rho^+ + B_\theta(\beta_r^+ - B_r\delta\rho^+) - \beta_\phi^+ B_{\phi,\theta} + \beta_r^+(-B_{r,\theta} + rB_{\theta,r}) \\
&\qquad +B_\phi\left(\frac{m}{\sin\theta}\beta_\theta^- - \frac{2}{\tan\theta}\beta_\phi^+ + \delta\rho^+ B_{\phi,\theta} - \beta^+_{\phi,\theta}\right) \\
&\qquad +B_r\left(\beta_\theta^+ - \beta^+_{r,\theta} + \delta\rho^+(B_{r,\theta} - rB_{\theta,r}) + r\beta^+_{\theta,r}\right)\Big] \qquad \text{(A.1.3)} \\
\partial_t f_\theta^- &= -\frac{1}{r\rho^2}(\gamma-2)\gamma P\delta\rho^-\rho_{,\theta} - \frac{1}{r\rho}\gamma P\delta\rho^-_{,\theta} + 2\Omega\cos\theta f_\phi^- \\
&\quad -\frac{1}{4\pi\rho^2}B_r\beta_\theta^-\rho_{,r} \;+\; \frac{1}{4\pi r\rho^2}\left(B_r\beta_r^- + B_\phi\beta_\phi^-\right)\rho_{,\theta} \\
&\quad +\frac{1}{4\pi r\rho}\Big[\frac{1}{\tan\theta}B_\phi^2\delta\rho^- + B_\theta(\beta_r^- - B_r\delta\rho^-) - \beta_\phi^- B_{\phi,\theta} + \beta_r^-(-B_{r,\theta} + rB_{\theta,r}) \\
&\qquad +B_\phi\left(-\frac{m}{\sin\theta}\beta_\theta^+ - \frac{2}{\tan\theta}\beta_\phi^- + \delta\rho^- B_{\phi,\theta} - \beta^-_{\phi,\theta}\right) \\
&\qquad +B_r\left(\beta_\theta^- - \beta^-_{r,\theta} + \delta\rho^-(B_{r,\theta} - rB_{\theta,r}) + r\beta^-_{\theta,r}\right)\Big] \qquad \text{(A.1.4)}
\end{aligned}
$$

$$
\begin{aligned}
\partial_t f_\phi^+ &= -\frac{1}{r\rho}\frac{m}{\sin\theta}\gamma P\delta\rho^- - 2\Omega(\cos\theta f_\theta^+ + \sin\theta f_r^+) \\
&\quad -\frac{1}{4\pi r\rho^2}\beta_\phi^+(B_\theta\rho_{,\theta} + rB_r\rho_{,r}) + \frac{1}{4\pi\rho}\beta_r^+ B_{\phi,r} \\
&\quad +\frac{1}{4\pi r\rho}\Bigg[B_\phi\left(\beta_r^+ + \frac{1}{\tan\theta}\beta_\theta^+\right) + \beta_\theta^+ B_{\phi,\theta} \\
&\qquad +B_\theta\left(-\frac{m}{\sin\theta}\beta_\theta^- + \frac{1}{\tan\theta}\beta_\phi^+ - \delta\rho^+\left(\frac{1}{\tan\theta}B_\phi + B_{\phi,\theta}\right) + \beta_{\phi,\theta}^+\right) \\
&\qquad +B_r\left(-\frac{m}{\sin\theta}\beta_r^- + \beta_\phi^+ + r\beta_{\phi,r}^+ - \delta\rho^+(B_\phi + rB_{\phi,r})\right)\Bigg] \qquad \text{(A.1.5)} \\
\partial_t f_\phi^- &= \frac{1}{r\rho}\frac{m}{\sin\theta}\gamma P\delta\rho^+ - 2\Omega(\cos\theta f_\theta^- + \sin\theta f_r^-) \\
&\quad -\frac{1}{4\pi r\rho^2}\beta_\phi^-(B_\theta\rho_{,\theta} + rB_r\rho_{,r}) + \frac{1}{4\pi\rho}\beta_r^- B_{\phi,r} \\
&\quad +\frac{1}{4\pi r\rho}\Bigg[B_\phi\left(\beta_r^- + \frac{1}{\tan\theta}\beta_\theta^-\right) + \beta_\theta^- B_{\phi,\theta} \\
&\qquad +B_\theta\left(\frac{m}{\sin\theta}\beta_\theta^+ + \frac{1}{\tan\theta}\beta_\phi^- - \delta\rho^-\left(\frac{1}{\tan\theta}B_\phi + B_{\phi,\theta}\right) + \beta_{\phi,\theta}^-\right) \\
&\qquad +B_r\left(\frac{m}{\sin\theta}\beta_r^+ + \beta_\phi^- + r\beta_{\phi,r}^- - \delta\rho^-(B_\phi + rB_{\phi,r})\right)\Bigg] \qquad \text{(A.1.6)}
\end{aligned}
$$

$$
\partial_t\delta\rho^+ = -\frac{2}{r}f_r^+ - \frac{1}{r\tan\theta}f_\theta^+ - \frac{m}{r\sin\theta}f_\phi^- - \frac{1}{r}f_{\theta,\theta}^+ - f_{r,r}^+ \qquad \text{(A.1.7)}
$$

$$
\partial_t\delta\rho^- = -\frac{2}{r}f_r^- - \frac{1}{r\tan\theta}f_\theta^- + \frac{m}{r\sin\theta}f_\phi^+ - \frac{1}{r}f_{\theta,\theta}^- - f_{r,r}^- \qquad \text{(A.1.8)}
$$

$$\begin{aligned}
\partial_t \beta_r^+ &= \frac{1}{r\rho}(-B_\theta f_r^+ + B_r f_\theta^+)\rho_{,\theta} \\
&\quad + \frac{1}{r}\Big[\frac{m}{\sin\theta}B_\phi f_r^- - f_\theta^+\left(\frac{1}{\tan\theta}B_r + B_{r,\theta}\right) + f_r^+ B_{\theta,\theta} \\
&\qquad + B_\theta\left(\frac{1}{\tan\theta}f_r^+ + f_{r,\theta}^+\right) - B_r\left(\frac{m}{\sin\theta}f_\phi^- + f_{\theta,\theta}^+\right)\Big] \qquad \text{(A.1.9)} \\
\partial_t \beta_r^- &= \frac{1}{r\rho}(-B_\theta f_r^- + B_r f_\theta^-)\rho_{,\theta} \\
&\quad + \frac{1}{r}\Big[-\frac{m}{\sin\theta}B_\phi f_r^+ - f_\theta^-\left(\frac{1}{\tan\theta}B_r + B_{r,\theta}\right) + f_r^- B_{\theta,\theta} \\
&\qquad + B_\theta\left(\frac{1}{\tan\theta}f_r^- + f_{r,\theta}^-\right) - B_r\left(-\frac{m}{\sin\theta}f_\phi^+ + f_{\theta,\theta}^-\right)\Big] \qquad \text{(A.1.10)} \\
\partial_t \beta_\theta^+ &= \frac{1}{\rho}(B_\theta f_r^+ - B_r f_\theta^+)\rho_{,r} + f_\theta^+ B_{r,r} - f_r^+ B_{\theta,r} \\
&\quad + \frac{1}{r}\Big[\frac{m}{\sin\theta}B_\phi f_\theta^- + B_r(f_\theta^+ + r f_{\theta,r}^+) \\
&\qquad - B_\theta\left(f_r^+ + \frac{m}{\sin\theta}f_\phi^- + r f_{r,r}^+\right)\Big] \qquad \text{(A.1.11)} \\
\partial_t \beta_\theta^- &= \frac{1}{\rho}(B_\theta f_r^- - B_r f_\theta^-)\rho_{,r} + f_\theta^- B_{r,r} - f_r^- B_{\theta,r} \\
&\quad + \frac{1}{r}\Big[-\frac{m}{\sin\theta}B_\phi f_\theta^+ + B_r(f_\theta^- + r f_{\theta,r}^-) \\
&\qquad - B_\theta\left(f_r^- - \frac{m}{\sin\theta}f_\phi^+ + r f_{r,r}^-\right)\Big] \qquad \text{(A.1.12)} \\
\partial_t \beta_\phi^+ &= \frac{1}{r\rho}(B_\phi f_\theta^+ - B_\theta f_\phi^+)\rho_{,\theta} + \frac{1}{\rho}(B_\phi f_r^+ - B_r f_\phi^+)\rho_{,r} - f_r^+ B_{\phi,r} + B_r f_{\phi,r}^+ \\
&\quad + \frac{1}{r}\Big[-f_\theta^+ B_{\phi,\theta} + B_\theta f_{\phi,\theta}^+ \\
&\qquad + f_\phi^+(B_r + B_{\theta,\theta} + r B_{r,r}) - B_\phi(f_r^+ + f_{\theta,\theta}^+ + r f_{r,r}^+)\Big] \qquad \text{(A.1.13)} \\
\partial_t \beta_\phi^- &= \frac{1}{r\rho}(B_\phi f_\theta^- - B_\theta f_\phi^-)\rho_{,\theta} + \frac{1}{\rho}(B_\phi f_r^- - B_r f_\phi^-)\rho_{,r} - f_r^- B_{\phi,r} + B_r f_{\phi,r}^- \\
&\quad + \frac{1}{r}\Big[-f_\theta^- B_{\phi,\theta} + B_\theta f_{\phi,\theta}^- \\
&\qquad + f_\phi^-(B_r + B_{\theta,\theta} + r B_{r,r}) - B_\phi(f_r^- + f_{\theta,\theta}^- + r f_{r,r}^-)\Big] \qquad \text{(A.1.14)}
\end{aligned}$$

## A.2 Artificial resistivity

As described in section 7.3.4, we find that a small amount of artificial resistivity helps to provide long-term stable evolution of the perturbed magnetic field. The induction equation may be written as

$$\frac{\partial \mathbf{B}}{\partial t} = \nabla \times (\mathbf{v} \times \mathbf{B}) - \eta \nabla \times (\nabla \times \mathbf{B}) \tag{A.2.1}$$

where $\eta$ is the resistivity. Note that this reduces to the correct perfect-MHD limit in the absence of resistivity ($\eta \to 0$) but *not* in the limit $\eta \to \infty$; however only the former limit concerns us here. By including this resistive term at small magnitude we are able to stabilise the magnetic evolutions without concern that it will pollute the results of what is meant to be a perfect-MHD time evolution; when $\eta$ is small, resistive effects will occur over a long timescale.

Throughout chapter 7 we have worked with $\boldsymbol{\beta} = \rho_0 \delta\mathbf{B}$, but since $\nabla \times (\nabla \times (\boldsymbol{\beta}/\rho))$ is rather messy we use $\delta\mathbf{B}$ itself to express the resistive term, the components of which are:

$$\begin{aligned}
[\nabla \times (\nabla \times \delta\mathbf{B})]^+_r &= \frac{1}{r^2}\Bigg[ \delta B^+_{\theta,\theta} - \delta B^+_{r,\theta\theta} + r\,\delta B^+_{\theta,r\theta} \\
&\quad + \frac{1}{\tan\theta}\left( \delta B^+_{\theta} - \delta B^+_{r,\theta} + r\,\delta B^+_{\theta,r} \right) \\
&\quad + \frac{m}{\sin\theta}\left( \frac{m}{\sin\theta}\,\delta B^+_{r} + \delta B^-_{\phi} + r\,\delta B^-_{\phi,r} \right) \Bigg] \qquad \text{(A.2.2)} \\
[\nabla \times (\nabla \times \delta\mathbf{B})]^-_r &= \frac{1}{r^2}\Bigg[ \delta B^-_{\theta,\theta} - \delta B^-_{r,\theta\theta} + r\,\delta B^-_{\theta,r\theta} \\
&\quad + \frac{1}{\tan\theta}\left( \delta B^-_{\theta} - \delta B^-_{r,\theta} + r\,\delta B^-_{\theta,r} \right) \\
&\quad + \frac{m}{\sin\theta}\left( \frac{m}{\sin\theta}\,\delta B^-_{r} - \delta B^+_{\phi} - r\,\delta B^+_{\phi,r} \right) \Bigg] \qquad \text{(A.2.3)}
\end{aligned}$$

$$
\begin{aligned}
[\nabla\times(\nabla\times\delta\mathbf{B})]^{+}_{\theta} &= \frac{m}{r^2\sin\theta}\left(\frac{m}{\sin\theta}\,\delta B^{+}_{\theta}+\frac{1}{\tan\theta}\,\delta B^{-}_{\phi}+\delta B^{-}_{\phi,\theta}\right)\\
&\quad+\frac{1}{r}\left(-2\,\delta B^{+}_{\theta,r}+\delta B^{+}_{r,r\theta}-r\,\delta B^{+}_{\theta,rr}\right) \qquad \text{(A.2.4)}\\
[\nabla\times(\nabla\times\delta\mathbf{B})]^{-}_{\theta} &= \frac{m}{r^2\sin\theta}\left(\frac{m}{\sin\theta}\,\delta B^{-}_{\theta}-\frac{1}{\tan\theta}\,\delta B^{+}_{\phi}-\delta B^{+}_{\phi,\theta}\right)\\
&\quad+\frac{1}{r}\left(-2\,\delta B^{-}_{\theta,r}+\delta B^{-}_{r,r\theta}-r\,\delta B^{-}_{\theta,rr}\right) \qquad \text{(A.2.5)}\\
[\nabla\times(\nabla\times\delta\mathbf{B})]^{+}_{\phi} &= \frac{1}{r^2}\Bigg(-\frac{m}{\sin\theta\tan\theta}\,\delta B^{-}_{\theta}+\frac{1}{\sin^2\theta}\,\delta B^{+}_{\phi}\\
&\qquad+\frac{m}{\sin\theta}\,\delta B^{-}_{\theta,\theta}-\frac{1}{\tan\theta}\,\delta B^{+}_{\phi,\theta}-\delta B^{+}_{\phi,\theta\theta}\Bigg)\\
&\quad+\frac{1}{r}\left(\frac{m}{\sin\theta}\,\delta B^{-}_{r,r}-2\,\delta B^{+}_{\phi,r}-r\,\delta B^{+}_{\phi,rr}\right) \qquad \text{(A.2.6)}\\
[\nabla\times(\nabla\times\delta\mathbf{B})]^{-}_{\phi} &= \frac{1}{r^2}\Bigg(\frac{m}{\sin\theta\tan\theta}\,\delta B^{+}_{\theta}+\frac{1}{\sin^2\theta}\,\delta B^{-}_{\phi}\\
&\qquad-\frac{m}{\sin\theta}\,\delta B^{+}_{\theta,\theta}-\frac{1}{\tan\theta}\,\delta B^{-}_{\phi,\theta}-\delta B^{-}_{\phi,\theta\theta}\Bigg)\\
&\quad+\frac{1}{r}\left(-\frac{m}{\sin\theta}\,\delta B^{+}_{r,r}-2\,\delta B^{-}_{\phi,r}-r\,\delta B^{-}_{\phi,rr}\right) \qquad \text{(A.2.7)}
\end{aligned}
$$

# Bibliography


[1] A. Alpar and H. Ögelman. Neutron Star Precession and the Dynamics of the Superfluid Interior. *Astron. Astrophys.*, **185**:196–202, 1987.

[2] P.W. Anderson and N. Itoh. Pulsar Glitches and Restlessness as a Hard Superfluidity Phenomenon. *Nature*, **256**:25–27, 1975.

[3] N. Andersson. Gravitational Waves from Instabilities in Relativistic Stars. *Class. Quantum Grav.*, **20**:R105–R144, 2003.

[4] N. Andersson, V. Ferrari, D.I. Jones, K.D. Kokkotas, B. Krishnan, J. Read, L. Rezzolla, and B. Zink. Gravitational Waves from Neutron Stars: Promises and Challenges. *arXiv:0912.0384*, 2009.

[5] N. Andersson and K.D. Kokkotas. The $r$-mode Instability in Rotating Neutron Stars. *International Journal of Modern Physics D*, **10**:381–441, 2001.

[6] G.B. Arfken and H.J. Weber. *Mathematical Methods for Physicists*. Harcourt Academic Press, 2001.

[7] W. Baade and F. Zwicky. Remarks on Super-Novae and Cosmic Rays. *Phys. Rev.*, **46**:76–77, 1934.

[8] G. Baym and C. Pethick. Neutron Stars. *Annu. Rev. Nucl. Sci.*, **25**:27–77, 1975.

[9] G. Baym and C. Pethick. Physics of Neutron Stars. *Ann. Rev. Astron. Astrophys.*, **17**:415–443, 1979.

[10] M. Bocquet, S. Bonazzola, E. Gourgoulhon, and J. Novak. Rotating Neutron Star Models with a Magnetic Field. *Astron. Astrophys.*, **301**:757–775, 1995.

[11] I. Bombaci. The Maximum Mass of a Neutron Star. *Astron. Astrophys.*, **305**:871–877, 1996.

[12] S. Bonazzola and E. Gourgoulhon. Gravitational Waves from Pulsars: Emission by the Magnetic Field Induced Distortion. *Astron. Astrophys.*, **312**:675–690, 1996.

[13] J.U. Brackbill and D.C. Barnes. The Effect of Nonzero $\nabla \cdot \mathbf{B}$ on the Numerical Solution of the Magnetohydrodynamic Equations. *J. Comp. Phys.*, **35**:426–430, 1980.

[14] J. Braithwaite. The Stability of Toroidal Fields in Stars. *Astron. Astrophys.*, **453**:687–698, 2006.

[15] J. Braithwaite. Axisymmetric Magnetic Fields in Stars: Relative Strengths of Poloidal and Toroidal Components. *Mon. Not. R. Astron. Soc.*, **397**:763–774, 2009.

[16] J. Braithwaite and Å. Nordlund. Stable Magnetic Fields in Stellar Interiors. *Astron. Astrophys.*, **450**:1077–1095, 2006.

[17] C. Van Den Broeck. The Gravitational Wave Spectrum of Non-Axisymmetric, Freely Precessing Neutron Stars. *Class. Quantum Grav.*, **22**:1825–1839, 2005.

[18] G.H. Bryan. The Waves on a Rotating Liquid Spheroid of Finite Ellipticity. *Phil. Trans. Roy. Soc. London*, **180**:187–219, 1889.

[19] P. Cerdá-Durán, N. Stergioulas, and J.A. Font. Alfvén QPOs in Magnetars in the Anelastic Approximation. *Mon. Not. R. Astron. Soc.*, **397**:1607–1620, 2009.

[20] S. Chandrasekhar. The Highly Collapsed Configurations of a Stellar Mass. *Mon. Not. R. Astron. Soc.*, **91**:456–466, 1931.

[21] S. Chandrasekhar. The Equilibrium of Distorted Polytropes I. *Mon. Not. R. Astron. Soc.*, **93**:390–406, 1933.

[22] S. Chandrasekhar. *An Introduction to the Study of Stellar Structure*. Univ. of Chicago Press, 1939.

[23] S. Chandrasekhar. *Hydrodynamic and Hydromagnetic Stability.* Dover, 1961.

[24] S. Chandrasekhar. A General Variational Principle Governing the Radial and the Non-Radial Oscillations of Gaseous Masses. *Astrophys. J.*, **139**:664–674, 1964.

[25] S. Chandrasekhar. Solutions of Two Problems in the Theory of Gravitational Radiation. *Phys. Rev. Lett.*, **24**:611–615, 1970.

[26] S. Chandrasekhar and E. Fermi. Problems of Gravitational Stability in the Presence of a Magnetic Field. *Astrophys. J.*, **118**:116–141, 1953.

[27] S. Chandrasekhar and N.R. Lebovitz. The Potentials and the Superpotentials of Homogeneous Ellipsoids. *Astrophys. J.*, **136**:1037–1047, 1962.

[28] S. Chandrasekhar and D.N. Limber. On the Pulsation of a Star in which There is a Prevalent Magnetic Field. *Astrophys. J.*, **119**:10–13, 1954.

[29] S. Chandrasekhar and K.H. Prendergast. The Equilibrium of Magnetic Stars. *Proc. Nat. Acad. Sci.*, **42**:5–9, 1956.

[30] J. Christensen-Dalsgaard and D.O. Gough. On the Dipolar $f$-mode of Stellar Oscillation. *Mon. Not. R. Astron. Soc.*, **326**:1115–1121, 2001.

[31] R. Ciolfi, V. Ferrari, L. Gualtieri, and J.A. Pons. Relativistic Models of Magnetars: the Twisted Torus Magnetic Field Configuration. *Mon. Not. R. Astron. Soc.*, **397**:913–924, 2009.

[32] A. Colaiuda, H. Beyer, and K.D. Kokkotas. On the Quasi-Periodic Oscillations in Magnetars. *Mon. Not. R. Astron. Soc.*, **396**:1441–1448, 2009.

[33] T.G. Cowling. The Non-Radial Oscillations of Polytropic Stars. *Mon. Not. R. Astron. Soc.*, **101**:367–375, 1941.

[34] J.P. Cox. *Theory of Stellar Pulsation.* Princeton University Press, 1980.

[35] C. Cutler. Gravitational Waves from Neutron Stars with Large Toroidal $B$ Fields. *Phys. Rev. D*, **66**:084025, 2002.

[36] C. Cutler, G. Ushomirsky, and B. Link. The Crustal Rigidity of a Neutron Star and Implications for PSR B1828-11 and Other Precession Candidates. *Astrophys. J.*, **588**:975–991, 2003.

[37] P.A. Davidson. *An Introduction to Magnetohydrodynamics*. Cambridge University Press, 2001.

[38] A. Dedner, F. Kemm, D.Kröner, C.-D. Munz, T. Schnitzer, and M. Wesenberg. Hyperbolic Divergence Cleaning for the MHD Equations. *J. Comp. Phys.*, **175**:645–673, 2009.

[39] V. Duez and S. Mathis. Relaxed Equilibrium Configurations to Model Fossil Fields I - A First Family. *arXiv:0904.1568*, 2010.

[40] R.C. Duncan and C. Thompson. Formation of Very Strongly Magnetized Neutron Stars — Implications for Gamma-Ray Bursts. *Astrophys. J.*, **392**:L9–L13, 1992.

[41] W.A. Dziembowski and P.R. Goode. Magnetic Effects on Oscillations in roAp Stars. *Astrophys. J.*, **458**:338–346, 1996.

[42] A. Einstein. Die Feldgleichungen der Gravitation. *Sitz. Preuss. Akad. Wiss. Berlin*, pages 844–847, 1915.

[43] V.C.A. Ferraro. On the Equilibrium of Magnetic Stars. *Astrophys. J.*, **119**:407–412, 1954.

[44] L.S. Finn. $g$-modes in Zero-Temperature Neutron Stars. *Mon. Not. R. Astron. Soc.*, **227**:265–293, 1987.

[45] D. Sigg (for the LIGO Science Collaboration). Status of the LIGO Detectors. *Class. Quantum Grav.*, **25**:114041, 2008.

[46] J.L. Friedman and B.F. Schutz. Lagrangian Perturbation Theory of Nonrelativistic Fluids. *Astrophys. J.*, **221**:937–957, 1978.

[47] J.L. Friedman and B.F. Schutz. Secular Instability of Rotating Newtonian Stars. *Astrophys. J.*, **222**:281–296, 1978.

[48] E. Gaertig and K.D. Kokkotas. Relativistic $g$-modes in Rapidly Rotating Neutron Stars. *Phys. Rev. D*, **80**:064026, 2009.

[49] D.V. Gal'tsov and V.P. Tsvetkov. On the Gravitational Radiation of an Oblique Rotator. *Phys. Lett. A*, **103**:193–196, 1984.

[50] U. Geppert and M. Rheinhardt. Magnetars Versus Radio Pulsars. MHD Stability in Newborn Highly Magnetized Neutron Stars. *Astron. Astrophys.*, **456**:639–649, 2006.

[51] K. Glampedakis and N. Andersson. Lagrangian Perturbation Theory for Rotating Magnetic Stars. *Mon. Not. R. Astron. Soc.*, **377**:630–644, 2007.

[52] K. Glampedakis, N. Andersson, and D.I. Jones. Stability of Precessing Superfluid Neutron Stars. *Phys. Rev. Lett.*, **100**:081101, 2008.

[53] N.K. Glendenning. *Compact Stars: Nuclear Physics, Particle Physics, and General Relativity*. Springer, 2nd edition, 2000.

[54] T. Gold. Rotating Neutron Stars as the Origin of the Pulsating Radio Sources. *Nature*, **218**:731–732, 1968.

[55] P. Goldreich and W.H. Julian. Pulsar Electrodynamics. *Astrophys. J.*, **157**:869–880, 1969.

[56] M. Goossens. Perturbations of the Radial and Non-Radial Oscillations of a Star by a Magnetic Field. *Astrophys. Space Sci.*, **16**:386–404, 1972.

[57] M. Goossens, S. Poedts, and D. Hermans. On the Existence of the Continuous Spectrum of Ideal MHD in a 2D Magnetostatic Equilibrium. *Solar Phys.*, **102**:51–66, 1985.

[58] M. Goossens and R.J. Tayler. On Unstably Stratified Toroidal Magnetic Fields in Stars. *Mon. Not. R. Astron. Soc.*, **193**:833–848, 1980.

[59] H. Grad. Magnetofluid-Dynamic Spectrum and Low Shear Stability. *Proc. Nat. Acad. Sci.*, **70**:3277–3281, 1973.

[60] H. Grad and H. Rubin. Hydromagnetic Equilibria and Force-Free Fields. In *Proceedings of the 2nd UN Conference on the Peaceful Uses of Atomic Energy*, volume **31**, pages 190–197, United Nations, Geneva, Switzerland, 1958.

[61] I. Hachisu. A Versatile Method for Obtaining Structures of Rapidly Rotating Stars. *Astrophys. J. Suppl.*, **61**:479–507, 1986.

[62] P. Haensel, A.Y. Potekhin, and D.G. Yakovlev. *Neutron Stars 1: Equation of State and Structure*. Springer, 2007.

[63] A.K. Harding and D. Lai. Physics of Strongly Magnetized Neutron Stars. *Rep. Prog. Phys.*, **69**:2631–2708, 2006.

[64] B. Haskell, L. Samuelsson, K. Glampedakis, and N. Andersson. Modelling Magnetically Deformed Neutron Stars. *Mon. Not. R. Astron. Soc.*, **385**:531–542, 2008.

[65] A. Hewish, S.J. Bell, J.D.H. Pilkington, P.F. Scott, and R.A. Collins. Observation of a Rapidly Pulsating Radio Source. *Nature*, **217**:709–713, 1968.

[66] C. Hirsch. *Numerical Computation of Internal and External Flows*. Butterworth-Heinemann Ltd., 2007.

[67] W.C.G. Ho and D. Lai. Atmospheres and Spectra of Strongly Magnetized Neutron Stars. *Mon. Not. R. Astron. Soc.*, **327**:1081–1096, 2001.

[68] R.A. Hulse and J.H. Taylor. Discovery of a Pulsar in a Binary System. *Astrophys. J.*, **195**:51–53, 1975.

[69] K. Ioka. Magnetic Deformation of Magnetars for the Giant Flares of the Soft Gamma-Ray Repeaters. *Mon. Not. R. Astron. Soc.*, **327**:639–662, 2001.

[70] R.C. Ireland, R.A.M. Van der Linden, A.W. Hood, and M. Goossens. The Thermal Continuum in Coronal Loops: the Influence of Finite Resistivity on the Continuous Spectrum. *Solar Phys.*, **142**:265–289, 1992.

[71] G.L. Israel, T. Belloni, L. Stella, Y. Rephaeli, D.E. Gruber, P. Casella, S. Dall'Osso, N. Rea, M. Persic, and R.E. Rothschild. The Discovery of Rapid X-Ray Oscillations in the Tail of the SGR 1806-20 Hyperflare. *Astrophys. J.*, **628**:L53–L56, 2005.

[72] D.I. Jones. Gravitational Wave Emission from Rotating Superfluid Neutron Stars. *Mon. Not. R. Astron. Soc.*, **402**:2503–2519, 2010.

[73] D.I. Jones and N. Andersson. Freely Precessing Neutron Stars: Model and Observations. *Mon. Not. R. Astron. Soc.*, **324**:811–824, 2001.

[74] D.I. Jones and N. Andersson. Gravitational Waves from Freely Precessing Neutron Stars. *Mon. Not. R. Astron. Soc.*, **331**:203–220, 2002.

[75] D.I. Jones, N. Andersson, and N. Stergioulas. Time Evolution of the Linear Perturbations of a Rotating Newtonian Polytrope. *Mon. Not. R. Astron. Soc.*, **334**:933–940, 2002.

[76] A.D. Kaminker, D.G. Yakovlev, A.Y. Potekhin, N. Shibazaki, P.S. Shternin, and O.Y. Gnedin. Cooling of Magnetars with Internal Layer Heating. *Astrophys. Space Sci.*, **308**:423–430, 2007.

[77] W. Thomson (Lord Kelvin). Dynamical Problems Regarding Elastic Spheroidal Shells and Spheroids of Incompressible Liquid. *Phil. Trans. Roy. Soc. London*, **153**:583–616, 1863.

[78] K. Kiuchi and K. Kotake. Equilibrium Configurations of Strongly Magnetized Neutron Stars with Realistic Equations of State. *Mon. Not. R. Astron. Soc.*, **385**:1327–1347, 2008.

[79] K. Kiuchi, M. Shibata, and S. Yoshida. Evolution of Neutron Stars with Toroidal Magnetic Fields: Axisymmetric Simulation in Full General Relativity. *Phys. Rev. D*, **78**:024029, 2008.

[80] K. Kiuchi and S. Yoshida. Relativistic Stars with Purely Toroidal Magnetic Fields. *Phys. Rev. D*, **78**:044045, 2008.

[81] M.M. Komesaroff. Possible Mechanism for the Pulsar Radio Emission. *Nature*, **225**:612, 1970.

[82] H.-O. Kreiss and J. Oliger. Comparison of Accurate Methods for the Integration of Hyperbolic Equations. *Tellus*, **24**:199–215, 1972.

[83] L.D. Landau and E.M. Lifshitz. *Mechanics*. Butterworth-Heinemann Ltd., 1976.

[84] S.K. Lander and D.I. Jones. Magnetic Fields in Axisymmetric Neutron Stars. *Mon. Not. R. Astron. Soc.*, **395**:2162–2176, 2009.

[85] S.K. Lander, D.I. Jones, and A. Passamonti. Oscillations of Rotating Magnetised Neutron Stars with Purely Toroidal Magnetic Fields. *arXiv:0912.3480*, 2009.

[86] J.M. Lattimer and M. Prakash. Neutron Star Structure and the Equation of State. *Astrophys. J.*, **550**:426–442, 2001.

[87] J.M. Lattimer and M. Prakash. The physics of neutron stars. *Science*, **304**:536–542, 2004.

[88] P. Ledoux and R. Simon. Sur les Oscillations d'une Étoile Gazeuse Possédant un Champ Magnétique Faible. *Annales d'Astrophysique*, **20**:185–195, 1957.

[89] U. Lee. Axisymmetric Oscillations of Magnetic Neutron Stars. *Mon. Not. R. Astron. Soc.*, **374**:1015–1029, 2007.

[90] Y. Levin. On the Theory of Magnetar QPOs. *Mon. Not. R. Astron. Soc.*, **377**:159–167, 2007.

[91] Y. Levin and C. D'Angelo. Hydromagnetic and Gravitomagnetic Crust-Core Coupling in a Precessing Neutron Star. *Astrophys. J.*, **613**:1157–1163, 2004.

[92] B. Link and R.I. Epstein. Precession Interpretation of the Isolated Pulsar PSR B1828-11. *Astrophys. J.*, **556**:392–398, 2001.

[93] K.H. Lockitch and J.L. Friedman. Where Are the $r$-modes of Isentropic Stars? *Astrophys. J.*, **521**:764–788, 1999.

[94] A.G. Lyne and F. Graham-Smith. *Pulsar Astronomy*. Cambridge University Press, 1998.

[95] R.N. Manchester, G.B. Hobbs, A. Teoh, and M. Hobbs. The Australia Telescope National Facility Pulsar Catalogue. *Astronom. J.*, **129**:1993–2006, 2005.

[96] P. Markey and R.J. Tayler. The Adiabatic Stability of Stars Containing Magnetic Fields — II. Poloidal Fields. *Mon. Not. R. Astron. Soc.*, **163**:77–91, 1973.

[97] R.W. McCormack. The Effect of Viscosity in Hypervelocity Impact Cratering. *AIAA*, Paper 69-354, 1969.

[98] P.N. McDermott, H.M. Van Horn, and J.F. Scholl. Nonradial $g$-mode Oscillations of Warm Neutron Stars. *Astrophys. J.*, **268**:837–848, 1983.

[99] L. Mestel, J. Nittmann, W.P. Wood, and G.A.E. Wright. The Internal Dynamics of the Oblique Rotator II. *Mon. Not. R. Astron. Soc.*, **195**:979–1000, 1981.

[100] L. Mestel and H.S. Takhar. The Internal Dynamics of the Oblique Rotator. *Mon. Not. R. Astron. Soc.*, **156**:419–436, 1972.

[101] M.J. Miketinac. Structure of Polytropic Models of Stars Containing Poloidal Magnetic Fields. *Astrophys. Space Sci.*, **35**:349–362, 1975.

[102] C.W. Misner, K.S. Thorne, and J.A. Wheeler. *Gravitation*. Freeman, 1973.

[103] J.J. Monaghan. Magnetic Fields in Stellar Bodies: I. Magnetic Fields in Polytropes. *Mon. Not. R. Astron. Soc.*, **131**:105–119, 1965.

[104] S.M. Morsink and V. Rezania. Normal Modes of Rotating Magnetic Stars. *Astrophys. J.*, **574**:908–919, 2002.

[105] J.R. Oppenheimer and G.M. Volkoff. On Massive Neutron Cores. *Phys. Rev.*, **55**:374–381, 1939.

[106] J.P. Ostriker and J.E. Gunn. On the Nature of Pulsars I: Theory. *Astrophys. J.*, **157**:1395–1417, 1969.

[107] J.P. Ostriker and F.D.A. Hartwick. Rapidly Rotating Stars. IV. Magnetic White Dwarfs. *Astrophys. J.*, **153**:797–806, 1968.

[108] J.P. Ostriker and J.W-K. Mark. Rapidly Rotating Stars. I. The Self-Consistent Field Method. *Astrophys. J.*, **151**:1075–1088, 1968.

[109] J. Papaloizou and J.E. Pringle. Non-Radial Oscillations of Rotating Stars and Their Relevance to the Short-Period Oscillations of Cataclysmic Variables. *Mon. Not. R. Astron. Soc.*, **182**:423–442, 1978.

[110] A. Passamonti, B. Haskell, N. Andersson, D.I. Jones, and I. Hawke. Oscillations of Rapidly Rotating Stratified Neutron Stars. *Mon. Not. R. Astron. Soc.*, **394**:730–741, 2009.

[111] J.A. Pons, J.A. Miralles, and U. Geppert. Magneto-thermal Evolution of Neutron Stars. *Astron. Astrophys.*, **496**:207–216, 2009.

[112] K.H. Prendergast. The Equilibrium of a Self-Gravitating Incompressible Fluid Sphere with a Magnetic Field. *Astrophys. J.*, **123**:498–507, 1956.

[113] D.J. Price and J.J. Monaghan. Smoothed Particle Magnetohydrodynamics - III. Multidimensional Tests and the $\nabla \cdot \mathbf{B} = 0$ Constraint. *Mon. Not. R. Astron. Soc.*, **364**:384–406, 2005.

[114] D.G. Ravenhall, C.J. Pethick, and J.R. Wilson. Structure of Matter below Nuclear Saturation Density. *Phys. Rev. Lett.*, **50**:2066–2069, 1983.

[115] J.W. Strutt (Lord Rayleigh). On a Theorem Analogous to the Virial Theorem. *Phil. Mag.*, **50**:210–213, 1900.

[116] A. Reisenegger and P. Goldreich. A New Class of $g$-modes in Neutron Stars. *Astrophys. J.*, **395**:240–249, 1992.

[117] F. Rincon and M. Rieutord. Oscillations of Magnetic Stars: I. Axisymmetric Shear Alfvén Modes of a Spherical Shell in a Dipolar Magnetic Field. *Astron. Astrophys.*, **398**:663–675, 2003.

[118] P.H. Roberts. The Equilibrium of Magnetic Stars. *Astrophys. J.*, **122**:508–512, 1955.

[119] I.W. Roxburgh. Magnetostatic Equilibrium of Polytropes. *Mon. Not. R. Astron. Soc.*, **132**:347–358, 1966.

[120] I.W. Roxburgh and B.R. Durney. The Effect of a Toroidal Magnetic Field on the Radial Oscillations of Stars. *Mon. Not. R. Astron. Soc.*, **135**:329–337, 1967.

[121] M. Ruderman. Pulsar Wobble and Neutron Starquakes. *Nature*, **225**:838–839, 1970.

[122] H. Saio. $r$-Mode Oscillations in Uniformly Rotating Stars. *Astrophys. J.*, **256**:717–735, 1982.

[123] B.F. Schutz. Gravitational Wave Astronomy. *Class. Quantum Grav.*, **16**:A131–A156, 1999.

[124] V.D. Shafranov. On Magnetohydrodynamical Equilibrium Configurations. *Soviet Phys. JETP*, **6**:545–554, 1958.

[125] J. Shaham. Free Precession of Neutron Stars: Role of Possible Vortex Pinning. *Astrophys. J.*, **214**:251–260, 1977.

[126] S. Shapiro and S. Teukolsky. *Black Holes, White Dwarfs and Neutron Stars.* John Wiley and Sons, 1983.

[127] H. Sotani and K.D. Kokkotas. Alfvén Polar Oscillations of Relativistic Stars. *Mon. Not. R. Astron. Soc.*, **395**:1163–1172, 2009.

[128] H. Sotani, K.D. Kokkotas, and N. Stergioulas. Alfvén Quasi-Periodic Oscillations in Magnetars. *Mon. Not. R. Astron. Soc.*, **385**:L5–L9, 2008.

[129] L. Spitzer. Influence of Fluid Motions on the Decay of an External Magnetic Field. *Astrophys. J.*, **125**:525–534, 1957.

[130] L. Stella, S. Dall' Osso, G.L. Israel, and A. Vecchio. Gravitational Radiation from Newborn Magnetars in the Virgo Cluster. *Astrophys. J.*, **634**:L165–L168, 2005.

[131] N. Stergioulas, T.A. Apostolatos, and J.A. Font. Non-linear Pulsations in Differentially Rotating Neutron Stars: Mass-shedding-induced Damping and Splitting of the Fundamental Mode. *Mon. Not. R. Astron. Soc.*, **352**:1089–1101, 2004.

[132] K. Strobel and M.K. Weigel. On the Minimum and Maximum Mass of Neutron Stars and the Delayed Collapse. *Astron. Astrophys.*, **367**:582–587, 2001.

[133] R.J. Tayler. The Adiabatic Stability of Stars Containing Magnetic Fields — I. Toroidal Fields. *Mon. Not. R. Astron. Soc.*, **161**:365–380, 1973.

[134] J.H. Taylor and J.M. Weisberg. Further Experimental Tests of Relativistic Gravity Using the Binary Pulsar PSR 1913+16. *Astrophys. J.*, **345**:434–450, 1989.

[135] C. Thompson, M. Lyutikov, and S.R. Kulkarni. Electrodynamics of Magnetars: Implication for the Persistent X-Ray Emission of the Soft Gamma Repeaters and Anomalous X-Ray Pulsars. *Astrophys. J.*, **574**:332–355, 2002.

[136] K.S. Thorne and Y. Gürsel. The Free Precession of Slowly Rotating Neutron Stars: Rigid-Body Motion in General Relativity. *Mon. Not. R. Astron. Soc.*, **205**:809–817, 1983.

[137] Y. Tomimura and Y. Eriguchi. A New Numerical Scheme for Structures of Rotating Magnetic Stars. *Mon. Not. R. Astron. Soc.*, **359**:1117–1130, 2005.

[138] W. Unno, Y. Osaki, H. Ando, H. Saio, and H. Shibahashi. *Nonradial Oscillations of Stars*. University of Tokyo Press, 1989.

[139] I. Wassermann. Precession of Isolated Neutron Stars — II. Magnetic Fields and Type II Superconductivity. *Mon. Not. R. Astron. Soc.*, **341**:1020–1040, 2003.

[140] A.L. Watts and T.E. Strohmayer. Neutron Star Oscillations and QPOs During Magnetar Flares. *Advances in Space Research*, **40**:1446–1452, 2007.

[141] D.G. Wentzel. On the Shape of Magnetic Stars. *Astrophys. J.*, **133**:170–182, 1961.

[142] D.T. Wickramasinghe and L. Ferrario. Magnetism in Isolated and Binary White Dwarfs. *The Publications of the Astron. Soc. of the Pacific*, **112**:873–924, 2000.

[143] L. Woltjer. A Magnetostatic Model for a Compressible Star. *Astrophys. J.*, **131**:227–229, 1960.

[144] G.A.E. Wright. Pinch Instabilities in Magnetic Stars. *Mon. Not. R. Astron. Soc.*, **162**:339–358, 1973.

[145] S. Yoshida and Y. Eriguchi. Equilibrium Configurations of Magnetised Rotating Polytropes: Effects of Strong Toroidal Magnetic Fields in Addition to Poloidal Magnetic Fields. *Astrophys. J. Suppl.*, **164**:156–172, 2006.

[146] S. Yoshida and U. Lee. Inertial Modes of Slowly Rotating Isentropic Stars. *Astrophys. J.*, **529**:997–1010, 2000.

[147] M. Zimmermann. Gravitational Waves from Rotating and Precessing Rigid Bodies: II. General Solutions and Computationally Useful Formulas. *Phys. Rev. D*, **21**:891–898, 1980.

[148] M. Zimmermann and E. Szedenits. Gravitational Waves from Rotating and Precessing Rigid Bodies: Simple Models and Applications to Pulsars. *Phys. Rev. D*, **20**:351–355, 1979.